ROBUST SYNTHESIS AND CONTINUOUS MANUFACTURING OF CARBON NANOTUBE FORESTS AND GRAPHENE FILMS

by

Erik S. Polsen

A dissertation submitted in partial fulfillment
of the requirements for the degree of
Doctor of Philosophy
(Mechanical Engineering)
in the University of Michigan
2013

Doctoral Committee:

Assistant Professor A. John Hart, Chair
Professor L. Jay Guo
Professor Michael J. Solomon
Professor Margaret S. Wooldridge

ACKNOWLEDGEMENTS

My time as a graduate student has been extremely fulfilling and exciting both on professional and personal levels. Attending the University of Michigan has exposed me to so many wonderful people that have great passion for what they do and strive to achieve excellence every day. Thank you to all who have made this thesis possible and who I have shared many wonderful experiences with:

- John Hart for your passion and enthusiasm in research and life, and for being a supportive research advisor that always made time to talk.
- The Air Force Office of Scientific Research, for granting me a National Defense Science and Engineering Graduate (NDSEG) Fellowship (2009-2012).
- The University of Michigan Mechanical Engineering Department, for granting me a Departmental Fellowship and supporting my research from 2008-2009.
- US Army TARDEC, for granting me a long-term training award and financial support.
- Collaborators on CNT and graphene work: Davor Copic, Eric Meshot, Sameh Tawfick, Mostafa Bedewy, Ryan Oliver, Sei Jin Park, Fabrice Laye, Dan McNerny, Adam Stevens, Georges Pavlidis, Prof. Gilbert Nessim at Bar Ilan University, and Desiree Plata at Duke University.
- All of my fellow Mechanosynthesis lab mates.
- My thesis committee: Profs. Jay Guo, Michael Solomon and Margaret Wooldridge.
- My many friends around the country whom I've shared stories and good times.
- My family who was always there when I needed them.
- My wife Leslie for being supportive, making me laugh, and giving me a wonderful daughter (Riley) who always making me smile.
- Last but not least, my mother Kathleen Polsen and my father Ralph Polsen. Thank you for always taking the time to guide me and give me advice on whatever I needed.

TABLE OF CONTENTS

LIST OF FIGURES

LIST OF TABLES

ABSTRACT

Successful translation of the outstanding properties of carbon nanotubes (CNTs) and graphene to commercial applications requires highly consistent methods of synthesis, using scalable and cost-effective machines. This thesis presents robust process conditions and a series of process operations that will enable integrated roll-to-roll (R2R) CNT and graphene growth on flexible substrates.

First, a comprehensive study was undertaken to establish the sources of variation in laboratory CVD growth of CNT forests. Statistical analysis identified factors that contribute to variation in forest height and density including ambient humidity, sample position in the reactor, and barometric pressure. Implementation of system modifications and user procedures reduced the variation in height and density by 50% and 54% respectively.

With improved growth, two new methods for continuous deposition and patterning of catalyst nanoparticles for CNT forest growth were developed, enabling the diameter, density and pattern geometry to be tailored through the control of process parameters. Convective assembly of catalyst nanoparticles in solution enables growth of CNT forests with density 3-fold higher than using sputtered catalyst films with the same growth parameters. Additionally, laser printing of magnetic ink character recognition toner provides a large scale patterning method, with digital control of the pattern density and tunable CNT density *via* laser intensity.

A concentric tube CVD reactor was conceptualized, designed and built for R2R growth of CNT forests and graphene on flexible substrates helically fed through the annular gap. The design enables downstream injection of the hydrocarbon source, and gas consumption is reduced 90% compared to a standard tube furnace. Multi-wall CNT forests are grown continuously on metallic and ceramic fiber substrates at 33 mm/min. High quality, uniform bi- and multi-layer graphene is grown on Cu and Ni foils at 25 - 495 mm/min. A second machine for continuous forest growth and delamination was developed; and forest-substrate adhesion strength was controlled through CVD parameters.

Taken together, these methods enable uniform R2R processing of CNT forests and graphene with engineered properties. Last, it is projected that foreseeable improvements in CNT forest quality and density using these methods will result in electrical and thermal properties that exceed state-of-the-art bulk materials.

CHAPTER 1: BACKGROUND AND OUTLINE

Over the past few decades, nanomaterials have become one of the leading areas of research due to their exceptional mechanical, optical, thermal and electrical characteristics, which provide significant performance increases over their traditional bulk counterparts. These materials, characterized by one or more dimensions below 100 nm, owe their superior characteristics to minimal defect sites within the atomic structures, and the potential wells that provide quantum confinement of the electrons [1].

Carbon nanomaterials have attracted particular interest, and two of the most prevalent nanomaterials in research today are carbon nanotubes (CNTs) and graphene, which are based on graphitic hexagonal carbon lattices comprised of (sp^2) bonds (Figure 1-1). The covalent bonding within this lattice structure enables a high in-plane strength, while interactions normal to the plane are determined by weaker van der Waals forces [2]. Along with their high strength, CNTs and graphene also enable high electrical and thermal conductivities that make them very attractive for multiple applications.

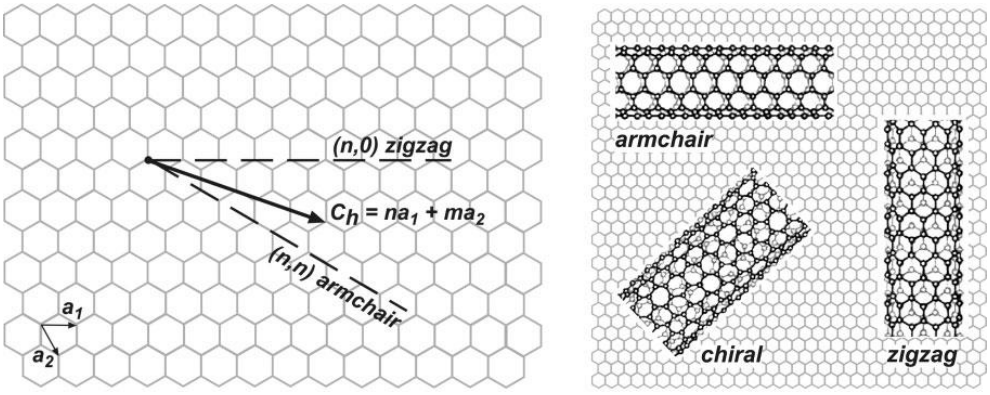

Figure 1-1: Models of graphene and CNT lattice structures [3].

1.1 CNTs

Whether single walled or multi-walled CNTs (SWNTs and MWNTs respectively), the walls of the CNTs can be thought of as a single atomic layer of graphite rolled into a seamless tube. These walls are defined by the chiral vector ($\hat{C}_h$) described by:

$$\hat{C}_h = n\hat{a}_1 + m\hat{a}_2 \quad (1)$$

where n and m are integer steps along the $\hat{a}_1$ and $\hat{a}_2$ unit vectors for the hexagonal lattice (Figure 1-1). While there are many possible values for $\hat{C}_h$, the two limiting cases that are not labeled simply as chiral (i.e., n≠m), produce structures known as armchair and zigzag CNTs, where the integers defined in Equation (1) are (n,n) and (n,0) respectively. The importance of this angle is the fact that for SWNTs it dictates the electrical properties of the CNT, and whether it is metallic or semi-conducting [4]. However, due to the multi-layer structure of MWNTs, having wall spacing similar to that of graphite (0.34 nm), they are always electrically conductive.

CNTs have been shown to have a Young's modulus of ~1.8 TPa [5], which when normalized to material density is ~19 times that of steel [6], simulated and measured thermal conductivities better than that of diamond, ~6000 and 3000 W/mK respectively [7,8], and electrical current densities on the order of 10^7 A/cm^2 with ballistic electron transport over micron length scales at room temperature [9,10]. Because of these exceptional properties, it is no wonder that CNTs have been proposed to replace standard materials such as Cu and Si in applications such as field emission devices [11], electrochemical device interfaces (i.e., batteries and capacitors) [12], sensors [13], hydrogen storage [14], nano- to micro-scale electrical devices [15], and composites [16]. However, while individual CNTs offer significant property benefits over current materials being used in applications, once integrated into a system, CNT density, alignment, and contact with each other and supporting matrix materials often reduce the magnitude of the previously mentioned characteristics.

While recent technological advances in material microscopy led to the characterization of CNTs in the early 1990's [17,18], evidence exists that processing of steel for swords over 400 years ago resulted in the formation of CNTs from nucleation sites in the steel [19]. Additionally, carbon filaments were often noted by others in the deposits of furnaces in the mid-1900's, and

multi-tube and "scroll" structures, formed by arc discharges, were described by Bacon in 1960 [20]. The work of Oberlin et al. [21] and Endo [22] kicked off vapor phase synthesis of carbon filaments, which later became essential for the mass production of CNTs using the floating catalyst technique. Finally, combining the work by Iijima et al. in the early 1990's, with additional TEM analysis by Baker [23] and Bethune et al. [24], helped the emerging CNT community visualize the unique cylindrical morphology of CNTs. Since then, mass manufacturing of MWNT powders has been applied to products such as electrostatic discharge plastics and rechargeable batteries [25], while applications requiring aligned and/or specific diameter and chirality tubes have remained limited to small, batch style quantities.

Synthesis of CNTs can be achieved through arc discharge [17,24,26], laser ablation [27–29], or chemical vapor deposition (CVD) methods [30–32], the latter of which can be accomplished using either a thermal or plasma enhanced CVD (PECVD). Typically, each of these processes relies on the use of transition metal (e.g., iron, nickel, cobalt, etc.) nanoparticles as catalytic nucleation sites for the growth of the CNTs. The diameter, length, and quality of the CNTs are controlled through the processing conditions of each method, namely the temperature, pressure, reaction atmosphere, and the catalyst particle size and density on the substrate.

Utilizing self-organization of the CNTs during growth is a promising path to overcoming challenges in assembly and scaling up properties of CNT arrays. If the density of catalyst particles is high enough, and a sufficient number of particles are activated during growth, the CNTs will crowd and develop a preferred alignment normal to the substrate, thus developing aligned CNT forests [33]. It is this vertically-aligned CNT (VACNT) structure, along with graphene, that will be the focus of the following chapters in this thesis.

1.2 Graphene

Graphene is a single atomic layer of graphite, where the carbon atoms are arranged in a hexagonal lattice due to their (sp^2) bonds (Figure 1-1). While this purest form of graphene is known as single-layer graphene (SG), research is also being conducted on bi-layer graphene (BG) and few-layer graphene (FG), where the number of layers is ≤ 10 [34]. Much like the dependency of CNT electrical properties on the chiral vector, $\hat{C}_h$, the bandgap of the graphene is determined by the substrate on which graphene is deposited, and the number of layers [35].

Since graphene typically exhibits a bandgap of zero (i.e., electrically conductive), the tailoring of the bandgap is necessary for many electrical applications, such as transistors, where a semiconductor is more suitable.

In the 1940's, several theoretical analyses of individual crystal layers of graphite suggested extraordinary electrical characteristics, most notably the work by Wallace in 1947 where he suggested an electrical conductivity 100 times greater within the plane than between planes [36]. In 1962, Boehm et al. produced thin layers of carbon, that contained only minor quantities of hydrogen and oxygen, through the chemical reduction of graphite oxide dispersions [37]. Among the thinnest layers observed in this study were layers with a measured thickness of 4.6 Å, deemed by the authors to consist of single carbon layers. Following Boehm's work, the generation of ring diffraction patterns using low-energy electron diffraction (LEED) by adsorbed layers of various carbon containing gaseous molecules onto a Pt (100) surface was shown by Morgan et al. in 1968 [38]. Further analysis of the diffraction patterns, which were the same as those generated on Pt (111) and Pt (110) surfaces, led to the hypothesis that single and multiple layers of a material with a graphitic structure were present after the adsorption process [39]. Later work by Land et al. showed that at high temperatures, the carbon dissolved in Pt and then formed single or multi-layers of graphite on the surface [40]. Additional techniques for the formation of graphene were also realized, such as the sublimation of Si from single crystal SiC at elevated temperatures and low pressure, forming monolayer flakes of graphene on the surface [41]. More recently, mechanical exfoliation of graphene layers from highly ordered pyrolytic graphite (HOPG) was demonstrated, creating multi-layer graphene in 1999 [42], and single layer graphene in 2004 [43]. Finally, multi-layer graphene created via CVD on silicon, quartz, and metal substrates was demonstrated by Malesevic et al. in 2008 [44], and this synthesis process remains at the forefront for the growth of large-scale graphene.

Graphene synthesis can be categorized into three main areas: mechanical cleaving, epitaxial growth on support substrates, and generation of colloidal suspensions [45]. Mechanical cleaving offers the direct transfer of high quality graphene through the abrasion or exfoliation of a graphitic substrate, such as highly oriented pyrolitic graphite (HOPG) [43,46]. However, this method is often limited to small discontinuous pieces of graphene, whereas the growth of graphene in solution, or on suitable substrates enables the potential production of larger samples.

Solution based formation of graphene colloids includes the production of graphene oxide (GO), followed by the separation of the hydrophilic GO layers via sonication in water, and subsequent chemical reduction to graphene flakes [47]. These graphene flakes, then need to be stabilized chemically or through electrostatic repulsion to keep them from agglomerating [48]. While this method offers a relatively straightforward approach to the production of graphene, additional work on the GO reduction needs to be completed towards full reduction of the oxidized surfaces. Synthesis of graphene on substrates through epitaxial growth have grown increasingly attractive because of the ability to prepare graphene over large areas. Two examples of this type of growth include the heating of SiC at low pressure, where the Si sublimates and leaves behind graphene on the surface [49], and the CVD production of graphene on a suitable substrate [50]. Improvements in substrate size and uniformity, along with reduction of growth temperature and increased processing pressure, are currently being investigated to bring the epitaxial growth of graphene to large scale applications.

Similar to CNTs, graphene has been shown to have a large Young's modulus (~ 1.1 TPa) [51], thermal conductivity (~5,000 W/mK measured, ~10,000 W/mK theoretical) [52], and current densities of 18 x 10^8 A/cm^2 for electrical interconnects on diamond [53]. Because of the similar structure and performance properties, it comes as no surprise that the potential applications for graphene flakes overlap a great deal with that of CNT powders. Unfortunately, the lack of a native bandgap will most likely prevent graphene from being integrated into high performance logic circuits in the near future [54]. However, because of its large potential 2D coverage, electrical conductivity, and optical transparency, graphene has the potential for replacing indium tin oxide (ITO) as the transparent conductive coating of choice [55,56]. And because graphene has a much higher fracture strain than ITO, flexible electronics and displays that require transparent conductive coatings, such as touch screens and flexible organic light emitting diodes (OLEDs), could be realized. Additionally, the quantum Hall effect and Berry's phase observed in graphene may open up avenues towards new electric and magnetic field-effect devices [57].

1.3 Need for scale-up

In order to realize integration of these materials, and other nanomaterials, into commercial applications, the production consistency and large-scale throughput of CNTs and graphene need

to be addressed. Figure 1-2 illustrates the current scales of manufacturing for CNT forests and graphene as compared to a few potential commercial applications. While research into improved or new properties with these nanomaterials still remain important, if the method of achieving these properties is not repeatable, or scalable, the cost of integrating these materials becomes too great for the market to bear.

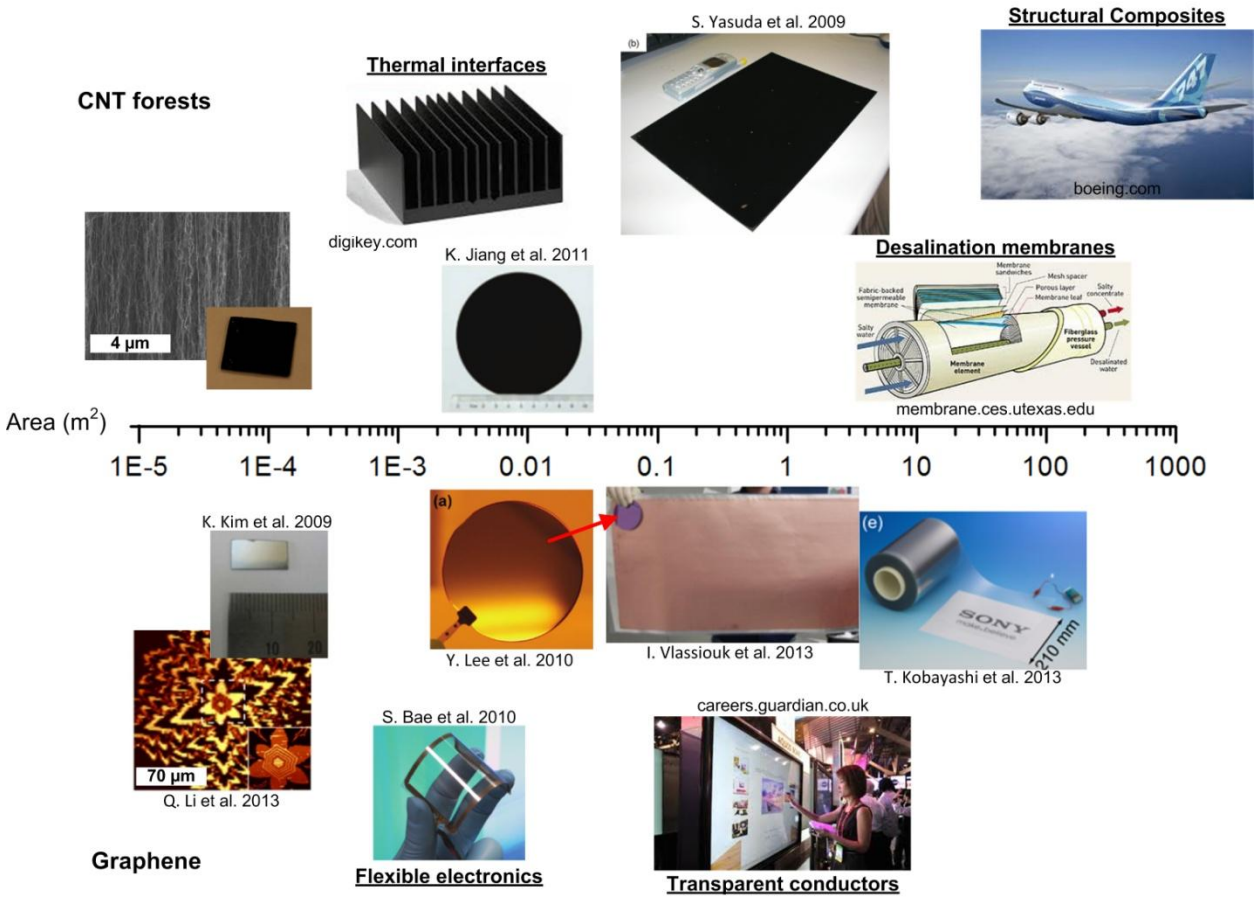

Figure 1-2. Current scales of CNT forest and graphene synthesis and potential applications. Horizontal centers of the images indicate the areal coverage on the scale.

Towards the scalable end of the spectrum, a noticeable shift towards CVD synthesis has been observed. CVD has become the preferred method since it is scalable and enables the engineering of characteristics through introduction of different materials (i.e., gases). This is apparent in the CNT industry where the primary method for CNT synthesis is carried out using a floating catalyst CVD process to produce tons of CNT powders per year. Within academia, multiple large-scale static CVD systems have been developed recently for growth of CNT forests and

graphene [58,59], along with dynamic roll-to-roll systems [60,61], but issues with quality, uniformity, and consistency still present problems for commercial integration.

With these thoughts in mind, this thesis presents a multi-faceted approach to continuous, large-scale growth of CNT thin films and graphene. Each step that was taken in this research ties back to the underlying task of scale-up and quality control, and culminates in the production of a novel roll-to-roll CVD reactor capable of synthesizing both VACNT films and graphene on flexible substrates. In addition, pre- and post-processing of the flexible substrates is also taken into account, which are also intended to be roll-to-roll compatible such that a complete pilot-scale manufacturing line can be realized in the near future.

1.4 Thesis Outline

Work towards this thesis began with the study of CNT forest growth via CVD, and the intent to design a process and machine that would enable continuous production of the CNT forests on a silicon wafer. During the course of the investigation, it was apparent that improvements in each step of the CVD process needed to be realized to enable the eventual commercialization of CNT forests. While limitations in the original design of the continuous growth process still require improvements, significant advancements in catalyst density control, processing repeatability, catalyst patterning and CVD reactor design were made towards roll-to-roll production of CNT forests on flexible substrates. Each of these topics, along with applicable results demonstrating CNT forest and graphene synthesis is presented in the following chapters:

Chapter 2 reviews the motivation for roll-to-roll processing of CNT and graphene films, along with applicable processing steps. The various types of processing techniques used in academia and industry to produce these materials are presented, in addition to the limitations on substrate materials, throughput and feature size. Limitations on successful application of continuous processing are then discussed.

Chapter 3 presents a CNT forest synthesis study aimed at identifying the processing variables that are most influential on the run-to-run variability of key material characteristics (e.g., density and height) (based on [62]). The results of a statistical analysis used to identify the aforementioned variables are highlighted, and key steps taken to reduce their impact are discussed.

Chapter 4 showcases a roll-to-roll compatible process for the decoupled control of CNT diameter and density, via the continuous convective assembly of pre-formed catalyst particles (extended from [63]). Results of particle packing fractions, as compared to typical deposited catalyst thin films, are highlighted, along with the control of carbon growth morphology, and CNT diameter and density control through the processing parameters. Finally, a machine design that applies this technique to a roll-to-roll process is presented.

Chapter 5 presents a low cost, scalable method for the deposition and patterning of catalyst for CNT growth through laser printing of nanoparticle containing toner (based on [64]). Three-level catalyst pattern control is illustrated through the use of pre-defined shapes, grayscale levels, and laser intensity to control the location, micropillar array density, and CNT density respectively. Demonstrations of large scale depositions and transfers, along with the application of CNT micropillar arrays as a dry adhesive are also shown.

Chapter 6 highlights the main feature of the thesis with the design, analysis, fabrication and synthesis results of a novel concentric tube, roll-to-roll CVD reactor. Along with an in-depth discussion of the design, CNT forest and graphene synthesis results are shown for multiple substrates under several operating conditions. The comparison of the operating conditions illustrates the control of the synthesized material characteristics that are afforded by the design.

Chapter 7 presents the work on the continuous manufacturing of CNT forests on silicon wafers (extended from [65,66]), including the design, fabrication and growth results. A preliminary look at a continuous delamination / transfer process for CNT forests is also addressed, along with CNT forest adhesion measurements, with the focus on post-treatment adhesion control.

Chapter 8 summarizes the findings from this work and highlights key contributions to the field. Key questions with respect to the continuous manufacturing of CNT and graphene thin films are presented, along with ongoing and proposed future work towards answering these questions.

CHAPTER 2: ROLL-TO-ROLL CVD OF CARBON NANOTUBE AND GRAPHENE FILMS

This chapter presents the state-of-the art in manufacturing of CNT and graphene films, with aim to identify the opportunities and challenges for roll-to-roll growth methods and machines. This knowledge motivates and justifies most of the technical work presented in the remaining chapters of this thesis. For both materials, the critical processing stages are reviewed, and the requirements for independent control of these stages are discussed along with the challenges of integrating the series of stages in continuous processes. Next, known examples of continuous CVD methods for CNTs and graphene, reported in literature, are reviewed. Finally, challenges for scale-up and process control are investigated for these materials, where items involving substrate choice and/or design, CNT density, graphene uniformity, temperature limitations, material patterning and an analysis of the required throughput of the individual processing steps for industrial roll-to-roll (R2R) processing applications.

While CNT and graphene films are typically presented as separate research areas, unifying them under the topic of synthesis highlights the vast similarities and challenges that these two materials have when investigating large scale production. Given that both materials are comprised of (sp^2) carbon bonds, it should be of little surprise that the thermal and chemical synthesis process is similar, where both materials typically utilize metal surfaces for the nucleation and support of growth, though the morphology of the metal surfaces is different, where nanoparticles are utilized for CNTs and flat (ideally atomically flat) surfaces for graphene. Likewise, CVD has been identified as the synthesis method of choice for enabling the integration of both materials into commercial applications because of its low cost and high throughput potential. Mastering each growth process requires unique attention to the independent control of each processing step, which is more complicated than traditional R2R growth; and, in principle a batch process done with separate nucleation and growth may not give the same results. For all of

these reasons, it makes sense to investigate the application of R2R CVD to the production of both CNT and graphene films simultaneously.

2.1 Stages of synthesis

The synthesis and application of both VACNT arrays (i.e., CNT films or CNT forests) and graphene via CVD occurs through the execution of several steps, which can have unique processing conditions in order to produce the desired material characteristics. This is also observed in current industrial manufacturing of materials, such as carbon fibers, where the initial material is subjected to separate pre-treatment, oxidation and thermal treatments to generate the final product [67–69]. Ideally, to maximize throughput, each of the steps is integrated into a continuous process. Whether part of a continuous or batch process, the synthesis of CNT forests must overcome several obstacles to make them suitable for most applications, including high density films with monodisperse CNTs. Likewise, growth of large-area, high quality/conductivity, uniform graphene with a controllable number of layers is also required for many applications. Throughout this section, the steps for CNT forest and graphene production will be examined by breaking them down into four main categories; substrate preparation, nucleation, growth, and delamination or transfer (Figure 2-1).

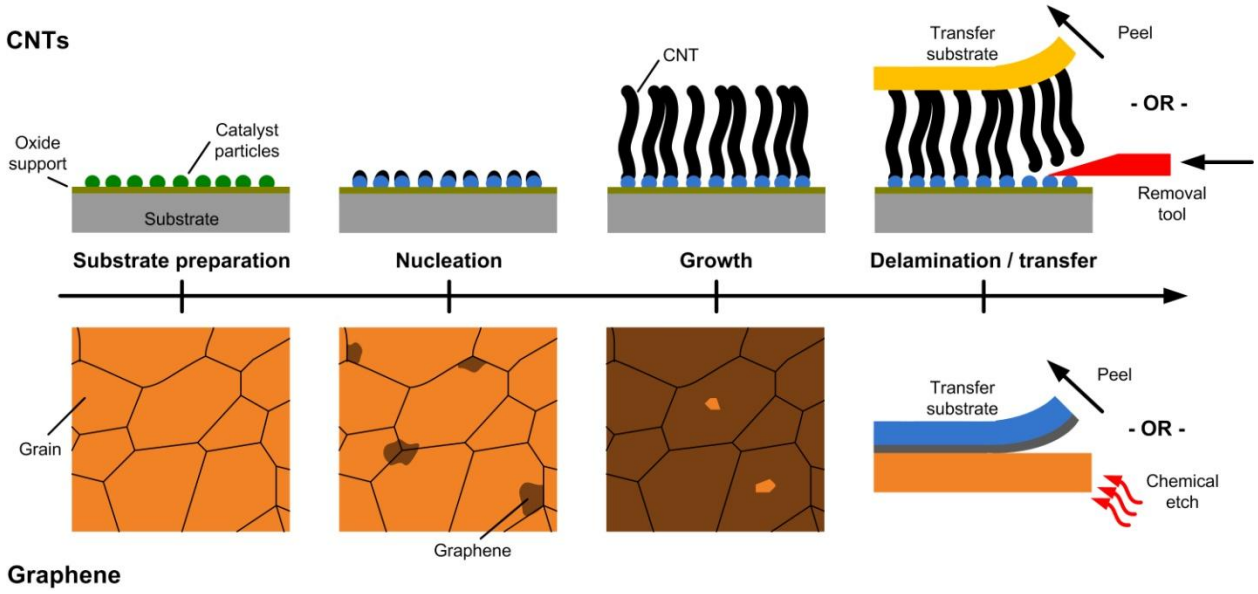

Figure 2-1: Schematic of CNT forest and graphene film growth steps.

The ultimate goal for R2R CVD growth of CNT forests and graphene is to create a fully integrated system that incorporates each of the processing steps through the use of a technique that is harmonious with the rest of the system. Naturally, each must be able to handle similar substrate materials, web sizes, and processing speeds. Because the processing speed is most directly linked with the system throughput (all methods discussed here can be scaled up to handle larger substrate widths), Table 2-1 below has been created as a quick reference for the processing speeds of each CVD step for both CNT forest and graphene growth on a 50 mm x 50 mm substrate. For the CNT forest growth a thermal interface with CNT heights of 100 μm is assumed. For graphene growth, a conductive screen requiring complete coverage is assumed. While the important processing steps for the growth of either of these materials are still the main focus of this chapter, the steps that require the largest processing times during a complete growth process are catalyst deposition, substrate annealing, growth and delamination. Normally the first two steps presented here would be within the substrate preparation step from Figure 2-1. From Table 2-1 it is apparent that either the process is fairly well balanced, or the annealing step would be the longest step and would need to be reduced for R2R processing. On the other hand, the longest step for the graphene growth is most likely the delamination/transfer step, where a wet chemical etch of the substrate could take upwards of 12 hours. Because of the long processing time and increased complexity of a chemical etch in a R2R system, it would benefit the throughput to select a different delamination/transfer method.

Table 2-1. R2R CVD processing step times.

Material	Catalyst Deposition	Annealing	Growth	Delamination / Transfer
CNT Forest	E-beam: ~ 2 min (0.1 Å/s)	~ 5 s - 20 min	1-3 min	1-3 min Scalable w/growth
	Conv. Assem.: ~ 50 s (1 mm/s)			
Graphene	N/A	~ 5 s - 30 min	1 - 80 min	Metal etch: ~12 h
				Poly. rem.: ~1 h

2.1.1 Substrate preparation

Unless beginning with a substrate that already contains catalyst materials that support CNT forest growth, preparing a substrate for CNT forest growth begins with the deposition of the

catalyst material. An alloy or single transition metal (typically Ni, Co, Fe, Mo) is deposited on the substrate using techniques such as thin film deposition (e.g., electron beam evaporation (e-beam), sputtering) [70,71], colloid assembly (e.g., convective assembly, layer-by-layer, spincoating) [72,73], or other techniques such as chemical solution deposition (CSD) (i.e., sol-gel method) [74–76]. Typically, e-beam and sputtering are the preferred methods for depositing the catalyst layer on the substrate. While this technique limits the substrate size by requiring the samples to fit within the high vacuum deposition chamber, several industrial processes including the sputtering of conductive layers on plastic sheets for flexible electrodes in solar cells [77] are enabled through the design of vacuum chambers for material handling. Utilizing these methods, the catalyst film thickness has been shown to directly correlate with the size of the catalyst particles formed upon dewetting (Figure 2-2) [78–80]. This enables the user to control the size of the catalyst nanoparticles, and in-turn, the size of the CNTs grown from them [81,82]. Of course, this can also be accomplished by starting with pre-formed catalyst particles of a given size and assembling them on the substrate surface using a colloid assembly technique [83–86]. Additionally, if the synthesis of graphene is desired, similar thin film deposition techniques are used to deposit a transition metal (typically Ni or Cu) layer on non-metallic substrates. However, if a transition metal foil is used as the substrate, this entire step can be eliminated since graphene synthesis only requires a flat metal surface to manage the carbon decomposition and reorganization.

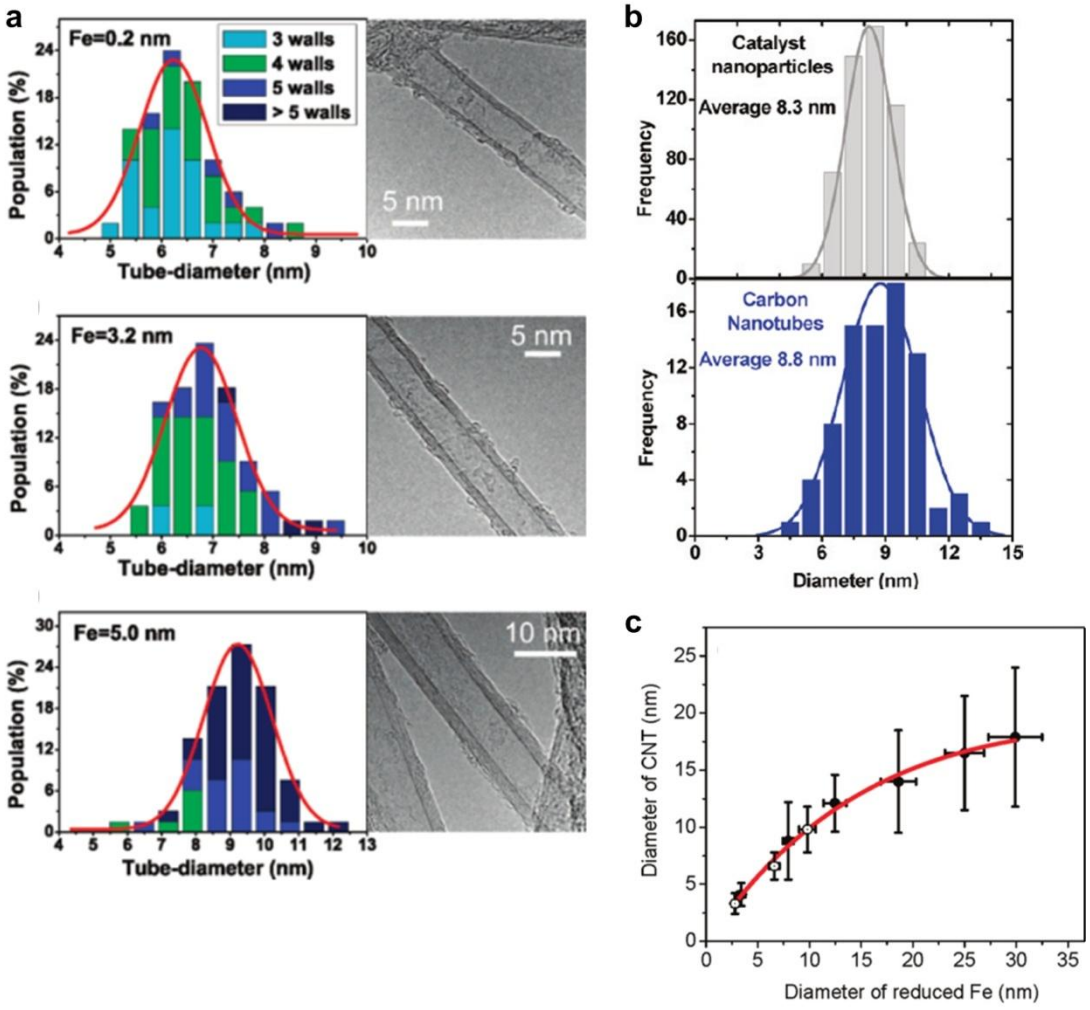

Figure 2-2. Control of catalyst particle and CNT diameters. (a) The tailoring of CNT diameters via the thickness of sputtered catalyst thin films [80], and the control of CNT diameter by the diameter of the catalyst particles they grow from (b,c) [83,86].

Thermal or plasma treatment of the substrate is the next phase of the substrate preparation step, and is required for both CNT forest and graphene growth. Catalyst deposited for CNT forest growth in the form of thin films is treated through one of these means to enable a dewetting process to occur (Figure 2-3a), and for catalyst nanoparticles to form through a reduction of surface energy [87,88]. The resulting size and spacing of the catalyst particles is dependent on the temperature and gas atmosphere during the process [89–91], but the maximum packing density of the particles is inherently limited by the dewetting process itself [92]. Because many applications of CNT forests require a high packing density of CNTs, and therefore a high packing density of catalyst particles, methods to increase the catalyst particle

density above and beyond dewetting limits, such as multiple catalyst depositions, have also been presented [93]. Likewise, the control of catalyst packing density towards increased CNT forest density has also been shown for deposition of preformed particles [63]. However, once catalyst particles are formed, extended processing time at elevated energies to tailor the particle size and density encounter the competing effects of Ostwald ripening and diffusion of the catalyst into the substrate [94] which limits CNT monodispersity and the lifetime of the catalyst for CNT growth (Figure 2-3b).

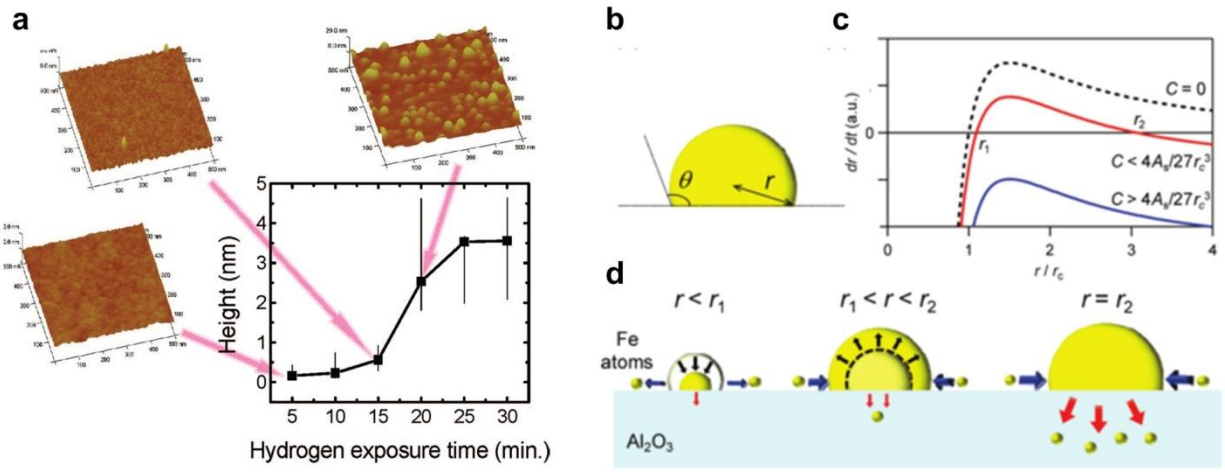

Figure 2-3. Dewetting of thin films and competing effects that control particle size. (a) The formation of particles from thin film dewetting in an elevated temperature, hydrogen rich atmosphere [90]. (b-d) Contact angle (θ) and particle radius (r) for a single nanoparticle, and rates of radius growth as compared to critical radii (r_1 and r_2) where dr/dt = 0 are shown for instances where subsurface diffusion rates are neglected (C = 0), low (red line) and high (blue line) [94].

A similar substrate treatment is also desired for the epitaxial growth of graphene films on metallic substrates. Currently, graphene synthesized on metallic substrates is predominantly accomplished through epitaxial growth on Cu or Ni films or foils [95–98], with limited work being done on other metals [99] such as Pt [100,101], Ir [102,103], and Ru [104,105]. However, there are still some discrepancies as to whether or not the growth on metallic substrates is epitaxial. While evidence has been shown that the crystal grains of the substrate dictate the orientation of the graphene layers [106] (Figure 2-4a, b), other studies such as the one by Robertson et al. show no preferential alignment of graphene with respect to the underlying structure [107], which indicates that epitaxial graphene growth is most likely determined by the

CVD conditions since both studies used Cu substrates. Regardless of the patterning of the graphene by the substrate crystal plane, the grain sizes on the surface of the metal directly dictate the largest area of uniform, N-layer graphene that can be grown (Figure 2-4c-f), since the grain boundaries provide multiple nucleation sites [108,109]. Although single graphene domains do grow across grain boundaries [110], the nucleation sites at these boundaries (discussed in the next section) can enable the formation of additional layers of graphene, and therefore single layer graphene is typically found in the center of the grains while multi-layer graphene is found at the grain boundaries for large area growth [108]. Thus, a thermal or plasma treatment, in conjunction with film deposition techniques for metallic thin films on non-conductive substrates, are used to anneal or induce grain growth in the substrate so as to control the size of uniform N-layer graphene flakes later grown on the substrate.

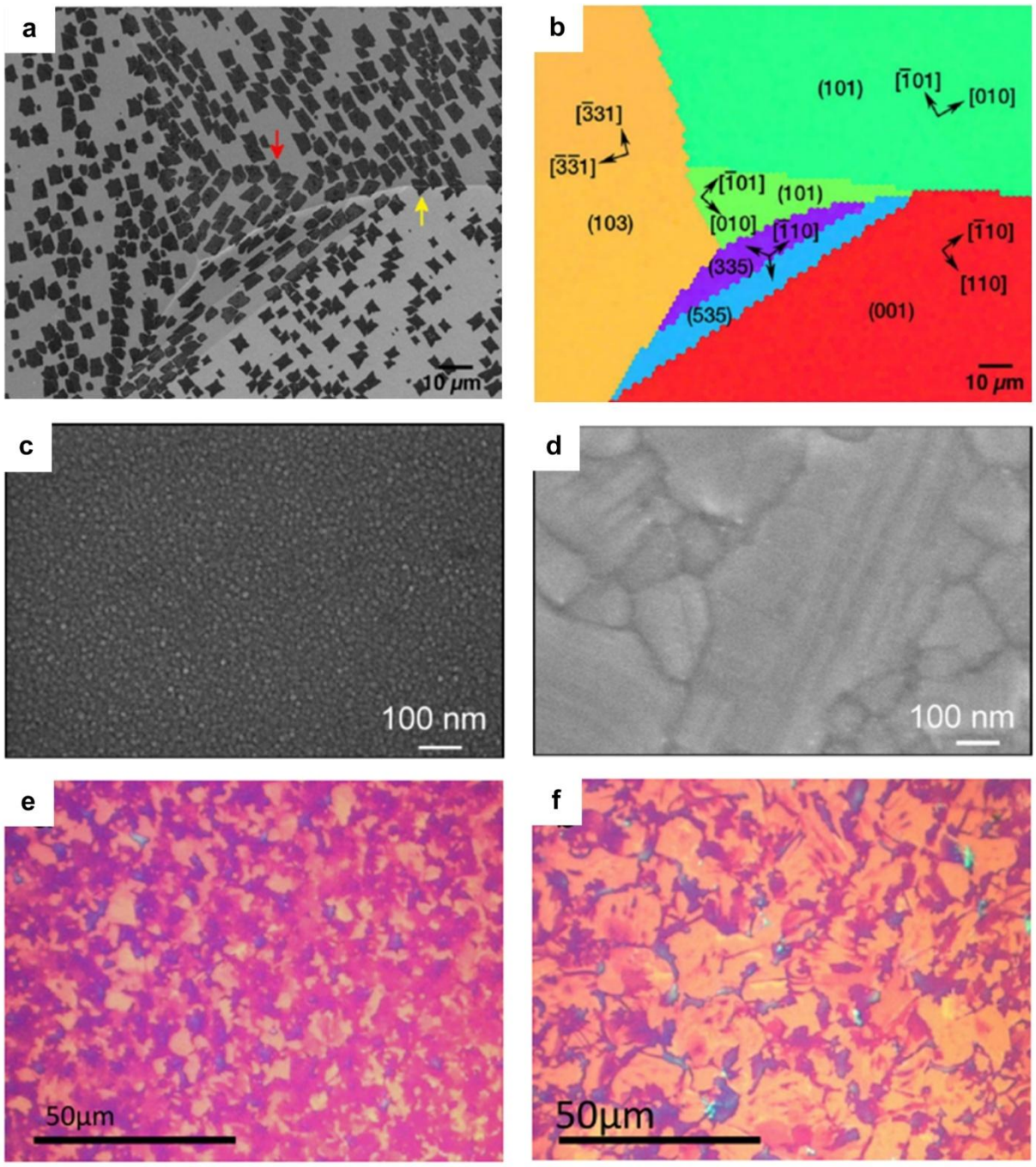

Figure 2-4. Annealing metal films to increase grain size and monolayer graphene growth. (a,b) SEM image of graphene crystal orientation on various Cu grains (a) with grain orientation EBSD map (b). (c,d) SEM images of Co film grain boundaries before (c) and after annealing (d) [109]. (e,f) Optical images of graphene growth on Ni films with small (e) and large grain sizes (f), where light pink represents monolayer graphene and the darker colors at the grain boundaries indicate multi-layer graphene [108].

Finally, exposure of the metallic substrates or metal catalyst films/particles to small amounts of oxygen transform the surface of the materials into an oxidized state. Due to the nature of CVD epitaxial growth of graphene, and that it has been shown that the metallic state of the catalyst particles is the preferential growth state of CNT catalysts [111,112], it is desirable to avoid the oxidized state of the metal films, foils and particles. While carbon atoms can be organized on oxides for graphene and CNT growth, the performance is much lower than that of metallic surfaces due to their reduced diffusivity and mobility of carbon atoms. Thus, the processes described above are typically carried out in a reducing atmosphere, and conclude with the catalyst nanoparticles and metal films or foils reduced to their metallic form, ready to facilitate CNT forest or graphene growth.

2.1.2 Nucleation

The nucleation step for both CNT forests and graphene includes the organization of carbon atoms into the desired structure on the catalyst particles or substrate respectively, and seamlessly follows the substrate preparation. This step is preempted by the introduction of a carbon precursor which is broken down and recombined into multiple compounds that are both favorable and unfavorable for CNTs and graphene growth [91,113–115]. The favorable carbon compounds adsorb to the catalyst surface, which can be in a solid or "liquid-like" state [112], and are reduced to either single or double carbon atoms, which then either diffuse into the bulk of the catalyst particle, or along its surface. Molecular dynamic simulations for iron catalyst particles illustrated that nucleation begins as carbon atoms diffuse into the bulk of the particle and create an iron carbide particle, later creating carbon strings or graphitic islands on the surface and eventually graphene sheets, CNTs or soot depending on the temperature [116]. For CNT growth, once the supersaturation level of carbon in the catalyst is reached, additional carbon added to the bulk is precipitated out of the particle and forms a "cap" or hemispherical top on the particle [112,117]. Illustrated in Figure 2-5a is an example of a carbon cap that is represented as half of a C60 fullerene that is located at a distance from the catalyst particle such that the interaction forces are in equilibrium. With additional time in the CVD environment, the catalyst particle increases in size and the change in interaction energies forces the new equilibrium state, "lift off" [118]. This new equilibrium state is based on the "wetting" or binding energy of the carbon cap with the catalyst particle being overcome by the spontaneous curvature and bending rigidity of

the cap. From this point, additional carbon then forms the walls and additional layers if MWNTs on each active catalyst particle, with specific nucleation points favoring the step edges of the catalyst structure (Figure 2-5c) [112]. During this process, it has been suggested that certain additives, such as H_2O, in the gas atmosphere, or the introduction of a plasma, increases the number of active particles and nucleation sites by either etching amorphous carbon off of the catalyst particle surface or favorably restructuring the carbon or catalyst [119–124]. The influence of an underlying oxide layer, typically alumina, in potentially feeding hydrocarbons to the catalyst [125], along with the possible effects of residual carbon on the substrate controlling the nucleation and growth of catalyst particles have also been suggested [126].

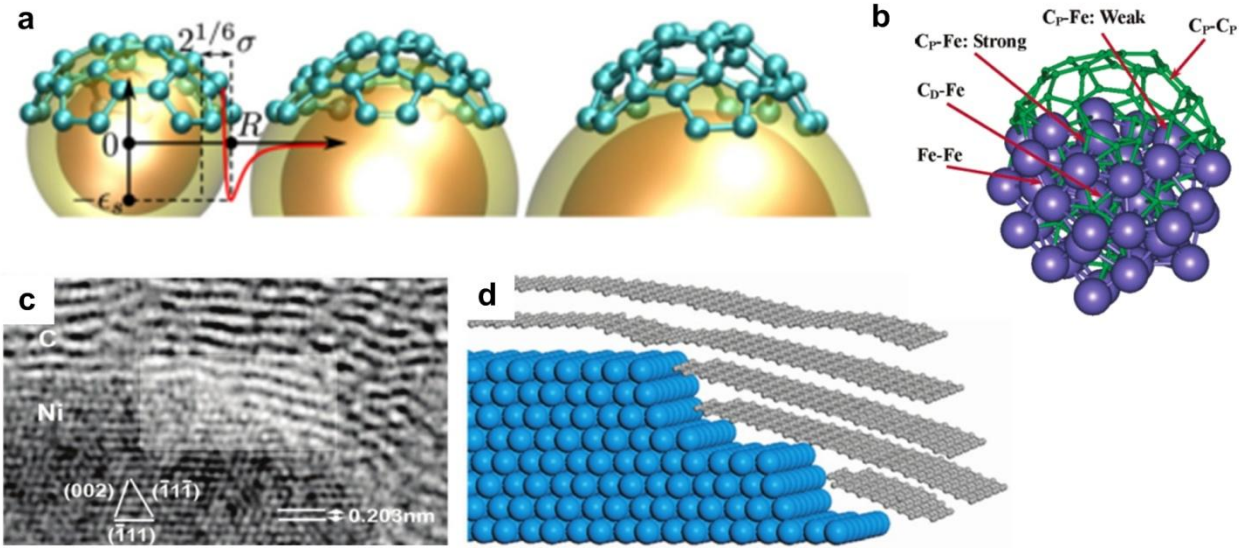

Figure 2-5. Nucleation of CNT growth and active catalyst sites. (a) An idealized C30 cap on top of Lennard-Jones catalyst particles where the equilibrium distance between the two is $2^{1/6}\sigma$, and an increase in catalyst diameter induces "lift-off" as the new equilibrium state [118]. (b) Potential energy surface used for a molecular dynamics simulation of CNT nucleation on iron particles where the interaction energies between the various C_D (dissolved), C_P (precipitated) and Fe atoms are calculated [116]. (c) HRTEM image of the tip of a CNT with a Ni catalyst particle, and a stick and ball representation of the step edge nucleation sites (d) as highlighted in (c) [112].

Similar to CNT forest nucleation, graphene follows a comparable nucleation method where the carbon precursor is broken down and adsorbed to the surface of the metal substrate. Depending on the solubility of carbon in the metal foil or film, the carbon either migrates along the surface to nucleation points, like on Cu, or diffuses into the metal and is later precipitated on the surface, as with Ni [98]. Regardless of the graphene assembly process, the nucleation sites

are similar, where edge defects and scratches have been shown to be the most active sites on the substrate, and smooth terrace sites are less active [127,128]. Figure 2-6 illustrates the nucleation of carbon at a step edge on Ni, along with the abundance of nucleation sites near scratches on Cu. In addition, these edge defects are abundant near the grain boundaries of the metal substrates, which causes the nucleation of multiple layers of graphene at these sites prior to multi-layer formation near the centers of the substrate grains. Recently, this was further supported by the observation of the nucleation of graphene on Cu using carbon isotope labeling revealed that all of the adlayers formed simultaneously between the first layer of graphene and the substrate, and that stacked adlayers nucleate from the same point (Figure 2-6c) [129]. Additionally, all of the graphene layers nucleating at the same spot were shown to have the same edge termination, which may or may not be determined by the surface crystal structure (as previously mentioned).

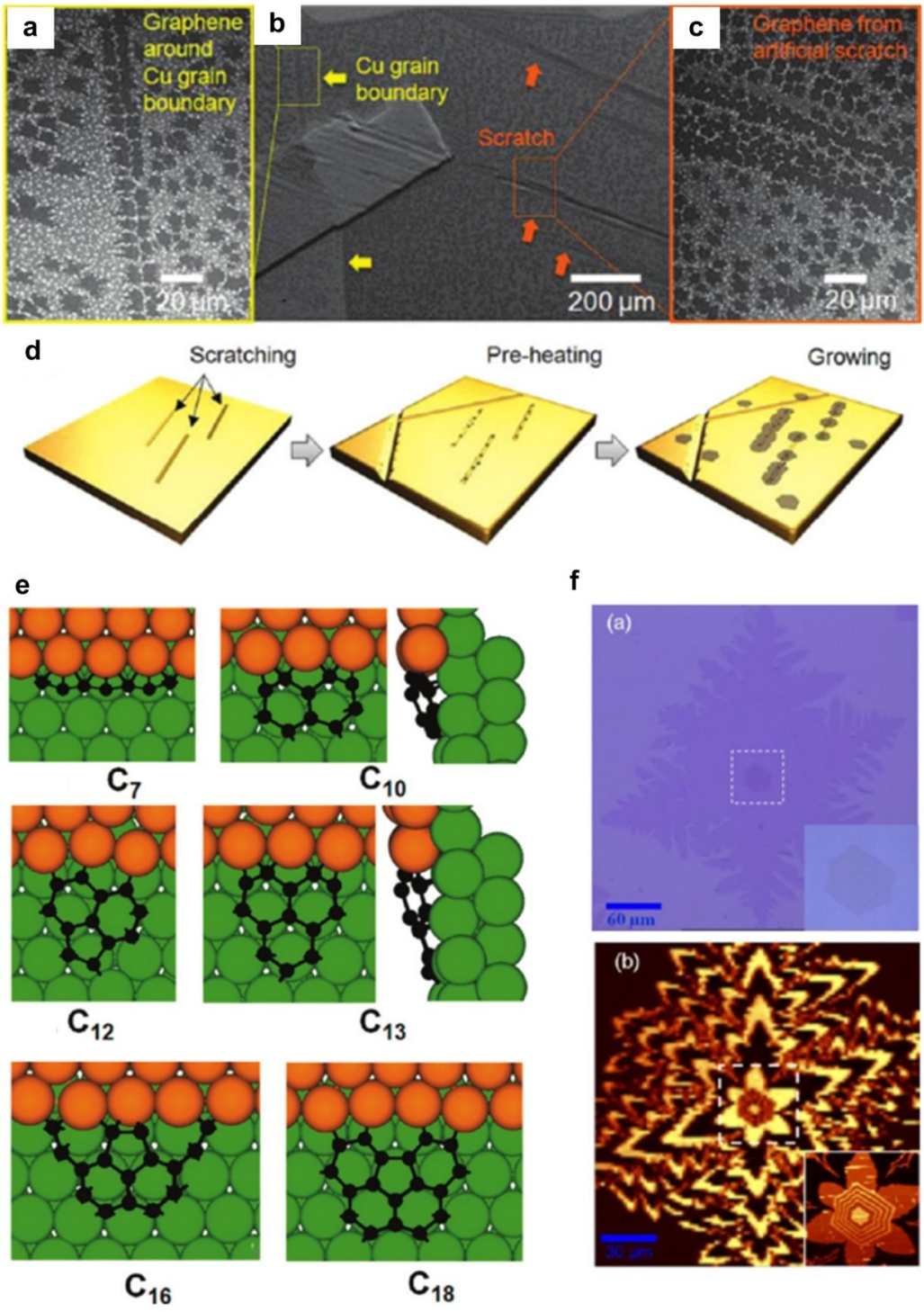

Figure 2-6. Nucleation of graphene. (a-c) SEM images of graphene nucleation at grain boundaries and scratches on a Cu substrate, and a schematic for the nucleation (d) [127]. (e) Optimized C_N nucleation structures on a Ni (111) surface near a step edge [128]. (f) An optical image of a single dendritic graphene grain with bi-layer formation (top) and a Raman map of the G_{12} intensity (bottom) [129].

2.1.3 Growth

Both CNT and graphene growth processes involve continued addition of hexagonally bonded carbon atoms to a lattice, mediated by the active sites at the metal-carbon interface. CNT growth emerges from the nucleation process once individual nanotubes begin to "lift-off" from the catalyst particles as additional carbon is added from the gas atmosphere. Illustrated in Figure 2-7a, this addition of carbon is included in the growth model of CNTs from catalyst particles described by Puretzky et al. [130], where there are competing rates of "good" and "bad" carbon deposition on the particle. Additionally, it has been hypothesized that as carbon atoms are added to the CNT walls, the chirality of the CNT is dictated by screw dislocations which minimize the energy barrier to growth of crystal lattice structures [131]. These dislocations, and the chirality of the CNTs, are dictated by the crystal planes on the catalyst particles themselves, as illustrated in Figure 2-7b, and thus the type of CNT created is determined early on in the growth phase [132]. U unless aligned by some other means such as an electric field [133–135], the CNTs continue to grow with a random orientation, which forms a tangled mat of CNTs around the catalyst particles. Once a sufficient density of CNTs is reached, crowding occurs and the CNTs begin to push against one another, driving them normal to the substrate, and lifting the tangled mat of CNTs (a.k.a., crust) off of the substrate [33]. These mechanical interactions align the growth and facilitate the formation of the CNT forest as shown in Figure 2-7c.

Although the CNT forests are dense enough to align through mechanical interactions, CNTs typically occupy < 10% of the forest volume, and as such the individual CNTs, while generally vertically aligned, are rather tortuous. Unfortunately, throughout the growth process, the unfavorable carbon compounds, typically larger hydrocarbons, adsorb to the catalyst particle surface and form an amorphous shell [130,136]. This shell nucleates at multiple points and undergoes island growth as additional amorphous carbon is deposited. As this shell grows, less surface area is available on the catalyst particle for favorable carbon to adsorb, and eventually the growth process terminates (unless terminated earlier by unfavorable CVD conditions). Scaling this up to an entire CNT forest, it has been observed that the density of growing CNTs slowly decays after a period of consistent growth, and once the growth density is sufficiently low, forest growth reaches termination. To combat CNT growth termination, mild etchants have been shown to increase the CNT forest yield from a given substrate by increasing the growth

period and putting off termination [137–139]. Because of this constant competition of deposition rates between amorphous and graphitic carbon during the CVD process, CNT forest quality and yield are highly dependent on the processing parameters. This points to the need for highly controlled growth parameters for large-scale synthesis, where some of the parameters such as temperature [91], pressure [136], gas flow patterns [58] and reactor wall deposits [140] have been shown to play a role in combinations of consistency, yield and quality of the CNT forest (A more in-depth study of growth consistency is given in the next chapter).

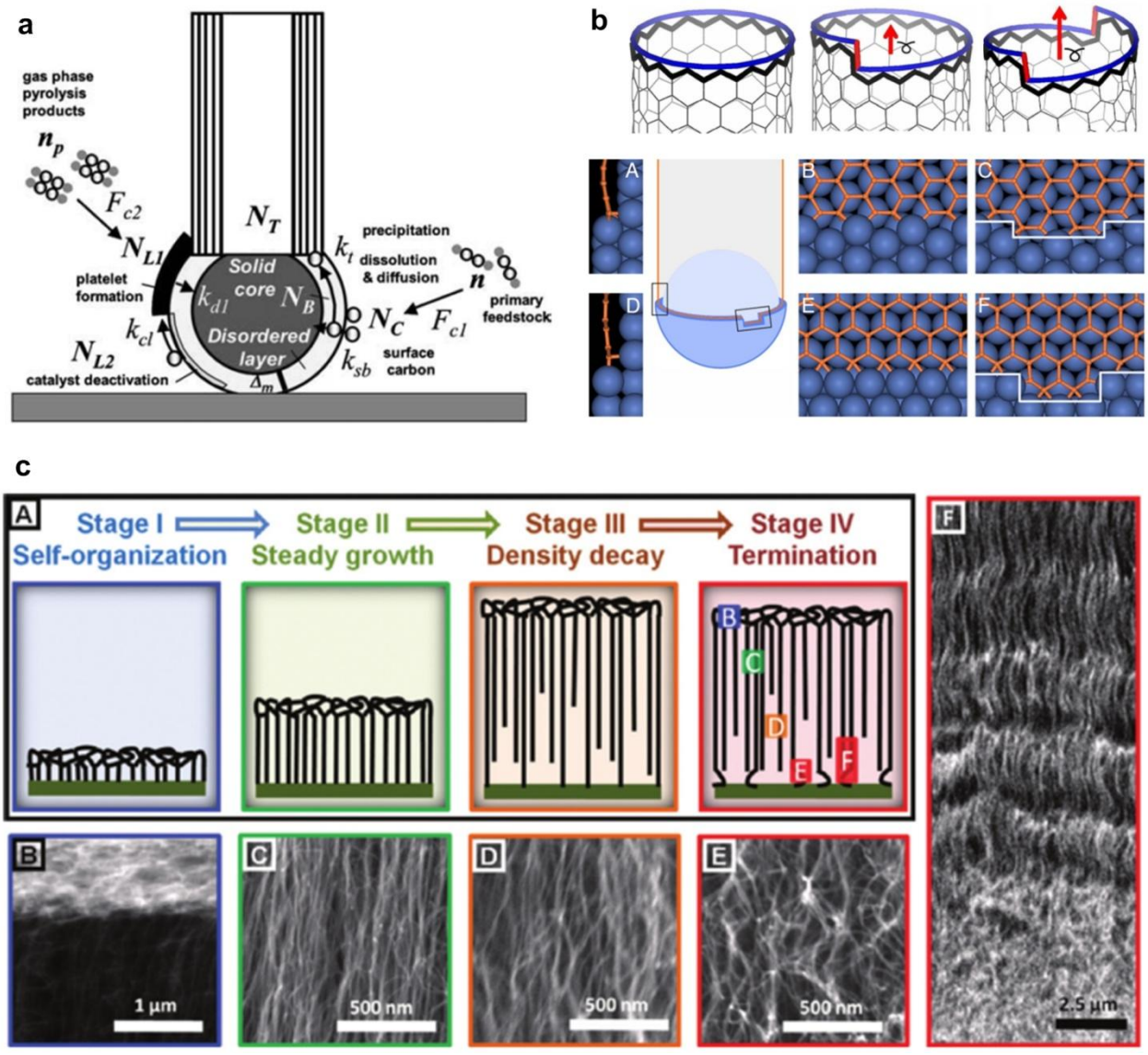

Figure 2-7. Mechanism of individual and collective CNT growth. (a) CNT growth model where the "good" and "bad" carbon species (n and n_p), are brought to the catalyst surface at individual rates (F_{c1} and F_{c2}), to form either an amorphous layer (N_{L1}, which forms at the rate of k_{cl} and dissolves into the catalyst bulk at a rate of k_{dl}) or a favorable carbon layer (N_C) [130]. Other variables include the formation of non-active surface areas (N_{L2}), the rate of carbon atoms dissolving into the catalyst particle from the surface or into the CNT (k_{sb} and k_t), the number of carbon atoms in the catalyst partice (N_B), and the number of carbon atoms in the CNT (N_T). (b) Zigzag and chiral CNTs with one or two kinks during growth are shown along with the nucleation of the next atomic row (orange) near a step edge on Ni(111) for armchair (A-C) and zigzag (D-F) CNTs (A and D are side views, B and E are front views, and C and F show the emerging row segment flanked by kinks) [131]. (c) Stages of CNT forest growth, along with SEM images of select locations [33].

Once nucleated, graphene growth proceeds through the addition of carbon atoms along the perimeter of the existing islands. Using density functional theory (DFT) calculations, Artyukhov et al. modeled that higher energy formations, such as defects, are unlikely to form unless the chemical potential of the carbon precursor atoms, or binding energy between the carbon atoms and the substrate is high enough to make them a probable result (Figure 2-8a) [141]. Likewise, dendritic crystal formations are a much higher energy formation than hexagonal crystals, and thus are much less likely to form. However, dendritic crystals have been shown numerous times on Cu substrates, especially at low pressure. This is because the binding energy between Cu and C is much higher than that of Ni and C, making the high energy formation more likely on Cu. Additionally, excessive amounts of carbon raises the chemical potential of the carbon atoms, which also enables defective or dendritic growth. Thus, the substrate and the CVD atmosphere play a very important role in the propagation of graphene growth. Whether dendritic or hexagonal, growth proceeds across the surface of the substrate until the graphene meets an atomic step edge either on the substrate surface, or in the form of another graphene grain. If two similar graphene grain edges meet they typically coalesce, but if they are dissimilar a line defect is typically created and the growth terminates for those edges [142]. However, when the graphene reaches a step edge on the substrate, the growth can either be terminated or continue. Whether or not the graphene edge accommodates additional carbon atoms and changes in the physical spacing with the substrate (*i.e.*, bridging grain boundaries or lifting to grow up a step edge) is most likely a function of the binding energy between the substrate and the carbon atoms. It has been shown on Ru that if the graphene is required to step "uphill," the growth can be almost completely stopped [104], but if a "downhill" step is required, the graphene typically continues unimpeded to the lower level. Whereas on Cu substrates, the graphene grains have been shown to bridge grain boundaries on the substrate, forming a single graphene crystal that covers several Cu grains with different orientations (Figure 2-8b) [110]. Regardless of whether or not the graphene edge terminates, the other edges continue to grow until the same circumstances are reached. But once sufficient carbon has been supplied to the substrate, and enough edges are no longer active to re-orient the carbon atoms on the first graphene layer, the nucleation sites begin to form an additional graphene layer between the substrate and the first layer of graphene (Figure 2-8c). Assuming conditions are favorable for highly ordered growth, Bernal (A-B) stacking is often observed between the layers of graphene growth [104,143].

Additional layers are added over time, and this process continues until the carbon atoms are no longer supplied to the graphene growth fronts of the islands. The number of graphene layers is typically controlled through the amount of carbon that is supplied to the substrate, through the control of concentration, pressure and/or time [144,145]. Likewise, the quality and domain size of the graphene layers can be controlled using the same techniques, such that a slower rate of carbon exposure leads to fewer nucleation, and potential defect sites. However, this control must be balanced with any potential impacts to the substrate morphology that would negatively affect the graphene. Successful implementation of this line of reasoning is illustrated by Yan et al., where they achieved growth of ~4.5 mm^2 graphene domains using a combination of chemical polishing (to reduce the number of nucleation sites), reduced carbon to hydrogen ratios, and increased growth temperature [146]. Similarly, Wu et al., studied the effects of carbon precursor pre-heating and hydrogen flow rates on the number of nucleation sites, graphene crystal morphology (i.e., dendritic or hexagonal crystals) and graphene grain size over time (Figure 2-8d) [147]. Finally, Chen et al., demonstrated the use of a confined reaction zone to create mm-scale graphene domains through the creation of smoother Cu surfaces due to the re-deposition of sublimated Cu from an adjacent Cu surface [148].

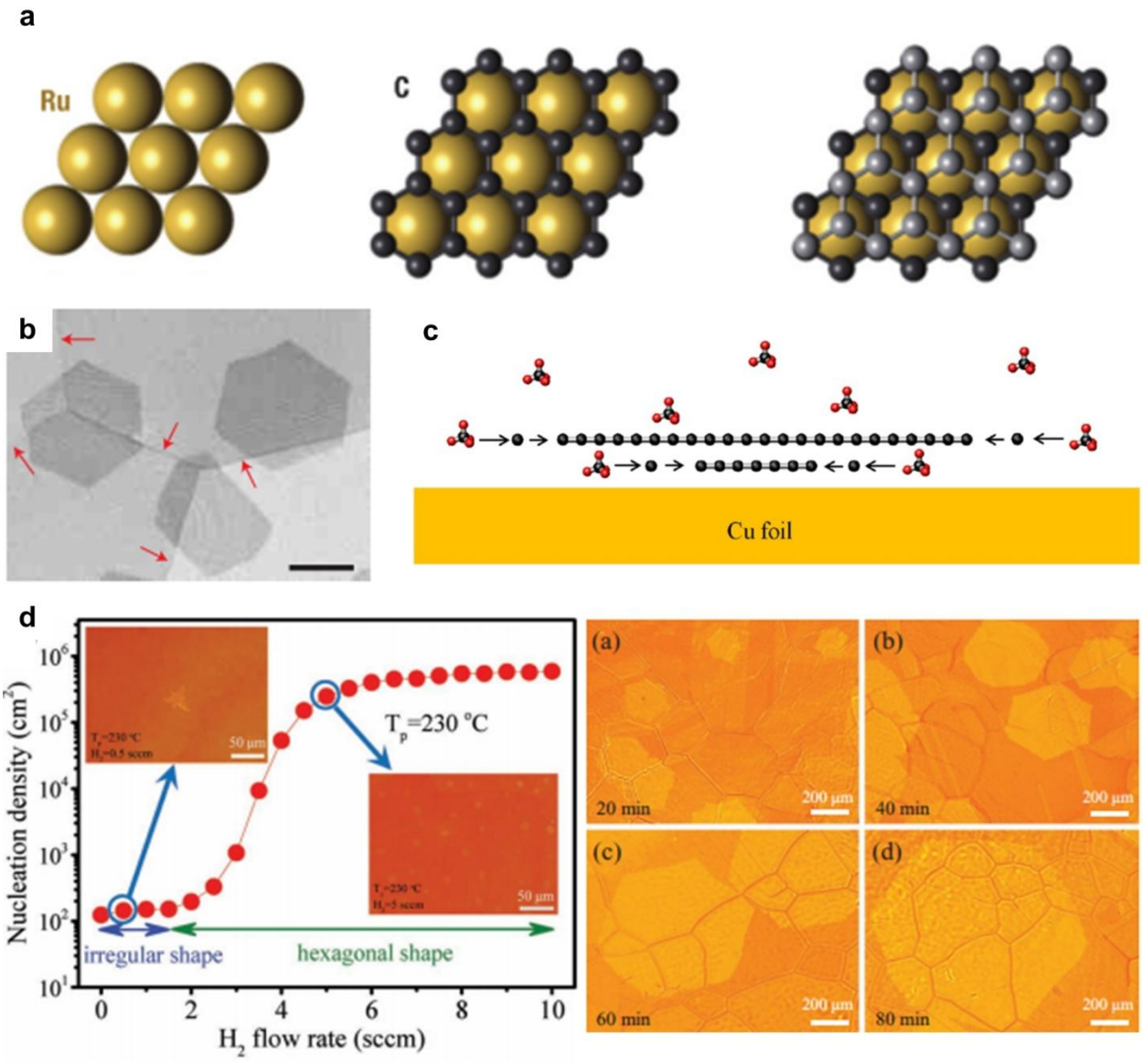

Figure 2-8. Graphene growth on metallic substrates. (a) Epitaxial growth of single (middle) and bi-layer (right) graphene on a Ru(0001) surface that exhibits Bernal (A-B) stacking [104]. (b) SEM image of single graphene domains grown across Cu grain boundaries (scale bar is 5 μm) [110]. (c) Schematic of adlayer graphene growth where additional layers are grown between existing graphene layers and the substrate [129]. (d) Control of nucleation density and graphene crystal morphology through H_2 flow rate (inset: 0.5 and 5 sccm H_2), and optical images of graphene crystal growth after 20, 40, 60 and 80 min (right) [147].

2.1.4 Delamination / Transfer

Once the growth of the CNT forest or graphene is completed, the optional delamination or transfer to a secondary substrate is carried out. This step is required for applications where the carbon nanomaterial is required to be located on a substrate that is unsuitable for the growth process such as prepreg layers for structural composites and polymer films for flexible electronics. For CNT forests this is typically accomplished through purely mechanical means, where the forest is either peeled from the growth substrate by adhering the top of the forest to a secondary substrate, or by cleaving the forest from the substrate by propagating a crack at the CNT-catalyst interface. Several examples of CNT forest transfer using these concepts have been demonstrated, including the patterning and transfer to flexible polymer substrates using laser welding [149], wafer scale transfer using a conformal metal coating and thermal release tape [150], transfer printing using structural composite prepreg layers (Figure 2-9a) [151], thermal bonding of polycarbonate to patterned CNT forests [152], and contact transfer using conductive substrates with solder [153].

Transfer of graphene grown through a CVD process typically requires chemical dissolution of the metal. First, the graphene is coated with a protective polymer layer, the metal substrate is chemically etched, and the polymer coated graphene is transferred to the secondary substrate, followed by the removal of the polymer. The most common form of this process utilizes a uniform layer of poly(methyl methacrylate) (PMMA) as the polymer layer, which is later rinsed away using acetone [95,154,155]. Improvements on this process have also been developed which offer either fewer steps or the elimination of wet processing steps. Bae et al. displayed a similar transfer technique for graphene on Cu foil, where the PMMA was replaced with a thermal transfer tape, which while more convenient, requires the removal of the adhesive residue from the graphene once the tape is released (Figure 2-9b) [59]. Another technique utilizes the PMMA layer but replaces the chemical etching of the substrate with electrolysis in a water bath to separate the PMMA/graphene assembly from the substrate via hydrogen bubble formation [156]. Pushing towards a dry transfer process, the use of polydimethylsiloxane (PDMS) has been show to not only eliminate the need for chemical etching, but also control the number of graphene layers removed during the peeling of the PDMS away from the substrate by the elastomer to curing agent ratio [157]. Additionally, another dry transfer technique using polyethylene

terephthalate (PET) mechanically pressed against the graphene layer, at an elevated temperature, enables the peeling of the graphene from the metallic substrate by the PET [158]. Each of these processes has been shown to be R2R compatible which allows for integration on a manufacturing scale, however, the uniformity of the graphene on the transfer substrates, which remains a key performance factor for scale-up, was not addressed in either case. Additionally, another factor to consider is that polymer or chemical-mediated transfer techniques leave residue on the graphene which can degrade its properties. Thus, a direct graphene transfer method is desirable to maintain the quality of the material.

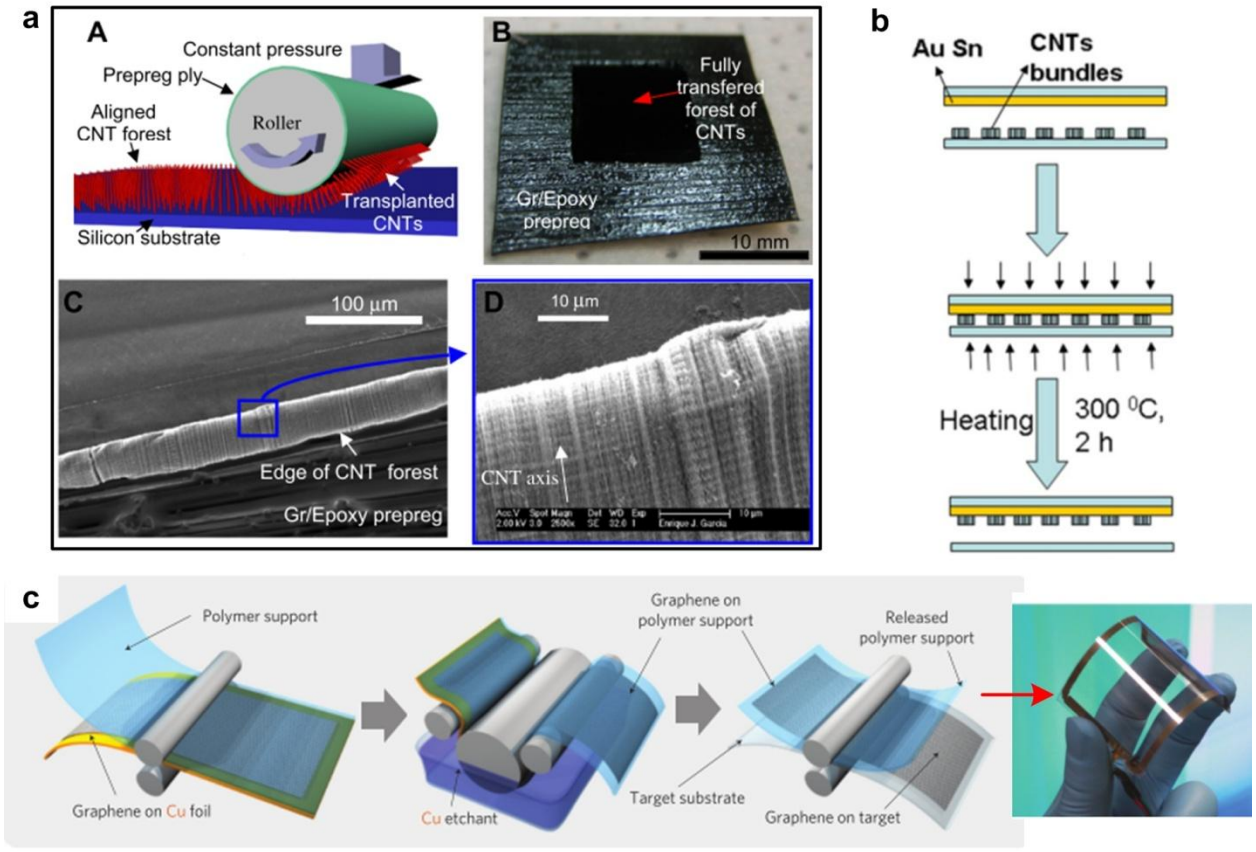

Figure 2-9. Delamination and transfer of CNT forests and graphene. (a) Transfer of a CNT forest to an adhesive coated prepreg layer using a roller, and subsequent SEM images of the assembly [151]. (b) Schematic of patterned CNT forest transfer using solder [153]. (c) Schematic of a R2R method for the transfer of graphene to a PET film, and photo of graphene on PET (right), using a thermal release adhesive layer and a wet chemical etch of the Cu substrate [59].

2.2 Continuous CVD methods for CNTs and graphene

Many methods of large scale CVD synthesis have been applied to CNT forests and graphene which fit into three distinct categories: batch-style (optionally with continuous feed), R2R, and floating catalyst (including fluidized bed reactors). While each method has advantages and drawbacks for particular applications of the synthesized materials, they have all made significant progress toward the goal of continuous manufacturing of CNT forests and graphene. However, what is lacking among these methods is the in-line inclusion of each processing step to enable the continuous manufacturing of highly uniform, high quality, tunable materials. In this section, a review of these continuous CVD methods found in literature is presented.

2.2.1 CNTs

Because CNT forests require a substrate for the support of the CNTs as they mechanically interact to self-align, the most straightforward path to continuous production of CNT forests is the scale-up of batch synthesis. In 2002, Jiang et al., began creating superaligned CNT forests (composed of MWNTs) for the creation of spun CNT yarns and fibers with the goal of scaling up production to meet application needs [159]. Since then, they have produced low-pressure CVD (LP-CVD) systems that enabled the controlled production of these CNT forests on 4" (2004) and 8" (2008) diameter wafers (Figure 2-10a) [160]. In 2009, Yasuda et al. combined several techniques such as water injection and gas delivery using a top-down showerhead approach into a furnace system that resulted in the largest areal growth of CNT forests known to date [58]. This process reported a carbon efficiency of 32% (vs. ~ 1% for typical lateral flow systems) and produced SWNT forests that covered substrate areas as large as an A4 sheet of paper, with uniform height over the area of ~1 mm (Figure 2-10b). While these examples exhibit large area single sample growth, another method to drive batch processing throughput is to continuously feed discrete substrates through the furnace. This was illustrated in 2009 by Guzmán de Villoria et al. as a step towards R2R processing, where individual Si substrate samples were fed through a custom CVD furnace using a conveyor belt approach [60]. By combining these approaches the throughput of a CNT forests produced on batch substrates would be significantly enhanced over the typical cm scale batch growth in CVD systems, but integration into R2R manufacturing processes such as the creation of structural composites would still require a similarly continuous substrate.

Steps towards R2R CNT forest production are often mentioned in the literature, but implementation of all stages in a continuously operating system has not been reported, to our knowledge. The only known examples are the growth of CNT forests on pre-annealed woven ceramic fibers and discrete SS belts at a rate of 1.3 cm/min, both demonstrated by Guzmán de Villoria et al. in 2011 (Figure 2-10c) [161], and the R2R growth of CNTs on glass fibers pre-coated with catalyst particles by a separate R2R process [162]. While the growth on the SS belt was not as well aligned as CNT forests grown on other substrates, many steps have been taken to increase alignment and uniformity on discrete metallic substrates [72,163–165]. Similar work has also been done on glass samples with the goal of implementation on glass fibers for R2R growth [70], and the use of a floating catalyst has been shown to enable the growth of CNT forests on non-pretreated substrates such as quartz that could be fed through the CVD reactor [166].

Finally, CNT forests have been created in a continuous fashion using fluidized bed reactors. Fluidized bed reactors offer a very large catalyst surface area for the production of large volumes of CNTs. Using ceramic spheres as the catalyst support, small clumps of CNT forests have been shown to orient in the radial direction on the surface [167], and by packing the reactor with spheres, a large volume of CNT forests is created [168]. The forests are then separated from the spheres using the shearing force of a high velocity gas and collected. While this is a very high throughput method for CNT forest growth, remounting the forests on a target substrate at similar throughput proves difficult, and so the delaminated forests are typically dispersed in a solution and not used in their native form. Thus, this method is used for bulk production of long CNTs with high purity.

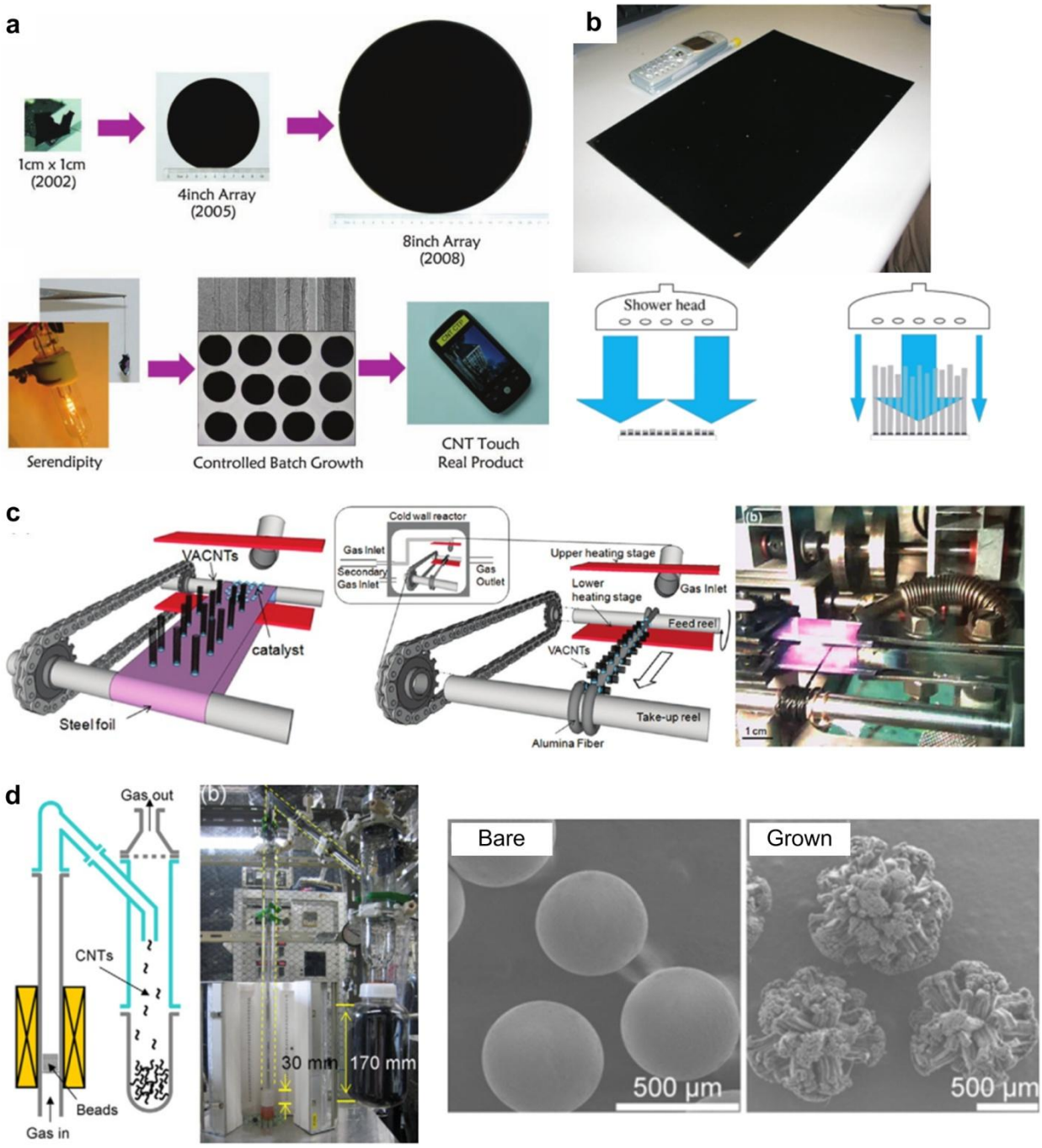

Figure 2-10. Continuous CVD CNT forest production. (a) Increasing batch growth size on Si wafers for implementation in yarns and fibers for bulb filaments and touch screens [160]. (b) 6 x 1.5 m batch CVD furnace for growth of uniform A4 size SWNT forests using a showerhead gas delivery system (bottom) [58]. (c) R2R growth of CNT forests on SS foil and ceramic fibers [161]. (d) Fluidized bed reactor for the growth of CNT forests on ceramic beads (right) [168].

2.2.2 Graphene

Similar to the large-scale production of CNT forests, most of the growth of graphene has been done using the batch method on increasingly larger substrates over the years. With the start of graphene growth on polycrystalline metal films via CVD in 2009 [95], centimeter scale continuous films of single to multi-layer graphene were synthesized on Ni and Cu surfaces [50]. At this scale, the potential for integrating graphene into flexible electronics was becoming a reality, and so a great deal of work went into large area CVD growth of graphene and subsequent transfer to insulating and flexible substrates. Centimeter scale patterned and non-patterned graphene growth and transfer from metallic substrates were the first to make an appearance (Figure 2-11a) [56,154], along with substrate free growth of graphene flakes using evaporated camphor as the carbon source and the reactor walls as the nucleation and deposition sites [169]. This work was shortly followed by wafer scale growth and transfer using metallic thin films deposited on Si and quartz wafers [170,171]. However, while the continuous areas of graphene production were growing, the individual graphene grain sizes were only on the order of tens of microns. Thus, work began on controlling and increasing the graphene grain sizes through fewer nucleation sites and reduced carbon deposition rates [146,148], leading to individual grain sizes of a few millimeters (~ 4.5 mm^2) as shown in Figure 2-11b.

Limited but impressive results for R2R and large-area graphene synthesis have been shown over the past few years. In 2011, Hesjedal published their work on R2R graphene synthesis using a tube furnace and a 25 μm thick, 1 m long Cu foil, which produced multi-layer graphene coverage over much of the sample at rates of 1 - 40 cm/min [172]. Yamada et al. took this process one step further in 2012 with a custom microwave plasma CVD (MWPCVD) furnace capable of handling a 294 mm wide Cu foil at translation rates of 1 - 50 cm/min (Figure 2-11c) [61]. This process produced complete coverage of 3 to 4 layers of graphene on the surface of the Cu (later transferred to PET) with grain sizes of nm to μm in diameter. While the MWPCVD process enabled low temperature growth (> 400 °C) which minimized Cu sublimation and illustrated the potential for substrates with lower melting temperatures, increased temperatures would benefit the graphene quality and grain size. Most recently, Kobayashi et al. produced high quality, predominantly single-layer graphene on a 230 mm wide, 100 m long, 36 μm thick Cu foil at 100 mm/min using a R2R process [173]. Following a R2R transfer of the graphene to

PET film, they reported a graphene areal coverage of 89 - 98%. Along with the successful demonstration of R2R graphene growth, uniform large-area (> wafer scale) batch growth has also made progress in two notable studies. In 2010, Bae et al. produced uniform graphene films on 30" diagonal Cu foils (Figure 2-11d) that were subsequently transferred to PET following a wet chemical etch of the Cu [59]. Then, this year, a very similar technique was used by Vlassiouk et al. to produce 40" diagonal films of graphene that also exhibited uniform coverage post transfer to PET [174]. Looking at the image in Figure 2-11a where the 40" sample is held with a 4" wafer, it is amazing how much progress has been made in the area of large-scale graphene production in a relatively short time span.

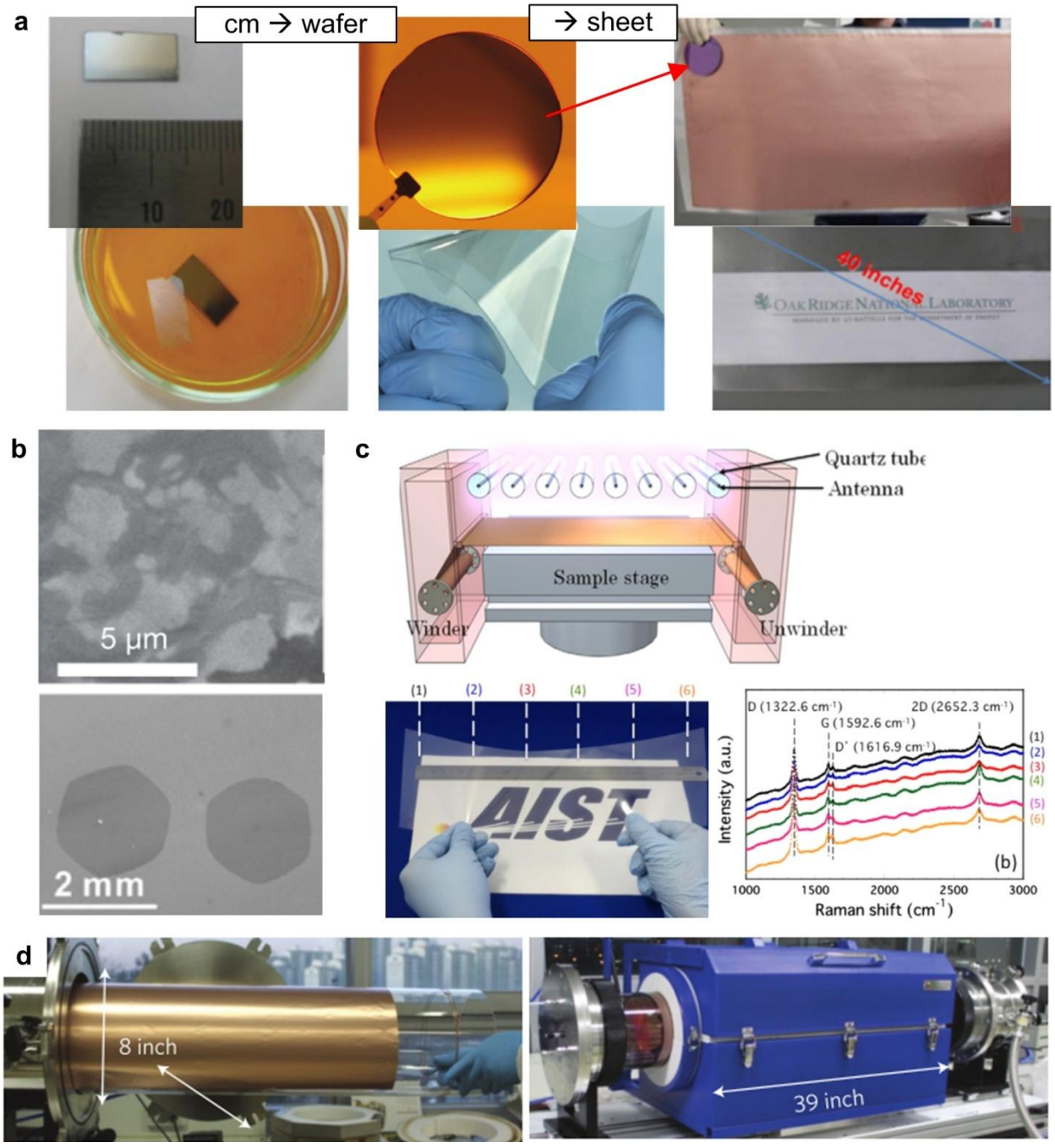

Figure 2-11. Large-scale and continuous CVD growth of graphene. (a) Scale of graphene growth since 2009 from cm-scale Ni coated substrates to 40" diagonal Cu foils [56,171,174]. (b) SEM images of small graphene flakes grown without size control (top) and large graphene grain growth using nucleation control techniques (bottom) [56,146]. (c) Schematic of a MWPCVD R2R graphene growth reactor and a graphene film transferred to PET with accompanying Raman spectroscopy curves [61]. (d) 30" diagonal Cu foil loaded into a tube furnace for CVD growth of graphene [59].

2.3 Challenges for scale-up and process control

R2R processing has been the focus for most large-scale nanomaterial synthesis, due to its low cost and scalability. It also enables applications such as flexible electronics, composite materials, and dry adhesives to be achieved through a direct approach. However, while R2R processing appears straightforward and easily implemented to the growth of CNT forests and graphene, several challenges exist for the processing materials and products themselves that need to be addressed for R2R implementation. In addition to the processing challenges mentioned earlier in Section 2.1, items such as substrate choice and/or design, CNT forest density, graphene uniformity, temperature limitations, material patterning and R2R package integration still present problems with large-scale manufacturing of these materials. Each of these items will be addressed in the following section with risk mitigation recommendations for each.

The R2R process by definition requires a flexible substrate, which limits substrate materials to metallic foils, composite and ceramic fibers, and polymer films. Additionally, since the growth method of choice for both CNT forest and graphene is CVD, the substrate must also be able to handle the extreme processing temperatures required to synthesis these materials. Unfortunately, even given the current state of low temperature methods of CVD growth, this limits the substrate material selection mainly to metallic and ceramic substrates.

2.3.1 CNT forest substrate selection

Metallic substrates suitable for CNT forest growth can be divided into two types: 1) metals with native catalyst particles and 2) metals without native catalyst particles. The metals that have native catalyst particles include alloys such as Ni-Cr and stainless steel (SS) where there is a high enough transition metal content such that subsequent thermal or chemical treatment of the material generates catalyst nanoparticles at or near the surface [175,176]. One such treatment for SS is an oxidation step, prior to the catalyst reduction, that enables the catalyst nanoparticles (i.e., Fe) embedded in the substrate to migrate to the surface. Once reduced, the catalyst particles at the surface of these alloys directly support CNT forest growth. In addition to other process parameters that were previously discussed, the alloy of these materials can be adjusted to have the appropriate amount of catalyst suitable for the desired CNT growth characteristics. If properly designed, the additional processing step to form the particles could be eliminated along

with the need to deposit a catalyst layer on the surface of the substrate during the R2R processing, therefore making it a desirable substrate selection.

Metallic substrates without native catalyst particles have also been used for CVD CNT forest growth with success. But much like Si substrates, a catalyst must be deposited on the surface for CNT forest growth. While floating catalysts have been directly deposited on metal foils to generate CNT forest growth [177,178], typically an oxide or "support" layer is also required between the substrate and the catalyst. Electron charge donation between the support layer and the catalyst particles has been identified as the primary factor for the need of the support layer, and direct evidence of its impact on the growth of CNT forests has been documented [125,179]. Among the various oxide layers to choose from, alumina has been consistently shown as one of the most beneficial materials, and because of its chemical structure, it also provides a diffusion barrier that slows the catalyst migration into the substrate bulk. Deposition methods for the alumina layer have included dip coating, e-beam evaporation, and laminates using aluminum which develops a native oxide layer [72,163,180]. Using these methods prior to catalyst deposition, metal ribbons including Ni, Cu, Ta and various others have been shown to produce CNT forests (Figure 2-12a) [72,181–183], but CNT height is limited when compared to standard Si substrates. Additionally, the addition of oxide and catalyst layers to the metal substrate in support of CNT forest growth adds cost in substrate preprocessing, and several processing steps to the R2R design if done in-line. While large volumes might bring the cost of the preprocessing to a competitive level with that of a custom alloy substrate previously described, in-line R2R processing could also reduce the throughput. These factors must be taken into account when deciding to use a non-alloy metallic substrate for CNT forest growth.

While not thought of as a substrate solution many of the CNT forest commercial applications, ceramic, glass or carbon fiber substrates offer distinct advantages to the structural composites market. Flexible, and able to withstand high temperatures in support of CNT growth without additional oxide depositions, ceramic fibers overcome many of the pitfalls normally associated with flexible substrates. However, as with the glass and carbon fibers, proper understanding of fiber heat treatment is needed to preserve the mechanical properties of the fibers. CNT growth on the fibers occurs normal to the surface, which creates a "fuzzy" or "mohawk" fiber, enabling additional mechanical interaction between fibers in a woven mat

(Figure 2-12b, c) [162,184,185]. Growth on pre-woven fabrics can then be infiltrated with resin to create composite materials with additional strength due to resistance to fiber "pull-out." This growth method recently entered the large-scale manufacturing market when Applied Nanostructured Solutions, LLC reported the commercialization of CNT forest growth on glass fibers [186].

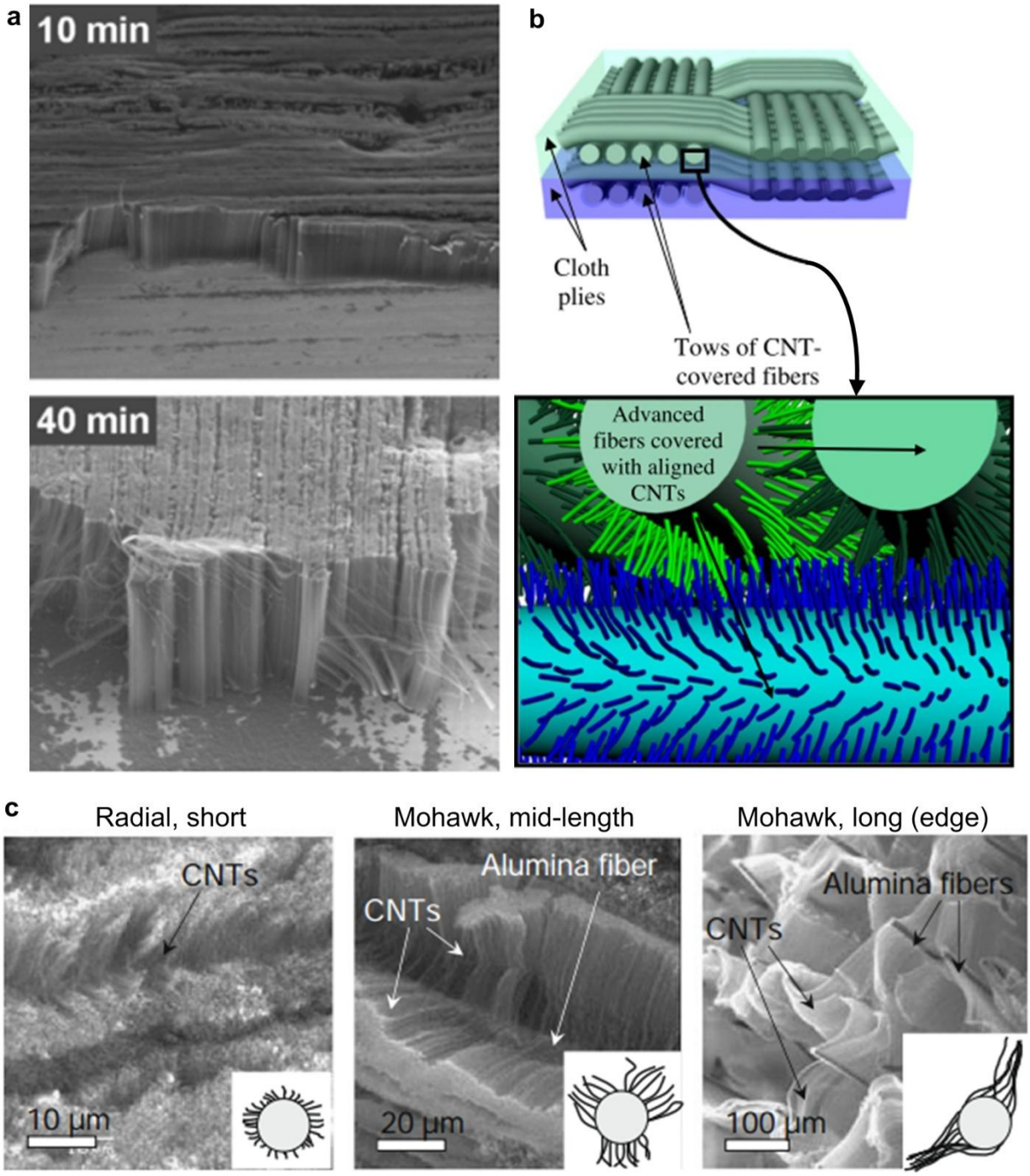

Figure 2-12. CNT forest and grapene growth on various substrates. (a) SEM images of CNT forest growth on Ni foil after 10 and 40 min [72]. (b) Schematic of CNTs grown axially on woven composite fibers [184]. (c) SEM images and inset schematics of radial and mohawk growth morphologies of CNTs on alumina fibers determined by the length of the CNTs [185].

2.3.2 CNT forest density

In order to match the performance characteristics of bulk materials used in electrical and thermal interfaces, the density of CNT forests needs to be much higher than typical thin film catalyst depositions allow. Although a lot of work has gone into increasing forest density on Si substrates [92,93,126], similar methods do not always work on the preferred R2R metallic substrates because the catalyst particles tend to diffuse to the grain boundaries [187]. This causes a heterogeneous areal density which is not conducive to the intended applications. Thus, either a metallic substrate that does not experience grain growth under the CVD condition, or a buffer layer such as the oxide support layer must be tuned to minimize cracking during the CVD process as the grain boundaries of the underlying metal migrate. Additionally, the catalyst deposition technique must be R2R compatible or scalable to large surface areas to meet the throughput demands of commercial manufacturing. Fortunately R2R ALD [188–190], sputtering [77] and printing techniques [191,192] all exist for deposition of the support and catalyst layers which solves the manufacturing integration, however additional research must still be conducted towards optimization of CNT forest density on metallic substrates. A detailed look at convective assembly of catalyst particles for CNT forest diameter and density control is presented in Chapter 4.

2.3.3 Graphene substrate selection

Because of the high probability that native catalyst particles will cause defects or additional nucleation points leading to layer control issues, metallic substrates without native catalyst particles are the preferred material for CVD graphene growth. The main considerations that govern the selection of the substrate are thickness and the crystal structure of the grains. As described earlier, the size of the grains dictate how many nucleation sites are available at the grain boundaries, and to the same end, the thickness of the metal substrate typically dictates the largest grain size that can be achieved (unless deposited on a secondary support) [99]. Additionally, the crystal structure of the grains can be controlled through an annealing process, which enables the quality of the graphene to be controlled by reducing the likelihood of defect formations (i.e., different crystal surfaces have different binding energies with carbon and dictate different graphene flake orientations, thus increasing or decreasing the probability of a defect

formation). Unfortunately, while the metal substrate can be directly used for graphene growth, the requirement for graphene transfer to insulating substrates for integration into devices or other materials adds a transfer step.

2.3.4 Graphene uniformity

As discussed previously, graphene uniformity is controlled by the average grain size of the metal surface and the flux of carbon precursor adsorbing to the surface. While the control of grain size and the formation of nucleation points at the grain boundaries leading to growth of additional graphene layers locally at these spots has been discussed at length, the implications of reducing the carbon flux at the substrate have not been addressed. During several batch growths, the carbon flux was reduced by either reducing the flow of the feedstock gases, increasing the H_2 to carbon precursor ratio, or by creating a very narrow reaction zone [146–148] (Figure 2-8d, 2-11b). These methods led to mm-scale single grain sizes of graphene growth, but required longer growth times to achieve large-area coverage. In addition to the large grain sizes, these methods also restricted the number of nucleation sites, which led to uniform single layer graphene without additional layers nucleated beneath. Unfortunately, by increasing the required growth time, the throughput of the R2R system is undesirably reduced. The only alternative to decreasing the throughput is to increase the size of the reaction zone such that the substrate can maintain a certain translational speed but remain in the reactant gas atmosphere longer. Thus, a balance of translational speed and reactant chamber design must be considered in a R2R graphene CVD system.

2.3.5 Temperature limitations

In addition to growth support, substrates are also limited by their ability to maintain favorable properties throughout the CVD process. Unfortunately, CVD processing is generally executed at temperatures above 700°C for CNT forest growth and 950°C for graphene growth, which exceeds the melting point of some metallic substrates. In an effort to combat this issue, and enable a wider variety of materials to be utilized as substrates, lower temperature CVD and PECVD processes have been applied to CNT forest and graphene growth with some success [61,193–195]. Although synthesis of CNT forests and graphene on polymer substrates has not been demonstrated, the ability to directly grow on a flexible polymer film would enable the

direct synthesis of flexible electronic devices on the target substrate without the need for a transfer process. The lower processing temperatures also combat another issue specific to metallic substrates, hydrogen embrittlement (Figure 2-13) [196,197]. Because the native oxide layers on metallic surfaces (substrates and catalyst particles) requires a reducing step, typically in a hydrogen rich environment, the result for some metals at the elevated CVD temperatures is the inclusion of hydrogen at the grain boundaries, resulting in vacancies that lead to a weak and brittle material. Although this does not prevent CNT or graphene nucleation and growth, the brittle nature of the substrate after growth renders it useless for integration in R2R applications, or for substrate re-use post CNT forest or graphene transfer. Thus, substrate material selection is dictated not only by whether or not it can support CNT forest or graphene growth, but also whether or not it can survive the continuous CVD process.

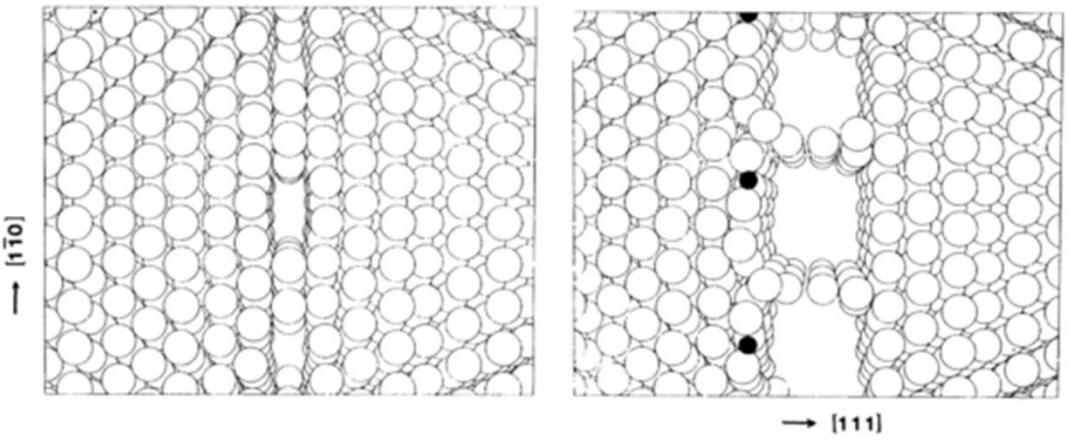

Figure 2-13. Hydrogen embrittlement of Ni at a defect site. Calculations showing the positioning of Ni atoms at a defect site (left) and the resulting defect growth due to increased stress caused by single hydrogen atoms (dark circles) at each of the three unit cells (right) [196].

2.3.6 Patterning

Applications such as electrical circuit components, sensors, probes, nano-composites and dry adhesives require the CNT forest or graphene to be discontinuous and patterned into smaller units. This can be accomplished for both materials through transfer printing, imprint lithography, laser transfer, or substrate/catalyst patterning, which are all R2R compatible. Transfer printing utilizes a soft stamp with the desired positive pattern to transfer the material

through an "inking" and "transfer" process [198], while imprint lithography used a hard stamp to create a surface feature on the desired substrate which in this case would be used to define the growth regions [199]. Laser transfer is similar to transfer printing only the pattern is made by the laser which locally changes the adhesion of the target substrate as it come in contact with the material to be transferred. Finally, patterning metallic thin films as catalyst for CNT forest growth or substrates for graphene growth can be accomplished through a variety of printing methods (i.e., slot-die coating, screen printing, gravure printing, etc.) [192,200,201] and lithography methods (i.e., soft lithography, photolithography, etc.) [202] which enables the direct growth of the desired pattern (Figure 2-14). Lithography methods are the most common for situations where the desired material can be directly grown on the target substrate, but regardless of the pattering method, each of them has been previously implemented in an industrial process, making it unlikely that this procedure will be the bottleneck in a R2R CNT forest or graphene growth system.

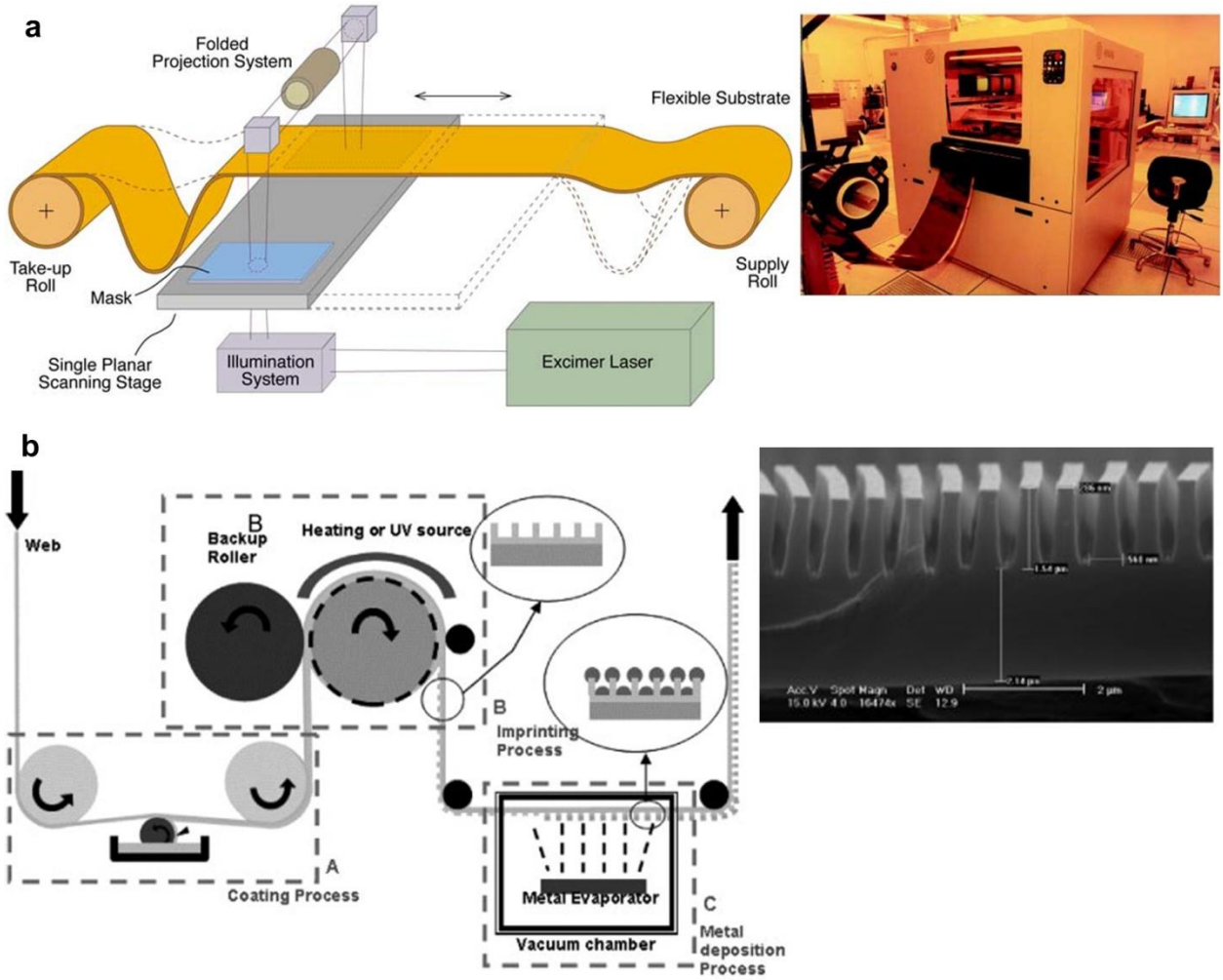

Figure 2-14. R2R lithography processes. (a) Schematic and optical image of a R2R photolithography system [202]. (b) Schematic of a lab-scale R2R nanoimprint lithography (NIL) process and a SEM image of the patterned substrate [199].

2.4 Summary

This chapter presented a comprehensive overview of the synthesis of CNT forests and graphene with the intent of R2R system integration. The individual processing steps for the CVD growth of CNT forests and graphene have been discussed and the definitions and limiting factors for each were presented. A table of process times for each material, during the catalyst deposition, annealing, growth and delamination stages was assembled to highlight the bottleneck points for an integrated R2R system which included the catalyst deposition for CNT forest

growth and delamination/transfer for graphene growth. Methods for controlling favorable characteristics of each material have been discussed and examples from literature have been highlighted for substrate preparation, nucleation, growth and delamination/transfer. Taking R2R integration into account, additional considerations including substrate selection, CNT forest density, graphene uniformity, temperature limitations, and material patterning have been presented and situations to avoid were discussed.

CHAPTER 3: ANALYSIS OF CNT FOREST GROWTH VARIATION AND RECOMMENDATIONS FOR IMPROVED CONSISTENCY

*Significant portions of this chapter with additional editing were published in: C. R. Oliver, E. S. Polsen, E. R. Meshot, S. H. Tawfick, S. J. Park, A. J. Hart, ACS Nano **2013**, DOI 10.1021/nn400507y; ref* [62].

This chapter presents a CNT forest growth study of 280 samples aimed at identifying variables that contribute to height, density and quality variations. First, a discussion of the problem with growth variation is presented, followed by the standardized growth procedure that we developed. Through the use of the standardized growth procedure, we identify significant variables that were both controlled (*e.g.*, CVD parameters, sample handling, etc.) and uncontrolled (*e.g.*, lab temperature, lab humidity, etc.) through the use of a statistical analysis. Next, each of the significant variables (i.e., ambient humidity, barometric pressure, and sample position) are presented along with a discussion on how they manifest variation in the system. A separate series of experiments are incorporated into this discussion where we identify the role moisture level has on the dewetting of the thin film catalyst, which in turn influences the CNT density. Additionally, the role of the permeability of water through polytetrafluoroethylene (PTFE) gas supply lines and subsequent contamination of high-purity source gases is also investigated in detail. Finally, recommended growth procedures for CVD CNT forest growth based on the findings of this study are presented. Implementation of these procedures and a brief analysis of CNT forest pattern growth are also mentioned at the end of the chapter, but details are omitted since that work was completed entirely by co-authors of the publication referenced above.

3.1 Variability CNT forest growth

Attaining consistent results is essential to the transfer of new materials processing methods from lab-to-lab and from lab-to industry. While lab-scale research efforts often focus on concept demonstration rather than quality control, a lack of process consistency can hinder knowledge

transfer and lead to inefficient use of resources in attempting to replicate published data. In the authors' opinion, this issue is particularly relevant to nanomaterials research, as many exciting lab-scale demonstrations now demand focus on detailed engineering and manufacturing research to create commercial value [203]. Moreover, the parameter space for nanomaterials synthesis process conditions is large and often incompletely known, which limits rigorous understanding and the ability to extrapolate research findings to new processes and applications.

For example, commercialization of new materials and devices incorporating vertically aligned carbon nanotubes (CNTs), or CNT "forests," requires precise control of structural attributes (*e.g.*, CNT diameter, quality, density, and alignment) as well as process performance (*e.g.*, growth rate, reaction efficiency). This control is essential to implementing principles of scale-up, and it is relevant for designing CNT forests to achieve target performance for applications such as thermal interfaces [204–206], and electrical interconnects [93,207,208]. There is a wealth of knowledge regarding the influence of several factors governing CNT growth by chemical vapor deposition (CVD), including hydrocarbon gas chemistry [113], process conditions (*e.g.*, pressure, temperature) [136], moisture content [119], reactor wall conditions [140], and other factors [3,209]. Regardless, experts still accept that CNT forest growth is highly non-repeatable under typical laboratory conditions.

This non-repeatability suggests that there are "hidden" factors that influence CNT growth, such as ambient conditions and differences in standard procedures, the details of which are sometimes difficult to learn from the literature. Moreover, limitations in consistency of CNT growth have, in the authors' opinion, led to excessive trial-and-error process tuning rather than systematic approaches guided by fundamental understanding. Researchers frequently endeavor to use low-cost atmospheric pressure CVD systems such as tube furnaces because they are easy to setup and operate, and sometimes perform research outside of a clean room environment in order to reduce facility cost and maintenance constraints. At the same time, this practice increases the risk of process variation, unless sources of variation are understood and appropriate controls are implemented.

For instance, it is well known that CNT growth can be influenced by ppm-level changes in the concentration of H_2O vapor (moisture) within the CVD reaction chamber [137,210,211].

However, it is not widely known how ambient humidity levels affect the CNT synthesis conditions. One example is the intrusion of air into an open CVD chamber during sample exchange, or the retention or permeation of moisture in porous system components. Due to rapid or seasonal weather changes, ambient humidity can fluctuate by 1-10,000 ppm, compared to the 100 ppm moisture level first shown to influence CNT forest growth [119,137]. Moreover, how moisture and other trace impurities/additives, such as oxygen [212] and alcohols [213], affects CNT growth is partially determined by the hydrocarbon and hydrogen mixture in the reactor, which is also known to evolve along the length of the tube due to thermally activated reactions [91,214]. Therefore, without rigorous methods to identify and eliminate sources of moisture and other potential sources of process variation, "hidden" conditions may influence CNT synthesis in an unknown way.

3.2 Standardized CNT forest growth procedure

In order to study the sources of variation in CNT (all references to CNT growth are referring to multi-walled nanotubes per our typical conditions [215]) forest synthesis, we used an atmospheric CVD system (Figure 3-1a) and defined a "reference" procedure, consisting of a list of operational variables (Table 3-1) and growth (Table 3-2) and baking (Table 3-3) recipes. The list of operational variables was constructed from known possible factors suspected to influence the outcome of a CNT growth experiment, in addition to the standard parameters of the growth recipe. For example, we had previously hypothesized that the original location on the source wafer from which the catalyst growth substrate was sampled could influence the CNT growth outcome. Also, we had observed that CNT growth results (*e.g.*, height, density) were different between the first experiment and subsequent experiments performed using the same CVD system in the same day. The growth recipe was based on our experience [33,216], and is consistent with processes used by several other groups [90,137,217].

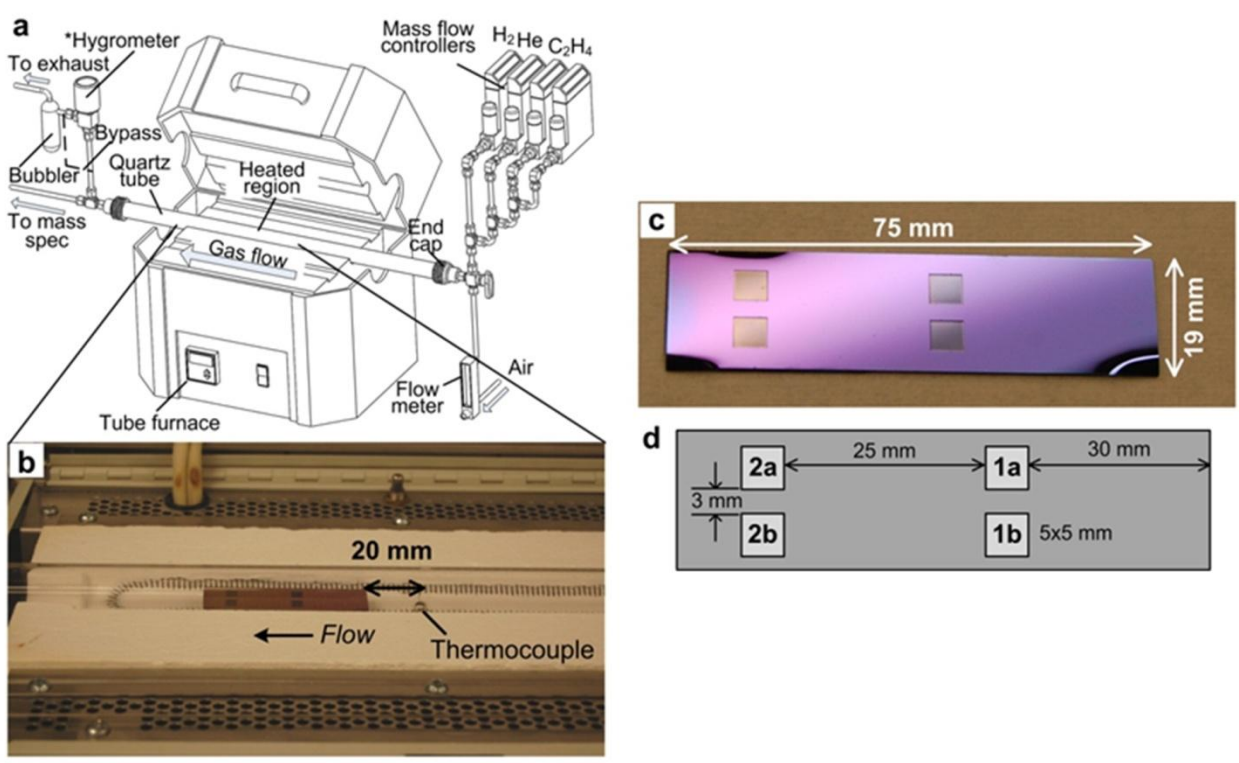

Figure 3-1. CVD system and sample configuration for reference growth study. (a) Schematic of CVD tube furnace system with hygrometer at output. (b) Image of silicon wafer "boat" inserted into the quartz tube and positioned in the furnace for a growth experiment. (c) Image of the boat with the cavities for sample placement. (d) Schematic of boat indicating dimensions and encoding of sample positions with respect to position along the tube (1,2) and side (a,b). Position 1 is upstream relative to position 2.

Table 3-1. Operational parameters of reference CNT growth procedure.

Process variable	Set value	Control method
Substrate dimensions	5x5x0.5 mm	Wafer etched
Samples per run	4	Counted
Boat dimensions	75x19x0.5 mm	Etched by DRIE
Boat location	60mm from tube end	Alignment ring on insertion rod
Experiments/week	2	Monday, Friday
Tube placement	Center of furnace	Alignment mark
Sample placement	Refer to Fig. 1	Etched into Si boat
Line pressure	20 psi	Gauge reading
Recipe	Refer to Table 2	Computer (LabView)
Alumina thickness	14-15 nm	AFM
Fe thickness	2.9-3.1 nm	AFM
Bubbler liquid level	10 mm	Visually verified

Table 3-2. CNT growth recipe.

Process time (min)	Step duration (min)	He (sccm)	H_2 (sccm)	C_2H_4 (sccm)	Set temperature (°C)
5	5	400	100	100	25
10	5	1000	0	0	25
15	5	400	100	0	25
25	10	400	100	0	775
35	10	400	100	0	775
45	10	400	100	100	775
50	5	1000	0	0	25

Table 3-3. Reactor baking recipe.

Time (min)	Air (sccm)	Set temperature (°C)
5	1000	25
10	1000	875
20	1000	875
5	1000	25

The procedure began with sample preparation. Two clean silicon (100) wafers, having 300 nm of thermally grown SiO_2, were first coated with photoresist on both sides, and then scored using a dicing saw (ADT 7100) to create 5×5 mm square lines on the back of the wafers, 50 μm deep. The photoresist was then removed from both sides of the wafers and then 10 nm of Al_2O_3, followed by 1 nm Fe (measured to be 3 nm by AFM after exposure to air), was deposited by e-beam evaporation on both wafers simultaneously in the same deposition run (SJ-26). The wafers were loaded simultaneously into the chamber and coated in the same deposition run. Then each wafer was broken into 5×5 mm samples that were numbered and cataloged based on their original location on the wafer, in order to later identify CNT growth variation that arose from non-uniformity in catalyst thickness across the wafer. Half of the samples from each wafer were randomly selected and put into separate polystyrene petri dishes, yielding four dishes. Two of the dishes, corresponding to half of each wafer, were placed inside a desiccator, while the other two dishes were stored outside of the desiccator, in the lab ambient. This separation of samples was done to investigate the effects of variations in the laboratory environment on the catalyst, and the effects of variations in user practices for storing and handling samples. Specifically, we wanted to investigate if absorption/absorption of water to the samples was a significant source of moisture in the reaction chamber during the CVD process. Thus, the desiccator was utilized to provide a dry environment for half of the samples.

We then determined a plan for experiments that would evaluate the influence of the operational variables on the height and density of the resultant CNT forests. Using standard *A priori* statistical power analysis (Optimal Design software [218]) we estimated that 70 experiments would be needed to achieve statistically significant results (power = 0.85). We

wanted to be able to detect a 40 μm shift in height caused by any variable being investigated, which we call the effect size. We calculated the number of experiments necessary to capture the effect size with 4 samples per experiment, which equaled 70 experiments.

Prior to beginning the series of "reference growth" experiments, each system component that was used for process control and/or measurement was calibrated and nominal values (baseline measurements) expected to remain unchanged for all experiments were collected. We collected baseline measurements from each of our sensors (*i.e.*, mass flow controllers, furnace thermocouple, exhaust bubbler, mass spectrometer, mass balance, laser displacement sensor for CNT height measurement, e-beam deposition crystal monitor, desiccator humidity gauge, ambient data logger, and Raman spectrometer) to ensure that each was within the calibration specification. Additionally, we performed the following procedures prior to any work completed for this study. We purged our gas supply lines (connecting the tanks to the CVD system) by evacuating each line (<10 Torr) while flowing 500 sccm He, 500 sccm H_2 and 200 sccm C_2H_4 for 30 minutes. Each gas line was approximately 8 m long, with a 10 mm inner diameter, thus constituting an internal volume of approximately 630 cm^3. The deposition thickness produced by the e-bean deposition machine was calibrated the week before the sample wafers were generated by atomic force microscopy (AFM) measurements of deposited thin films on other samples. AFM imaging was performed in tapping mode in a Veeco Dimension Icon. The calibration of the laser displacement sensor used to measure CNT forest height was verified *via* a gauge block (Mitutoyo 080076) before each set of height measurements. A MFC configured to be a mass flow meter (Aalborg Model #GFC17) was used in-line with the CVD system MFCs to calibrate the flow rates at four equally spaced points between 0 sccm and the maximum flow of the MFC to be calibrated (1000 sccm for He, 100 sccm for C2H4 and 1000 sccm for H_2). The tube furnace (Lindberg Blue M) temperature profile at a 775 °C set point (Figure 3-2) was measured by inserting a K-type thermocouple through an Ultra-torr (Swagelok) fitting attached to the furnace tube end cap, and translating it in cm increments along the furnace axis. To ensure consistent operation over the entire study, the baseline measurements and calibrations were performed again, and compared to the initial baseline (N = 0), at experiment numbers N = 35 and N = 70. No corrections were needed throughout the study. In addition, a log of gas tank

replacement was kept to rule out the effect of tank contamination in this study and no correlation was found.

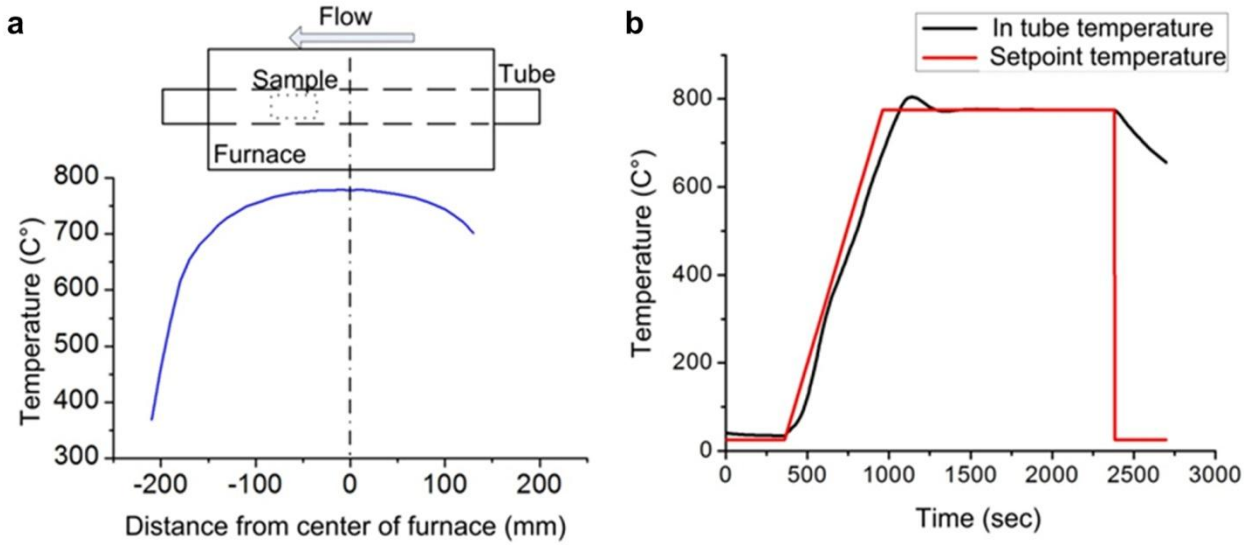

Figure 3-2. Temperature profiles. (a) Thermocouple measurement along central axis of reactor tube, with furnace set to 775 °C. (b) Comparison of transient profiles of setpoint temperature and in-tube temperature during a single experiment.

Each experiment began by randomly selecting one sample (*i.e.*, a 5×5 mm substrate) from each of the four petri dishes, weighing the samples using a microbalance (Ohaus Discovery, taking the average value of 4 measurements for each sample), measuring the sample dimensions using a set of digital calipers, and placing the samples in cavities (250 μm deep) on the etched silicon carrier substrate ("boat") shown in Figure 3-1c. Samples taken from the desiccator were placed in positions 1a and 2b on the boat, and samples stored in ambient were placed in positions 1b and 2a. On alternate experiment days, the relative positions were switched. Then, the boat was loaded into the quartz tube (22 mm ID x 762 mm long) such that the leading edges of samples 1a and 1b were 50mm downstream of the center of the furnace (the location of the control thermocouple). Based on our previous work, this was the general "sweet spot" for this recipe.

The furnace temperature, gas flows, and process sequence were controlled and recorded using a custom LabView program. Ultrapure (99.99%) H_2, He, and C_2H_4 gases were controllably delivered using MFCs (Omega and Aalborg, Model #GFC17) to the horizontal tube

furnace (25 mm OD, 300 mm heated length). As listed in Table 3-2, VACNT arrays were grown at atmospheric pressure, with flows of 100/100/400 sccm C_2H_4/H_2/He, at 775°C for 10 min, preceded by an annealing step at 775°C for 10 min with flows of 100/400 sccm H_2/He. The CNTs were rapidly cooled in a He atmosphere until the chamber temperature reached 150 °C, at which point the samples were removed. During each experiment the gases at the output of the furnace tube were sampled using an inline quadrupole mass spectrometer (Pfeiffer Vacuum Technology, Model #GSD301O3) to enable the variation in gas species from experiment to experiment to be analyzed (Figure 3-3). At the conclusion of the growth sequence, the boat was removed from the tube, each sample was weighed, and the mass of each CNT film was calculated by subtracting the mass of the corresponding catalyst substrate before CNT growth. Height measurements were averaged over three measurements across five points around the chip (4 corners and center) using a laser displacement sensor (Keyence, Model #LK-G152), and the volumetric and areal density of each sample was calculated using the measured dimensions, height and mass.

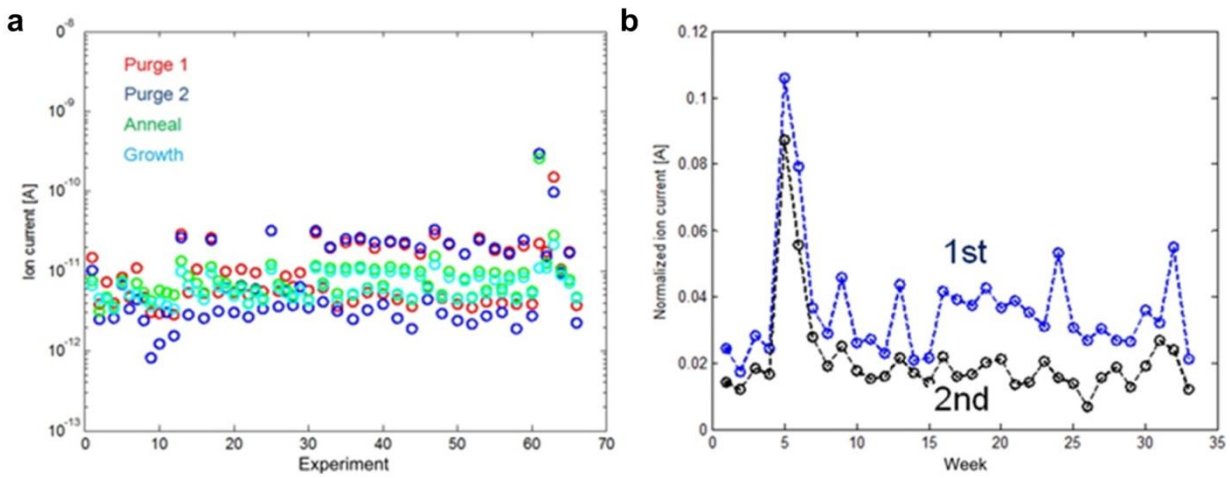

Figure 3-3. MS data with trends of particular gases vs. time for annealing and growth (a) Ion current for A.M.U. of 18 taken by mass spectrometry at the start of each step in the experiment by run. (b) Normalized ion current values for A.M.U. 18 taken when C2H4 is introduced into the reactor for the first and second experiment of the day.

After each experiment, the empty boat was placed in the tube, and the system was heated to 875^{o}C under a flow (1000 sccm) of zero grade dry air, metered *via* a manual flow meter (McMaster-Carr, Model #5079K63), and held for 30 minutes (Table 3-3). The purpose of this step was to oxidize carbon that was deposited on the quartz tube interior and boat during the

CNT growth experiment, and thus to keep the quartz tube in a consistent condition over the course of the study. The air bake ("bake-out") after the first daily experiment was done directly before the second daily experiment, whereas the bake-out after the second daily experiment occurred directly after the second daily experiment. As a result, the tube and boat were exposed to the lab atmosphere prior to the first daily experiment, which allowed us to study how storing the reactor tube in ambient conditions affects CNT growth.

3.3 Batch sample characterization

In addition to the characterization conducted on the individual samples as part of every experiment (i.e., mass, height, area), CNT quality, structure, average diameter and alignment were characterized for a set of samples after all of the growth experiments were complete. These samples were selected to provide a subset that spanned the entire range of ambient conditions. CNT structural quality was evaluated by Raman analysis (Dimension P2, Lambda Solutions, λ = 533 nm) from the top of the forest (sidewalls were not measured due to the low average heights of the forests) using the ratio of the IG and ID peaks. SEM imaging was performed using a FEI Nova Nanolab to provide structural and alignment information on the forests, and CNT diameter and alignment were calculated using small angle X-ray scattering (SAXS) patterns.

X-ray scattering measurements were collected, by placing the CNT forests on a motorized stage in the beampath of the G1 beamline at Cornell High Energy Synchrotron Source (CHESS). A beam energy of 10 $\pm$ 0.1 keV (wavelength $\approx$ 0.13 nm) was selected with synthetic multilayer optics (W/B4C, 27.1 Å d-spacing), and the beam was focused down to $\approx$ 20 μm using upstream mechanical slits. The beam size was measured by scanning the beam over a pinhole slit mounted on a motorized stage while measuring the beam intensity. The downstream X-ray intensity measurements were normalized to the upstream measurements in order to eliminate the effect of the drift in synchrotron intensity over time. A standard sample of silver behenate powder (d_{001} = 58.380 Å) was used to calibrate the pixel-to-q ratio for the detector. Line scans from the 2D SAXS patterns were fitted using a mathematical model for lognormally distributed hollow cylinders, which were obtained by integrating intensities within $\pm$ 10° from the reference direction (x-axis) of the inverse space parameter q (chosen to be the direction of maximum intensity). The fitting code used an iterative approach in searching for the best fit within a user defined fitting range. By including the low q part of the data, a good fit was achieved that selects

a probability density function (PDF) for diameter distribution as well as for the ratio c = ID/OD, where ID is the inner diameter of the CNT and OD is the outer diameter.

3.4 Results and discussion

Using the reference growth procedure, we performed 70 CNT forest growth experiments, each with four substrate samples, therefore totaling 280 samples. For the first 32 experiments, two experiments were performed each day, two days a week. For the remainder of the study, we performed two experiments per day, one day a week. This resulted in a total study time of approximately 6 months.

Histograms of height and density for the full population of samples are shown in Figure 3-4. The coefficient of variation for height and density are 31% and 63% respectively. Frankly, we had tolerated these variations throughout our previous research, and had noticed that, under the same recipe, CNT forests grew taller in the winter months than the summer months, presumably due to significant changes in ambient humidity/temperature at our location (Ann Arbor, Michigan). However, this was the first time we quantified the variation, and to our knowledge it is the first time this has been quantified and explained in the literature.

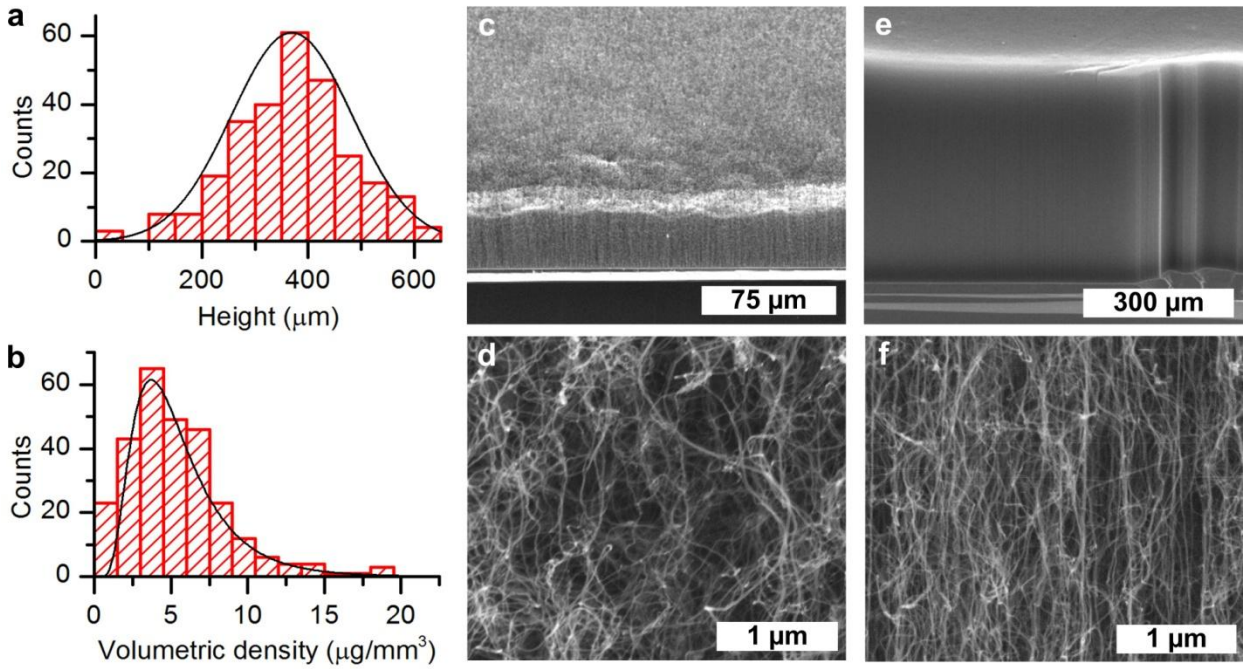

Figure 3-4. Variation in CNT forest height and density during the reference growth study. (a) Histogram of height measurements taken from 280 samples for the complete study. (b) Histogram of volumetric density measurements taken from 280 samples for the complete study. (c,d) SEM image of the sidewall of a short CNT forest and corresponding magnified image. (e,f) SEM image of the sidewall of a tall CNT forest and corresponding magnified image. Magnified images show clear differences in CNT alignment and density.

Ambient conditions (temperature, humidity, barometric pressure) fluctuated over a wide range during the course of the study (Figure 3-5), as measured using an electronic data logger (UEi, Model# THL1) placed next to the reactor in the lab. Comparing the trends of height and density to ambient conditions appeared to validate our hypothesis that ambient factors contributed to growth variation. Sharp changes in humidity appear to cause changes in CNT height and density, for example, between the weeks of 20 and 25.

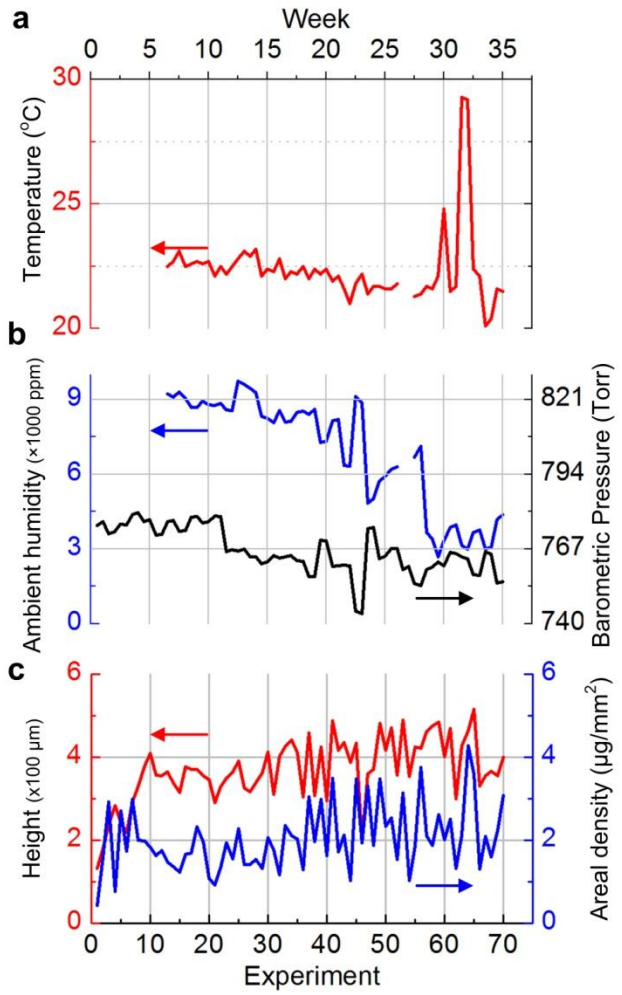

Figure 3-5. Ambient laboratory conditions. Plots of (a) temperature and (b) humidity and barometric pressure for each experiment. Data points represent the value in the lab at the beginning of the experiment with a start date of 23 July 2010. Temperature and humidity data was not collected for weeks 0-6. Data was lost for week 27 due to a sensor malfunction. (c) Plot of CNT forest height and areal density for each experiment.

Further trends are revealed by separating the full data set according to the order of experiments on each day of the study, as well as the position of the sample along the reactor tube, as shown in Figure 3-6. Significant variation is present in both subsets of first and second daily experiments (Figure 3-6a,b), yet the sample position and experiment order present well-defined differences in mean CNT height and areal mass density (Figure 3-6c,d). Moreover, *via* scatter plots of height and density versus ambient humidity (for the same respective experiment of the day and sample position), we noted an apparently parabolic relationship with ambient humidity.

We compared the quality of fitness values for linear and parabolic relationships between humidity and the measured CNT forest height, and the parabolic relationship showed an adjusted R^2 value twice that for a linear relationship. However, we acknowledge that the multi-variate nature of the experiments result in a weak relationship with the data, as pointed out by a low Pearson's correlation coefficient for these fits. We also note chemical reaction rates typically exhibit a parabolic relationship with control variables, and so it should be expected that both too little, and too much water would not be best for the chemical reactions that produce CNTs. The parabolic relationship is consistent with previous studies of CNT growth where much smaller amounts of moisture were added directly to the CVD furnace [119]. Therefore, although there is significant scatter in this data, it suggested there may be optimal humidity level(s) that maximizes CNT height and/or density for a particular growth recipe.

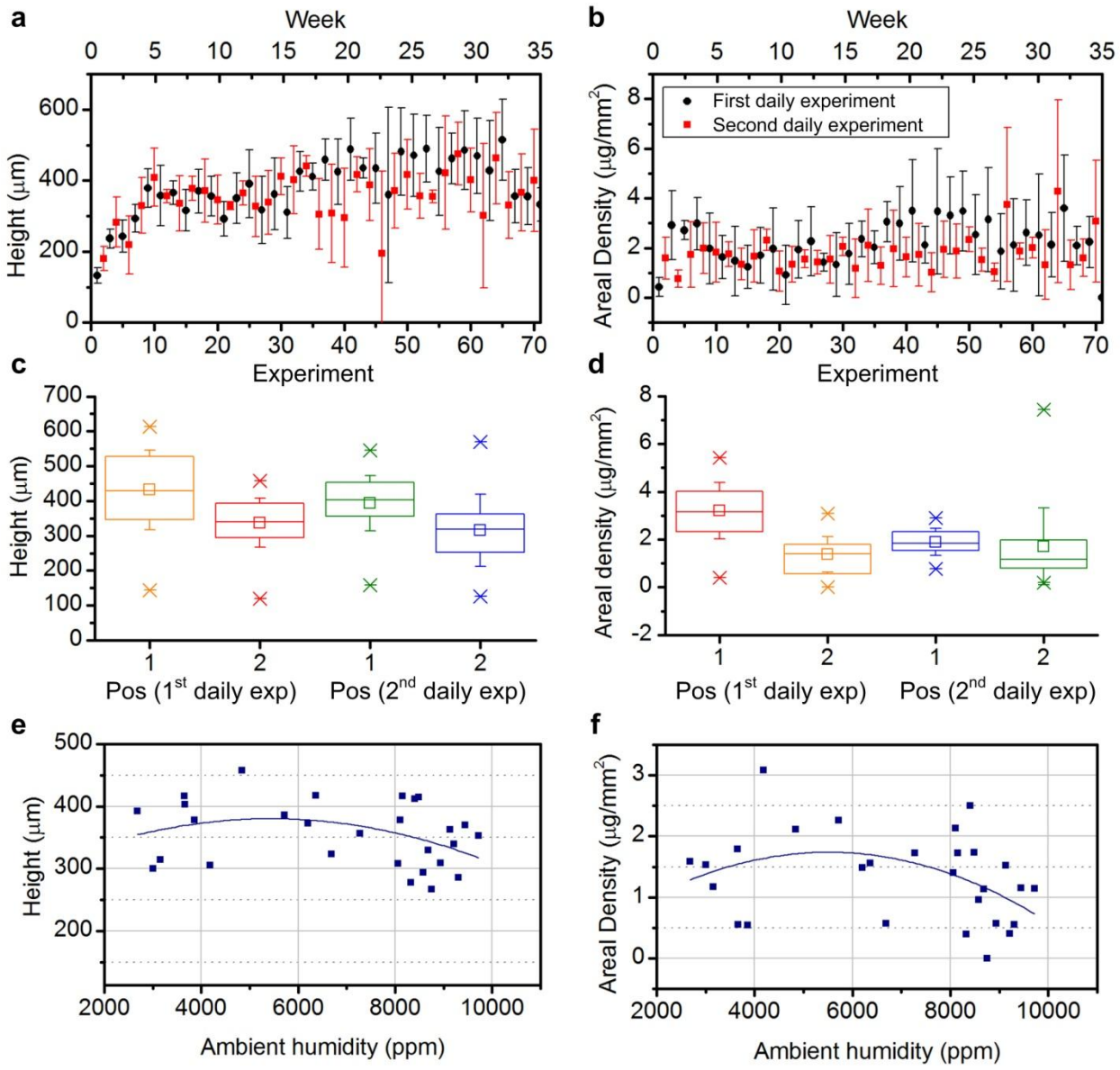

Figure 3-6. Initial analysis of reference growth variation, according to experiment order, sample placement, and measured ambient humidity. (a) Forest height versus experiment number, separated for the first and second experiment of each day. (b) Areal density versus experiment number. (c) Height data separated according to sample position in reactor and experiment order. (d) Areal density data separated according to sample position in reactor and experiment order. (e) Scatter plot of height versus ambient humidity for samples grown in position 2 and during the first experiment of the day, fitted with polynomial relationship. (f) Scatter plot of areal density versus ambient humidity for samples grown in position 2 and during the first experiment of the day. In (e) and (f), the height values are the average of sample positions 2a and 2b. They show that an optimal value of ambient humidity maximizes either sample height or areal density.

In order to more rigorously identify the causes of CNT growth variation, we performed a multivariate linear regression among height, density, and 8 of the operational and process variables (Table 3-1). The correlation coefficients between CNT growth results and five selected operational variables are shown in Table 3-4. Statistical significance was determined using the p-value criterion, which determines if observed variation is due to chance or due to a known factor that may or may not be controlled. We used a widely accepted threshold of $p = 0.05$. A p-value greater than 0.05 cannot conclude that the factor did not influence the measured outcome, and a p-value less than 0.05 indicates that the factor influenced the measured results. We also computed the r-value, called Pearson's correlation coefficient, to provide the degree of correlation. An r-value of 1 indicates perfect correlation, while an r-value of 0 indicates no correlation; the sign of the r-value indicates the direction of relationship (inverse or direct). Using the p-values, we found statistically significant correlations: height was correlated to ambient humidity ($p = 0.00$, $r = -0.22$) and sample location in the furnace ($p = 0.01$, $r = 0.16$); and areal density was correlated to ambient humidity ($p = 0.06$, $r = -0.17$), sample location in the furnace ($p = 0.04$, $r = 0.12$) and ambient barometric pressure ($p = 0.02$, $r = -0.19$). Importantly, we also found that several operational variables did not indicate a relationship with CNT forest characteristics: the storage of the samples in a desiccator (versus ambient), the ambient laboratory temperature, and the location on the source wafer from which the catalyst substrate was sampled.

Due to the duration (6 months) of the study, we considered whether or not to investigate the potential influence of catalyst age. However, prior studies on native oxide growth on Fe and Si surfaces indicate that for nanoscale Fe layers, oxidation occurs in several nanoseconds upon exposure to oxygen at room temperature, and oxidation of clean Si wafer surfaces stabilize after ~7 days under the same conditions [219–222]. Because the samples were stored in the lab ambient air for more than two weeks prior to the start of the study, it was assumed that the samples had reached a stable oxidation state.

All absolute r-values for significant variables fell between of 0.10-0.30, indicating that each factor contributed to experimental variation, even if only subtly. This is in part due to the multivariate nature of the process; however, we later show that improving process control reduces growth variation significantly, thus reducing the size of the unknown parameter space,

and enabling future work to characterize individual variable-outcome correlations. Having identified major causes of variation we now present a detailed analysis of each variable that we found contributes to variability.

Table 3-4. Calculated correlation coefficients between selected operational variables and CNT forest height, areal density, and volumetric density. Highlighted values represent statistically significant correlations.

	Dependent Variable p-Value		
Variable	Forest Height	Areal Density	Volumetric Density
Sample Location (1a,1b,2a,2b)	**.01**	**.06**	.20
Desiccator (In/Out)	.49	.73	.88
Wafer within batch (1,2)	.36	.75	.60
Ambient Humidity (ppm)	**.00**	**.04**	.20
Barometric Pressure (Torr)	.32	**.02**	**.00**

3.4.1 Relationship between ambient humidity and reactor humidity

While we found that CNT forest height and areal density correlate with the ambient humidity in the laboratory, the humidity in the reactor tube is more relevant to the results of the growth experiment. Therefore, we had to determine the relationship between ambient humidity and reactor humidity. Additionally, because commercial hygrometers are sensitive to, and contaminated by, the hydrocarbons generated during CNT growth, we were not able to directly measure the moisture content in the hydrocarbon mixture exiting the furnace. Instead, we used the hygrometer to calibrate the H_2O ion current reading (AMU 18) from the quadrupole mass spectrometer. Calibration was performed using heated mixtures of H_2 and He/O_2, where H_2 and O_2 combined to form H_2O when heated above 550 °C [138].

We found that the H_2O ion current measured by the mass spectrometer was directly related to the water content in ppm reported by the water vapor sensor, and we generated a linear correlation function. The correlation between ionization current (I) and reactor humidity (H) was derived from data gathered between 10 ppm and 4000 ppm, and is captured by the relationship:

$$H = -490 + (1.84 \times 10^{14})I. \quad (1)$$

The y-intercept of this equation is negative due to the finite baseline detection limit on the mass spectrometer. Applying this correlation function to the mass spectrometry data from the reference growth study enabled calculation of the reactor humidity during each experiment (Figure 3-7). This method of estimation verifies that there are significant fluctuations in the reactor humidity as well. However, we reiterate that this method of calculating reactor humidity is just an estimate but should be an ordinal indication of the humidity level within the reactor.

By this approach, we predict that the humidity within the reactor (mean steady-state value during the He purging step) was on average 15% of the ambient humidity in the laboratory during each corresponding experiment of the reference growth study. As shown in Figure 3-7b, the reactor humidity was highest during the anneal step of the first experiment of each day, after the tube was resting open to air for multiple days. With each progressive operation during the day (*i.e.*, first growth, second anneal, second growth, *etc.*) the reactor humidity decreased. As a result, the reactor humidity during any growth step was always less than that of the prior annealing step.

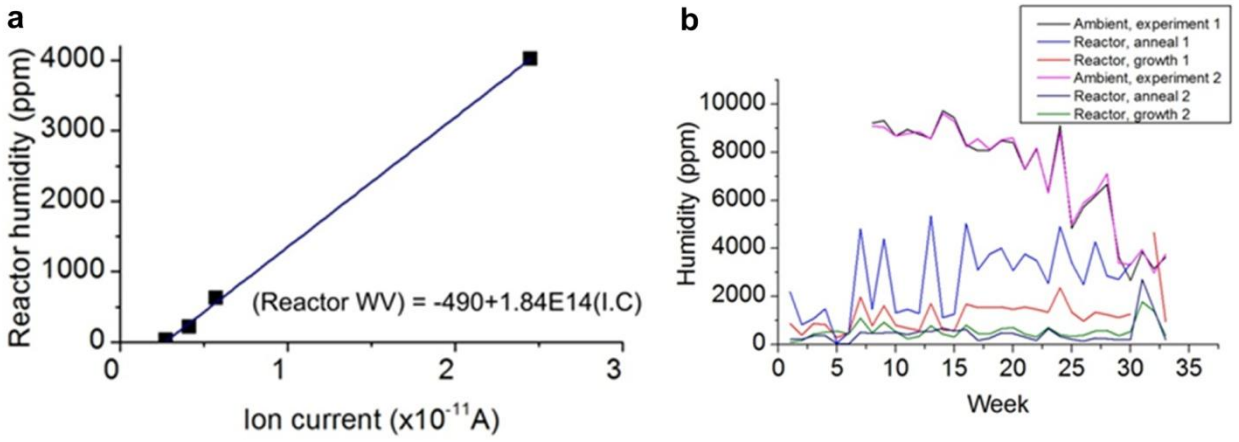

Figure 3-7. Measured relationship between ambient humidity and reactor humidity measured by mass spec. (a) Linear relationship between reactor humidity and ionization current (AMU 18) of mass spectrometer. (b) Comparison of ambient humidity and calculated reactor humidity during anneal and growth.

Throughout the study, the estimated average difference between the average reactor humidity during the first (1272 ppm) and second (570 ppm) experiment of the day was 702 ppm. By comparing these relative humidity levels in Figure 3-7, we concluded that performing a bake-out of the reactor immediately before an experiment reduces the amount of water vapor in the system by approximately 50% on average. However, even though the tube is baked after the first daily experiment, there is still a correlation between the humidity in the reactor during the second daily experiment, and the ambient humidity in the lab. This suggested that some of the system components had a continuous influence on the reactor humidity level, as further indicated by decreasing moisture levels after subsequent bake-outs (Figure 3-8).

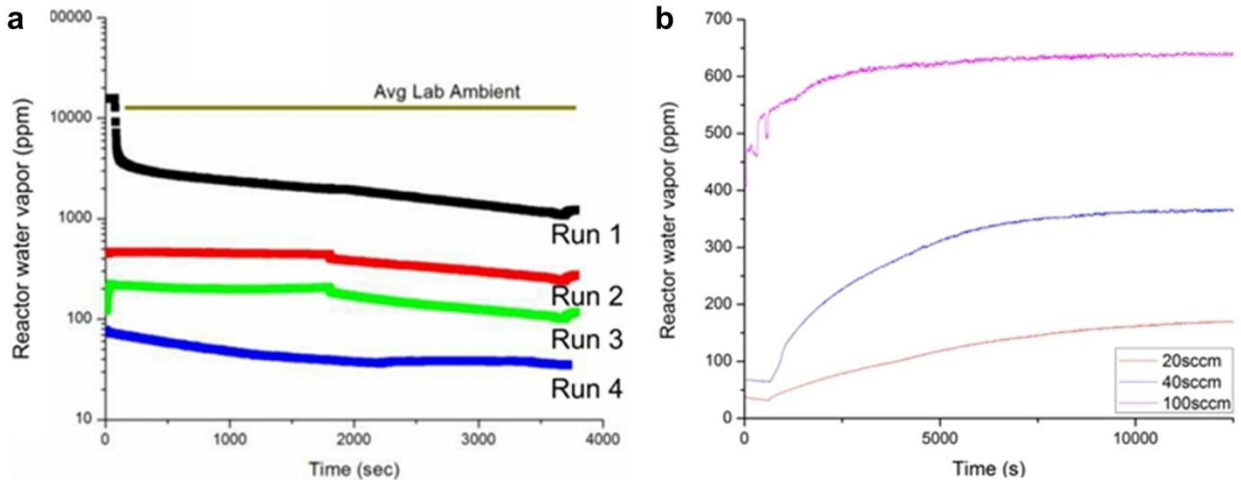

Figure 3-8. Hygrometer measurements of reactor water vapor (inside the quartz tube). (a) Decreasing water vapor levels in the reactor with consecutive experiments in a single day. (b) Generation of H2O via flow of HeO2 flows (rates indicated in legend), starting with a fully dry system.

3.4.2 Reactor tube age and gas piping material

To identify means by which ambient lab humidity influences reactor humidity, we first investigated the influence of the age of the quartz reactor tube. A previous study suggested that the surface of the tube becomes coated with carbon over time, and this was shown to improve CNT forest growth [140]. We found that the inner surface of the quartz tube becomes more hydrophobic with age (Figure 3-9a inset), possibly due to graphitic deposits; however there is no change to adsorbed water vapor. We showed this in experiments (separate from the reference growth study) in which we dried two tubes—one that had been used for months of routine experiments, and another that was new—by flushing the tubes with ultra-high purity (UHP) He for twelve hours. We then let the tubes rest overnight in the lab ambient. Then, the tubes were each inserted into a reactor system that had been pre-dried overnight using another tube and a 500 sccm flow of UHP He, which reached ~6 ppm of H_2O as measured using the online hygrometer. Next, the furnace was heated to 750 ^oC with the same flow of 500 sccm of UHP He. As shown in Figure 3-9a, 1-2 ppm additional moisture was released by the old tube compared to the new tube.

This contrasted our finding that significantly higher humidity levels are present in the CNT growth gases during a normal experiment. We next hypothesized that moisture was permeating the PTFE gas supply tubing, and thereby becoming entrained in the gas mixture delivered to the CVD process. To quantify the moisture trapped in the gas flows, the reactor system was sealed with a dry quartz tube and left undisturbed (without any flow in the system) for 24 hours, while 500 sccm of dry grade air was flowed through the hygrometer to keep moisture from collecting on the sensor. Then, the flow through the hygrometer was stopped and the hygrometer was opened to the furnace lines. While measuring the moisture at the output (without heating of the furnace), the gas flows were activated sequentially starting with 500 sccm He, and later adding 400 sccm H_2 and then 100 sccm C_2H_4 after the hygrometer reading had stabilized at each flow.

As shown in Figure 3-9b, use of PTFE tubing (Swagelok, PFA-T4-062-100) to deliver the gases resulted in 10-50 ppm added moisture, with different values for each gas. The tubing was approximately 2 m long from the tank supply to each respective mass flow controller (MFC), and 1m from the output of the MFCs (where the gases become mixed) to the input of the reactor. We repeated this experiment after replacing the PTFE tubing with stainless steel tubing (Swagelok, Part # SS-T4-S-035-20). Now, the measured moisture levels were less than 10 ppm, and negligible changes occurred when the different gases were introduced. Although these water vapor values seem low when compared to the values during the various growth experiments, it should be noted that the tubing experiments were conducted when ambient conditions were fairly dry. Summing the total ppm from each gas line and the tube (according to Figure 3-9a and 3-9b), we estimate a contribution of ~100 ppm. This value is one third of the value measured for a "dry" day mass spectrometry reading during the first growth of the day. While this is a large difference, we argue that this error could still be due to the estimation of the ion current conversion to ppm (especially at lower ppm values). Further, based on the specifications for the gas cylinders (from PurityPlus), the H_2 tank should have < 3 ppm H_2O and the He and C_2H_4 tanks should have < 2 ppm H_2O. Gas cylinders of this purity have been used in previous work documenting CNT growth sensitivity studies [223,224]. Therefore, we concluded that permeability of the tubing was a major contribution to reactor humidity variation in our system.

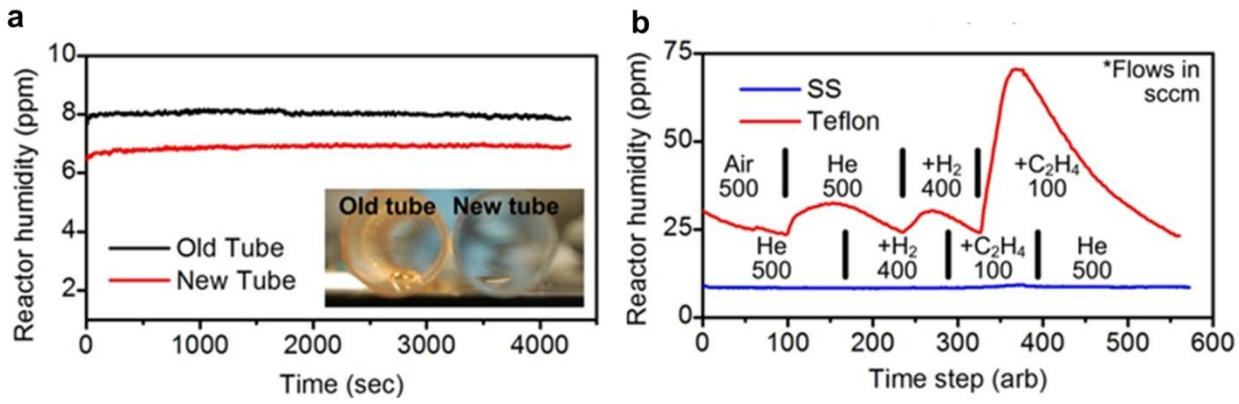

Figure 3-9. Effect of reactor tube age and gas delivery tube material reactor humidity. (a) Moisture released from an old (> 6 months) and new (< 1 week) quartz tube upon heating. Inset picture shows that the contact angle of water on the interior of the quartz tube changes with age downstream of the sample. (b) Comparison of moisture vapor released from PTFE and stainless steel (SS) gas delivery lines, with all other conditions identical.

3.4.3 Influence of H_2O content on catalyst morphology, CNT diameter, and CNT quality

Next, we quantified variations in alignment and diameter of CNTs within our forests using non-destructive SAXS. SAXS images were analyzed according to the procedure described by Wang *et al.* and Meshot *et al.* [225,226]. Using a subset of samples, taken from experiments representative of the observed spread in ambient humidity, we determined correlations of alignment and diameter with process variables. The Hermans orientation parameter was calculated as a quantitative measure of CNT alignment, and the CNT diameter distribution was calculated by fitting a core-shell form factor model to line scans of the SAXS images. This procedure was previously verified to agree with TEM measurements of CNT diameter [215].

As shown in Figure 3-10, we found that the mean CNT diameter increased with the ambient humidity. We also coupled CNT diameter with volumetric density of the CNT forests to calculate number density (number of CNTs per area), which showed an inverse relationship/correlation with ambient humidity. Because the thin-film catalyst was the same initial film thickness on each sample, a reduction of CNT number density is to be expected with an increase of average CNT diameter. This assumes that the volume of the catalyst thin film is conserved.

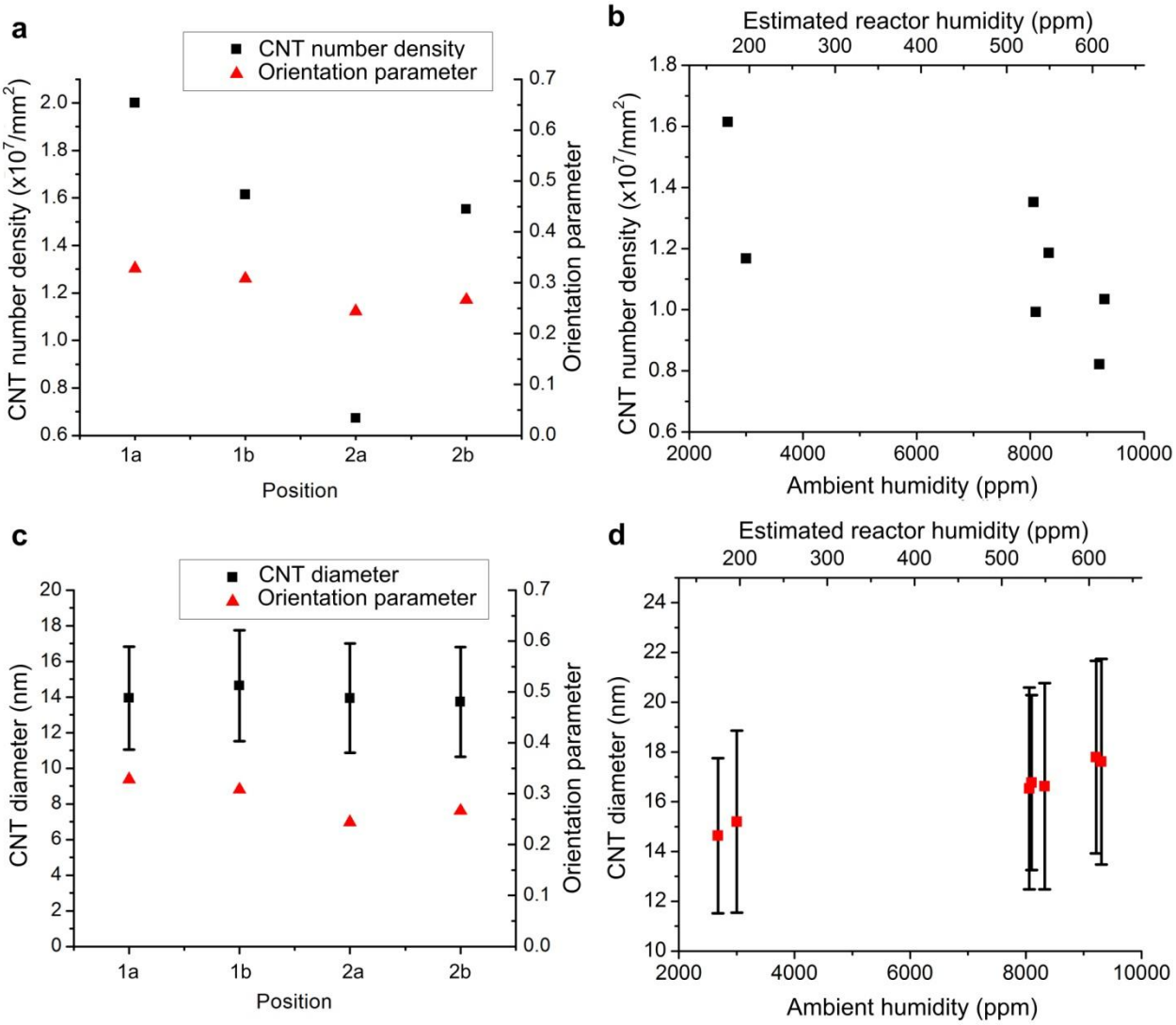

Figure 3-10. Impact of ambient humidity and substrate position on CNT diameter and number density. (a) Average CNT number density and Herman's orientation parameter versus substrate position on the boat. (b) CNT number density (average of all four samples) versus ambient humidity. (c) Average CNT diameter and Herman's orientation parameter versus substrate position on the boat. (d) Average CNT diameter versus ambient humidity.

Previous studies suggest that moisture can influence the dewetting of catalyst thin films, the migration of catalyst atoms on the substrate [227], and the lifetime of the catalyst during the growth process [123]. In order to determine the variables that govern the inverse relationship between CNT number density and reactor humidity, we focused on the annealing (dewetting) process which determines the particle size and density on the substrate. Accordingly, we annealed catalyst substrate samples under controlled levels of reactor humidity. Guided by the

reactor humidity derived from mass spectrometry for the reference growth experiments, three humidity levels were chosen: 37, 908 and 1668 ppm. Before preparing each sample, the CVD system (with SS gas delivery lines) was purged overnight to establish a baseline below 30 ppm H_2O. Then, in order to control the reactor humidity, a small amount of O_2 (*via* a mixture of 1% O_2 in He) was added to the nominal H_2/He gas flow used for annealing to generate H_2O, which we previously showed occurs when O_2 reacts with H_2 above 550 $^{\circ}$C [138]. After the furnace temperature and humidity had stabilized, the substrate was moved to the heated zone, by translating the entire tube 25 cm so that the sample moved from outside the furnace to the standard growth location for sample positions 1a and 1b (Figure 3-1). Fifteen minutes after insertion, the sample was removed and cooled in the same gas atmosphere. We note that, compared to the more frequent means of introducing moisture using a bubbler first shown by Hata *et al.* [137], the He/O_2 method enables wide range control of the humidity level *via* conventional gas flow control hardware. However, residual O_2 is also present in the reactor due to incomplete conversion to H_2O.

AFM characterization revealed a significant increase in catalyst particle diameter, height and spacing with increasing reactor humidity. This trend is evident by inspection of the images in Figure 3-11, and we further analyzed particle spacing by applying a quantitative Voronoi-decomposition method to the images [87]. The relationship between particle spacing and reactor humidity is shown in Figure 3-12. This relationship explains why we observe larger CNT diameter and lower areal density with increasing humidity. Although we report merely an estimate of reactor humidity by Eqn. (1), the trend of increasing particle size and spacing (Figure 3-11) with humidity is unequivocal, but may be affected by residual O_2 from the method used to generate H_2O for the samples. Even if this is the case, we conclude that the humidity range experienced during the reference growth study was broad enough to significantly change the catalyst morphology. The consequent effect on the CNT density is illustrated in Figure 3-11b, where CNTs are grown from the annealed samples in Figure 3-11a. As the humidity increases, the CNT morphology transitions from a vertically aligned forest to a tangled mat of CNTs caused by a decrease in the density of catalyst particles.

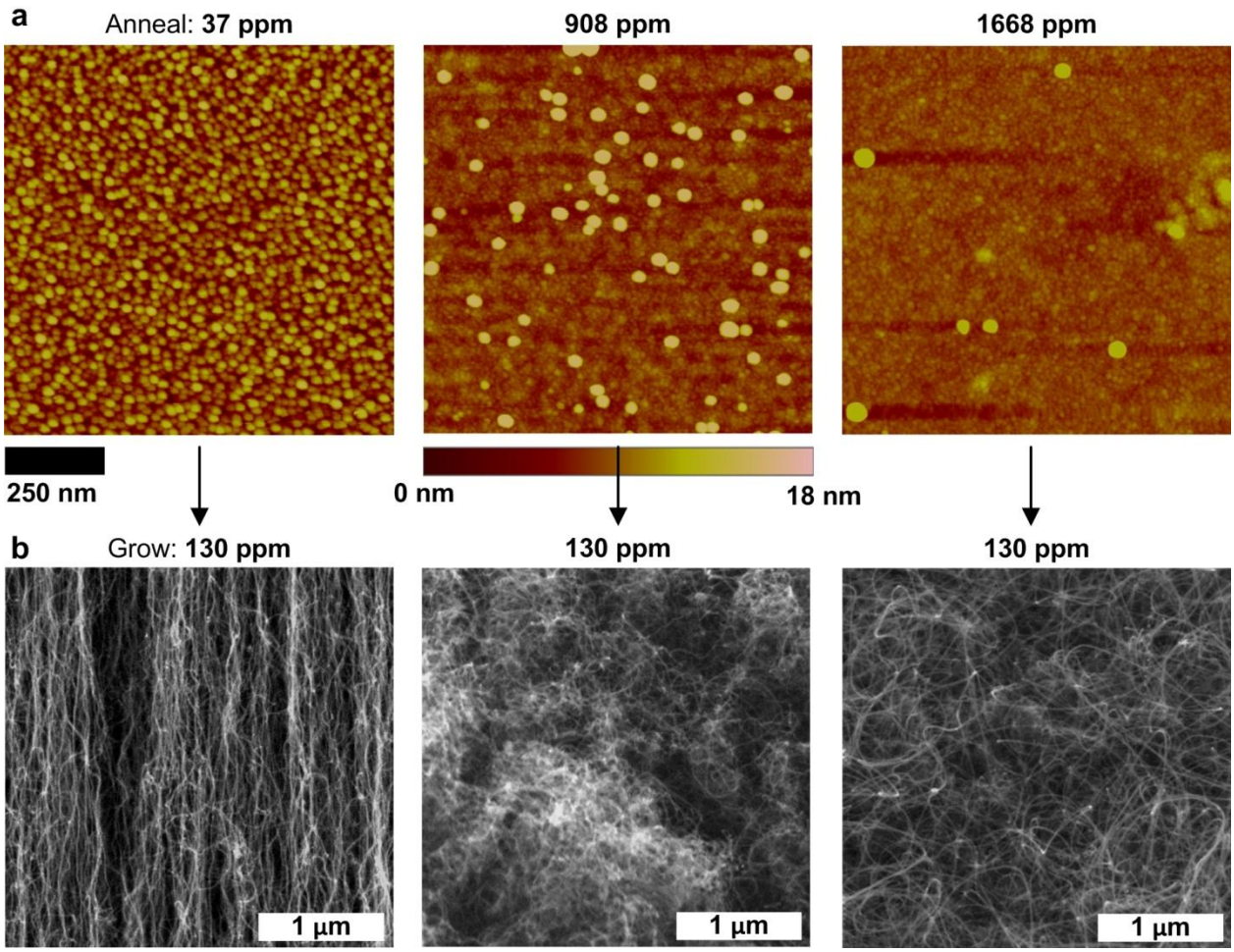

Figure 3-11. Effects of water content on catalyst particle size and density. (a) AFM images of catalyst films annealed in 37, 908 and 1668 ppm (left to right) H_2O. (b) SEM images of CNT growth morphology from the samples in (a). For (b) all samples were grown under identical conditions with 130 ppm of H_2O measured at the outlet of the reactor before flowing C_2H_4 in the reactor.

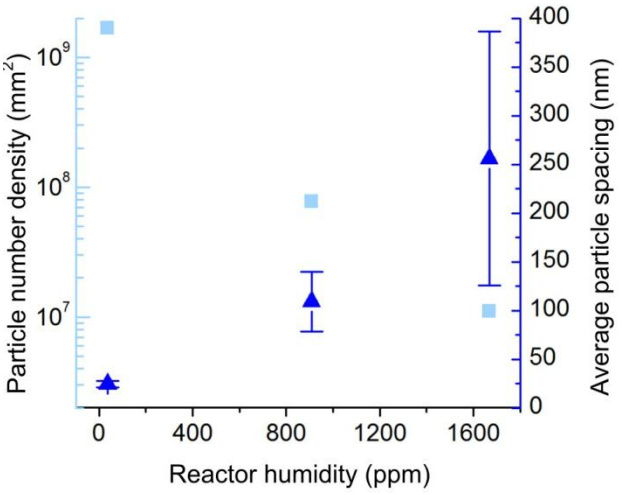

Figure 3-12. Measured relationship of particle number density and average particle spacing with reactor humidity.

Nevertheless, important topics for future work include investigating how the humidity can influence the kinetics of activation and deactivation of catalyst Fe nanoparticles, which we have recently shown to be diameter dependent [228]. In addition, the role of Al_2O_3 and its interaction with H_2O during nucleation and growth, which may influence the catalyst stability and the ability of hydrocarbons to adsorb and possibly react on the oxide surface [229,230], needs to be studied further.

Last, the CNT quality was measured for 10 forests representing a range of ambient conditions using Raman spectroscopy. Raman spectroscopy was measured from the top surface of the forest so that both tall and short forests could be similarly compared (Figure 3-13). The G/D peak ratio, signifying structural quality of the CNTs, ranged from 1.12-1.88 with a median of 1.18. The majority (80%) of samples fell between 1.12-1.37, and no significant relationship was found between the G/D ratio and any of the documented variables. Because the Raman signature of MWNTs is generally weak compared to the strong resonant effect for SWNTs, we cannot conclude that the variations in reactor ambient influenced the quality of the CNTs within the forests. Although we did not find a systematic difference in CNT quality, the presence of moisture may etch amorphous carbon depositions on the catalyst and/or the CNT walls [123,137].

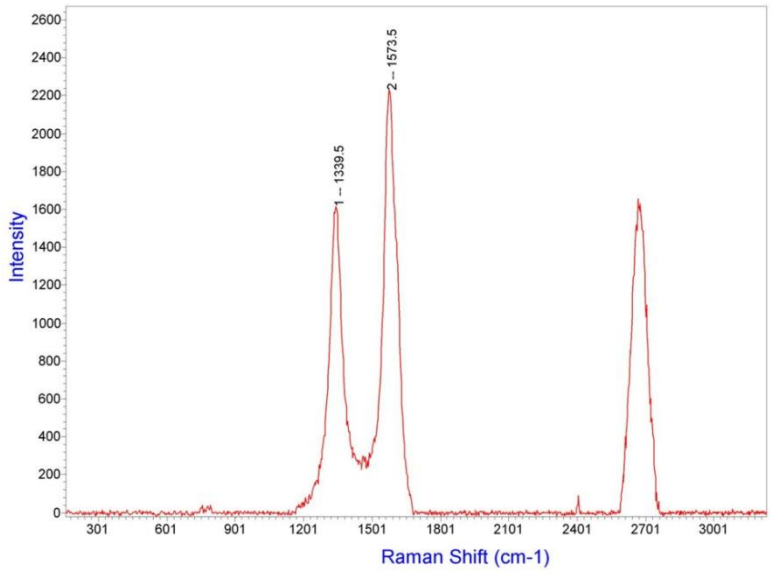

Figure 3-13. Representative Raman spectrum taken from a sample in the study.

3.4.4 Sample location in the furnace tube

It is known that sample position along the length of the quartz tube affects the height and uniformity of CNT forests and that there typically exists a "sweet spot" within the heated zone for CNT forest growth [216,231]. The sample position effect is caused by thermal history and the ensuing evolution of hydrocarbon chemistry along the length of the tube furnace. As the feedstock gas mixture of C_2H_4 and H_2 flows through the furnace, the thermal energy enables formation and recombination of myriad hydrocarbon species that can support or hinder CNT growth. For instance, alkynes (triple-bonded carbon molecules) are important for efficient growth [113,114,232], whereas much larger molecules, such as polycyclic aromatic hydrocarbons (PAHs), formed with increased thermal treatment, may either assist in productive growth pathways or promote soot formation [115,232,233].

With this in mind, we found that the CNT forest height and density are also correlated to the sample position along the length of the quartz tube. We made this conclusion by comparing the mean height and density values from one sample position to every other position, using an ANOVA multiple comparison of means test. Specifically, the height in the upstream positions (1a, 1b) was on average 150 µm taller than in the downstream positions (2a, 2b), and areal

density was greater by 0.75 µg/mm^2. Differences within the two side-by-side pairs were not significant (Figure 3-14). The temperature difference between sample positions 1 and 2 was < 15 °C. Also, SAXS analysis confirmed that CNT diameter and alignment did not vary according to the sample position, indicating that the height and density correlation with position was due to local gas composition during growth.

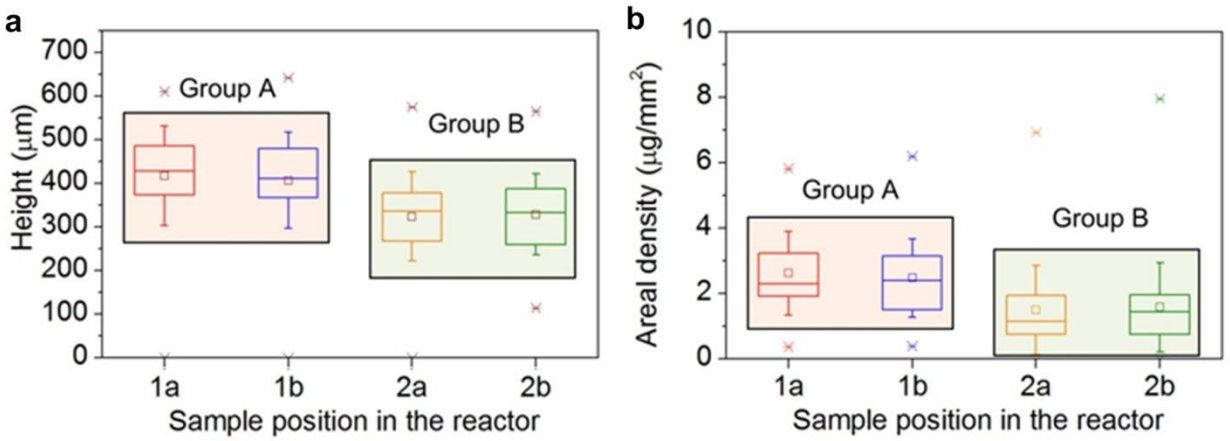

Figure 3-14. Comparison of subpopulations of the reference growth study according to sample placement within the reactor. (a) Height population differences based on the sample chip position on the boat. b) Areal density population differences based on the sample position on the boat. In both cases a Bonferoni test of means was used to determine which chip positions on the boat were grouped. Positions (1a,1b) form one group while (2a, 2b) form a second group.

We concluded that the composition of the feedstock gases arising from thermal treatment in the reactor is the main source of the sample position effect in our study, although a previous study has suggested that reactive gases generated by the catalyst on the upstream samples can influence growth on the downstream samples [224]. To further support this point, we conducted experiments where single samples were placed at positions 1 and 2 for separate growth runs and found that the upstream samples were approximately 260 µm taller than the downstream samples.

Moreover, by analysis of the full data set (Figure 3-6c, d) we found that a larger portion of the variability in height and density was from sample position in the reactor (*i.e.*, experiments from the same relative time of the day over multiple days) than from ambient factors (*i.e.*, the differences in consecutive (nominally identical) experiments). Thus, there is a need for strict control of sample position within tube furnace systems or development and evaluation of

systems that generate spatially more uniform temperature and gas conditions, in addition to controlling ambient exposure.

3.4.5 Barometric pressure

We also found that ambient pressure can influence CNT growth results. Stadermann and colleagues reported that CNT forest height is sensitive to the reactor pressure and that precise control of pressure, in concert with controlled introduction of water vapor (1500 ppm), improves process consistency [136]. In our system, ambient pressure is communicated to the reactor tube *via* the exhaust bubbler, and thus, a change in pressure downstream of the bubbler changes the pressure inside the tube. We verified this using an inline pressure transducer. The volume of the oil inside the bubbler can also affect the pressure, but this was kept constant throughout the study.

During the reference growth study, we measured ambient pressure averaging 766 Torr with a standard deviation of 8 Torr. Within a range of 740-780 Torr, we found an inverse relationship ($r = -0.19$) between ambient pressure and CNT forest density; therefore, higher density forests were produced on average at lower pressure, and more importantly precise control of reactor pressure is important to achieve highly consistent results. We hypothesize that such slight pressure fluctuations influence the partial pressures of the complex hydrocarbon mixture that evolves thermally with flow through the reactor. This is one aspect of Le Chatelier's principle: when the system is exposed to an increase in total pressure the volume of the reactants changes resulting in a shift of the equilibrium of the reaction. Thus, improved control of reactor pressure will stabilize the reaction over multiple runs.

3.4.6 System modifications and process improvement

Guided by the results of the reference growth study and follow-up experiments, we made several modifications to our CVD system, designed to reduce sensitivity to ambient fluctuations while maintaining flexibility in configuration and operation. These modifications were made after the conclusion of the reference growth study, and during investigation of the factors that contributed to variation. Specifically we installed a hygrometer (Cermet II) upstream of the furnace to monitor system water content, replaced the PTFE gas delivery lines with stainless

steel lines to limit the transfer of water into the system from the surrounding lab environment, and implemented a continuous purge of He (100 sccm, UHP grade) to keep the system clean and dry when not in use for CNT growth. Combined with a custom automated furnace [234], these modifications resulted in decreased variation of both CNT forest height and density by 50% and 54%, respectively during a follow-on study. Details of this work can be found in the main publication [62].

Last, we summarize a list of recommended control practices, which, in addition to the synthesis recipe, will reduce variability in CNT growth outcomes particularly when operating in a normal lab environment.

- Continuous purging of the system under a slow flow of inert gas (*e.g.*, 100 sccm He) or dry air to control moisture level while at rest.
- Use of stainless steel tubing throughout the system rather than polymer (*e.g.*, Tygon or PTFE) tubing, except for the quartz reaction tube.
- Use of a single quartz tube for all experiments that involve the same materials for the substrate and catalyst. Use dedicated quartz tubes for each different set of materials or significantly different process conditions (*e.g.*, gas mixture, temperature range).
- Baking of the quartz tube and boat with a flow of air after every growth experiment, for at least 10 minutes at a temperature equal to or greater than the CNT growth temperature.
- Consistent placement of the sample, with ~mm repeatability with respect to the position of the furnace thermocouple.
- Calibration of all mass flow controllers, such as using a bubble flow meter, at intervals recommended by the manufacturer.
- Measurement of the deposited catalyst thickness using AFM, and calibration of thin film deposition crystal gauges accordingly.

Complementary to these recommendations, a detailed video procedure for CNT forest growth from micro-patterned catalysts has been published by Copic *et al.* [235]. This shows our methods for loading and unloading the reactor before and after the CNT growth process, and provides a visual description of the catalyst preparation method and the CVD system.

Additionally, a similar growth study was also conducted on patterned CNT forests that showed a coefficient of variation of 19% for height, as compared to 31% for the non-patterned forests shown here. Additional details of this work can be found in the main publication [62].

CHAPTER 4: CONTROLLABLE CONTINUOUS CATALYST DEPOSITION METHOD FOR CNT FOREST GROWTH USING CONVECTIVE ASSEMBLY

Significant portions of this chapter were published in: E. S. Polsen, M. Bedewy, A. J. Hart, Small ***2013****, DOI 10.1002/smll.201202878; ref* [63]. *This includes sections 4.1-4.4. Sections 4.5 & 4.6 are not included in currently published work.*

This chapter presents a method for continuous-feed convective assembly of pre-formed catalyst nanoparticle arrays, and its application towards decoupled control of CNT forest density and diameter. We first review the previous methods for CNT catalyst deposition such as e-beam evaporation an sputtering, and then present the governing fundamentals of convective assembly of particles. Next, the steps taken to prepare the silicon wafer samples and execute subsequent convective assembly of iron oxide nanoparticles from a ferrofluid by translating the sample under a fixed blade are presented in detail. The CVD growth procedure and sample characterization techniques including SEM, AFM and SAXS are presented next. Control of the carbon morphology and CNT forest density is then presented as a function of the convective assembly parameters, where CNT forests are created from catalyst particles assembled at speeds up to 0.4 mm/s. We show that CNT forest densities are not only controllable, independent of catalyst particle diameter, but are 3-fold higher than achieved using a standard single deposition of thin film catalyst. Following these results, CNT forest samples grown from catalyst with various monodisperse particle diameters are presented along with X-ray scattering analysis of the alignment and CNT diameters for all of the forest samples in this study. Next, we discuss the path forward for improving and scaling this method, along with a comparison of the presented data to the thin film dewetting process. Last, a brief analysis of higher speed convective assembly for use with a custom built desktop machine that can perform R2R convective assembly on continuous metal foils is presented. Design and process characteristics of the machine are also presented in detail.

4.1 Catalyst deposition techniques for CNT forest growth

Owing to the growing interest in developing products that use organized assemblies of carbon nanotubes (CNTs), high throughput and cost-effective manufacturing methods are required. Specifically, continuous processes are needed to scale-up the production of CNT forests to large-area applications, such as filtration membranes, dry adhesives, and thermal and mechanical interface layers [151,206,236–238]. Moreover, in order to engineer the performance of CNTs in these applications, it is necessary to control the diameter and packing density of the CNTs within the forest [184,206,239–241]. Nevertheless, both fundamental and practical understanding of CNT forest growth by chemical vapor deposition (CVD) remains largely limited to empirically derived recipes that used in batch processes, such as on silicon wafers or pieces of wafers. As a result, the packing density of CNT forests is typically no more than a few percent relative to an ideal CNT solid, and the diameter, alignment, and spacing of individual CNTs within the forest are not uniform [91,93,112].

The size and organization of the catalyst particles are critical to determining the characteristics of the resultant CNT forest. It is well known that the catalyst particle size dictates the CNT diameter [81]. Moreover, because each particle can give rise to one CNT, the density of the particles, and their activation according to the growth conditions, determines the CNT forest density. The most prevalent method of catalyst preparation for substrate-bound CVD growth of CNTs is by annealing thin films deposited by electron beam evaporation or sputtering. Upon heating in a controlled atmosphere, the internal stresses and defects in the thin film catalyst cause it to form particles; this general process is known as thin-film dewetting [87]. Although the average size (diameter) of the particles can be controlled by the film thickness and the dewetting conditions (e.g., duration, temperature, atmosphere), dewetting of a thin film always results in a wide distribution of sizes that continue to evolve during subsequent annealing and even during CNT growth [89–91,242]. Due to this polydispersity of catalyst particle sizes, CNTs grown by this method typically exhibit a wide distribution of diameters and resultant properties. In addition, this variance in particle diameter leads to a distribution of particle activation behavior. Typically, only 1% to 10% of the all particles on the substrate yield CNTs, and this may be governed in part by the size distribution of the catalyst particles [215].

Moreover, the achievable areal density of particles is inherently limited by the thin-film dewetting process and diffusion of the catalyst into the substrate. Recently, Esconjauregui and colleagues showed that CNT forests with record high packing density can be made by iterating sputtering and annealing operations to achieve high-density catalyst arrays [93]. A bulk density equal to 62% of a closely packed array was reported for double-wall CNTs with 2.4 nm average outer diameter. However, because of the need for vacuum deposition equipment and iterative processing, it is desirable to explore alternative methods to achieve high-density catalyst arrays, which leverage scalable wet chemistry synthesis of nanoparticles.

Methods for continuous solution-based coating of thin films are widespread in industry, including gravure and slot-die coating (also called zone- or tape-casting) [243,244], which are easily implemented by spreading a thin film of liquid onto a moving web such as a metal foil. Convective self-assembly, which is analogous to slot-die coating, can be used to assemble organized arrays of micro- and nanoparticles on substrates in a continuous-feed manner. In this process, which is sometimes called "doctor blade coating" or "blade casting," particles are spread by convection as the blade is translated across the surface of the substrate (or vice-versa). Depending on the balance between the evaporation rate at the meniscus and rate of meniscus translation across the substrate, monolayers or multilayers of particles can be achieved [245–249]. Blade casting has been used to assemble both microparticles [245–247,249] and nanoparticles [248] over macroscopic areas. This evaporative self-assembly process is scalable and potentially cost-effective compared to vacuum deposition methods because an indefinite substrate as a flexible foil or film can be used, because the process can occur at ambient conditions, and because 100% of the particles end up in the final assembly.

However, most previous research on convective assembly has focused on assembly of relatively large particles (e.g., 0.1-1 μm diameter polymer particles for photonic applications), compared to the small sizes and different materials (metals) that are suitable as catalysts for CNT growth. Additionally, while the goal of convective assembly is often to create close-packed monolayers, for CNT forest engineering it would be desirable to control the packing fraction by understanding of the governing assembly mechanisms and exploration of the parameter space.

Monodisperse Fe oxide nanoparticles can be made by several wet chemistry methods [250–254], and incidentally Fe oxide nanoparticle solutions are the basis of "ferrofluids" which have many commercial applications including liquid seals for rotating shafts, contrast agents for magnetic resonance imaging (MRI), damping and heat transfer fluids for audio speakers, magnetofluid lubricants, and active suspension systems. Due to their broad commercial applications, ferrofluids are available in large quantities at low cost. For this reason, we chose to investigate blade-casting of ferrofluids as a low-cost means of catalyst array manufacturing for large-area CNT film growth. In previous work, CNT films and forests have been grown from pre-made nanoparticles deposited on substrates, including particles from ferrofluids [83,255,256]; however, the typical method of spin-coating to deposit the particles is not readily scalable to continuous-feed processing [84,85], which is needed to develop roll-to-roll manufacturing of CNT forests on flexible substrates.

4.2 Governing principles

Assembly of pre-made nanoparticles into an organized array potentially allows decoupled control of the particle diameter and packing fraction. Drawing from previous studies of microparticle assembly by blade-casting, a necessary condition is for the supply of particles to the moving meniscus to match the deposition rate of particles into the array at the liquid interface. Hence, the required volume of particle solution needed to achieve a monolayer of particles having a certain packing fraction can be calculated ahead of time, as shown in Figure 4-1.

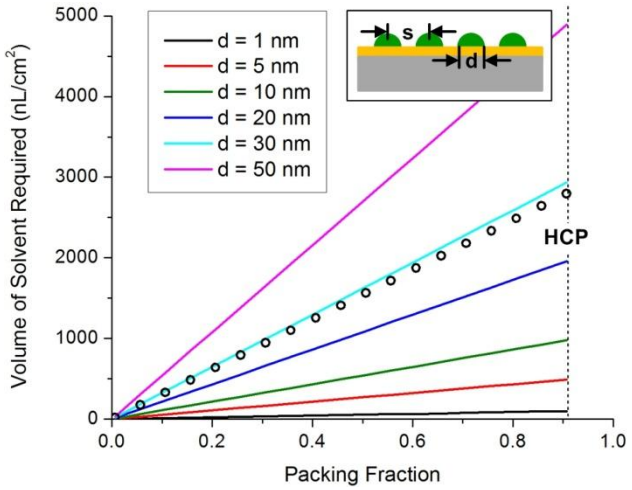

Figure 4-1. Volume of solvent required for convective assembly of a particle monolayer of desired packing fraction. This chart is based on a 3.20 mg/ml particle mass concentration, and individual data points represent the ferrofluid (MSGW11, FerroTec) used in this study.

As the moving blade draws the solution across the substrate, the stretched meniscus slips over the substrate surface (Figure 4-2). Evaporation of the solvent causes convective flow of particles toward the meniscus. The particles in this region may assemble into well-ordered arrays by two complementary mechanisms, depending on the particle size and surface chemistry, the liquid surface tension, and other process parameters [246,257–260]. For polymer microparticles, Dimitrov et al. first discussed how particles from the bulk solution are drawn into the meniscus via convective flow due to the evaporation of the solvent, then lateral capillary forces draw the particles together into an ordered configuration as the interstitial solvent evaporated [260]. Studying dodecanethiol-ligated gold (Au) nanoparticles dispersed in toluene Bigioni et al. showed that the particles are drawn to the air-liquid interface due to convective flow, where ordered islands of particles form at the interface and are eventually pinned to the substrate as the meniscus recedes along the three-phase contact line [259]. During this pinning process, lateral capillary forces draw the islands into contact.

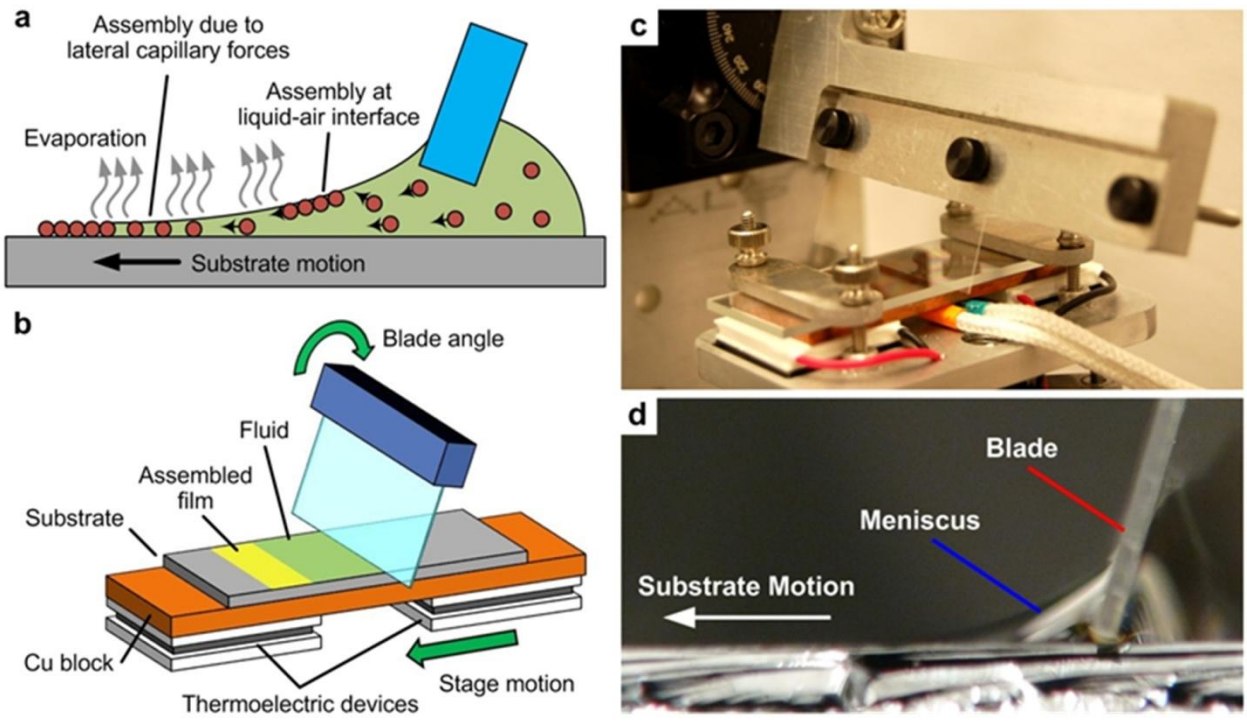

Figure 4-2. Nanoparticle array manufacturing by blade-casting. (a) Schematic of blade-casting process and mechanism of particle assembly at the liquid interface. (b) Schematic and (c) photograph of setup used for blade-casting, where silicon wafer substrate is placed on a copper platform supported by two thermoelectric chips. (d) Photograph during blade-casting of 27.20 mg/ml ferrofluid at 25 μm/s. Although this apparatus has temperature control capability, all experiments in this study were performed at room temperature.

Because water-based nanoparticle solutions in our present work have a relatively low evaporation rate (of solvent), we believe the convective assembly model first proposed by Dimitrov is appropriate for analysis in the present study. Also, the mechanism explained by Bigioni depends on a certain surface functionalization to the Au nanoparticles, in order to promote the interaction between the particles and the air-liquid interface that causes assembly at the air-liquid interface.

According to Dimitrov and Nagayama, the linear growth rate (v_c) of a particle monolayer or multilayer, undergoing convective assembly is equal to [260]:

$$v_c = \frac{\beta l j_e \varphi}{h(1-\varepsilon)(1-\varphi)}, \quad (1)$$

where β is a coefficient of proportionality, j_e is the volumetric evaporation flux per unit area of the solvent, l is the evaporation length, φ is the particle volume fraction in the suspension, h is

the thickness of the layer, and ε is the porosity of the array. In order to maintain a steady growth rate of a particle monolayer according to Equation (1), the relative motion speed between the blade and the substrate (v_r) must equal v_c. If $v_r > v_c$, a non-close-packed particle layer will be formed, whereas if $v_r < v_c$, multiple particle layers will be formed. This model is later used to interpret our findings of how the blade-casting process parameters for nanoparticles are related to the array morphology, and to the resultant CNT films grown from these particles by CVD. Moreover, this model can be used to determine the volume of solution (Figure 4-1) needed to form a monolayer of nanoparticles on the substrate, in contrast to the coupling between film thickness and particle size that is observed for thin film dewetting.

The coefficient of proportionality is defined as the ratio between the macroscopic mean velocity of the suspended particles (v_p)and that of the solvent molecules (v_s).

$$\beta = v_p / v_s \tag{2}$$

Stronger particle-particle interactions and particle-substrate interactions decrease the value of β, whereas non-adsorbing particles and dilute solutions increase β close to a value of 1. The evaporation length, *l*, is the ratio between the evaporation flux per unit length at the leading edge (J_{evap}) and j_e.

$$l = J_{evap} / j_e \tag{3}$$

Both J_{evap} and j_e are dependent on the local surrounding conditions illustrated by the Langmuir equation:

$$\frac{dM}{dt} = \left(p_v - p_p\right)\sqrt{\frac{m}{2\pi RT}} \tag{4}$$

where p_v is the vapor pressure of the solvent, p_p is the partial pressure of the solvent in the local atmosphere, m is the mass of a single solvent molecule, R is the ideal gas constant and T is the temperature. Dividing the Langmuir equation by the density of the solvent yields j_e.

$$j_e = \left(\frac{dM}{dt}\right)/\rho \tag{5}$$

As temperature increases, p_v increases, increasing the evaporation flux based on the Clausius-Clapeyron relation and results in an increased evaporation flux. Additionally, increases in the relative humidity of the surrounding air limits the rate at which the solvent molecules can be incorporated into the local atmosphere, which also increases p_p if the solvent is water. The use of Equation (2) has been shown to be valid for particles with diameters down to 79 nm, however, the mechanism of assembly with smaller particles still applies. While functionalized particles on the order of 6 - 11 nm have been shown to include island formation at the air-liquid interface prior to being pinned to the substrate [248,259], the non-functionalized particles used in this study did not display the formation of islands at the air-liquid interface.

4.3 Materials and methods

First, 10 nm of Al_2O_3 was deposited by e-beam evaporation on (100) silicon wafers coated with 300 nm of thermally grown SiO_2. The wafers were then manually scribed and fractured into 15 mm x 25 mm samples. Optionally, the wafer pieces were plasma treated (Harrick Plasma PDC-32G) in air at 200 mTorr, at 6.8 W, for 5 minutes. The samples were then immediately removed from the plasma chamber and loaded onto the blade-casting machine for particle deposition.

The custom-built blade-casting apparatus controlled the substrate motion using a Thorlabs PT1/M-Z8 single axis translation stage with a Z825B DC servo and TDC001 T-Cube DC motor controller. The blade, a 0.13 mm thick glass cover slide, was mounted rigidly to a vertical support and oriented 20° from the vertical axis. The blade edge was first brought into contact with the substrate using a vertical micrometer stage (Thorlabs PT1/M), and 6 µL of the ferrofluid solution (Ferrotec MSGW11 and Oceantech SHP-10, SHP-20 and SHP-30) was placed at the interface between the blade and the substrate, using a handheld micropipette. The solution spread along the interface, forming a static meniscus between the two surfaces over the 15 mm width of the substrate. After the meniscus was formed, the substrate motion was activated at a constant velocity. During this time, the dynamic contact angle and meniscus shape were observed to determine if the meniscus was pinning sufficiently to the substrate to enable particle deposition. Once the blade reached the end of the substrate, the remaining ferrofluid was removed from the substrate using the edge of a clean Kimwipe, which gently wicked the fluid away from the deposited area. Finally, the sample was placed on a hotplate at 75 °C for 30 min

to ensure the complete evaporation of water. All blade casting experiments were conducted with local ambient temperature and relative humidity values at 22.0 $\pm$ 0.3 °C and 31.3 $\pm$ 4.9% respectively.

CNT growth was performed in a Lindberg Blue M horizontal tube furnace (22 mm ID, 300 mm heated length) at atmospheric pressure, with flows of 100/100/400 sccm C_2H_4/H_2/He, at 775 °C for 20 min, preceded by an annealing step at 775 °C for 10 min with flows of 400/100 sccm H_2/He. The CNTs were rapidly cooled in the growth atmosphere before purging the CVD chamber with He when the thermocouple reading drops below 200 °C. An identical recipe was used for all experiments reported in this paper, and this recipe yielded the different morphologies discussed in the text.

AFM imaging was performed in tapping mode in a Veeco Dimension Icon. Mass measurements of the substrates were collected after nanoparticle deposition and after CNT growth, using an Ohaus Discovery microbalance, and the differential represented the mass of CNTs grown on the substrate. The areal coverage of each VACNT array was calculated using contrast pixel counting in Adobe Photoshop CS6, using images taken by a Nikon D40 camera. SEM imaging was performed using a FEI Nova Nanolab, and CNT diameters and forest heights were measured directly from SEM images at different magnifications. The combination of the mass, area and height measurements was used to calculate the areal and volumetric densities of the VACNT arrays. TEM images of the "flakes" structures were collected using a JEOL 3011 HREM.

For X-ray scattering measurements, the CNT sample was placed on a motorized stage in the beam path of the G1 beamline at Cornell High Energy Synchrotron Source (CHESS). A beam energy of 10 $\pm$ 0.1 keV (wavelength $\approx$ 0.13 nm) was selected with synthetic multilayer optics (W/B4C, 27.1 Å d-spacing), and the beam was focused down to $\approx$20 μm using mechanical slits upstream. The beam size was accurately measured by scanning the beam over a pinhole slit mounted on a motorized stage while measuring the beam intensity. A standard sample of silver behenate powder (d_{001} = 58.380 Å) was used to calibrate the pixel-to-q ratio. Linescans from the 2D SAXS patterns are fitted using a mathematical model for lognormally distributed hollow cylinders. These scans were obtained by integration of intensities within $\pm$ 10° from the

reference direction (x-axis) of the inverse space parameter q (chosen to be the direction of maximum intensity). The fitting code used an iterative approach in searching for the best fit within a user defined fitting range. By including the low q part of the data, a good fit was achieved that selects a probability density function (PDF) for diameter distribution as well as for the ratio c = ID/OD, where ID is the inner diameter of the multi-wall CNT and OD is the outer diameter [91,225].

4.4 Results and Discussion

4.4.1 Nanoparticle Film Assembly by Blade-Casting

We first investigated the convective assembly of iron oxide (magnetite, Fe_3O_4) nanoparticles, which were obtained commercially as a water-based dispersion (ferrofluid MSGW11, FerroTec). The average particle diameter of this dispersion, as measured by dynamic light scattering (DLS), was 28.6 $\pm$ 11.2 nm (Figure 4-3). The particle concentration of the fluid was controlled by diluting the as-received fluid with deionized water.

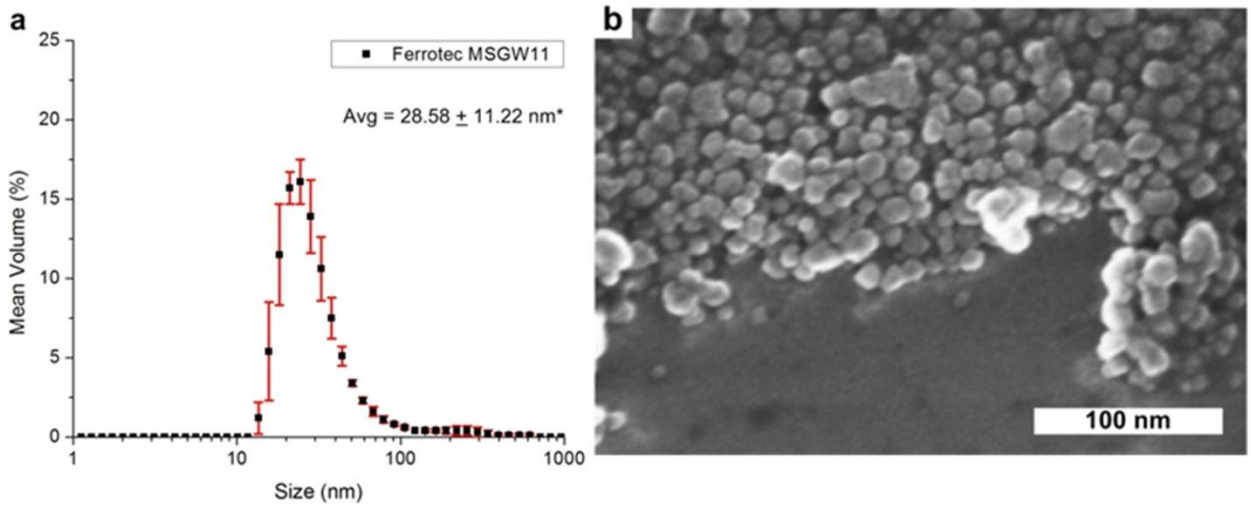

Figure 4-3. Particle size distribution and morphology for Ferrotec MSGW11 ferrofluid. (a) DLS diameter distribution data from four separate measurements. (b) SEM of iron oxide particles from a 27.20 mg/ml solution blade casted at 25 µm/s on a substrate. *Average diameter values are based on size data < 70 nm (which did not significantly impact the measurement, nor did the larger particles get deposited on the substrates during blade casting).

Using the custom-built apparatus shown in Figure 4-2c, solutions with varying particle concentrations from 0.33 to 163.2 mg/ml were blade-casted onto 15 × 25 mm silicon wafer

pieces. The substrates had been previously coated with 10 nm Al_2O_3 by sputtering (see Materials and methods). A droplet of fluid was applied at the interface between the blade (angled at 20° from the vertical axis) and the substrate using a handheld pipette, and the substrate motion was started at a constant speed. For each experiment, the substrate speed was maintained at a constant value between 10 μm/s and 500 μm/s. Once reaching steady-state, the dynamic contact angle between the meniscus and the substrate did not change considerably because a sufficient solution volume was used such that the evaporation of the solvent during the process did not cause a change the contact angle. After the blade reached the end of the substrate, the remaining fluid was removed from the substrate. Any extra fluid must be removed quickly, before de-pinning of the meniscus from the blade, in order to prevent a backflow of the fluid onto the deposited area.

We found that the blade-casting parameters and substrate surface energy significantly influenced the density and uniformity of the assembled nanoparticle layers. Figure 4-4 shows AFM images of nanoparticle layers obtained at speeds ranging from 10-50 μm/s, with and without oxygen plasma treatment of the substrate prior to blade casting. As expected from the governing principles of convective assembly, the coverage of the substrate with particles decreases with increasing deposition speed. Below the speed at which a uniform monolayer is observed, multilayer particle arrays are formed. Above this speed, reductions in the monolayer packing fraction are observed, and eventually we observe intermittent areas of particles on the substrate. For example, this is seen by comparing the results at v_r = 10 μm/s (multilayer) to v_r = 50 μm/s (intermittent). We also observed that the particle coverage is proportional to the particle concentration in the starting solution (Figure 4-5).

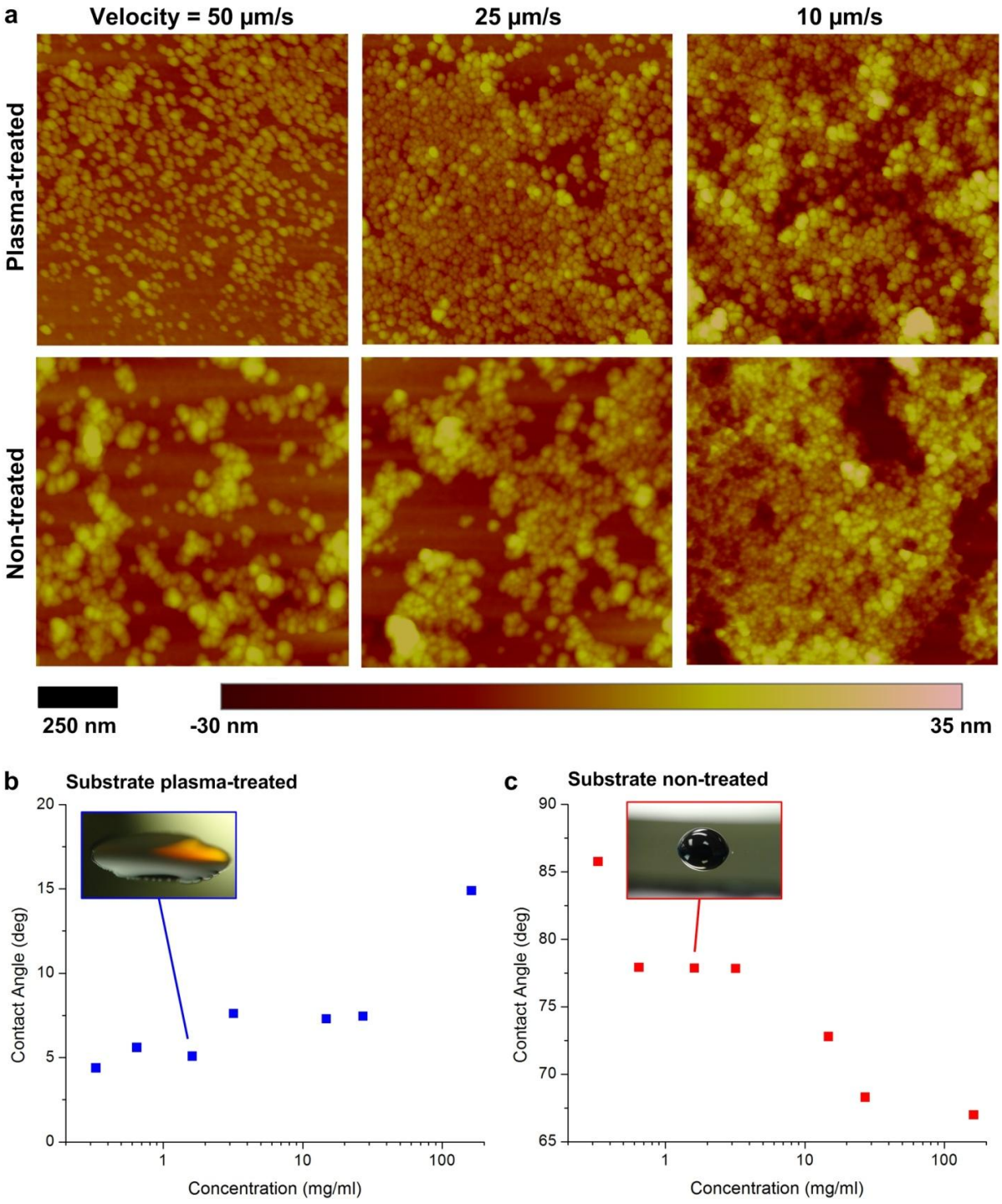

Figure 4-4. Nanoparticle arrays assembled by blade-casting at various conditions. (a) AFM images of Al_2O_3-coated Si wafer substrates after blade-casting of 3.20 mg/ml ferrofluid solution, for plasma-treated substrates (top) and non-treated substrates (bottom), at speeds of 50, 25 and 10 µm/s. Static contact angles between ferrofluid solution and (b) plasma-treated and (c) non-treated substrates.

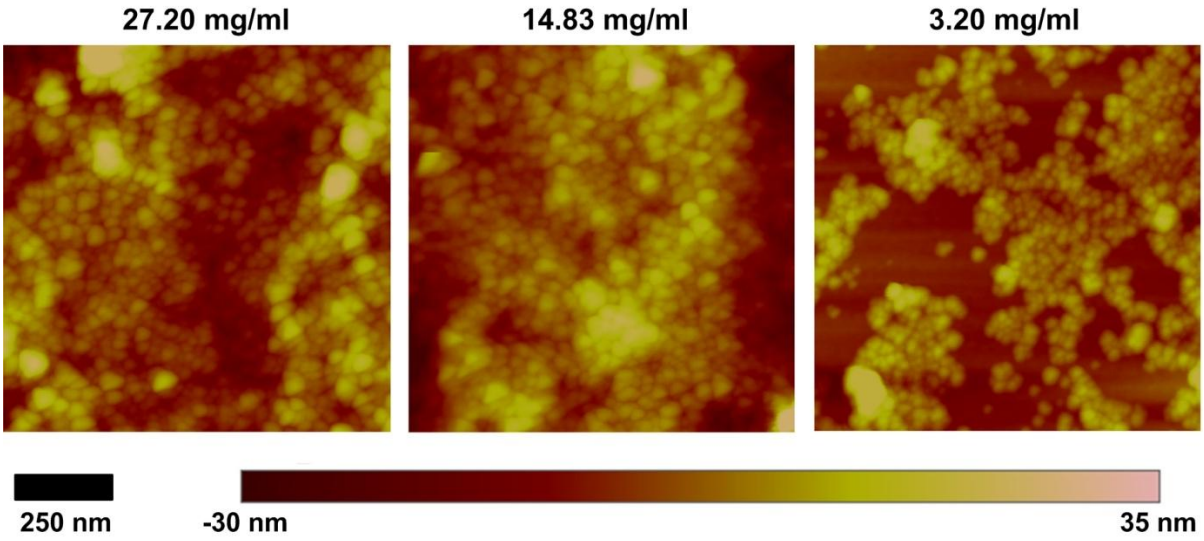

Figure 4-5. Iron oxide nanoparticle assembly using ferrofluid particle concentrations of 27.20, 14.83 and 3.20 mg/ml on non-treated substrates at 25 μm/s.

On substrates that were not plasma treated prior to blade-casting, we observed non-uniform multi-layer aggregates of particles rather than uniform monolayers. We attribute this difference to the influence of plasma treatment on the wetting of the substrate; as shown in Figure 4-4b and 4-4c, plasma treatment results in a significantly lower contact angle between the fluid and the substrate. The large contact angles measured on the non-treated substrates confirm that the interaction between the solution and the Al_2O_3 was too weak to enable meniscus pinning during blade casting, and therefore the iron oxide nanoparticles were not uniformly deposited on the substrate when pinning does not occur.

Further, on non-treated substrates, we observed that at the lower particle concentrations, or at high velocities (exceeding those shown in Figure 4-4), the ferrofluid did not wet the substrate well enough to form a low contact angle meniscus. Because of this, the meniscus slid across the substrate surface and did not pin. This resulted in samples where no visible film of particles was present after the deposition. Malaquin et al. previously studied convective assembly of polymer microparticles, and observed that where above a critical contact angle, typically >20°, the particles are no longer pinned to the substrate by the meniscus and are instead carried away by the evaporation front [246]. However, we observed that at the higher particle concentrations, the meniscus did form a lower contact angle, but at increased velocities the pinning to the substrate was not sufficiently strong to prevent a stick-slip motion of the evaporation front of the ferrofluid

as it moved across the substrate with the blade. This motion of the meniscus resulted in visible striations on the substrate surface parallel to the blade edge once the deposition was complete. Conversely, the fluid on the plasma-treated substrates always exhibited a low contact angle meniscus that had a stable, pinned evaporation front, and generated uniform particle films on the substrates. Samples processed within this range of the parameter space of concentrations and blade velocities had a uniform color (Figure 4-6); this was a straightforward means of screening the results.

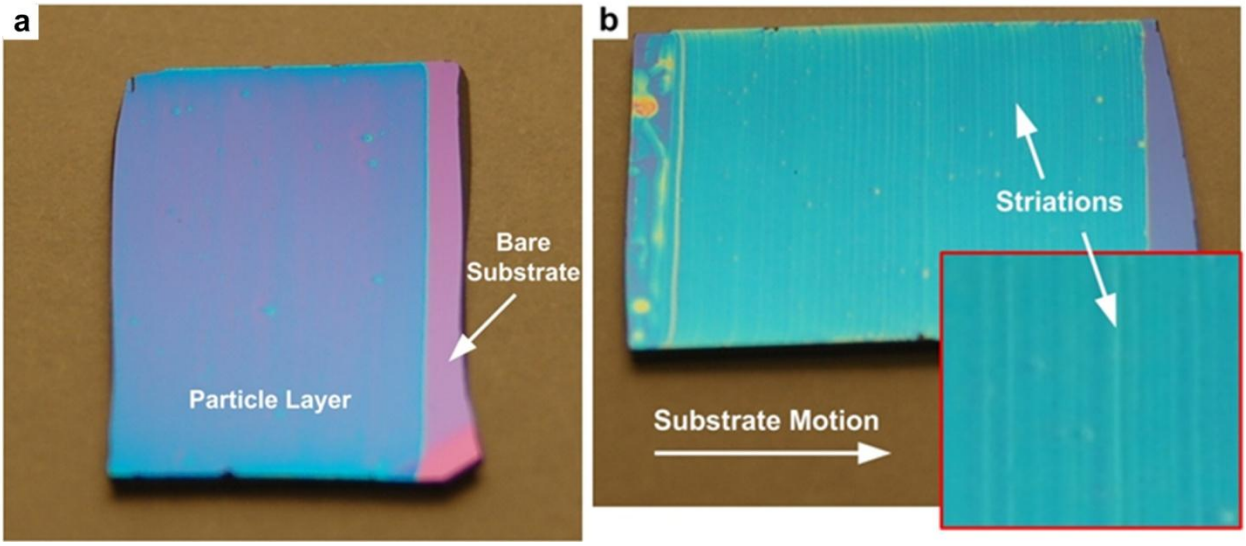

Figure 4-6. Optical images showing how blade-casting parameters influence particle layer uniformity. (a) 3.20 mg/ml solution blade casted at 50 µm/s. (b) 27.20 mg/ml solution blade casted at 400 µm/s [inset: magnified image showing striations].

Additionally, on non-treated substrates at high velocity, a negligible coverage of particles was deposited because the contact angle is high and the evaporation front moves too rapidly to allow particles to deposit on the surface. However, because the contact angle between the ferrofluid and the plasma-treated substrates was significantly lower than that of non-treated substrates, particles were deposited under a broader range of solution concentrations and substrate velocities. Also, the static contact angle of the fluid was found to decrease with particle concentration on the non-treated substrates (Figure 4-4c), which was expected due to the direct coupling between particle concentration and surfactant concentration. However, the opposite trend was observed on plasma-treated substrates (Figure 4-4b), and this is most likely explained by the development of charged surface groups on the substrates due to the plasma treatment, and

their interaction with similarly charged particles in the ferrofluid (zeta potentials from -30 to -50 mV).

4.4.2 Control of CNT morphology and density

After blade-casting, all nanoparticle-coated substrates were exposed to the same CVD recipe, involving a reduction step (775 °C, 100/400 sccm He/H_2), followed a hydrocarbon exposure step (775 °C, 400/100/100 sccm $He/H_2/C_2H_4$). We found that the existence of closely spaced yet isolated particles on the plasma-treated substrates resulted in little agglomeration upon annealing in H_2/He prior to CNT growth (Figures 4-7). Moreover, we found that the density of nanoparticles was directly related to the morphology of carbon nanostructures that are grown on the substrate using a standard atmospheric pressure thermal CVD process [216].

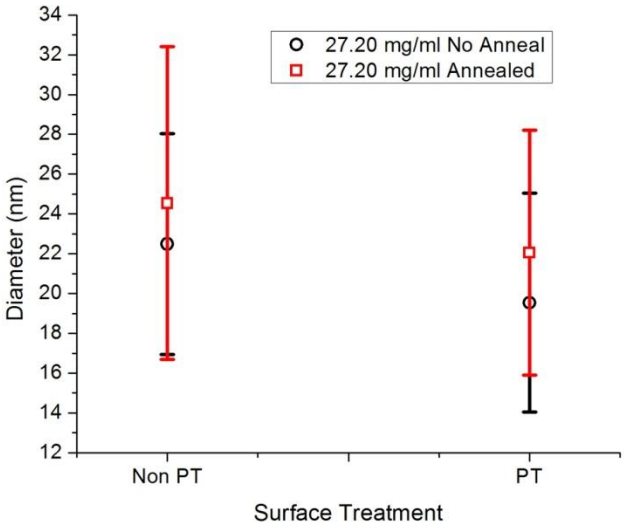

Figure 4-7. AFM analysis of iron oxide particle diameters before and after annealing. This analysis was done for plasma-treated and non-treated substrates, blade casted from a 27.20 mg/ml solution at 25 µm/s.

Analysis of the CVD results identified a "phase diagram" (Figure 4-8a) with three distinct morphologies of carbon nanostructures: sparse, tangled CNTs; vertically aligned CNTs ("forests"); and high-density carbon "flakes." SEM images of these morphologies are shown in Figure 4-8b-d, respectively. We expect that an abrupt transition occurs between tangled and aligned CNTs, as the particle density passes a critical threshold whereby the CNTs are close enough to self-organize into a cooperatively aligned array [33]. When a tangled CNT layer was

observed, the corresponding catalyst particle arrays had been fabricated with an insufficient fluid concentration or an excessive blade velocity to form a uniform monolayer, as predicted by Equation (2). As shown in Figure 4-8a, reduction of the blade velocity at equivalent concentration resulted in growth of a CNT forest. CNT forests were also observed on substrates blade-casted at conditions that we found resulted in multiple layers of nanoparticles.

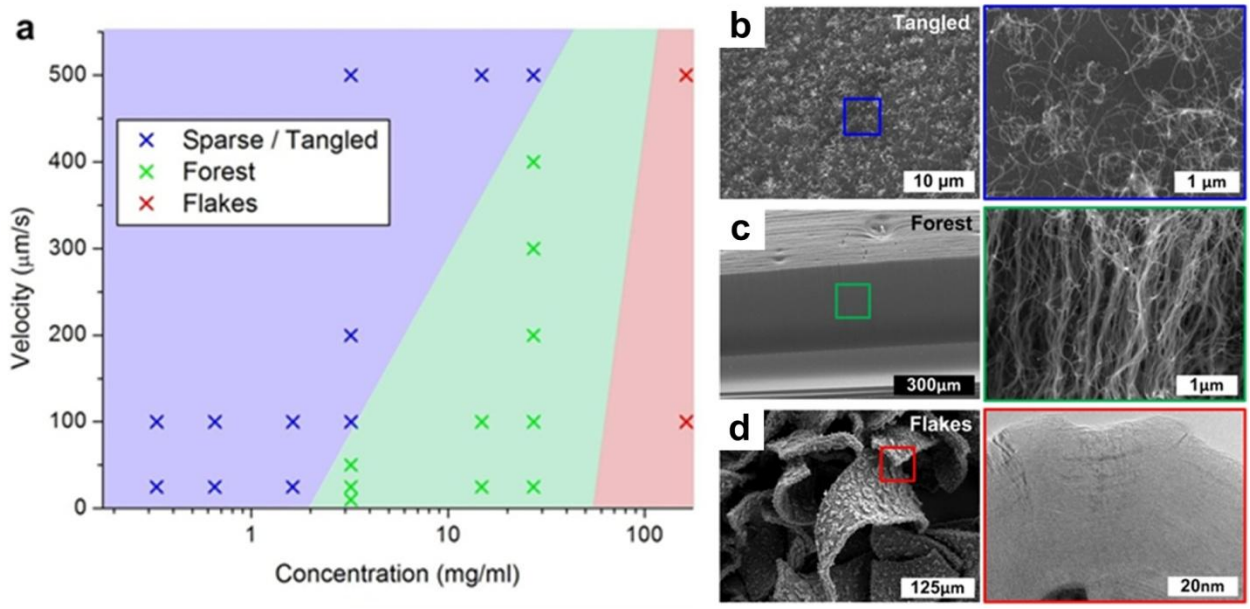

Figure 4-8. Control of carbon nanostructure morphology by blade-casting parameters. (a) Relationship between blade velocity, particle solution concentration, and film morphology (tangled, forest, flakes). Data points are from experiments, and lines are drawn to indicate approximate boundaries. (b-d) SEM images for the tangled, forest, and flakes morphologies, respectively. The close-up image in (d) was taken by high-resolution TEM.

At even greater particle concentrations in the fluid, the CVD process created the "flakes" morphology, where the carbon is deposited on the catalyst particles in onion-like layers, and these carbon-coated particles form a rigid plate-like microstructure. The carbon is deposited in spherical layers over the catalyst particles, which when combined with the neighboring particles, forms contiguous curled sheets [261–263]. Very few CNTs are formed in this regime, but both TEM imaging (Figure 4-8d) and Raman spectroscopy (Figure 4-9) of the samples support that the carbon deposited around the catalyst particles is graphitic. The thick multilayer of iron oxide nanoparticles that are deposited in this regime (verified both by optical color shifts and AFM analysis) yields a large number of particles that are not in contact with the Al_2O_3 substrate.

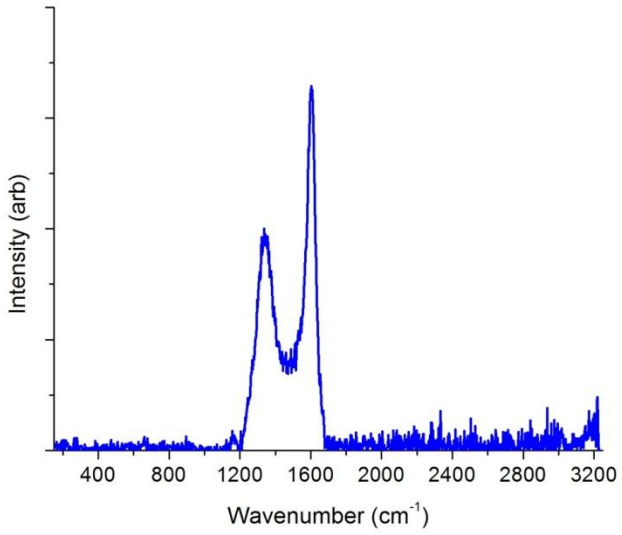

Figure 4-9. Raman spectroscopy of carbon "flake" structure illustrating graphitic G and D peaks.

Focusing within the processing regime that leads to CNT forests, we then investigated how the density of the CNT forest could be controlled by the blade-casting process parameters. The volumetric density of each CNT forest was calculated using the measured mass, top-view area, and average height of the forest. We found (Figure 4-10) that the CNT forest density was controllably influenced by the velocity of blade casting and the concentration of the nanoparticle fluid. Notably, we find that blade-casted catalyst arrays result in CNT forests with densities at least 3-fold higher than those grown from comparable standard thin film dewetting, which typically gives forest densities of 15 to 30 $\mu g/mm^3$ for the same CVD conditions [215]. Spanning our results, blade-casting uniquely enabled tailoring of the CNT forest density from ~1 $\mu g/mm^3$ to 90 $\mu g/mm^3$ simply by specifying the blade velocity and the concentration of the particle solution.

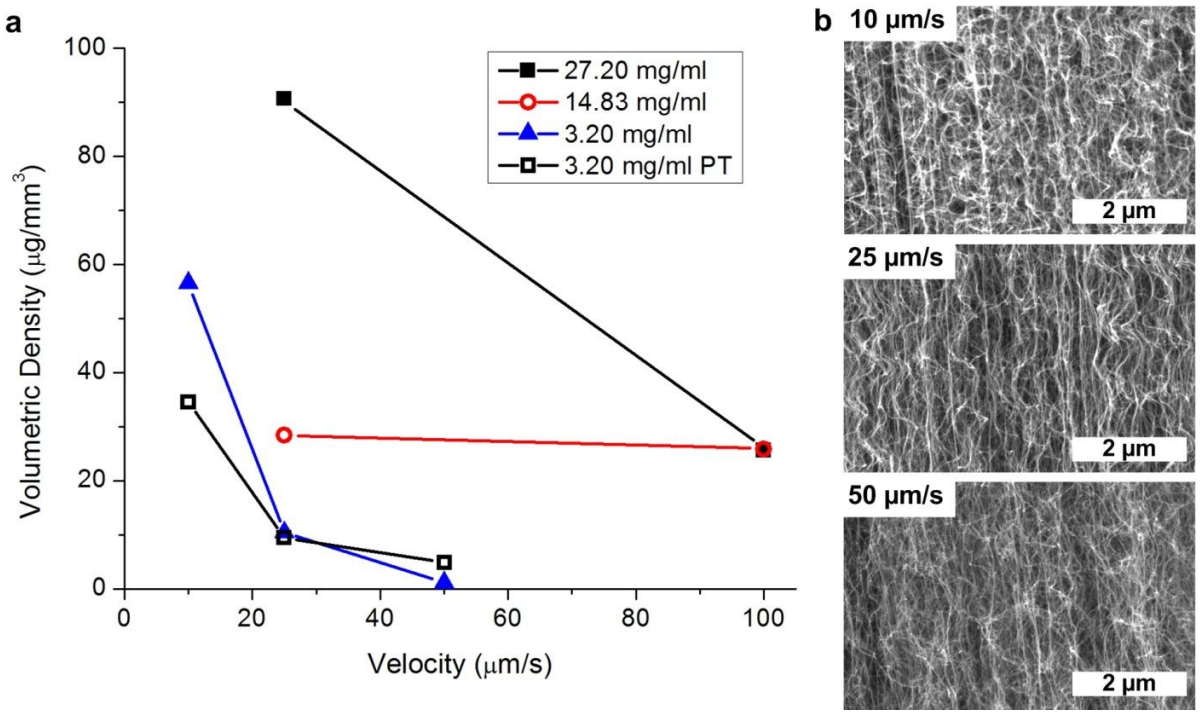

Figure 4-10. Wide-range control of CNT forest density by blade casting velocity and ferrofluid concentration. (a) Relationship between CNT forest volumetric density and process conditions. (b) SEM images of CNT forest sidewalls grown corresponding to 3.20mg/ml ferrofluid solution at 10, 25 and 50µm/s (top to bottom).

To correlate the CNT density to the morphology and density of the particle layer, we quantified the particle densities from the AFM images of the blade-casted substrates before the CNT growth step. The number of particles was determined using a custom code developed in Matlab™ and modified from our previous work [87,215], which identifies the locations of particle peaks in the AFM data. These peaks were then used to perform a Voronoi cell analysis to determine the average particle spacing over the sampled area. Each of the samples that had monolayer particle arrays was analyzed, and a sample of the resulting analysis is presented in Figure 4-11a. The particle density exhibited an inverse relationship with the blade casting speed, as previously illustrated in Figure 4-4, which qualitatively matches with the trend in CNT forest density.

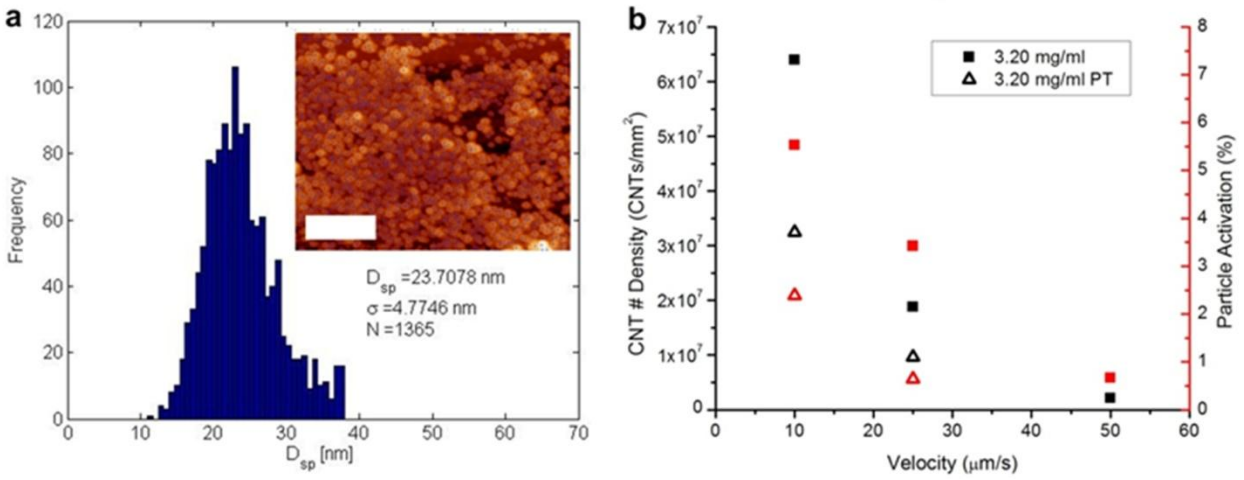

Figure 4-11. Quantitative analysis of particle density in blade-casted arrays on Al2O3 substrates. (a) Distribution of inter-particle spacing (Dsp) based on the Voronoi triangulation analysis of a plasma-treated substrate with 3.20 mg/ml ferrofluid solution blade casted at 25 μm/s (inset: AFM image used from this analysis with an area of 1 x 1 μm, and a 250 nm scalebar). (b) CNT areal density and particle activation measurements for plasma-treated and non-treated substrates.

4.4.3 CNT diameter and alignment analysis

Next, small angle X-ray scattering (SAXS) was used to non-destructively measure the CNT diameter distribution within the CNT forests [91,215,225]. We found (Figure 4-12a), that CNT diameter increases slightly with increasing particle number density on the substrate. This trend is consistent for blade-casting conditions that give monolayers and multilayers of catalyst particles. This is due to the presence of additional iron oxide nanoparticles that are in close proximity to each other, which causes the particles to agglomerate during the annealing and reduction phase prior to hydrocarbon exposure. AFM images (Figure 4-13) comparing blade-casted substrates before and after annealing show that the magnetite particles coarsen slightly and transition from smooth to highly faceted particles.

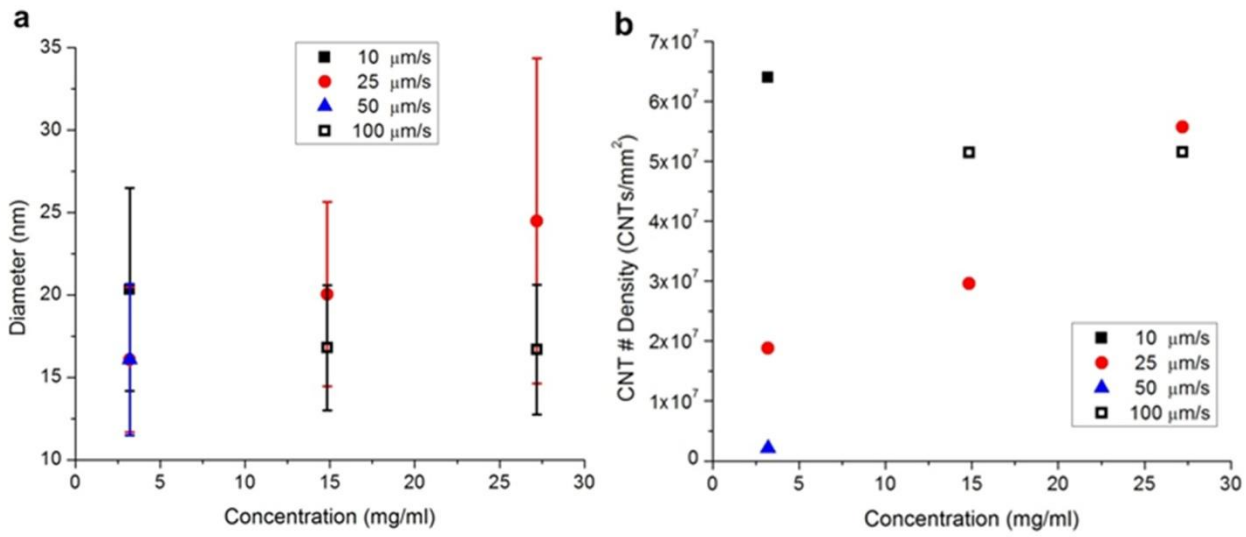

Figure 4-12. Relationships between CNT diameter, ferrofluid concentration and CNT density. (a) CNT diameter vs. ferrofluid concentration, and (b) CNT number density vs. ferrofluid concentration for process conditions giving vertically aligned forests.

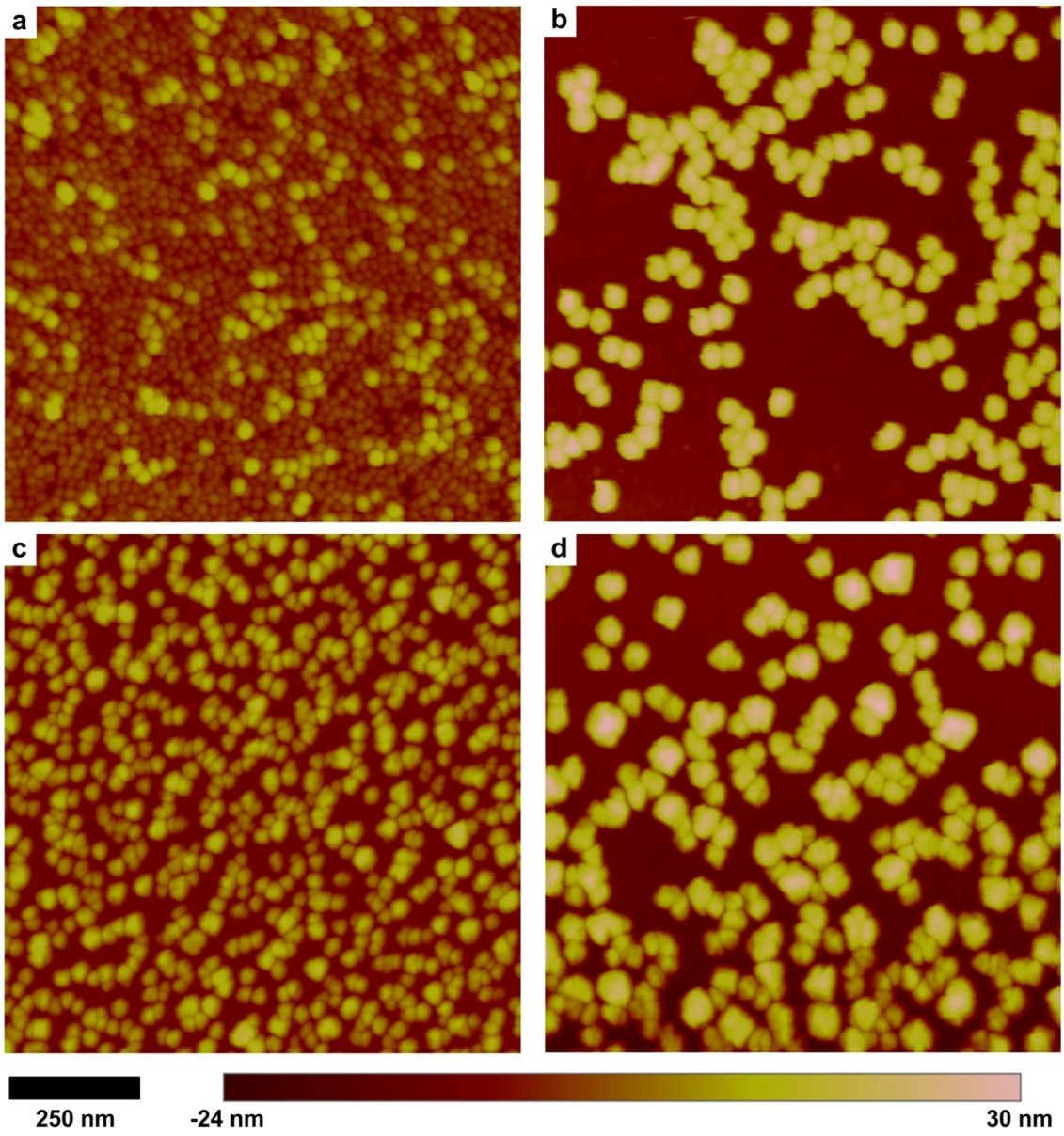

Figure 4-13. Coarsening and faceting of annealed particles. (a) As-cast 20 nm particles, (b) as-cast 30 nm particles, (c) annealed 20 nm particles, and (d) annealed 30 nm particles from 3.20 mg/ml ferrofluid solutions blade casted at 25µm/s.

Combining the measurements of CNT diameter and wall thickness by SAXS, the Hermans orientation parameter by SAXS, and the volumetric density, we then calculated how the number density of CNTs per unit area changes with the process conditions. From the SAXS data, the arithmetic mean of the lognormal distribution of CNT diameter (D_O) within the forest, and the average wall thickness (t) of the CNTs were used to calculate the number of walls (n) for the

multi-walled CNTs, assuming a wall spacing equal to the interplanar spacing of graphite (0.34 nm)

$$n = \frac{D_O - t}{0.34}, \tag{6}$$

where D_O and t are in nm. The total distance around the sum of the circumferences of each CNT wall was calculated next

$$\mathrm{C} = \sum_{x=0}^{n-1} \pi\left(\mathrm{D_0} - 0.68x\right) \tag{7}$$

The height of the CNT forest (h) measured from SEM imagery, was then divided by the number of SAXS measurements collected over the forest height (s) to obtain the height of a single slice of the forest

$$\Delta h = \frac{h}{s} \tag{8}$$

Taking CNT tortuosity into account, the average length of the CNTs (L) were calculated using (Δh) from Equation (8) and the Hermans orientation parameter (H) that was obtained for each slice of the CNT forest via SAXS

$$\mathrm{L} = \sum_{x=1}^{s} (\Delta \mathrm{h}) \cos\left(\cos^{-1}\sqrt{\frac{2H_x + 1}{3}}\right) \tag{9}$$

Considering the hexagonal lattice of carbon atoms that make up the sidewall of CNTs, we estimated the number of atoms in the average CNT within the forest. Figure 4-14 shows a portion of a hexagonal lattice of carbon atoms where the unit cell is highlighted by the dotted line. The separation between carbon atoms in this configuration is 0.142 nm, and so we calculated the spacing between unit cells in the x and y directions (shift to blue and red positions respectively) as 0.426 and 0.246 nm respectively. With these dimensions we then calculated the number of atoms (N) for an average CNT (neglecting any cap) using the result from Equation (9) in nm

$$N = 4(L/0.246)(C/0.426) \tag{10}$$

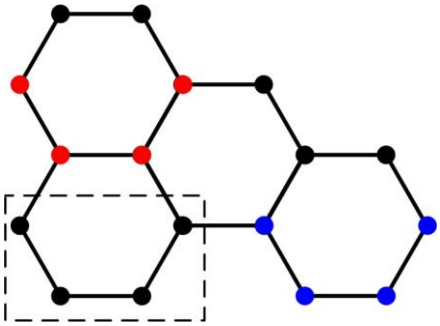

Figure 4-14. Hexagonal lattice of carbon atoms.

Finally, we calculated the number of CNTs per unit area using (h), (N) and the measured volumetric density of the forest (ρ)

$$CNTs\ /area = \frac{\rho h N_A}{N(m_C)} \tag{11}$$

where (N_A) is Avogadro's Number and (m_C) is the atomic mass of carbon.

Comparing the average number of catalyst particles pre-growth, and the average number of CNTs per unit area allowed the particle activation percentage to be calculated (Figure 4-11b). While the activation percentage for these samples was low, between 0.5 and 6%, there was an increase in catalyst particle activation with an increase in particle packing density, and subsequent VACNT forest volumetric density. Therefore, the tunability of CNT number density is both a direct effect of the particle number density from blade-casting as well as a cooperative increase in the activation percentage (i.e., the proportion of particles that grows CNTs) as shown in Figure 4-11b. This correlation between the particle areal density and the catalytic activation of particles for CNT growth, suggests a cooperative or autocatalytic nature of CNT growth from catalyst nanoparticles in close proximity [215,264].

It is generally accepted that high-yield activation of catalyst particles for CNT growth on a substrate such as silicon requires an oxide support layer such as Al_2O_3 [125,265]. This is illustrated by the lack of VACNT growth on a silicon substrate without Al_2O_3, which was prepared identically to a substrate with Al_2O_3 that produced a forest. Thus we expected that the significant majority of CNTs grow from particles that are in contact with the Al_2O_3 support layer. Accepting this hypothesis suggests that the additional layers of iron oxide nanoparticles

influence the activity of the particles in contact with the substrate, such as by increasing the local decomposition of the hydrocarbon source, but these particles do not directly grow CNTs.

4.4.4 CNT Diameter and Substrate Engineering

Another key attribute of the blade-casting process is that the CNT diameter can be specified a priori by the diameter of nanoparticles in the blade-casting solution. To further demonstrate this point, additional experiments were performed using iron oxide nanoparticle solutions (COOH-functionalized, Ocean NanoTech) with nominal diameters of 10, 20 and 30 nm diameter iron oxide particles, each having a reported size tolerance of +/- 2.5 nm. Because the effective particle diameter in solution is influenced by the surface functionalization, we performed DLS on each as-received solution (Figure 4-15).

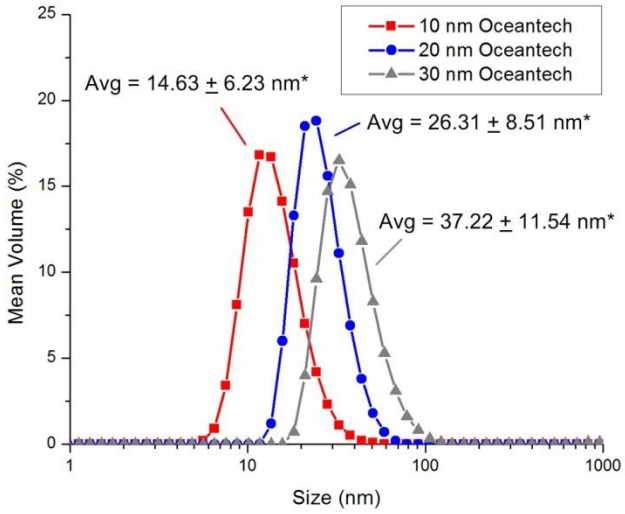

Figure 4-15. Particle size distributions for Oceantech ferrofluid samples. Averaged DLS data for three runs per sample of 10, 20 and 30 nm iron oxide particles. * Average diameter values are based on size data < 70nm (which did not significantly impact the measurement, nor did the larger particles get deposited on the substrates during blade casting).

Based on our findings in the previous sections, solutions with 3.20 mg/ml concentration were blade-casted onto plasma-treated substrates at v_r = 25 µm/s. As shown in Figure 4-16a, under these same blade-casting conditions, we obtained a multi-layer deposition of the 10 nm particles, a near-monolayer of the 20 nm particles, and a sparse array of the 30 nm particles. Because the blade casting parameters were held constant, and the same solution concentration was used with

each fluid, blade casting of larger diameter particle solutions resulted in fewer particles per unit area, as predicted by Equation (1).

CNT forests were obtained on all samples; however, forests grown from successively larger particles were less dense and less well-aligned (Figure 4-16b), due to the larger spacing between the catalyst particles on the substrate. A quantitative SEM analysis of the grown forests is shown in Figure 8c and 8d, and not only is the trend in VACNT array height and density apparent, but the correlation of CNT diameter to catalyst particle diameter is also very clear. We see that for the three different particle solutions of 10, 20 and 30 nm particles (14.6 $\pm$ 6.2 nm, 26.3 $\pm$ 8.5 nm, 37.2 $\pm$ 11.5 nm respectively from DLS data), the CNTs grown from them have average diameters of 10.6 $\pm$ 1.0 nm, 16.03 $\pm$ 3.5 nm, 18.3 $\pm$ 2.6 nm, respectively.

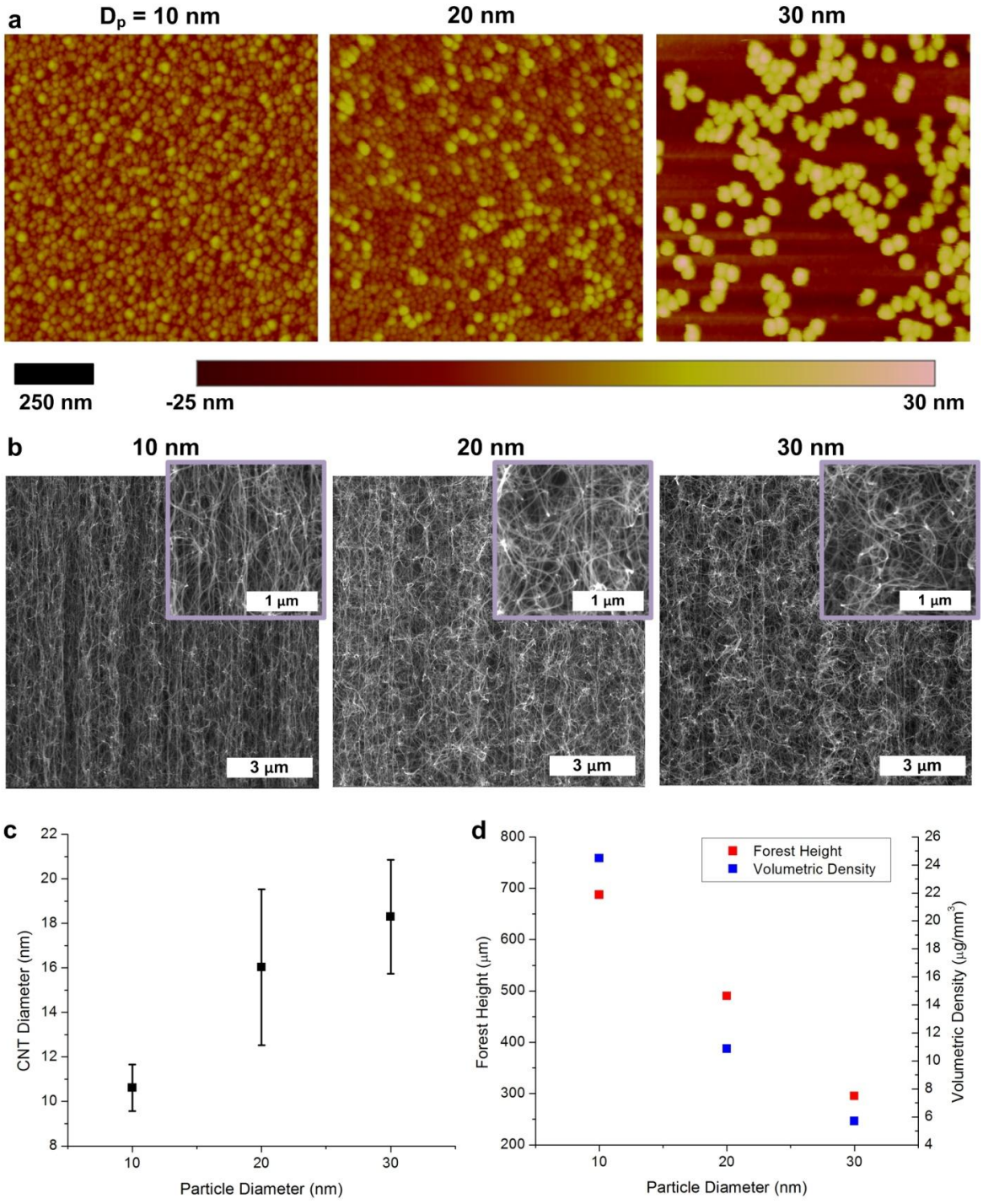

Figure 4-16. Engineering CNT diameter within forests by specification of the particle diameter in the blade-casting solution. (a) AFM images of 3.20 mg/ml ferrofluid solutions with particle diameters of 10, 20 and 30 nm (left to right) blade casted at 25 µm/s. (b) SEM images of CNT forest sidewalls grown from the three ferrofluid depositions in (a). (c) Average CNT diameters for the three CNT forests in (b), and (d) corresponding CNT forest height and volumetric density.

However, while there is a direct correlation between particle size and CNT diameter, the correlation is sub-linear. This finding suggests that the CVD conditions (e.g., feedstock mixture, pressure, temperature) are most favorable for a certain range particle diameters, and that tuning of the CVD conditions would shift the size range of active catalyst particles. Additionally, due to the increasing spacing and decreasing number density with increasing particle diameter in the fabricated arrays, an inverse relationship between particle diameter and forest height, as well as particle diameter and forest density, was observed. Although the particle densities shown here are low due to the parameters chosen, we are confident that optimization of the blade casting parameters could give highly dense arrays of particles of any relevant size. To illustrate this, near-monolayer arrays of the 30 nm particles were created by blade-casting the 30 nm particle solution both at a slower speed, and at a higher concentration (Figure 4-17).

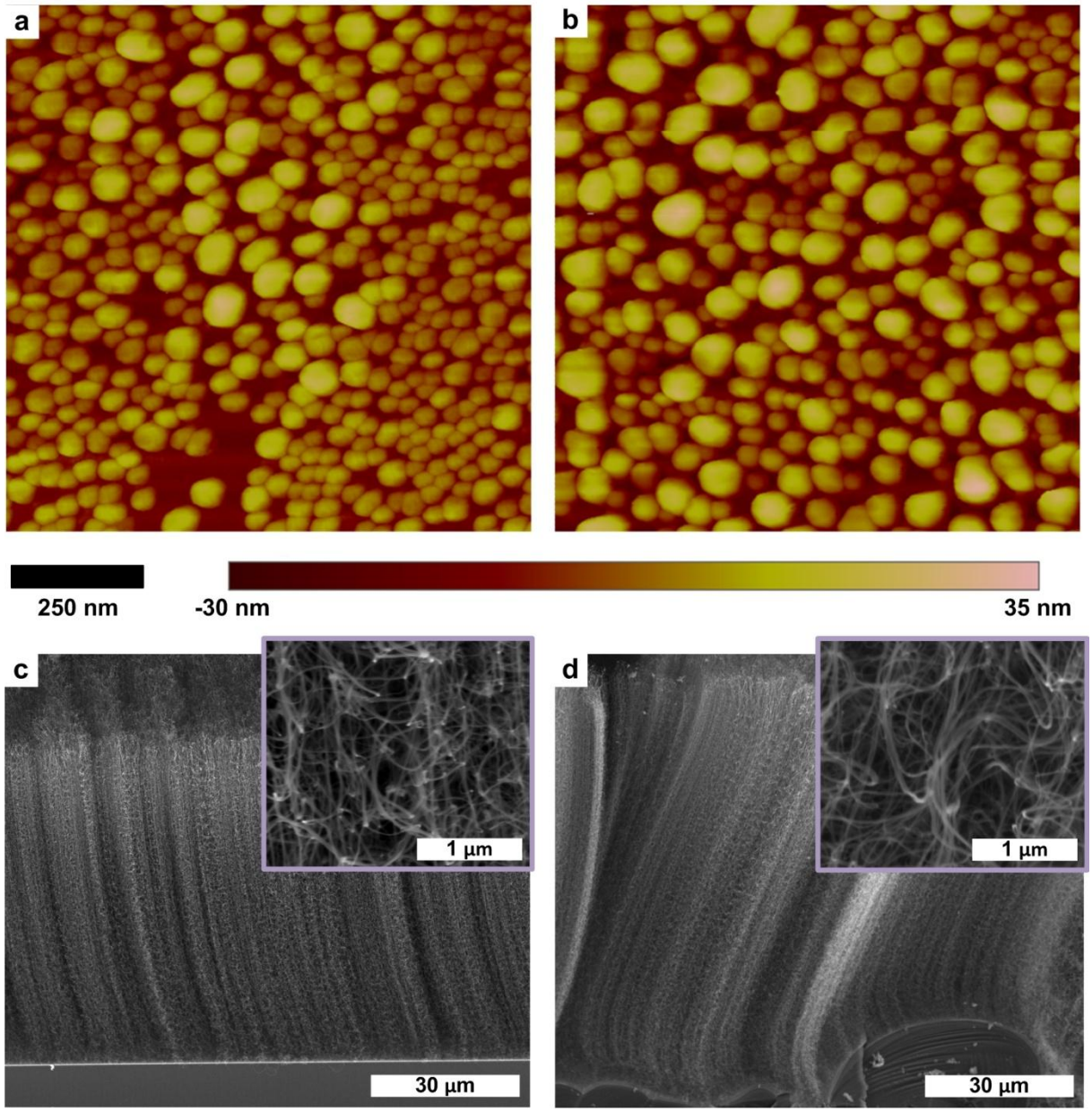

Figure 4-17. High-density 30 nm catalyst particles and corresponding CNT forest growth. AFM images from annealed, blade-casted samples of (a) 3.20 mg/ml at 10 µm/s, and (b) 12.0 mg/ml at 25 µm/s. (c,d) SEM images of CNT forest growth from samples (a) and (b) respectively.

Last, we comment on the viability of the blade-casting process to obtain truly dense monolayers of nanoparticles. Although we showed that the arrangement of catalyst nanoparticles can be controlled from a sparse sub-monolayer to stacked multi-layers, we did not obtain closely-packed (HCP) monolayers in any experiments. To enable this in the future, it will be most important to use more monodisperse nanoparticle solutions, as are typically used in

assembly of "superlattice" monolayers for other applications [266–268]. Also, to make the process repeatable, precise control over the ambient conditions during blade-casting (e.g., temperature and relative humidity) will be required. The relative humidity of the surrounding environment impacts not only the evaporation rate of the solution during blade-casting, but also can cause considerable effects on the activity and lifetime of CNT growth catalysts [119,137,210,211].

The ability to vary the packing fraction, while maintaining a constant average diameter, enables the user to overcome the limits established by dewetting of a thin film, which couples the film thickness, particle diameter, and packing fraction. For this analysis, we denote the packing fraction of particles on the substrate as

$$f = N_P A_P, \tag{12}$$

where (N_P) is the number of particles per unit substrate area and (A_P) is the projected area of a single particle on the substrate. Conservation of the volume of material deposited as a thin film establishes an inverse relationship between particle diameter and packing fraction after dewetting [92], as shown in Figure 4-18. This family of curves assumes the particles are hemispherical in shape.

For a 1 nm film thickness (which is typical for CNT film growth), with 15 nm diameter particles, the packing fraction is near 20%, and in order to obtain a larger packing fraction, the catalyst particles would have to be smaller. However, due to the constraint established by minimization of Gibbs free energy, the dewetting of a thin film is limited to a maximum packing fraction of 50%, and thus cannot reach a closely-packed organization. Moreover, because of the complex thermomechanical processes that govern dewetting and stabilization of nanoparticles, it is difficult to independently control the particle diameter and packing fraction, even if the initial film thickness can be very accurately specified. The polydispersity of particle size that is introduced by real attributes of thin film dewetting (e.g., growth of holes, surface roughness), and the propensity for nearby particles to coarsen, further limits the packing fraction to a value below the ideal maximum. Compounded with the typically low yield of CNTs from catalyst particles, this often leads to CNT forests with low packing density and therefore limited properties. In contrast, while the ultimate closely-packed CNT array was not achieved in this

work, the monolayer arrays made by blade-casting have packing fractions ranging from less than 10% to approximately 87% with the same average particle diameter of 28.6 nm.

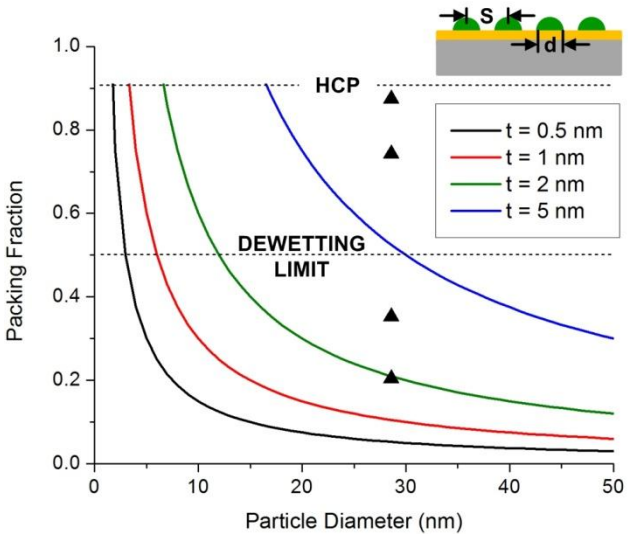

Figure 4-18. Comparison of thin film dewetting and convective assembly packing fractions. Relationships between particle packing fraction and diameter, for ideal dewetting of films of different thickness are represented by the various curves, while the data points represent several packing fractions achieved from the convective assembly of a 3.20 mg/ml ferrofluid (each of which resulted in a CNT forest).

However, because it is challenging to achieve monodisperse nanoparticles with <5 nm diameter, thin films may remain advantageous in depositing ultrathin catalyst layers (i.e., <1 nm films), which can generate particles small enough to support SWCNT growth, but at limited densities. For thicker films, especially those generating >10 nm particles, the versatility of our approach is clear because it is not possible with any single film thickness to achieve such high packing fractions of catalyst particles and CNTs. Thus, even without meeting the optimal limit of the particle packing, this method for catalyst deposition allows the catalyst particles and thus the VACNT arrays to be tailored to a much higher degree than with standard thin film deposition, while maintaining compatibility with a continuous-feed process.

4.5 Towards continuous convective assembly

Looking ahead, there is a strong opportunity to use blade-casting in concert with R2R processing of flexible substrates. Hence, it is also attractive to grow CNTs on metal foils that are flexible and less expensive than silicon wafers. As an initial demonstration, using the same ferrofluid as earlier in the paper, a 3.20 mg/ml solution was blade-casted onto a Cu foil (first

coated with 10 nm Al_2O_3) at 25 µm/s. Subsequent growth on the sample resulted in a CNT forest that visibly covered the area of the Cu foil that was coated with iron oxide nanoparticles (Figure 4-19). SEM analysis of the sample showed good alignment of the CNTs at the sidewall of the forest, but due to both the native topography of the substrate and the blade casting conditions, the forest exhibited a high density of micro-cracks. CNT forests on metal foils are particularly desirable for supercapacitor electrodes and thermal interfaces [182,269–271], and optimization of this process to a continuous-feed apparatus would enable the engineering of CNT forests on flexible substrates. Based on previous work, it is anticipated that the adhesion can be modulated for specific applications by post-growth treatment, such as cooling the substrate in a hydrocarbon or hydrogen atmosphere [272] (this will be discussed briefly in Chapter 7). The CNT forests created in this study generally have weak adhesion to the substrate and can be easily removed using a razor blade.

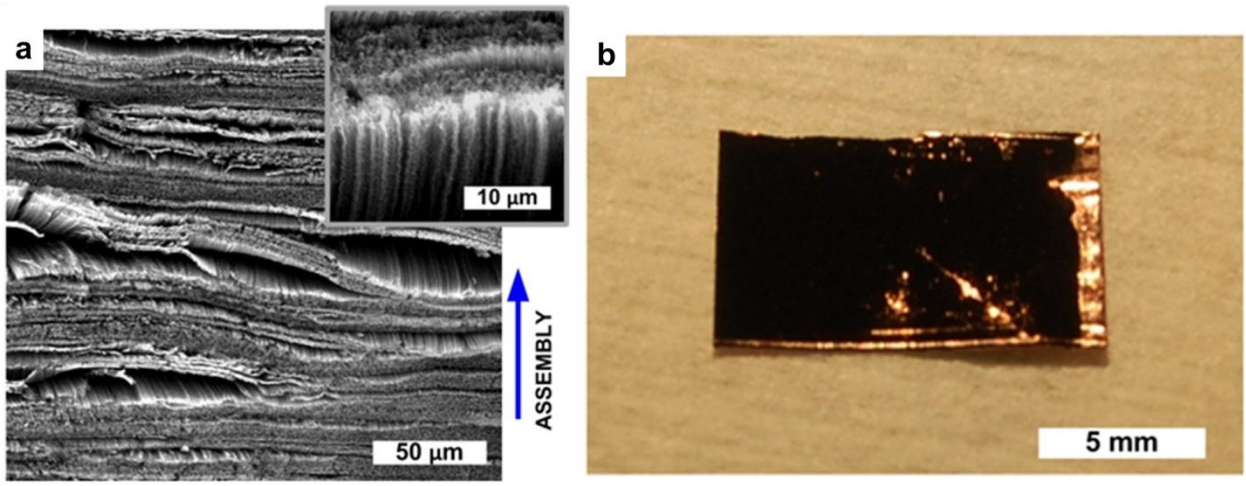

Figure 4-19. CNT forest grown on Cu foil substrate coated with ferrofluid catalyst array by blade-casting. (a) SEM images of the top and sidewall (inset) of CNT forest grown on Cu foil from a 3.20 mg/ml ferrofluid solution blade casted at 25 µm/s (direction indicated by the arrow). (b) Optical image of the sample from (a). The striped texture of the forest is due to stick-slip of the meniscus, perpendicular to the direction of blade motion.

In addition to flexible substrates, commercial adoption would require the speed at which the catalyst particles are assembled to be greater than the sub-mm/s speeds shown in this study. Looking back at Equation (4) it becomes apparent that the best way to increase the evaporation rate is to increase the vapor pressure (p_v) of the solvent in the particle solution (assuming the partial pressure (p_p) is constant). This can be done either by increasing the temperature (T), or

selecting another solvent for the solution that has a higher p_v. Because ferrofluid solutions are available in several forms commercially, we elected to investigate applying a more volatile solvent to the convective assembly process.

To compare only the effects of the solvent, an isopropyl alcohol (IPA) based ferrofluid (Ferrotec, NF3263L) with the same iron oxide particle distribution as the water based solution used previously was procured. Figure 4-20a illustrates the DLS data for both solutions. Following the same processes laid out in section 4.3 (Materials and methods), several samples deposited with varying speeds were created using a concentration of 3.20 mg/ml. AFM confirmed that a convective assembly speed of 1 mm/s resulted in a packing fraction similar to that of the 50 µm/s sample produced in Figure 4-4a. The resulting density of the CNT forest growth from the sample was also comparable to the previous sample (Figure 4-20b), but at an assembly speed 20x that of the original. Finally, a 10 nm average diameter toluene based ferrofluid (Sigma-Aldrich, #700312) that was more monodisperse than the other solutions used previously (Figure 4-20c) was procured. Unfortunately, particle arrays with similar packing fractions as the other samples were unable to be created because the device used to perform the convective assembly had a maximum speed of 2 mm/s (Figure 4-20d, right). However, initial AFM results indicate that at 2 mm/s there are still multiple layers of particles assembled on the surface, and that the assembly speed to create monolayers of particles is significantly higher.

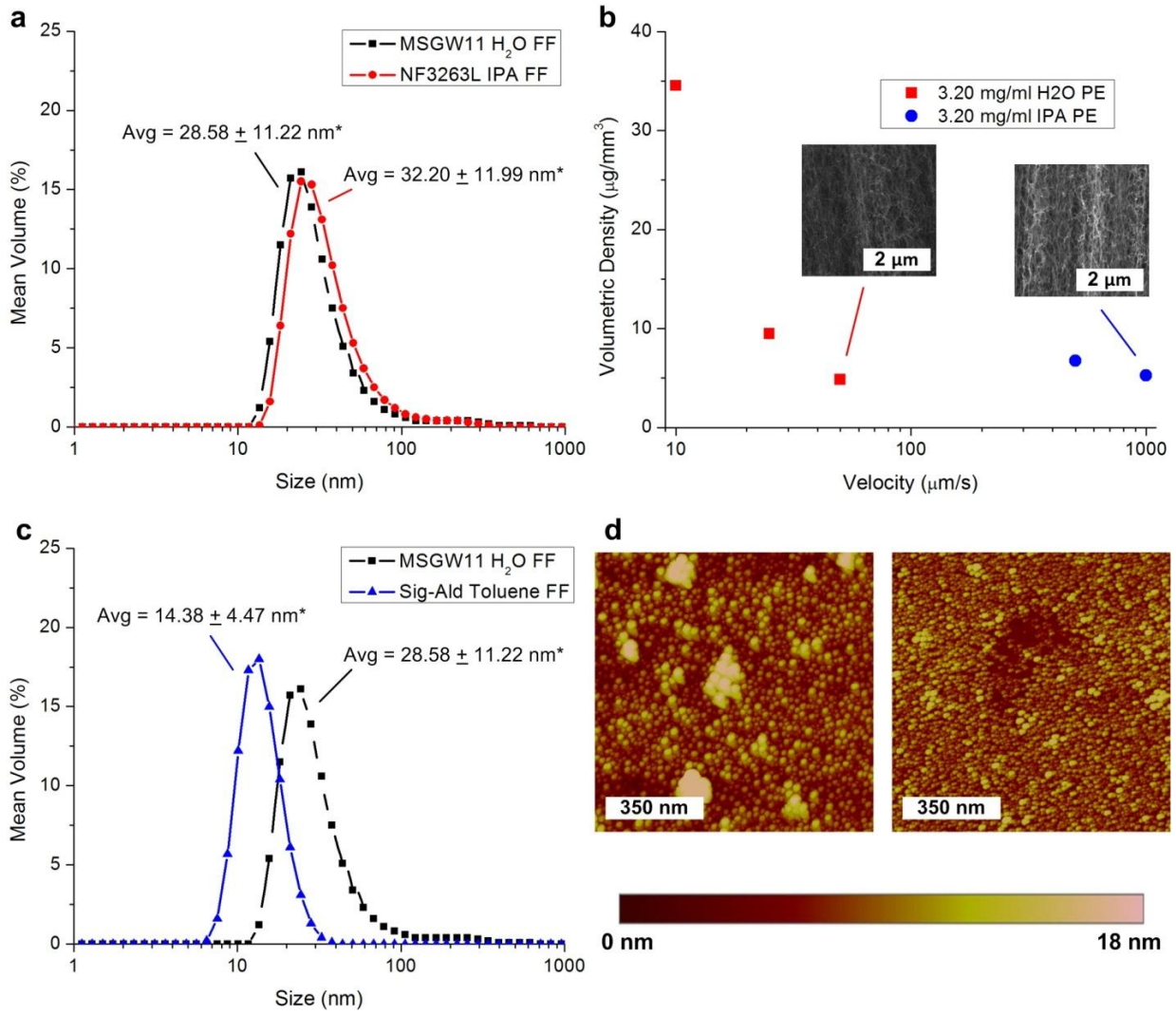

Figure 4-20. Increased convective assembly speed via organic solvent ferrofluids. (a) DLS data for the original water based and IPA based ferrofluids. (b) CNT forest density vs. convective assembly velocity for the two ferrofluids in (a). (c) DLS data for the original water based and Sigma-Aldrich ferrofluids. (d) AFM images for the Sigma-Aldrich ferrofluid at 100 µm/s (left) and 2000 µm/s (right).

4.6 Benchtop machine for R2R convective assembly

The final piece to implementation of this method to flexible substrates is a R2R machine. Figure 4-21 illustrates the machine that was designed and built by the author for the continuous convective assembly of catalyst particles on flexible films. Currently the machine is designed to handle 6 mm wide metal foils using an adjustable clutch (design described in Chapter 6) on the

supply roller to maintain tension on the foil, and a stepper motor (Omega, OMHT17-075) on the take-up roller to provide translational speeds between 1 μm/s and 1 m/s. In order to accomplish this large range of speeds, an adjustable micro-step motor controller was implemented (All-Motion, EZHR17EN). Based on the optional substrate heating that could be implemented in the future, the foil translates across a curved substrate support to ensure constant contact over the entire length for optimal heat conduction. Additionally, to minimize the risk of having rough blade edges interfere with the assembly process, a curved blade made out of quartz to provide a smooth surface for the meniscus to wet was utilized. The curved blade also features through holes that enable the meniscus size to be constantly maintained with a steady supply of ferrofluid from a syringe pump. Finally, a translational stage allows for optimal placement of the blade in the z-axis, and enables multiple foil thicknesses to be used with the setup. Although to date this machine has not been used for continuous convective assembly, this machine shows the possibility to integrate catalyst assembly with the R2R CVD machine presented in Chapter 6. Experiments to optimize catalyst assembly and CNT growth on metal foils are currently underway and this data will be presented in the future.

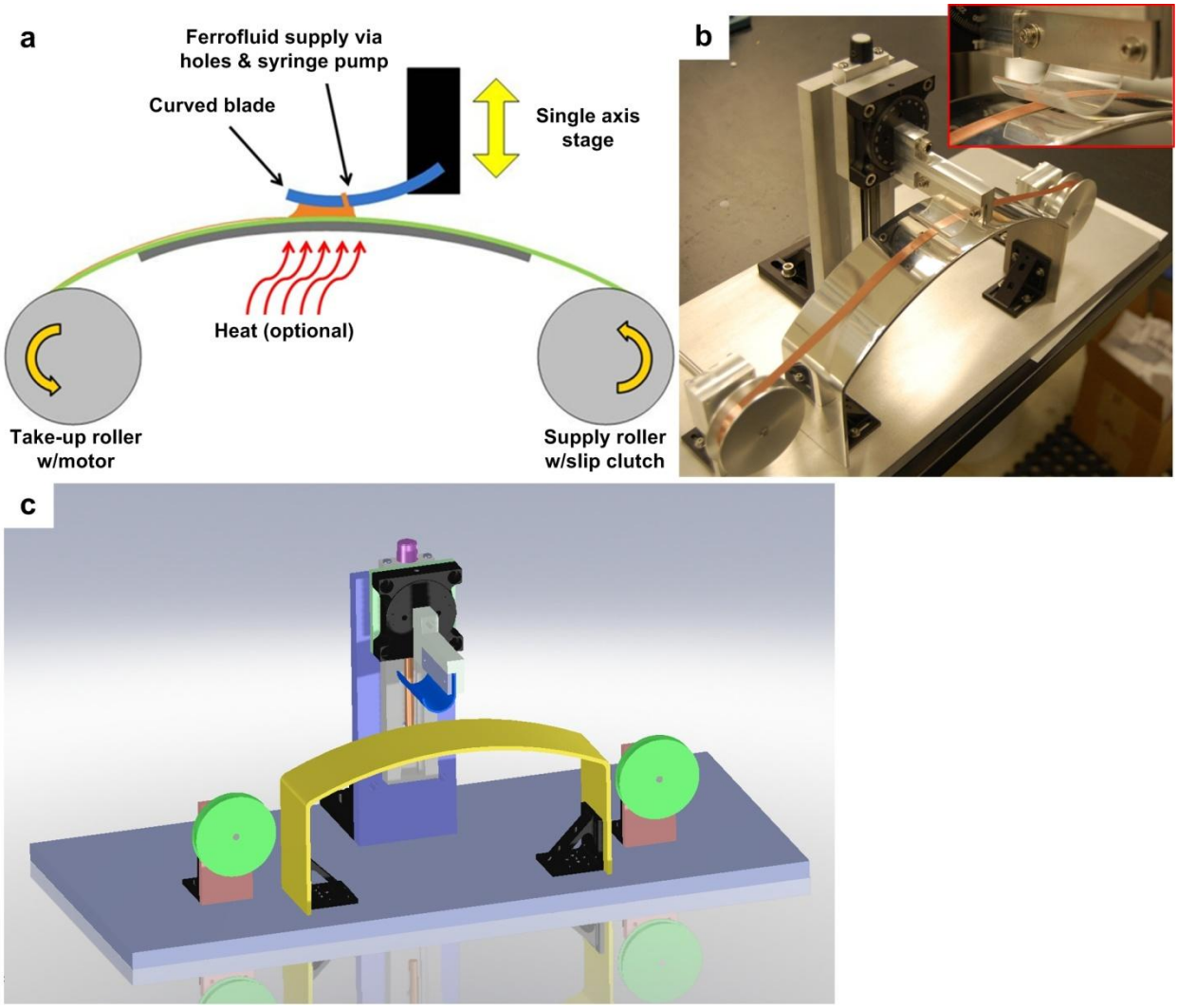

Figure 4-21. Continuous catalyst deposition machine. (a) Schematic of the machine components. (b) Optical image of the machine assembly with a Cu foil substrate installed and close-up of the blade assembly (inset). (c) CAD of the machine assembly.

CHAPTER 5: MICROPATTERNED CNT FOREST GROWTH VIA LASER PRINTING OF CATALYST

*Significant portions of this chapter with additional editing were published in: E. S. Polsen, A. G. Stevens, A. J. Hart, ACS Applied Materials & Interfaces **2013**, DOI 10.1021/am400148t; ref* [64].

This chapter presents a method for patterning CNT forest growth through the laser printing of magnetic ink character recognition (MICR) toner containing iron oxide catalyst particles. A brief review of techniques currently used to pattern and print thin-films or particles is presented first, followed by the methods used in this study to create and characterize laser printed patterns of MICR toner with subsequent CNT forest growth. Next, the laser printing process and modifications to a standard office printer for catalyst deposition control are presented, resulting in the printing of patterns onto flexible polymer (polyimide), and their transfer to a rigid substrate (silicon or alumina) under heat and mechanical pressure for CVD processing. A detailed discussion of the native toner particle composition and minimum feature sizes both printed catalyst (70 μm) and subsequent CNT forest growth (140 μm) is highlighted along with the digital control of patterned CNT growth via the laser intensity, which controls the CNT density; and via the grayscale level, which controls the pixelation of the image into arrays of micropillars. Through SEM imaging and small angle X-ray scattering (SAXS) analysis of these CNT forests are shown to have comparable CNT diameter, alignment, and density to those grown with standard thin-film catalysts. Finally, we demonstrate that the grayscale CNT patterns can function as dry adhesives, and that large-area catalyst patterns can be printed directly onto metal foils or transferred to ceramic plates. This illustrates that laser printing is a promising technique for enabling high-speed micro patterning of nanoparticle-containing thin films under ambient conditions, possibly for a wide variety of nanostructures by engineering toners containing nanoparticles of desired composition, size, and shape.

5.1 Printing and lithography based patterning

High-speed printing technologies, including letterpress, inkjet, and imprint methods are used widely for patterning consumer products ranging from plastic bags to flash memory [273,274]. Industrialization of printing has been enabled both by innovations in the formulation of inks, as well as in the printing method and machine technology. The growing availability of chemically synthesized nanostructures such as semiconductor, oxide, and polymer particles, indicates potential for adopting printing technology to manufacturing of patterned nanostructured materials. Nevertheless, most research on fabrication of nanostructured thin films still leverages photolithography methods, and it remains an important need to invent scalable methods for patterning nanostructures, which combine engineerable control of feature size and density with high throughput.

Moreover, printing methods that are compatible with low-cost desktop machines, such as inkjet and laser printers, offer promise for customized materials design and fabrication, and their integration with traditional microfabrication and thin film lamination technologies. Laser printing has been used to fabricate microfluidic devices where the toner either defined the thickness and width of the channels, on both polymer and paper substrates [275], or where the toner defined a wet chemical mask for the creation of microfluidic devices in glass [276]. The scalability and accessibility of this is particularly attractive for paper-based point-of-care diagnostic devices, originally envisioned by Martinez et al. [277]. The basic principle of laser printing – electrostatic attraction of charged particles to a surface – has also been adapted for direct patterning of nanoparticle clusters [278].

Much like microfluidic devices, several applications of vertically aligned CNT (VACNT) forests such as, hierarchical composite structures [151], dry adhesives [279], and contact probe arrays [280], require large-area patterning methods to become commercially viable. The deposition of patterned catalysts for CNT growth traditionally involves vacuum deposition methods combined with batch-style photolithography [216]. Inkjet printing has been used to print CNT catalyst and a wide variety of other nanoparticle solutions, but the wetting of the liquid and the drying kinetics of the solution can limit the uniformity and minimum feature size of the resulting patterns [281]. Micro-contact printing has also been applied to pattern catalyst solutions for subsequent growth of CNT forests [198,282]. Additionally, deposition of metal-

loaded block co-polymers can control the diameter and areal density of CNTs, and this method has been implemented by spin-coating as well as micro-contact printing [89,283]. However, use of these techniques in a continuous fashion and/or over large scales requires specialized equipment, and in the case of contact printing methods replacement of the soft stamp may be required. Thus, there remains a need for a highly flexible and scalable method for patterning nanoparticle catalyst for CNT manufacturing on alternative (e.g., flexible/metallic) and large-area substrates.

5.2 Experimental and characterization methods

The samples were prepared by starting with a custom pattern generated using CAD software (AutoCAD) and scaled to the desired dimensions. Kapton film (0.001" thick) was mounted to a sheet of 22 lb. paper, as a reinforcing layer, with adhesive tape around the perimeter to create the printing substrate. The substrate was loaded into a modified laser printer (Hewlett Packard 2015DN) that then printed the MICR toner in the pattern dictated by the user file. Neutral density filters (Thorlabs, Model # NE203B) were optionally placed between the laser and the photoreceptor drum to control the thickness of the deposited toner. After printing, the patterns were transferred to a suitable growth substrate, as described in section 5.4.

CNT growth was performed using a Lindberg Blue M horizontal tube furnace with a 25 mm OD quartz tube (22 mm ID, 300 mm heated length) at atmospheric pressure, with flows of $He/H_2/C_2H_4$ (400/100/100 sccm), at 775°C for 15 min, preceded by an annealing step at 775°C for 10 min with flows of 100/400 sccm He/H_2. The samples were rapidly cooled in the growth atmosphere before purging the CVD chamber with He when the thermocouple reading dropped below 250 °C.

Two-part epoxy was used to attach a piece of thread to the back of the grown substrate, and the other end of the thread was tied around a washer. Using isopropyl alcohol (IPA), a glass microscope slide was wiped clean and the forest was pressed onto the slide with finger pressure. The slide was then mounted in a ring clamp such that the washer hanging on the thread was loading the sample in shear. A metal hanger was hooked on the washer which allowed additional washers to be added to increase the shear load on the sample. The sample was loaded until failure occurred, and the final stable weight was recorded.

Mass measurements of the substrates were collected before and after MICR transfer to the substrate, and again after CNT growth, using a microbalance (Ohaus Discovery). The differential between the measurements before and after MICR transfer was multiplied by the percent value of iron oxide in the toner that was obtained through thermogravimetric analysis (TGA) to obtain the mass of the catalyst particles. Subtracting the mass of the catalyst particles, and the mass of the bare substrate, from the sample mass with CNT growth represented the mass of CNTs grown on the substrate. The areal coverage of each VACNT array was calculated using contrast pixel counting in Adobe Photoshop CS6, using images taken by a Nikon D40 camera. SEM imaging was performed using a FEI Nova Nanolab, and forest heights were measured directly from SEM images at different magnifications. The combination of the mass, area and height measurements was used to calculate the areal and volumetric densities of the VACNT arrays.

For X-ray scattering measurements, the CNT forest was placed on a motorized stage in the beampath of the G1 beamline at Cornell High Energy Synchrotron Source (CHESS). A beam energy of 10 ± 0.1 keV (wavelength ≈ 0.13 nm) was selected with synthetic multilayer optics (W/B4C, 27.1 Å d-spacing), and the beam is focused down to ≈ 20 μm using upstream mechanical slits. The beam size was accurately measured by scanning the beam over a pinhole slit mounted on a motorized stage while measuring the beam intensity. The downstream X-ray intensity measurements were normalized to the upstream measurements in order to eliminate the effect of the drift in synchrotron intensity over time. A standard sample of silver behenate powder ($d_{001} = 58.380$ Å) was used to calibrate the pixel-to-q ratio of the detector. Linescans from the 2D SAXS patterns were fitted using a mathematical model for lognormally distributed hollow cylinders. These scans were obtained by integrating the intensities within $\pm 10°$ from the reference direction (x-axis) of the inverse space parameter q (chosen to be the direction of maximum intensity). The fitting code used an iterative approach in searching for the best fit within a user defined fitting range. By including the low q part of the data, a good fit was achieved that selects a probability density function (PDF) for diameter distribution as well as for the ratio c = ID/OD, where ID is the inner diameter of the multiwalled CNT and OD is the outer diameter of the multi-walled CNT.

5.3 Laser printing of nanoparticle toner micropatterns

Figure 5-1a illustrates the general method of laser printing, where a laser beam is rastered across a photosensitive drum. This induces a positive charge on the drum surface, which in turn attracts negatively charged toner particles to the appropriate locations. The drum rotates continuously, and the pattern of toner particles is then pressed against, and adheres to, the target substrate, such as a sheet of paper. Heat and pressure applied to the substrate using a set of contacting rollers causes the toner particles to soften and adhere. This also forms continuous dot features on the paper, by coalescence of groups of particles that were attracted to the same focal spot of the laser.

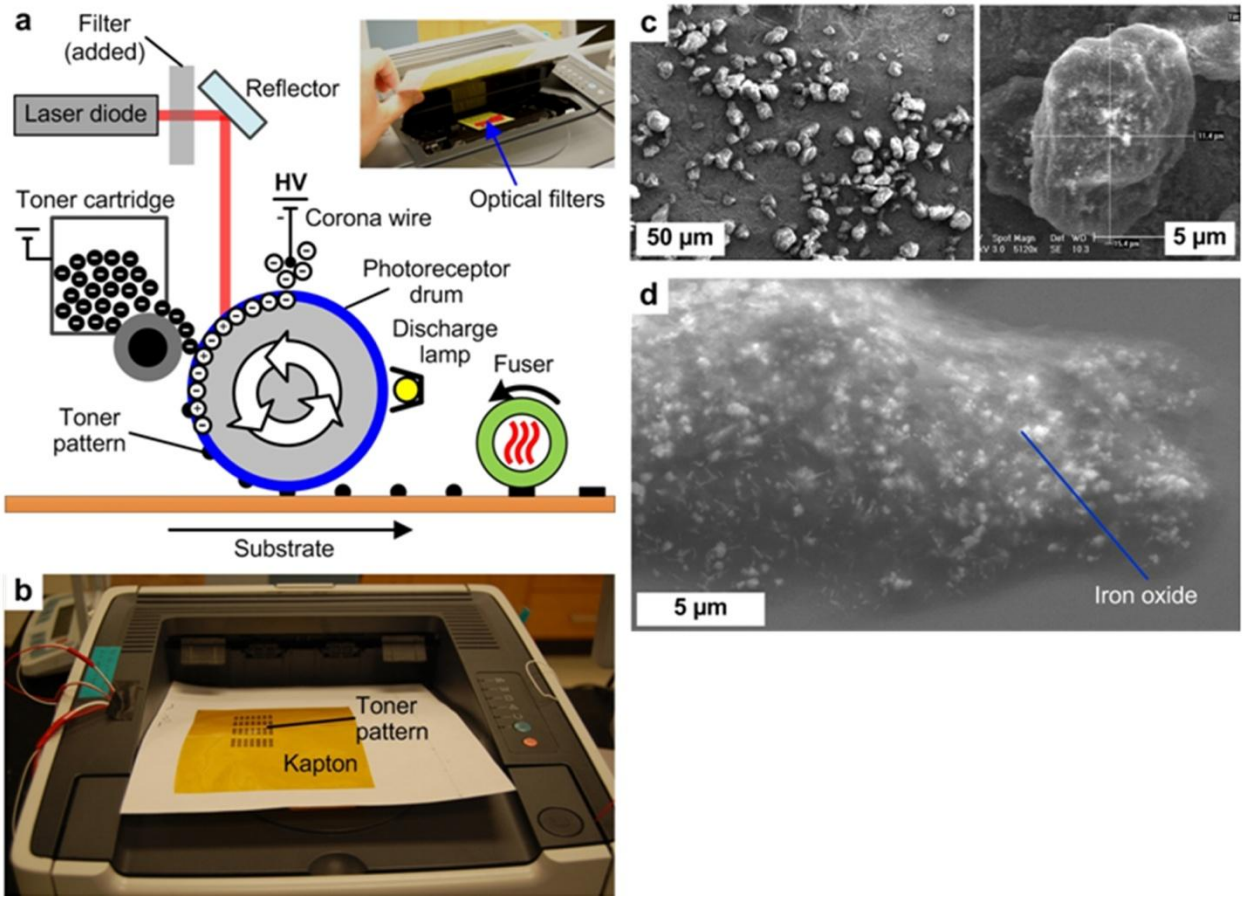

Figure 5-1. Modified laser printing for large-area manufacturing of micropatterns with nanoparticle toner. (a) Schematic of laser printer mechanism, indicating placement of filter for modulation of laser intensity. (b) Optical image of printer during operation with Kapton substrate. (c) SEM images of individual MICR toner particles harvested from the toner cartridge (single particle from left image is on the right). (d) SEM image of a printed toner particle, where high contrast dots are iron oxide nanoparticles.

We found that a low-cost home/office laser printer (Figure 5-1b) is capable of patterning micro-scale toner features containing metal nanoparticles, with feature size limited by the laser spot size and toner particle size. Specifically, we studied the printing of commercially-available magnetic ink character recognition (MICR) toner, which is widely used throughout the financial industry to enable the electronic processing of checks. The magnetic properties of the printed toner are established by inclusion of iron oxide particles within the toner,[284] and the wide usage of this toner in industry has driven the compatibility with most office printers. However, to our knowledge the details of the particles within this toner have not been studied previously in the context of micro/nano-fabrication research.

Toner used in this study (Figure 5-1c, d) was purchased as a sealed cartridge for use in the printer (micrpro.com, HP Q7553X), and by SEM imaging we determined that the toner microparticles have irregular shapes and are roughly 10-20 μm wide. By TGA (Figure 5-2), we determined that the toner contains approximately 40% polymer, which thermally decomposes below 500 °C; the remnants are carbon black (to provide optical contrast), and iron oxide (to impart magnetic read properties).

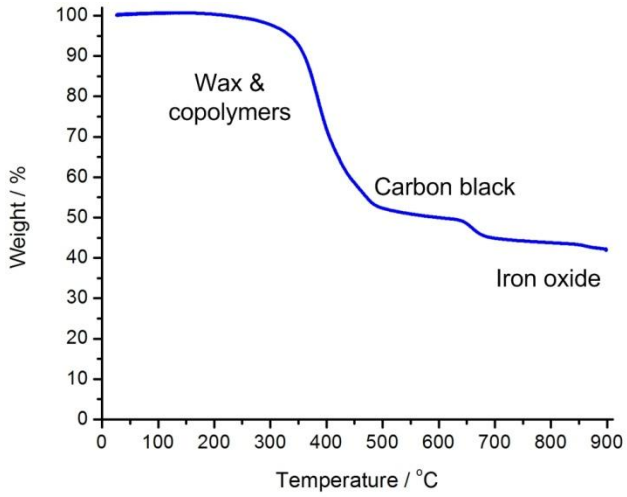

Figure 5-2. TGA of as-received MICR toner. The graph indicates the mass loss plateaus for each primary component as a function of temperature.

Because iron nanoparticles are used widely as the catalyst for CNT growth, we studied the applicability of MICR laser printing for direct-write manufacturing of catalyst patterns for CNT growth. To fabricate the patterns, we first designed the pattern using computer software

(AutoCAD), printed the pattern onto a polyimide (Kapton) substrate using the laser printer, and then transferred the pattern to an oxide-coated silicon wafer, completing preparation for subsequent CNT growth using a standard thermal CVD process (Figure 5-3). Because laser printing on paper deposits many layers of toner particles in order to achieve high optical contrast, we made one modification to the printer to reduce the amount of toner deposited. A series of neutral density filters (each with 50% transmission) were installed between the laser diode and the photosensitive drum (Figure 5-1b). The filters therefore reduced the charge density on the drum by reducing the laser intensity incident upon the drum. This enabled control of the density of toner particles independently from the design of the printed image and grayscale level. While patterns could be created using any software, use of CAD software facilitated comparison of the designed pattern with the dimensions of the features at each stage of the process.

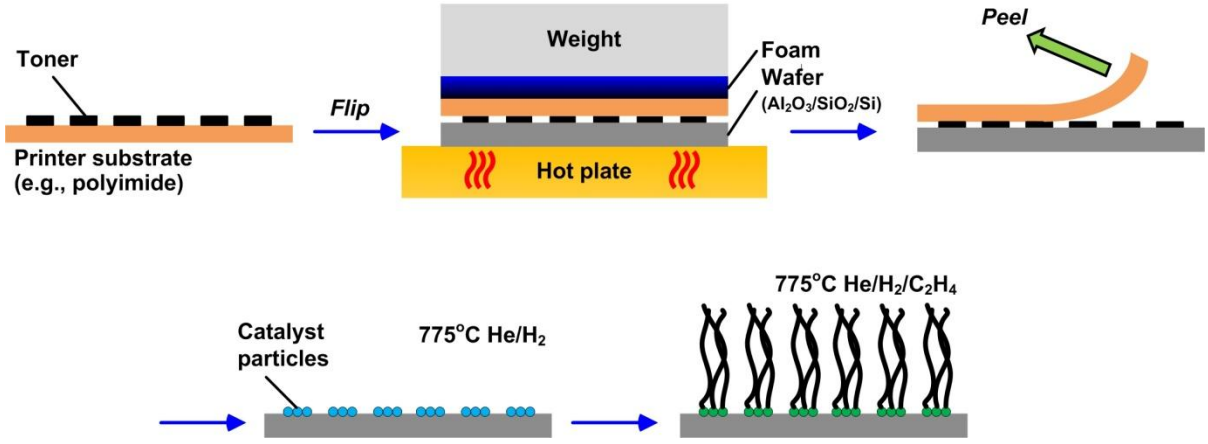

Figure 5-3. Printing, transfer and growth process of VACNT pillars via patterning of MICR toner.

5.4 Pattern transfer

After printing, the MICR pattern on the polyimide sheet was transferred to a silicon wafer for CNT synthesis. The Kapton sheet was cut from the paper backing with a razor blade and placed toner-down on a substrate that consisted of 10 nm of Al_2O_3 deposited by e-beam evaporation on silicon (100) wafers coated with 300 nm of thermally grown SiO_2 (Figure 5-4a); this alumina support layer stabilizes the catalyst particles against agglomeration at high temperature and influences CNT nucleation and growth [125]. A 5 mm thick layer of silicone foam was placed

on top of the inverted Kapton film as insulation, followed by an aluminum block which due to its weight exerted a uniform pressure of approximately 180 kPa. This stack was transferred to a hotplate (Heidolph MR Hei-Standard) preheated to 150 ºC for six seconds. After removing the heat source, and the pressure, and letting the stack cool to room temperature (approximately 1 minute), the Kapton was manually peeled back from the silicon substrate, leaving behind the patterned toner (Figure 5-4b). As discussed in detail previously, the patterned image transferred to the silicon wafer results in patterned CNT growth via a standard atmospheric pressure thermal CVD recipe, such as the example word “MECHANO” in Figure 5-4c.

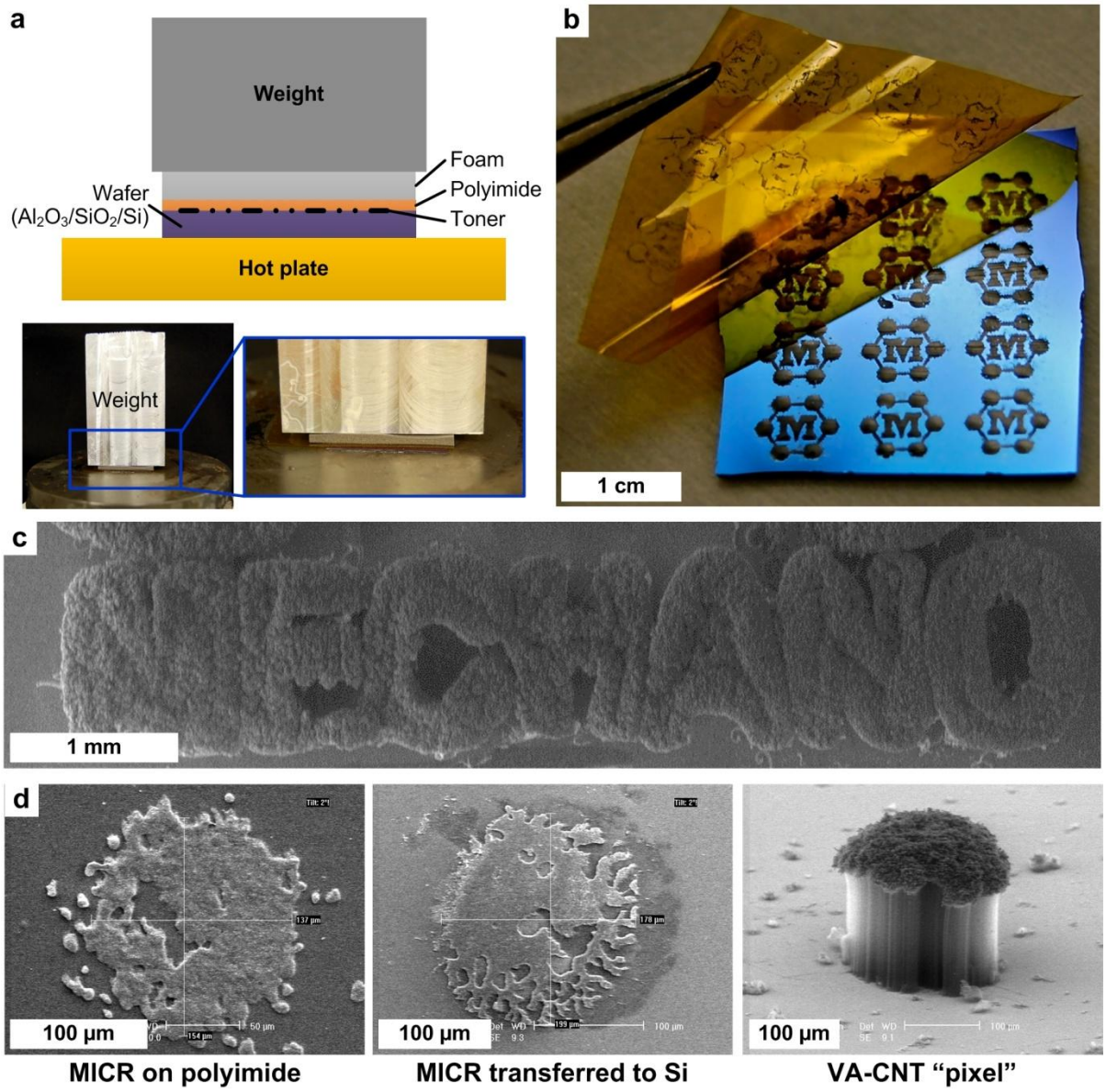

Figure 5-4. Thin-film transfer process and resulting micropatterns. (a) Schematic and photograph of transfer setup. (b) Photograph of the removal of the Kapton substrate, leaving nanoparticle micropatterns behind. (c) SEM image of the top view of "MECHANO" pattern after CNT growth, where the pattern was created by laser printing of 2 point font. (d) SEM images of individual 2 point "." characters as printed (left), transferred (middle) and grown (right).

SEM imaging of single dots ("." characters, 2 point font size) before and after the transfer process revealed that the area of the printed pattern increases by 60% due to the re-flow of the melted toner under pressure (Figure 5-4d). These features are approximately 140 µm and 190 µm wide, respectively, and are patchy due to the non-uniform distribution of the toner which is

easily seen at this high magnification. The transferred patterns result in growth of CNT forest structures ("pixels") of equivalent size, which are interestingly more continuous than the micro-scale catalyst features due to reflow of the toner at high temperature. Catalyst features as small as 70 μm were printed on Kapton, but these did not uniformly transfer to the silicon wafer. Nevertheless, the smallest feature that could potentially be created is limited by the size of the toner particles, and this is much smaller than the smallest feature that is consistently produced by the printer that was used. And, each toner particle still contains thousands of nanoparticles which can yield individual CNTs.

5.5 Digital control of CNT growth

The same CVD recipe was used to produce CNT forests with scales ranging from centimeter-wide patterns (Figure 5-4c) to individual dot features (Figure 5-4d), with heights controllable by the growth time. However, due to the excess quantity of nanoparticles and binder in the toner, as well as the polydispersity of the particles, the CNT forest grown from MICR has a dense "crust" on its top surface (Figure 5-5a). As determined by Raman spectroscopy and TEM (results not shown), this crust comprises amorphous carbon and carbon "onions" which overcoat larger nanoparticles or aggregates that do not grow CNTs. Incidentally, the CNT forest growth directly after transfer to the wafer can be delaminated, and the same substrate can be used to grow a second layer of CNTs without additional catalyst deposition. In this case, a thin layer of catalyst particles is left behind on the wafer, and the resulting second CNT forest has a much flatter top surface (Figure 5-5b). As is typical in a CNT growth process, the substrate is treated in a reducing atmosphere immediately prior to CNT growth to reduce the iron oxide [285,286]. This experiment verified that the CNTs grow at the interface between the toner and the substrate.

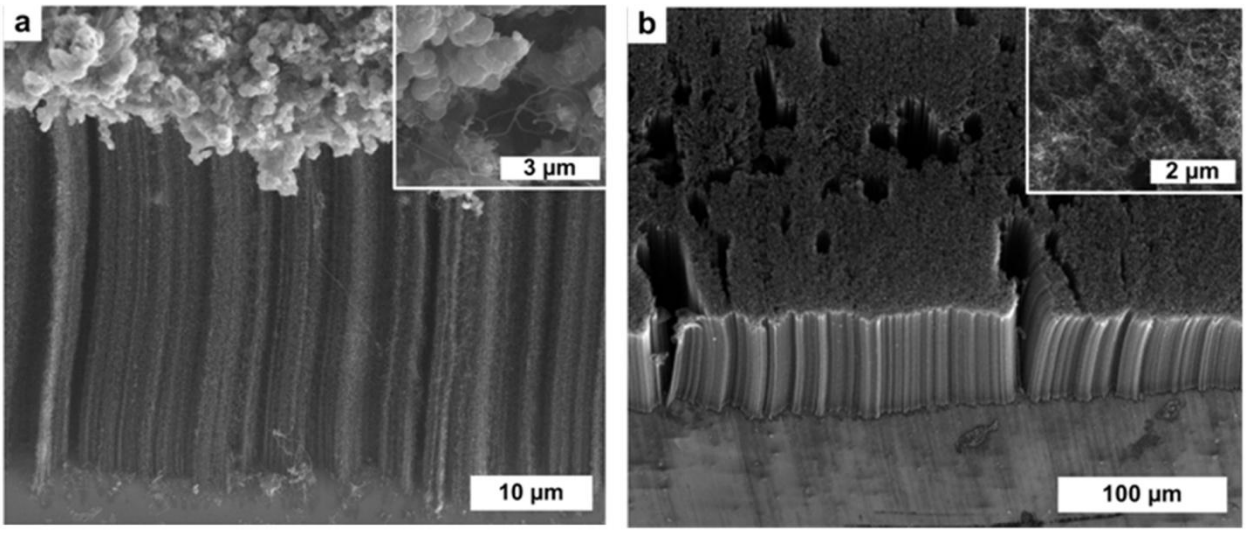

Figure 5-5. Comparison of top "crust" crust morphologies on original and re-grown substrates. (a) SEM image of a CNT forest and crust grown from a transferred MICR toner pattern. (b) SEM image of the same MICR toner pattern after delamination of the VACNT forest in (a) and a subsequent repetition of the CNT growth recipe. Inset SEM images show the crust morphology of the forests.

The capability to independently adjust the shape and grayscale intensity of the pattern, along with the modification of laser intensity (using the installed features) enables hierarchical control of the CNT forest structure. CNT forests were grown on substrates printed with 25-100% of the nominal laser intensity (0-2 installed filters), and importantly we found that the laser intensity determined the mass density of the CNT forest (Figure 5-6d). Therefore, the number of toner particles printed, and therefore the number of active catalyst nanoparticles for CNT growth, is proportional to the laser intensity. Within the measurement error computed for the three values investigated, a linear trend can be extrapolated. A more precise trend could be obtained via finer control of the laser intensity by direct modulation or using a different series of filters.

We also found that the CNT diameter does not change along with the density. The CNT diameter distribution was quantified using transmission SAXS [91,225], by fitting linescans of the SAXS images to a mathematical model of the CNTs as a lognormally distributed population of hollow cylinders. For all intensity levels, the average CNT diameter was 10 ± 2 nm. The diameter statistics were also verified by TEM imaging. The measured variance of ± 2 nm is comparable to that achieved by dewetting of thin film catalysts for CNT growth [215]. Therefore, the ability to engineer CNT density by the laser printing intensity does not come at

the expense of larger CNT diameter due to agglomeration of the catalyst particles, in spite of the surplus quantity of toner that is printed onto the substrate. Additionally, we expect that control of the catalyst nanoparticle size within the toner would enable control of the CNT diameter [83].

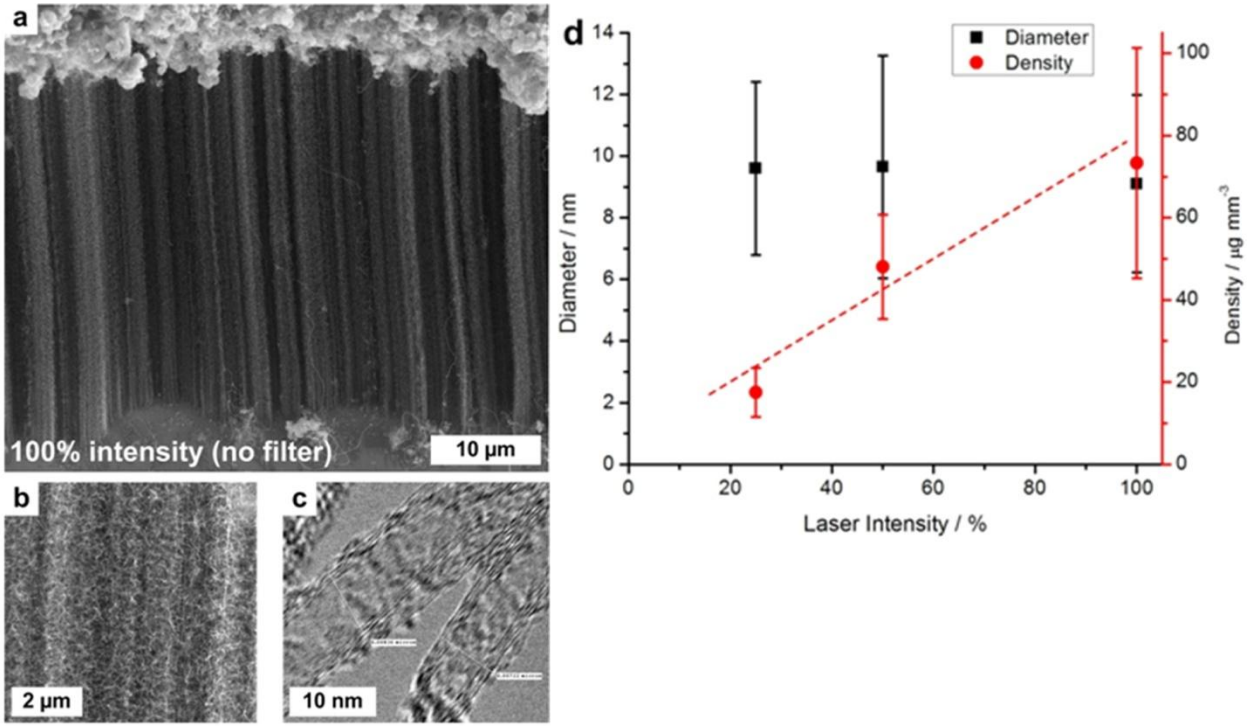

Figure 5-6. Characterization of CNT forests grown from MICR catalyst nanoparticles. (a) SEM image of CNT forest sidewall. (b) Magnified SEM image showing CNT tortuosity and density from sample in (a). (c) TEM image of few-walled CNTs from the forest, with indicated diameters approximately 8 nm and 7 nm. (d) CNT diameter and density statistics versus laser intensity, showing that CNT forest mass density is controlled by the laser intensity, yet CNT diameter distribution is invariant.

Moreover, we found that printing of grayscale patterns enabled growth of regularly spaced CNT micropillar arrays, where each grayscale dot led to a single micropillar. This is because a standard printer driver converts a grayscale tone to an equivalent size and density of evenly spaced dots, rather than adjusting the density of the printed toner particles without pixellation. Increasing the grayscale level (i.e., from dark to light) decreases the dot size, thus increasing the white space between dots on the printed page. Optical images of MICR patterns at different grayscale levels are seen in Figure 5-7a, along with an exemplary array of CNT micropillars growth from the 50% grayscale pattern in Figure 5-7b. The diameter of each micropillar in the 50% grayscale pattern is approximately 150 µm (Figure 5-7c), and the micropillars are arranged

in a hexagonal lattice pattern. As discussed earlier, this is close to the resolution limit of the present catalyst printing and transfer process. Micropillars grown from a 75% grayscale pattern are also shown in Figure 5-7d, where the additional free space between the pillars and the smaller pillar diameters allow them to tilt. However, at the edges of both of these patterns, we found much smaller CNT forest features that appear to have grown from stray MICR toner particles. These tall slender forests were found with diameter as small as 5 μm (Figure 5-7e). This indicates that ultimate resolution of the process will be determined by the size and uniformity of the toner particles, in concert with the resolution of the charge pattern created by the printer mechanism. Therefore, we expect that higher resolution laser printers, which have higher fidelity of charge patterning in the printing mechanism, will allow for printing of higher resolution micropatterns for CNT growth and other applications.

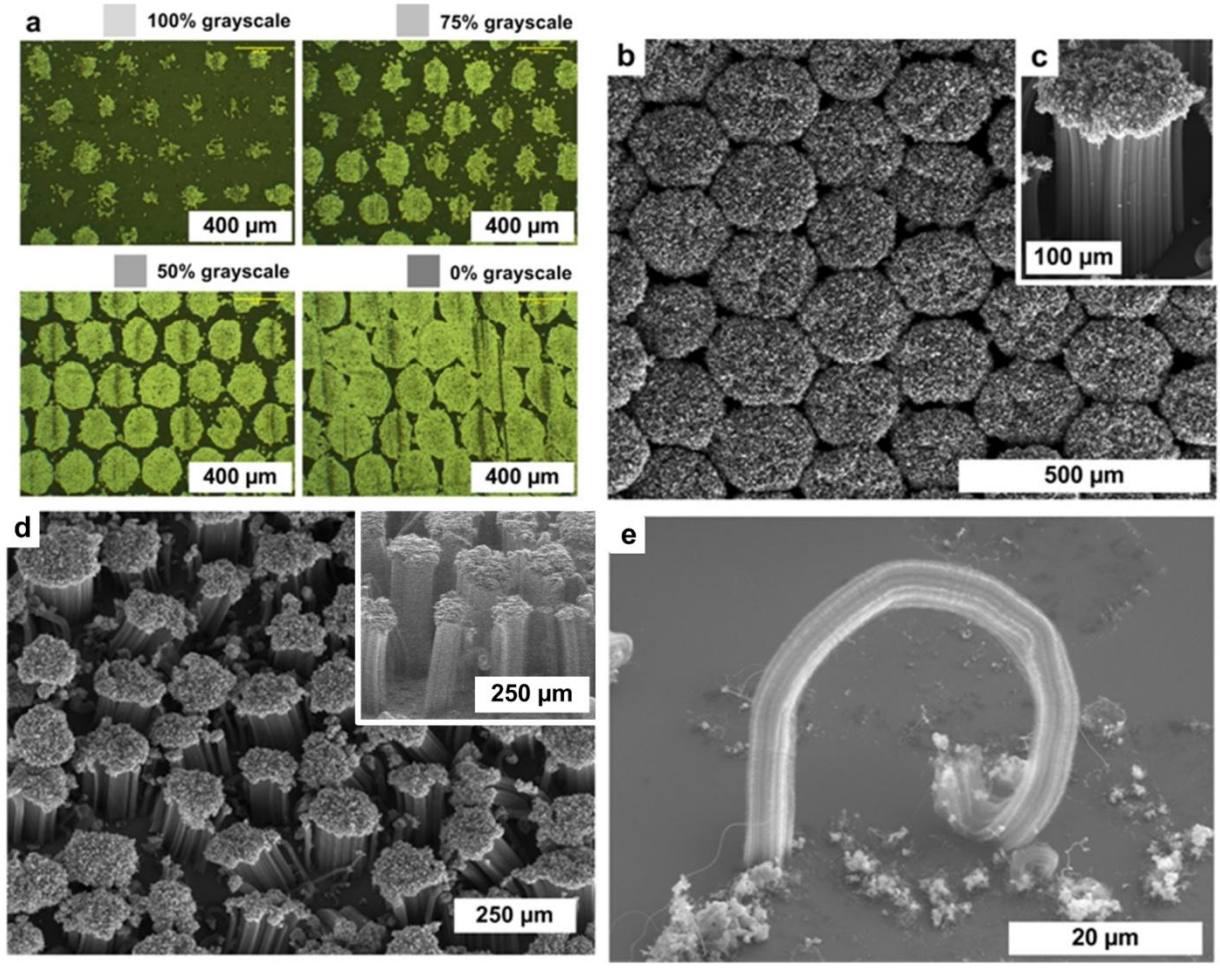

Figure 5-7. Grayscale-controlled printing of CNT micropillar arrays. (a) Optical micrographs of MICR on alumina substrate, showing increasing pattern density with decreasing grayscale lightness (as seen on-screen). (b) SEM image of a an array of CNT micropillars, from a 50% grayscale pattern, and an SEM image of a single micropillar at the edge of the patttern (c). (d) SEM image of CNT micropillar tops generated from a 75% grayscale pattern, and a side view (inset). (e) Small isolated micropillar grown from a single errant toner particle, indicating the potential for increased printing resolution via charge patterning.

5.6 Application demonstrations

Previous studies have shown that CNT forests can function as dry adhesives, and that patterning of the CNT forests enables control of the interface compliance while maintaining large numbers of micro- and nanoscale contacts [71,287]. Therefore, we hypothesized that the large area uniformity and tunable properties of laser printed arrays would make our material an attractive large-area dry adhesive. An array of microstructures patterned using 50% laser

intensity and a grayscale gradient (transitioning from no toner to full black) was fabricated using the same printing, transfer and CVD process described above. Using finger pressure, the sample was pressed onto a clean glass microscope slide and additional weight was added until the sample detached from the glass (Figure 5-8a). Before detaching, the sample supported 85 grams, which is approximately 1.2 N cm^{-2} overall, and 25 N cm^{-2} based on an estimate of the CNT area in contact with the glass slide. These values are lower than previous reports using CNT forests grown from thin film catalysts (up to 100 N cm^{-2}) [279,287]; however, we expect that much higher strength could be achieved by engineering the laser-printed growth process to have a thinner top layer, so that a greater number of CNTs contact the glass directly. Additionally, we observe that during compression and detachment some of the CNT micropillars are bent to the side, suggesting that the measured adhesion is determined by contact of the CNTs on the micropillar sidewalls with the glass (Figure 5-8b).

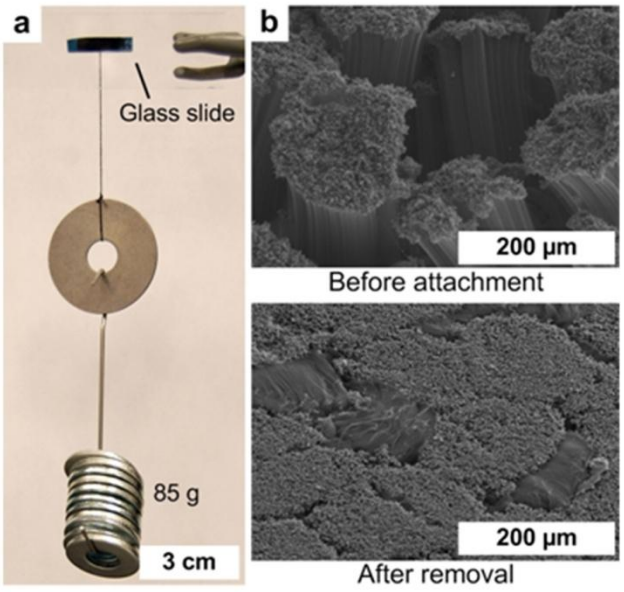

Figure 5-8. Demonstration of the applicability of MICR printing to dry adhesives. (a) Micropatterned MICR-catalyzed CNT forest supporting load in shear. (b) Before/after SEM images of CNT forest used as a dry adhesive, showing resulting forest deformation.

Last, we demonstrate the ability to scale the laser printing process to larger areas. An enlarged (100 mm wide) image of the 2004 United States Buckminster Fuller postage stamp was printed directly onto a sheet of aluminum foil as shown in Figure 5-9a. This image contains the full range of grayscale levels; and we verified that the MICR printing and transfer process can

accurately reproduce this image. The same pattern was also printed onto polymide and transferred to an alumina plate (Figure 5-9b). This demonstration also emphasizes that the use of Si substrates in the present study was a matter of convenience rather than necessity, and future work will focus on adaptation of the CNT growth recipe for MICR toner patterned on large-area ceramic plates and metal foils. We also found that large-area transferred patterns can exhibit small voids due to entrapment of air beneath the polyimide. Therefore, application of uniform pressure by a roller could enable continuous pattern transfer that is compatible with continuous laser printing of the toner pattern.

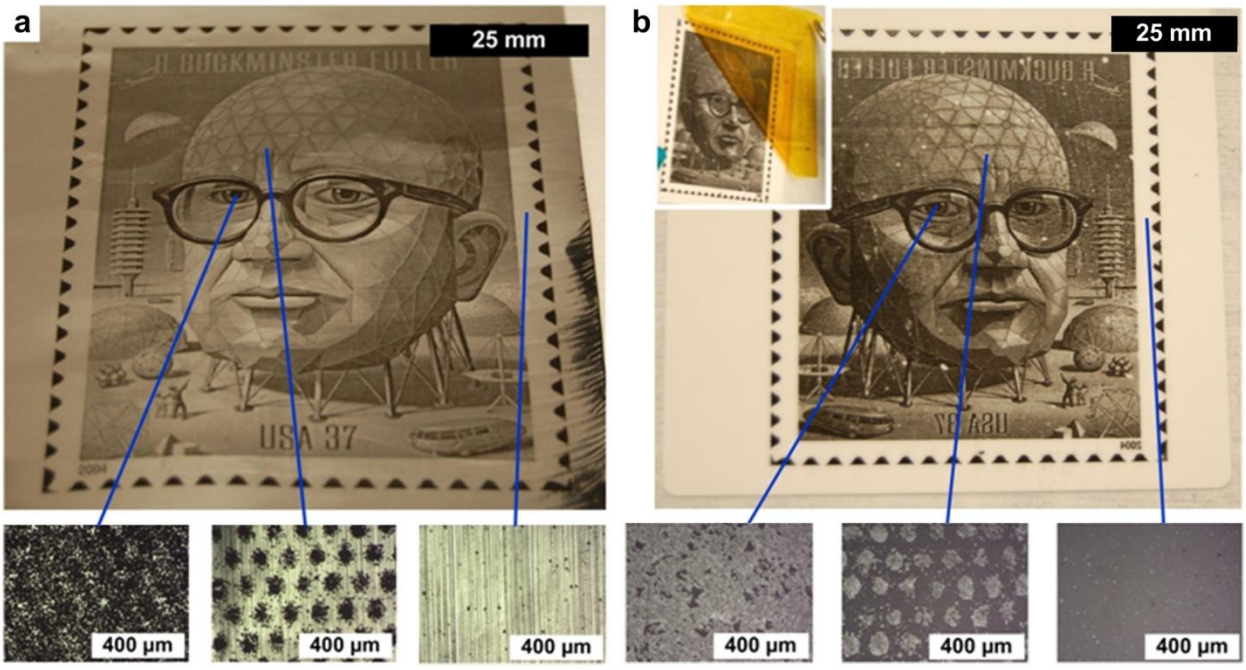

Figure 5-9. Demonstration of the applicability of MICR printing to large areas. (a) Large area MICR printing of an enlarged Buckminster Fuller United States postage stamp image on an aluminum foil sheet, with optical micrograph close-ups showing grayscale gradients. (b) Large area transfer to alumina of the same image in (a) with magnified optical micrographs of the grayscale dot patterns.

CHAPTER 6: CONCENTRIC TUBE REACTOR FOR ROLL-TO-ROLL THIN FILM DEPOSITION ON FLEXIBLE SUBSTRATES

This chapter presents the design, fabrication, and validation of a novel reactor design for the continuous R2R growth of CNT forests and graphene on flexible substrates. Key attributes of CVD reactor designs for CNT forest and graphene growth, including temperature uniformity, energy usage, and processing integration are presented first. The implementation of these attributes into a concentric tube CVD (CTCVD) reactor design is detailed next, including the use of a helically wrapped substrate around an inner tube that injects growth gases downstream of an annealing zone that is established between the concentric tubes. CFD analysis confirms the separation of annealing and growth treatment zones within the CTCVD reactor. An adjustable web tension brake along with optional inner tube counter-rotation also enables a continuous substrate motion over various speeds. Additionally, process gas savings of over 90% is achieved over a comparable tube furnace reactor. Next, the material and component selection for the fabrication of a benchtop prototype is presented where selected off-the-shelf components offer easy integration and the ability to perform both low and atmospheric pressure CVD. Finally, growth of 20 - 100 μm tall CNT forests on Cu and ceramic fiber substrates at 33 mm/min, and high quality bi- to multi-layer graphene on Ni and Cu at speeds of 25 - 495 mm/min are presented.

As previously discussed in Chapter 2, many important considerations that go into the design of a R2R CVD system for the production of CNT forests and graphene. While typical lab based CVD systems are focused on material processing and not overall system efficiency or scale-up potential, the system design presented in this chapter takes a holistic approach to the R2R processing of CNT forests and graphene by also minimizing operational cost and energy consumption. The CTCVD system eliminates additional furnaces for temporally segregated substrate treatments, minimizes the process gas consumption through the reduction of the reactor cross sectional area, and the helical substrate path in conjunction with the concentric tube design

offers a high surface-to-volume ratio. Combined, all of these factors offer a system with unique capabilities over current R2R systems that were assembled for the synthesis of CNT forests and graphene on flexible substrates.

6.1 Considerations for R2R CVD processing

The type of CVD reactor, and the features that are implemented in the operational design, ultimately control the quality, scalability and substrate material selection for CNT forest and graphene film growth. Among the most important of these features is the application of uniform thermal and processing gas environments, which determine the largest feasible substrate area for growth of uniform materials. The uniformity of the temperature and gas atmosphere has been shown to impact not only the morphology and nucleation of graphene islands [288,289], but also the quality, average diameter [290–292] and growth kinetics of CNTs [91]. While each of these studies was conducted on batch substrates where the processing temperature was assumed to be uniform, it is readily apparent that thermal fluctuations across a larger substrate would negatively impact the uniformity of the carbon nanomaterial. Likewise, it has been shown that the gas precursor plays an important role in the growth of CNT forests [113,115], and that the thermal decomposition and recombination of the feedstock gases throughout the CVD chamber influences the density, quality, and purity of the CNTs. Additionally, studies suggest that the confinement of the reaction zone above the substrate [148], and control of the flow direction of reaction gases [58,293] can have a significant impact on the uniformity of both graphene and CNT forests.

The means of heating the substrate and/or gases in a CVD reactor can also take on many forms, each offering advantages to the process (Figure 6-1) [3]. Plasma enhanced CVD (PECVD) generally offers lower temperature processing for the growth of CNT forests [294,295] and graphene [61,296], enabling the growth on alternative substrates that cannot survive the high temperature processing usually associated with thermal CVD. Unfortunately the low temperature processing comes at a price, in that the quality of the synthesized material is typically lower when compared to higher synthesis temperatures. Whether combined with PECVD or as a stand-alone process, thermal CVD utilizes increased temperature to provide the energy for the process.

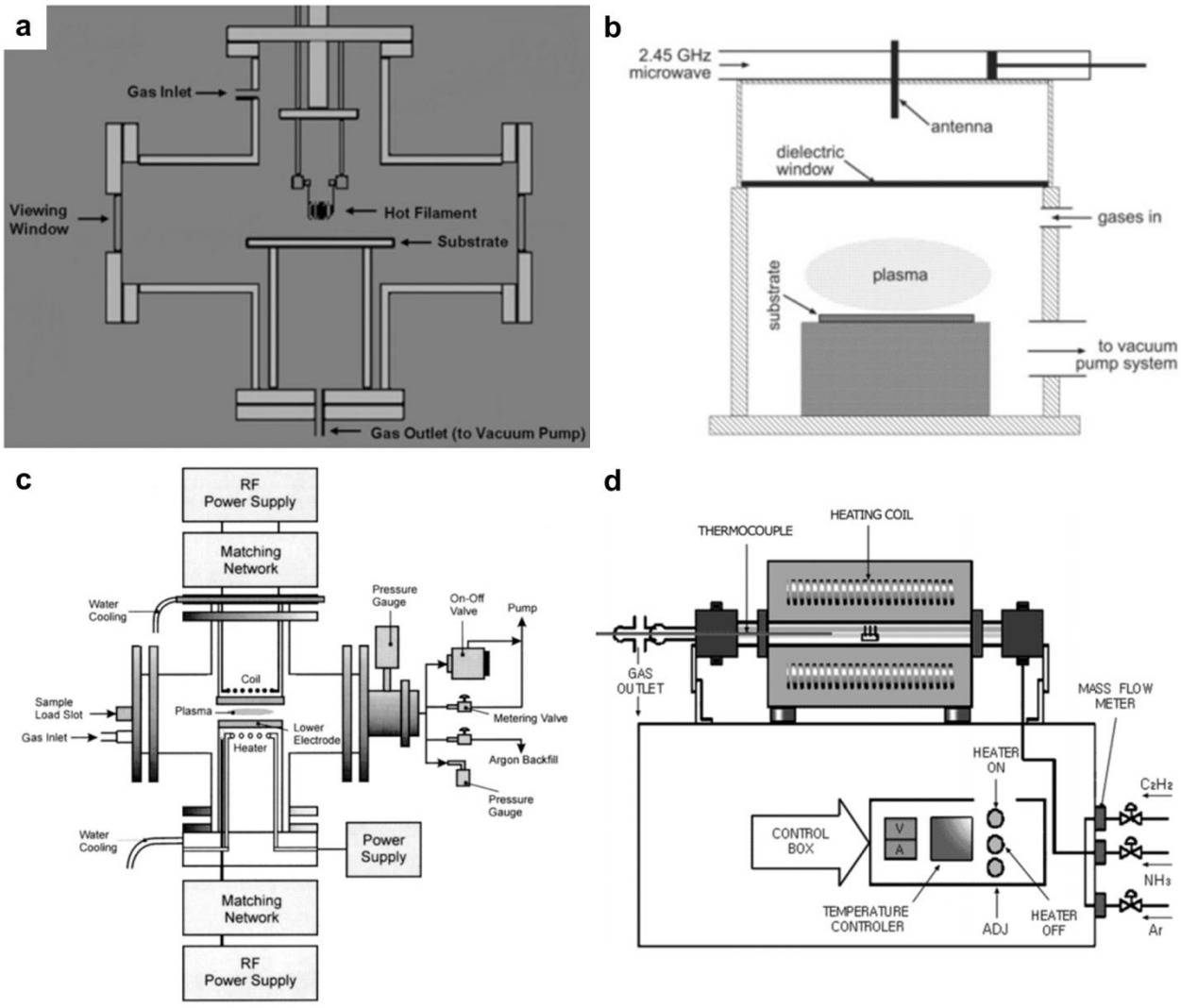

Figure 6-1. Schematics for various CVD reactors. (a) Hot filament CVD (HFCVD), (b) microwave enhanced CVD (MWCVD), (c) radio frequency power CVD (RFCVD), and (d) thermal CVD [3].

Thermal CVD systems for both graphene and CNT forest synthesis typically consist of a tube furnace where the entire reactor chamber (*e.g.*, quartz tube) is brought to an elevated operating temperature (*i.e.*, hot-wall). Because the reaction atmosphere is physically separated from the furnace, the method and materials used for heating are virtually unlimited. However, in cold-walled designs only the target substrate is at the operating temperature and the heating element is located within the reaction chamber. Thus, the materials used for the heating element must be inert for the processing of CNT forests and graphene [297–300]. In addition to the material restrictions for the cold-wall heating element, a pre-heater for the thermal decomposition of the

feedstock gases is also sometime required to ensure the proper gas composition at the substrate [113].

With large scale CVD systems cost and environmental impact also become significant drivers of the design. The energy consumption needed for the thermal or plasma treatment in the CVD reactor needs to be considered when selecting the method to adopt. For instance, while the specialized materials required for a cold-wall heater cost more initially, the operational cost might be lower than that of a larger hot-wall furnace configuration. Minimizing the usage of gases, while also increasing the efficiency at which they are converted into the desired material is also important from a cost and environmental standpoint. While the desired gas feedstock represents a direct cost, the unused byproducts from the CVD gases are ultimately released into the environment and should be minimized [214,301]. Therefore, the conversion efficiency of the gases should be maximized, and this involves both managing the chemistry of the growth reaction, and the contact/time area between the gases and the active material (i.e., the catalyst).

Additionally, the CVD system needs to incorporate several processing steps which require unique environments. For the growth of CNT forests and graphene these steps include; substrate preparation, nucleation, growth and delamination or transfer. While catalyst deposition for CNT forest growth and delamination or transfer of either material could be conducted in a process separate from the CVD reactor, the annealing portion of the substrate preparation, along with the nucleation and growth steps all require similar CVD processes. Thus, either separate in-line CVD systems or one contained unit with distinguishable processing locations would need to be applied. However, given that both materials can synthesized under vacuum or atmospheric pressures, the additional sealing and material requirements for a vacuum system in either configuration also need to be addressed.

6.2 Roll-to-Roll CVD reactor design

The novel design presented here centers around a concentric tube reactor where the materials are synthesized in the gaps between nested tubes, thus reducing the volume of gas required and increasing the flow uniformity. In addition to designing a R2R CVD reactor with the ability to be scaled up for increased throughput, the intent was to utilize commercial off-the-shelf components for the initial prototype to minimize cost and fabrication time. With this in mind

efforts were focused on the use of a standard tube furnace (Lindberg Blue M, 25 mm diameter x 30 cm heated zone) to create a hot-wall reactor, and designed the system around this requirement. This furnace size was selected because it has been used extensively by many groups within the community to perform batch growth of CNT forests and graphene. Thus, by keeping the overall heating and size constraints similar to growth studies that have been conducted, adaptation of individual batch procedures and recipes into this R2R system should be straightforward.

The thermal decomposition of the feedstock gases and subsequent creation of a favorable environment for CNT forest and graphene growth is key to a successful system. Because gases have a very low heat capacity, they readily increase and decrease in temperature with an applied thermal flux. Considering the volumetric flow rates typical of most CVD processes (> 2 L/min), the temperature change of the gas in the reactor is solely based on residence time (i.e., velocity) and not the gas mass required to be heated. In other words, one can expect that the gas composition along the length of the heated zone of a 1 and 2000 sccm flow to be similar if their velocities through the heated zone are the same. In order to have the same velocity (V), the cross sectional area (A) must scale with the volumetric flow rate (Q) where

$$Q = VA \tag{1}$$

Thus, in order to minimize the gas flow in the system for a given recipe, the cross sectional area of the reaction chamber must be reduced. Instead of simply reducing the diameter of the quartz tube in the furnace, a high aspect ratio cross section both reduces the area and provides a confined, uniform flow desirable for CNT forest and graphene growth. Unfortunately, the desire to create a system compatible with both vacuum and atmospheric pressure growth presents two challenges with a rectangular cross section tube. First, sealing a tube such as this would require a custom ISO type flange or a custom adaptor to a circular sealing arrangement. Second, flat planes are not structurally sound for the application of large pressure differentials across the face. Thus, the use of a rectangular cross section would require substantial reinforcement and material to make it compatible for vacuum CVD. The concentric tube design, where the CVD process takes place in the gap between the tubes, solves both of these issues. This design eliminates the need for custom sealing provisions, and given a fixed outer tube, the cross sectional area reactor

is adjusted simply by changing the diameter of the inner tube. By increasing the inner tube diameter, a reduced gas consumption of over 90% for CVD processes using commercially available quartz tubes is achieved (Figure 6-2).

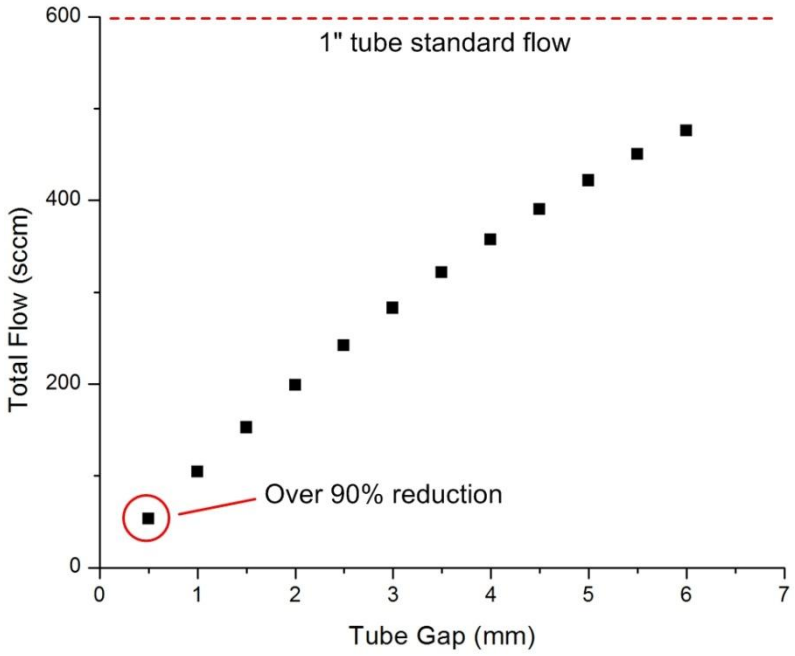

Figure 6-2. Concentric tube reactor gas consumption. This data is based on a standard recipe for CNT forest growth in a 1" tube furnace (600 sccm) where the same gas residence time is achieved with significantly lower flow rates using a concentric tube design.

Unlike the direct feed path utilized for a rectangular cross section furnace [61,302], a helical substrate path was selected for the concentric tube reactor. As shown in Figure 6-3, the helical path allows the flexible substrate to be supported by the surface of the inner tube while also increasing the amount of material that is being processed in the heated zone at any given time. Because the substrate slides along the inner tube in the defined helical path, each point on the foil "experiences" the same thermal and gas environments, which when coupled with the gap confinement, should lead to very uniform CVD processing. Although at large scales the impact of the substrate being drawn over the curved surface of the inner tube is not an issue, for a benchtop prototype such as this the smaller inner tube diameter could lead to additional stress on the synthesized material. While stress at the graphene-substrate interface has been shown to impact the physical wrinkling of the graphene [303], the stress needed to cause the formation of cracks in a CNT forest was determined to be the critical parameter. By bending delaminated

CNT forests, a minimum inner tube diameter of ~10 mm was found to be the limit for a 500 µm tall forest prior to cracking. Therefore, the inner tube diameter for this design was kept to above this limit.

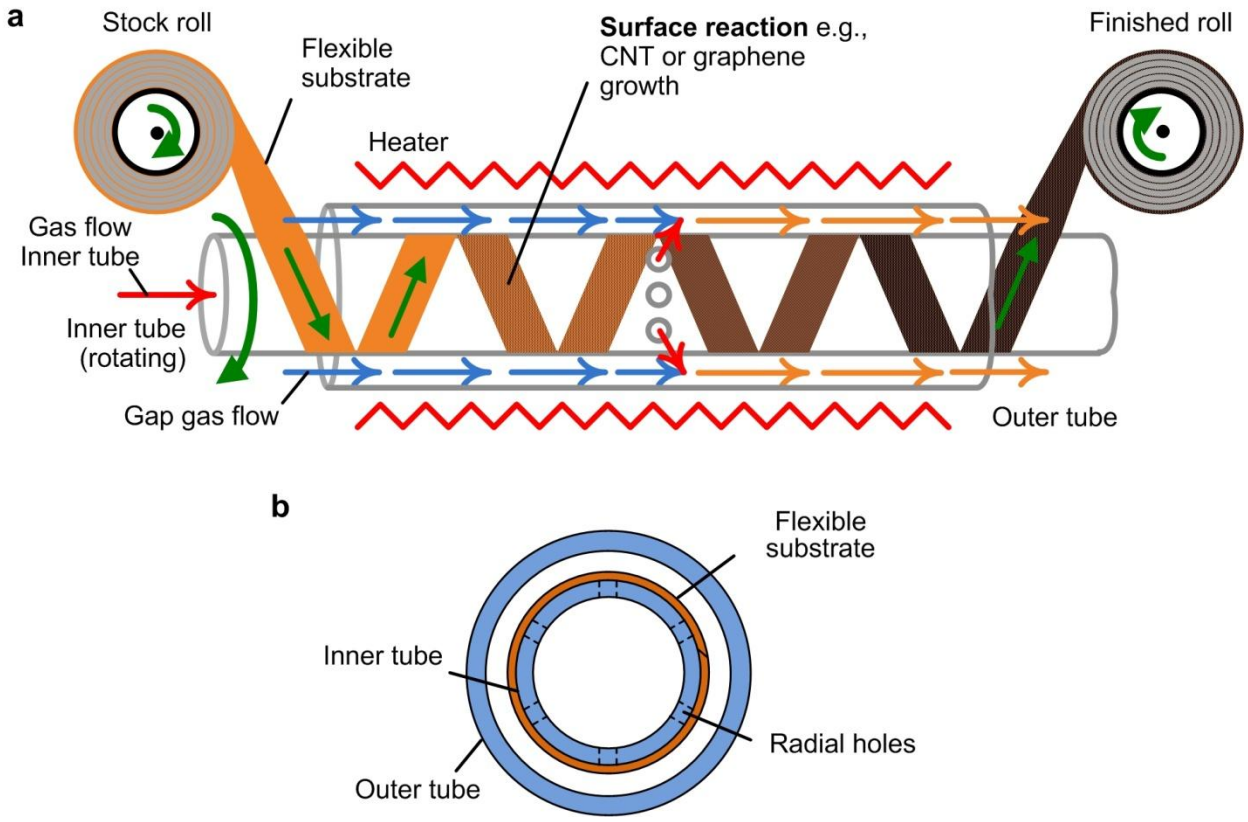

Figure 6-3. Schematic of the concentric tube reactor and substrate handling. (a) Side view of the system showing the helical substrate path and the separation of treatment gases. (b) Cross section of the concentric tube reactor.

The option of counter-rotating the tube and axial holes in the inner tube were added to increase functionality further. The rotation of the inner tube is meant to counteract "stick-slip" motion of the substrate at low translational speeds across the inner tube. By providing a counter-rotation with respect to the translating substrate, the interface will be kept in the kinetic friction regime and minimize the complexity of the substrate handling mechanism. The inner tube was also designed to have a wall in the center, and axial holes just upstream of the wall. Similar to the work by Hesjedal [172] where they injected CH4 in the heated zone to minimize the risk of rendering the Cu catalytically inactive with cold CH4 interactions, the inner tube allows for the injection of the carbon precursor into the gap at some distance within the heated zone. However,

where a concentric tube setup allows for uniform gas distribution, the injection by Hesjedal is located near the floor of the tube where the gas diffuses into the larger volume above, creating a gradient of CH4 concentration in the z-axis.

By flowing a reducing atmosphere in the gap an annealing zone is created upstream of the holes in the inner tube, and a growth zone downstream. This separation of gas treatment zones enables multiple processing steps within the confines of a single continuous heated zone, which is beneficial for both CNT forest and graphene growth. Treatment zone separation was confirmed through a computational fluid dynamics (CFD) simulation using a comercial software (StarCCM+). Figure 6-4 illustrates the mass fraction of C_2H_4 throughout the concentric tube design where He and H_2 are flowing in the gap and C_2H_4 is flowing in the inner tube at representative velocities for CNT forest growth. Although the C_2H_4 diffuses slightly upstream of the holes, the annealing and growth zones are distinctly defined through the gas flow. It is also worth noting that additional zones can be added by including additional inner tubes into the design.

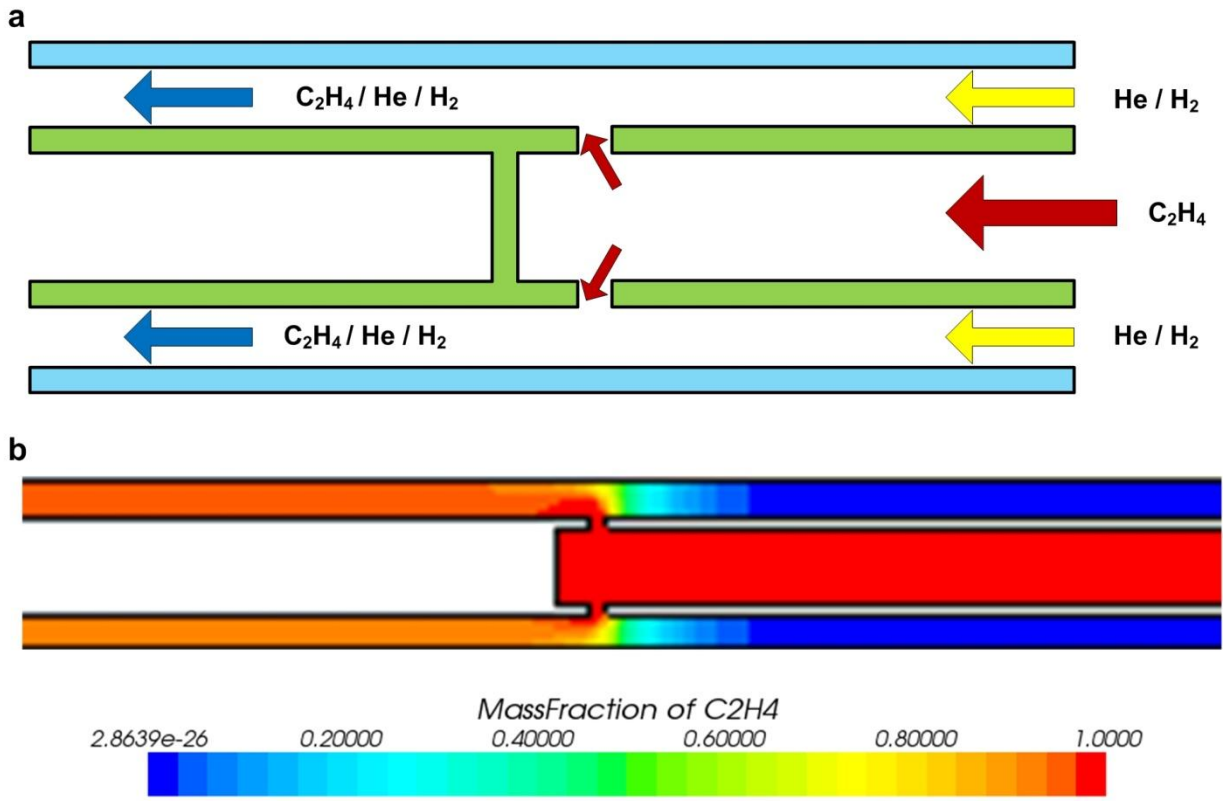

Figure 6-4. Gas treatment zone separation. (a) Axial cross-section schematic of the concentric tube design with gas compositions at various points. (b) Mass fraction of C_2H_4 calculated by CFD for the geometry in (a).

To make all of these features possible, a significant amount of time was spent designing the substrate or "web" handling system. Beginning with the tension applied to the substrate during operation, the shape of the flexible substrate span between the inner tube and the supply roller was approximated as a catenary (Figure 6-5) defined by

$$H = \frac{wL^2}{8f} \tag{2}$$

where (H) is the horizontal component of the substrate tension, (w) is the weight per unit length of substrate, (L) is the span length and (f) is the deflection or sag. Given the fixed size of the outer tube, and the author's experience with batch growths on metal foils, the substrate selected for the design was 6 mm wide and 25 μm thick Cu or Ni foil. The material and thickness was also based on several batch growth studies of CNT forests and graphene [72,158,304]. Based on the substrate dimensions, a span length from the inner tube to the supply roller of 100 mm was

determined to be an appropriate value, which allows the substrate to gradually roll 90° from the face of the tube to the face of the roller. Finally, to ensure consistent translation speed and uniform processing, the substrate must be taut at all times. Thus, the sag parameter was set equal to the thickness of the substrate (25 μm). Using each of these values along with material density, the minimum tension required for each substrate was calculated to be ~0.07 N (Table 6-1). Additionally, given the dimensional requirement for (L) and (f), the tension (T) and its horizontal component (H) can be considered to be equal.

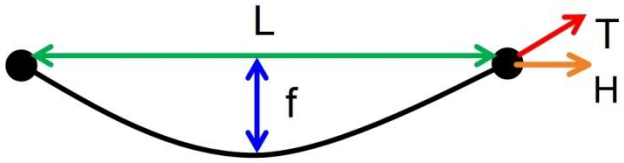

Figure 6-5. Schematic of a catenary formed by a wire suspended at its ends.

This resulting tension is defined as the holding force (F_B) that is applied to a flexible substrate wrapped around a cylinder, whose resulting required translation force is defined by the Capstan equation

$$F_A = F_B e^{\mu\gamma} \tag{3}$$

where (F_A) is the force required to induce slip, (μ) is the coefficient of friction between the substrate and the inner tube and (γ) is the total angle swept by all of the turns of the substrate (Figure 6-5a). It should be apparent from Equation (3) that F_A grows exponentially with an increase in γ, illustrating why a boat sail is easily controlled by a single person through the use of a rope wrapped a couple times around a winch. Assuming that the force exerted by the motor used to translate the substrate is unlimited, the limiting factor becomes the yield strength of the substrate itself (Table 6-1). Thus, the number of wraps that the helical path can have is limited. However, as depicted in Figure 6-6a, because this is a helically wrapped substrate, F_B is actually the radial component of the holding tension calculated earlier. Therefore, increasing the pitch of the helical path enables additional wraps to be utilized for the same given holding tension. For this type of system the tension equations can be broken into components where radial component from Equation (3) becomes

$$F_{A,r} = \sin\theta \, T e^{\mu\gamma} \tag{4}$$

the axial component is

$$F_{A,a} = \cos\theta \, T \tag{5}$$

and the force on the substrate required to induce slip is defined as

$$F_A = \sqrt{{F_{A,r}}^2 + {F_{A,a}}^2} \tag{6}$$

Using a length of 762 mm (standard length of a 25 mm diameter tube for batch growths) as the design contact length between the substrate and the inner tube, Figure 6-6b illustrates the maximum number of wraps possible for the entire range of holding tensions (T) for these substrates (assuming an inner tube diameter of 13 mm). The data points correspond to the possible number of wraps in the helical path where the possible configurations correspond to N + 0.5 (where N is an integer 0, 1, 2,...) wraps. This is based on the orientation and location of the rollers as depicted in Figure 6-3.

Table 6-1. Material properties and calculated values for catenary tension and yield tension.

Material	Yield Stress (MPa)	Density (kg/m3)	w (g/m)	μ (w/quartz)*	H = T (N)	Yield Tension (N)
Cu (99.9%)	70	8940	1.3410	0.3	0.0671	10.50
Ni (99.6%)	150	8890	1.3335	0.3	0.0667	22.50

*Note: μ represents the average kinetic coefficient of friction value for clean (~ 0.5) and carbon covered (~ 0.1) metals.

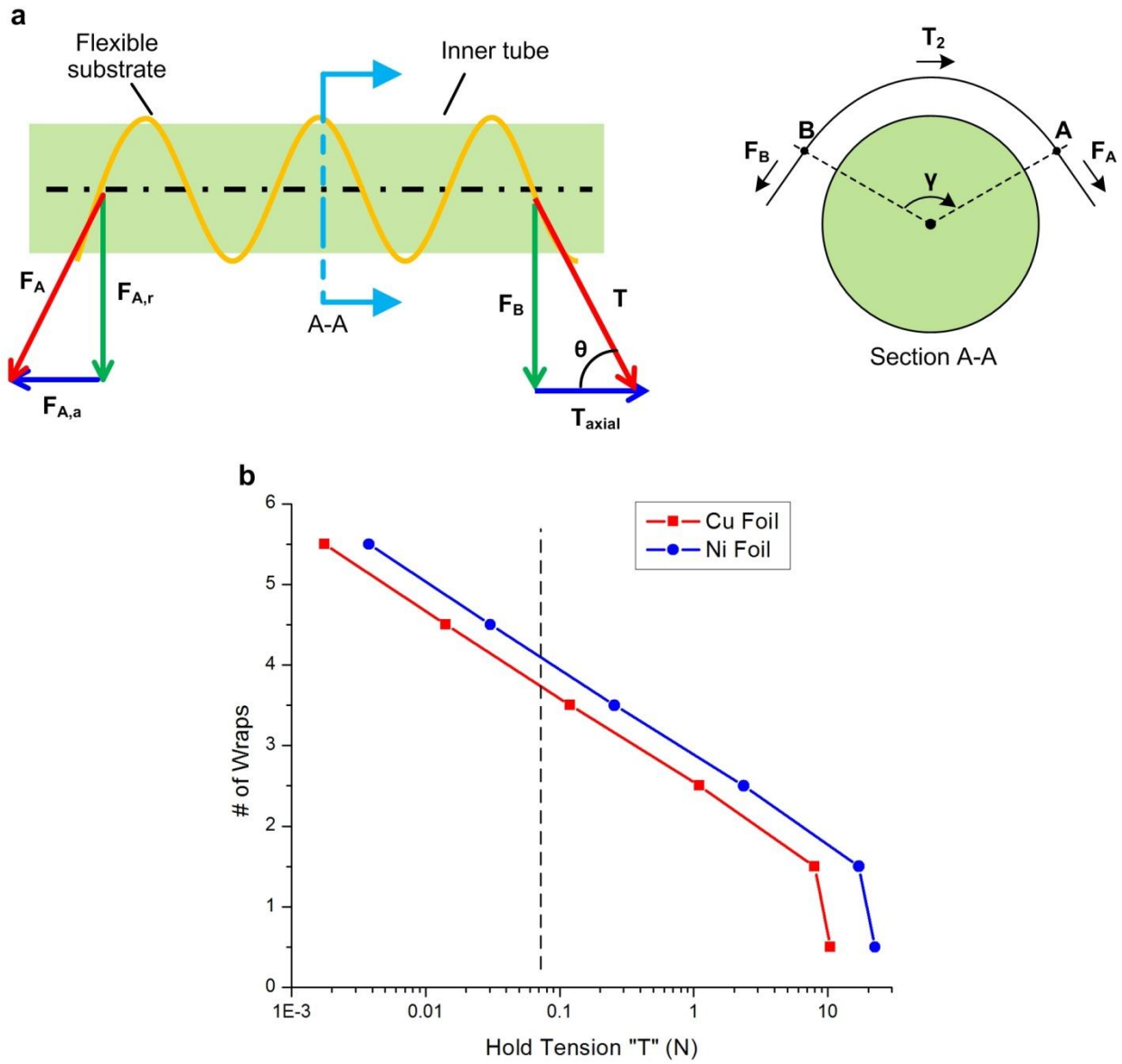

Figure 6-6. Helical substrate variables and limits. (a) Schematic of the Capstan variables for a helical path. (b) Comparison of the possible number of wraps in the helical path to the hold tension (T). The vertical line represents the minimum hold tension for this design as defined by the catenary model.

Finally, a friction based web tension brake is required to implement the holding force (F_B) that keeps the tension on the substrate at all times. However, the design of the brake also needed to be as flexible as possible to account for roller inertia and other substrate materials that could be used in the future. Based on these criteria, an adjustable brake based on the compression of a coil spring was selected for its compact design and tunable characteristics. Figure 6-7 shows a

schematic of the concept where the friction material is located between the roller and its corresponding shaft bushing mounting plate. The roller is then pulled against the friction material by a coil spring located on the roller shaft whose load is determined by an adjustable nut that compressed the spring against the opposite side of the bushing mounting plate. This design embodies flexibility by allowing multiple substrate materials, rollers, and number of wraps that the substrate takes in the helical path, all with a single adjustment.

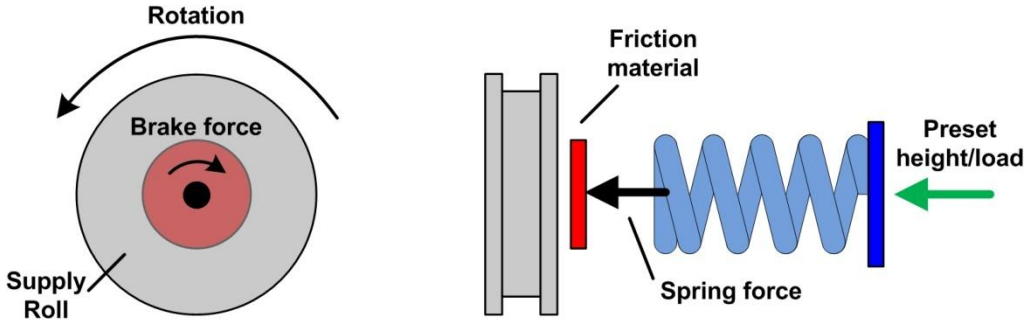

Figure 6-7. Web tension brake schematic.

6.3 Benchtop prototype of CTCVD reactor

Implementation of the R2R CTCVD reactor design began with the selection of the end chambers that provide a sealed environment for all of the substrate handling components. Keeping with a compact design, the end chambers were specified to be 10.5" tall with ISO200-K flanges (pipe O.D. is 8") at the top and bottom. A KF50 branch port was welded to the side of each chamber, offset 6" from the bottom, to create the reducer tee geometry (Figure 6-8). The material selected for the custom end chambers was 304L stainless steel, which was used for all other components creating the closed system. ISO200 blanks, machined to accept the additional substrate and gas handling hardware close off the top and bottom of the end chambers. To provide ports for the pass through of electrical wiring and the integration of processing instrumentation (*i.e.*, pressure transducers, mass spectrometer, etc.), a KF50/KF40 reducer cross (MDC Vacuum, 725014) was selected to mate with the KF50 branch port of the downstream, "outlet," end chamber. Finally, to enable the two chambers to be connected to the outer concentric tube, KF50 to 1" quick connect adaptors (Lesker, QF50XVC100) were selected.

All mounting hardware for the substrate handling system was fabricated out of 6061 Al plate and mounted to the end chamber base ISO200 blanks using 90° micro mounts (Thorlabs, MSAP90). In the outlet chamber, two support brackets were fabricated to create mounts for the high torque NEMA-17 stepper motors (Omega, OMHT17-075) for the substrate translation and inner tube rotation. The wiring for the motors is routed through a vacuum compatible 19-pin bayonet connector (Lesker, IFTRG197018B), mounted to the reducer cross, to two 256 µ-step motor controllers (All-Motion, EZHR17EN) outside of the CVD system. Mating of the stepper motor to the inner tube is accomplished through a custom adaptor that was fabricated to accept inner tube diameters from 13 - 20 mm. The inner tube is clamped in this adaptor using set screws against PTFE pads. For the web translation, 60 mm x 10 mm pulleys with trapezoidal grooves (Misumi, MBRDA60-5-P5) were selected and mated directly to the motor in the outlet chamber, and to a 1/4" shaft in the inlet chamber.

In the inlet chamber, all of the mounting hardware was similar to that of the outlet chamber, with the exception that the mounting plates housed PTFE bushings to support the inner tube and supply roller shaft instead of the two motors. The web tension brake located on the supply roller was created using an o-ring as the friction material between the specified pulley and the support bracket. Adjustment of the brake is accomplished by turning a nut on the threaded end of the pulley shaft to compress a coil spring between two PTFE washers. Additionally, a custom adaptor for the inner tube gas flow was fabricated and installed in the support plate for the inner tube. This adaptor features a design that allows the inner tube to slide over an o-ring that is located in a groove on the adaptor body. The o-ring seals the body of the adaptor to the inner surface of the inner tube, enabling the growth gases to pass through the inlet chamber via flexible SS line and to the inner tube without mixing with the annealing gases that are flowing through the rest of the inlet chamber.

Finally, the concentric tubes connect the two end chambers together, forming the complete CVD system. All of the tubes for this system are fused quartz supplied by Technical Glass Products, Inc. The outer tube is a standard 25 mm OD x 22 mm ID tube with a length of 30", while the two inner tubes were fabricated out of 20 mm OD x 17 mm ID and 13 mm OD x 10 mm ID tubing with lengths of 48". The inner tubes feature a fused quartz disc at their center (blocking the flow on the inside) and six (6) equally spaced radial 2 mm holes through the

sidewall 0.25" upstream of the disc. Prior to installation, the ends of the inner tube are cut and polished to position the radial holes in the center of the furnace. In order to prevent the concentric tubes from breaking during assembly and disassembly of the CVD chamber, a rail system was also fabricated out of 1" x 1" 80-20 extrusion to maintain alignment between the end chambers and the furnace. While the outlet chamber is fixed to the rails, the inlet chamber is free to move in the axial direction through the implementation of dovetail guides and carriers (Thorlabs, RLA2400, RC2). This allows the system to be opened and closed for insertion or removal of the substrate material without losing alignment.

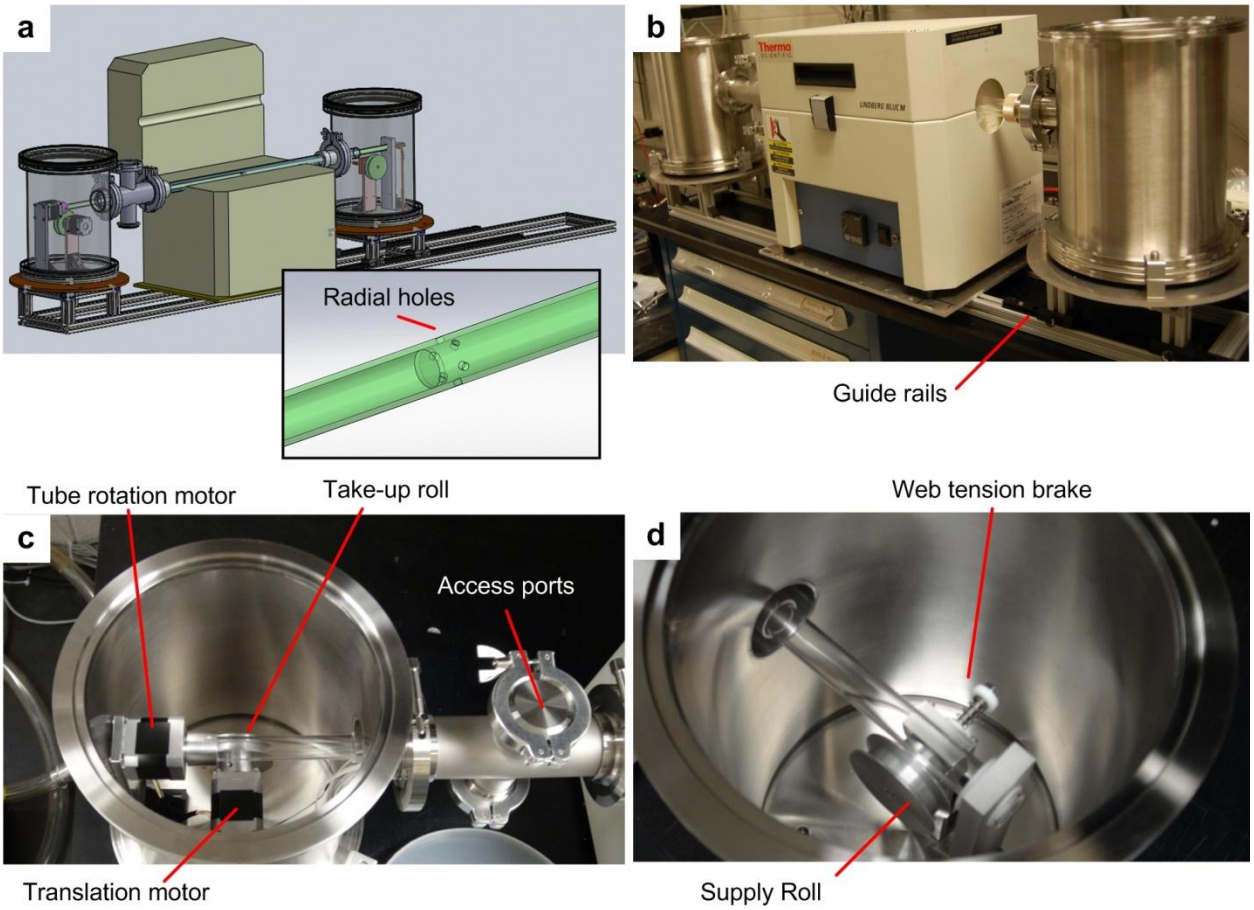

Figure 6-8. R2R CVD benchtop prototype machine. (a) CAD of the R2R CVD system with a representation of the inner tube geometry (inset). (b) Operational R2R CVD system. (c) Outlet end chamber interior and substrate handling components. (d) Inlet end chamber and web tension brake on the supply roll.

6.4 R2R CVD growth

All materials synthesized in this section used the same LabView control program and equipment for temperature (Lindberg Blue M) and gas flow control (Aalborg MFCs), with only changes in the CVD process conditions between materials. Prior to each growth, the system was "baked out" at a furnace temperature of 875 °C with a dry-grade airflow of 500 sccm for 30 min. This step removed all carbon deposits on the surfaces of the concentric tubes and created a consistent baseline for each experiment. Additionally, prior to the beginning of the experiment, a vacuum was pulled on the system while flowing He to remove the air that was introduced during the installation of the substrate material.

6.4.1 CNT forests

Both Cu foil and Nextel ceramic fibers were used as substrate materials for the growth of CNT forests in the R2R CVD reactor. Both substrates were 6 ft long and were wiped with acetone twice, followed by two wipes with isopropyl alcohol to remove any oils or contaminants from the production process. In order to provide an oxide support layer for the catalyst, the Cu substrate (H. Cross Company, 6 mm wide x 50 µm thick with a purity of 99.99%) was coated with 10 nm of Al_2O_3 via electron beam evaporation, followed by an oxygen plasma etch to promote the convective assembly of iron oxide nanoparticles from a ferrofluid (Ferrotec, MSGW11) at 25 µm/s (as described in Ch. 4). Without the need for an additional oxide layer, the 1/8" diameter woven sleeve of Nextel ceramic fibers (Omega, XC-18) was coated with the same catalyst particles through the wicking action of droplets placed on the surface.

Both materials were loaded into the CVD reactor one at a time on the 13 mm inner tube with 1.5 wraps, and the system was purged under vacuum. Once purged, the pressure was brought back to atmospheric using a He flow. Next, the furnace temperature was increased to 775 °C in 10 min and held at the elevated temperature for 10 min while flowing 195/65 (He/H_2) in the tube gap and 130 H_2 in the inner tube (all values are sccm). The gas flow in the inner tube was then altered (65/65 H_2/C_2H_4) to develop the growth region while keeping the tube gap flow the same. At this point the take-up roller motor was engaged and the substrate began translating at 33 mm/min allowing each point on the substrate to translate through the annealing and growth zones

in 4.6 min each. Once the end of the substrate was reached, the translation was stopped and the system was cooled to 100 °C in 10 min under a 1000 sccm He flow.

Figure 6-9 illustrates the CNT forest growth on the Cu substrate. While the formation of a CNT forest is clear, the height of the forest was only ~30 µm, which corresponds to a growth rate of ~0.1 µm/s. Typically a growth rate of 0.1 - 8 µm/s is expected, but given the furnace configuration it is know from prior batch experiments that CNT forests form best in an area about 60 mm long, 50 mm downstream of the current hole locations in the inner tube. Therefore, the decomposed feedstock gases might not favor CNT forest growth outside of this area, which would lead to a growth rate closer to 0.3 µm/s. Additionally, the forest has noticeable discontinuities in it caused by the striations in the Cu substrate and the crowding of catalyst particles at these locations. Thus, for CNT forest growth on metal substrates, the growth rate and substrate uniformity need to be considered further prior to system scale-up.

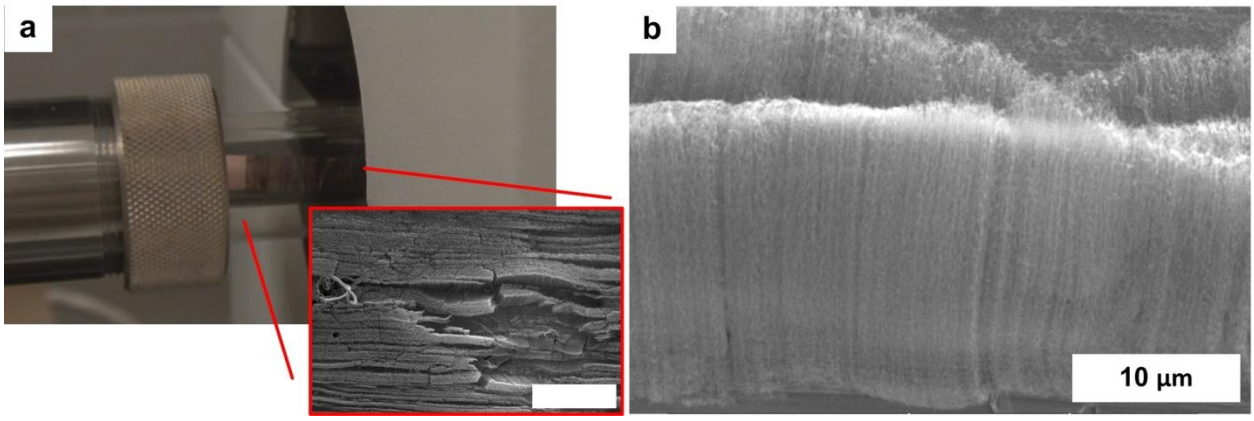

Figure 6-9. CNT forest growth on flexible Cu substrate. (a) Photograph of the Cu substrate translating out of the furnace with a CNT forest where catalyst particles were deposited and a SEM image of the forest (inset; scale bar is 40 µm). (b) SEM image of the CNT forest sidewall from the sample in (a).

CNT forest growth on the Nextel fibers displayed similar growth rates as the Cu, but localized areas appear to have produced forest heights of ~100 µm (or ~ 0.9 µm/s). Figure 6-10 illustrates the radial CNT forest growth from the individual fiber surfaces. The localized curvature of the ceramic fibers splits the forest into blades similar to the work by Guzmán et al. and García et al. [151,161]. While these forests are not usable as electrical or thermal interconnects, the growth on ceramic and composite fibers has been shown to increase

mechanical strength and electrical conductivity of composite systems. Finally, each of these experiments were terminated prior to the portion of the substrate with CNT forests reaching the take-up roller. Undoubtedly the winding and layering of these materials on the take-up roller would negatively affect the CNT forest structure, thus the material would have to go directly to a post-processing step to either encase the CNTs in a protective layer, or transfer them to a desired substrate.

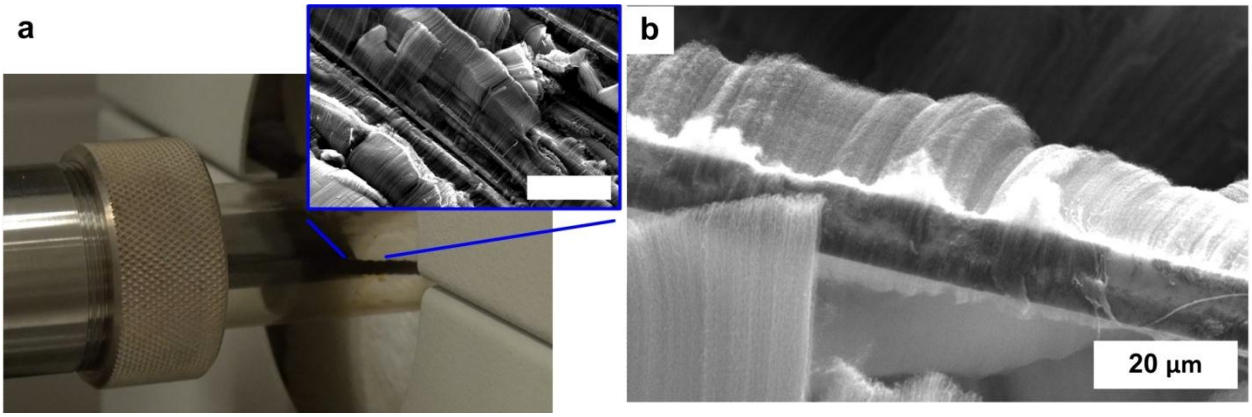

Figure 6-10. CNT forest growth on woven Nextel ceramic fiber sleeve. (a) Photograph of the ceramic fiber sleeve translating out of the furnace with a CNT forest growth and a SEM image of the CNT forest growth on several fibers (inset; scale bar is 100 µm). (b) Magnified SEM image of a single ceramic fiber with CNT forest growth from the sample in (a).

6.4.2 Graphene growth by CTCVD

In order to showcase the application of the CTCVD system to graphene growth, experiments were performed using Ni foils (H. Cross Company, 6 mm wide x 50 µm thick with a purity of 99.9%) based on the work by Chae et al. [305]. After performing a similar cleaning step as with the CNT forest substrates, the foil was loaded into the CVD reactor on the 13 mm inner tube with 1.5 wraps, and the system was purged. However, during these growths, the pressure remained in the 5 Torr range until the substrate was unloaded. The furnace temperature was ramped to 1000 °C in 20 min under a flow of 100 sccm H_2 in both the gap and inner tube. Translation of the substrate then began as the gas flows were adjusted to develop the growth atmosphere (300 H_2 in the tube gap and 300/25 H_2/C_2H_4 in the inner tube). Once the end of the substrate was reached, the system was cooled at a rate of 100 °C/min under a 1000 sccm He

flow. Figure 6-11 illustrates the zone separation by the formation of graphene and Ni-C layers on a static substrate near the radial holes in the inner tube. It is particularly interesting to note that even the slight upstream diffusion of the carbon source gas is very similar between the model and the experiments.

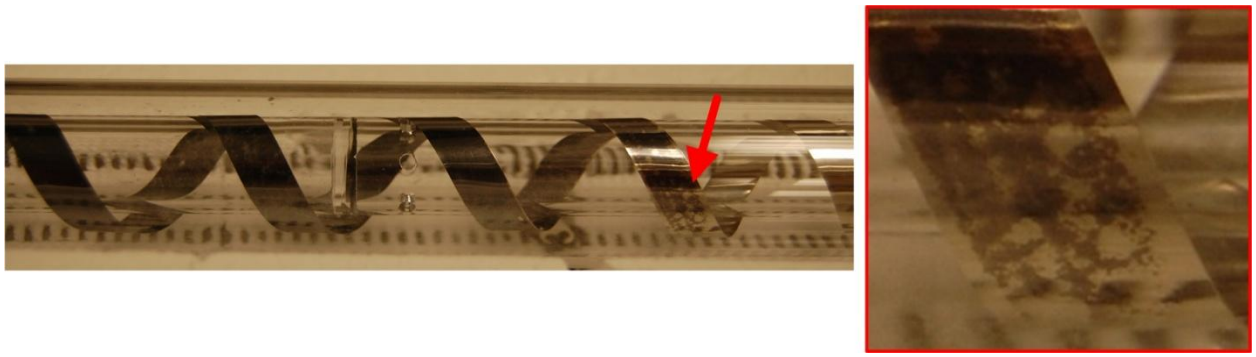

Figure 6-11. Separation of treatment zones on a Ni substrate. The red arrow indicates where the graphene and Ni-C layers begin to form upstream of the radial holes (magnified image on the right).

To investigate the correlation between graphene quality and number of layers grown with translation speed, experiments were performed at a series of speeds with consistent temperature and gas flows. The quality of the graphene was analyzed along the length (every 75 mm) and width (3 points, both edges and middle) of the substrate using Raman spectroscopy. Under these conditions, regardless of the translation speed, strong G and 2D peaks were observed, but a corresponding signal for the D peak was never observed (Figure 6-12a). The lack of a D peak suggests that the graphene, while ranging from bi-layer to multi-layer (3+) does not exhibit many defects. In order to determine whether or not the concentric tube design offered uniform graphene growth across the sample, Raman spectra were collected across the width and length of each sample. Although the uniformity across the width of the substrate was very good (Figure 6-12b), the variation along the length of the sample still leaves room for improvement. This is clearly illustrated by the spread of data in the 2D/G ratios found across all of the samples (Figure 6-12c). Additionally, a clear pattern of increasing graphene layers, as depicted by a decreasing 2D/G ratio, does not appear to be correlated with decreasing substrate velocity as one would expect.

Finally, while the visual inspection of the Ni foils post growth indicated the desired separation of treatment zones (Figure 6-11), the benefit of having multiple treatment zones remained unconfirmed. Raman spectra were collected at three positions corresponding to sections of the Ni foil that started and stopped at varying locations in the CTCVD system to answer whether or not the separate treatment zones were beneficial. As shown in Figure 6-12d, Ni that started outside of the furnace and ended in the annealing zone did not have graphene present, Ni that started in the annealing zone and ended in the growth zone exhibited high quality graphene growth, and Ni that started in the growth zone and ended downstream of the furnace had highly defective graphene growth. Similar findings were also observed on Cu substrates where the 2D/G ratios as a function of substrate velocity are plotted in Figure 6-13.

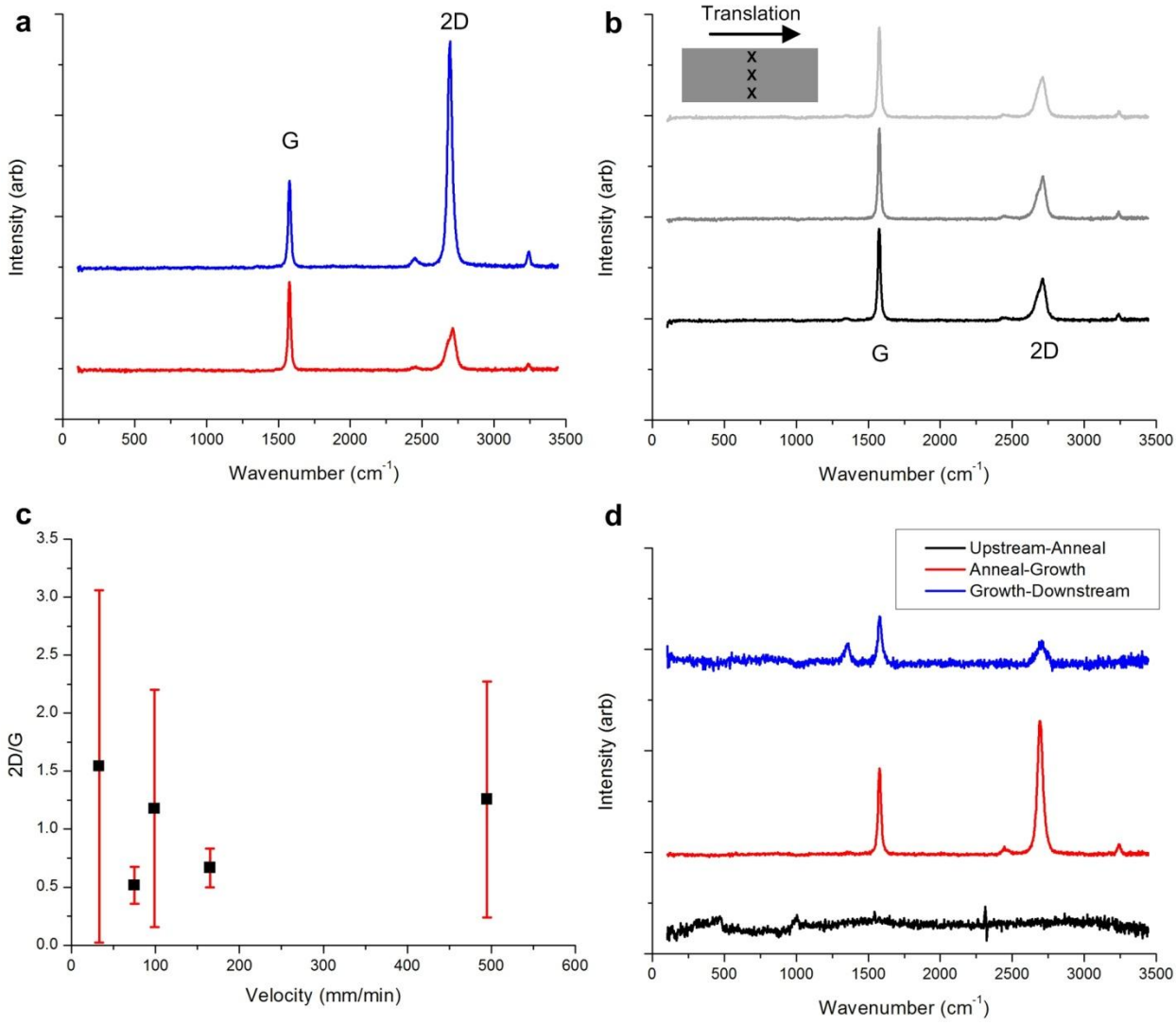

Figure 6-12. Raman spectroscopy data for graphene grown on Ni foils. (a) Raman spectra for low (red) and high (blue) 2D/G ratios generated from graphene grown on Ni foils. (b) Graphene uniformity across the width of a Ni substrate roughly at positions 1, 3 and 5 mm from the edge of the foil (foil sample diagram highlights the data collection locations). (c) 2D/G ratios versus the feed rate of the Ni foil. (d) Raman spectra for Ni that started and stopped in various positions in the CTCVD system highlighting the importance of multiple treatment zones (positions include upstream or downstream of the furnace and anneal or growth zones).

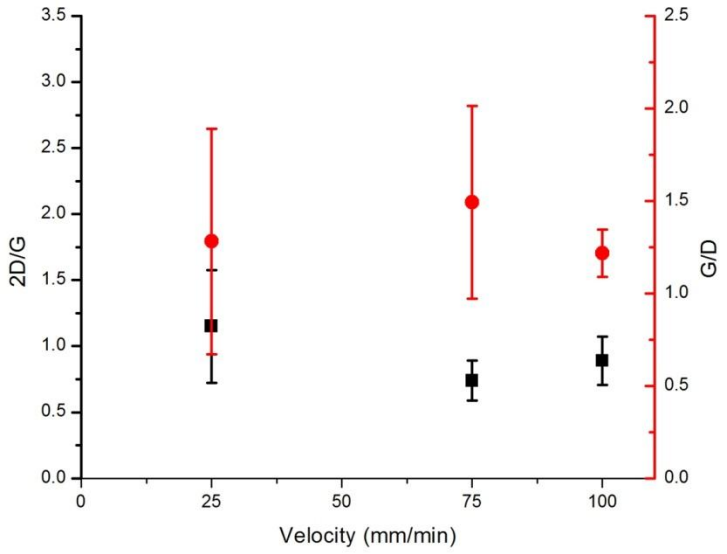

Figure 6-13. 2D/G ratios versus substrate velocity for graphene on Cu.

While the system still requires some optimization, it is to our knowledge the first R2R CVD system that incorporates separate treatment zones for CNT forest growth, and only the second to do so for graphene growth. This enables further tuning of the nanomaterial properties and in-line processing without the need for temporally segregated substrate treatments. Additionally, the gas savings based on the concentric tube design enables a much higher efficiency as compared to larger volume reactors. However, the full impact of these system features requires additional graphene characterization.

CHAPTER 7: REVOLVING SUBSTRATE CVD SYSTEM AND MEASUREMENTS OF CNT-SUBSTRATE ADHESION

Significant portions of this chapter were published in: E. S. Polsen, S. M. Perkins, E. R. Meshot, D. Copic, M. Bedewy, A. J. Hart, A. Arbor, S. Figueredo, B. L. Wardle, in Proceedings of the 17th Annual International Conference on Composite Materials (ICCM), ***2009****; ref* [65]*, and E. S. Polsen, S. H. Tawfick, E. R. Meshot, A. J. Hart, in 38th Annual North American Manufacturing Research Conference,* ***2010****; ref* [66]*. This includes sections 7.1-7.4. A portion of section 7.4 (growth results and 3D CFD) and all of 7.5 are not included in currently published work.*

This chapter showcases an alternative approach to the continuous CVD synthesis of CNT forests based on the concept of *in situ* delamination of the CNTs, and repeated use of the catalyst. First, the catalyst re-use method is compared to the general R2R method for CNT forest growth, along with potential application of CNT forest growth for interlaminar composite reinforcement. Next, the design and fabrication of a benchtop system intended to achieve continuous CVD growth of CNT forests on a revolving Si wafer is presented. Initial CNT growth results are then presented along with challenges associated with the design and supporting CFD analysis. Unfortunately, challenges with achieving uniform CNT growth in this machine, and the development of the CTCVD method presented in Chapter 6, mean that further work was not pursued. Finally, results from a brief batch study on the adhesion of CNT forests to the substrate are reviewed with a focus towards the tailoring of forest delamination.

7.1 Methods for continuous CNT forest manufacturing

Low-cost deposition [63,306] and/or re-use of the catalyst [307,308] are attractive attributes for continuous production of CNT forests since the catalyst represents a significant component of the cost of forest growth at large volumes. Illustrated in Figure 7-1, continuous feeding of a catalyst-coated substrate such as a metal foil or fiber (as presented in Chapter 6) [161,185] does not re-use the catalyst, and instead the substrate is treated as a "one time use" material even if the CNTs are delaminated. However, continuous growth and delamination using a revolving substrate [309], relies on multiple growths from the same catalyst to provide a continuous

process within a closed system. It has been shown that the growth of aligned CNTs, on crystal structured materials, is generated at the base of the CNTs [310], allowing the catalyst to remain on the substrate after CNT removal for re-use. Additionally, single catalyst layers can easily grow aligned CNT forests to several millimeters, while layers of only 100 μm or less are useful for multifunctional interfaces, including interlaminar reinforcement of laminated composites. Therefore, even without advances in long-life catalysts or re-deposition of catalyst, dozens of growth cycles could be achieved from a single catalyst deposition. And operational cycles could also be completed in a few seconds or less due to rapid (>> 1 μm/s) CNT forest growth.

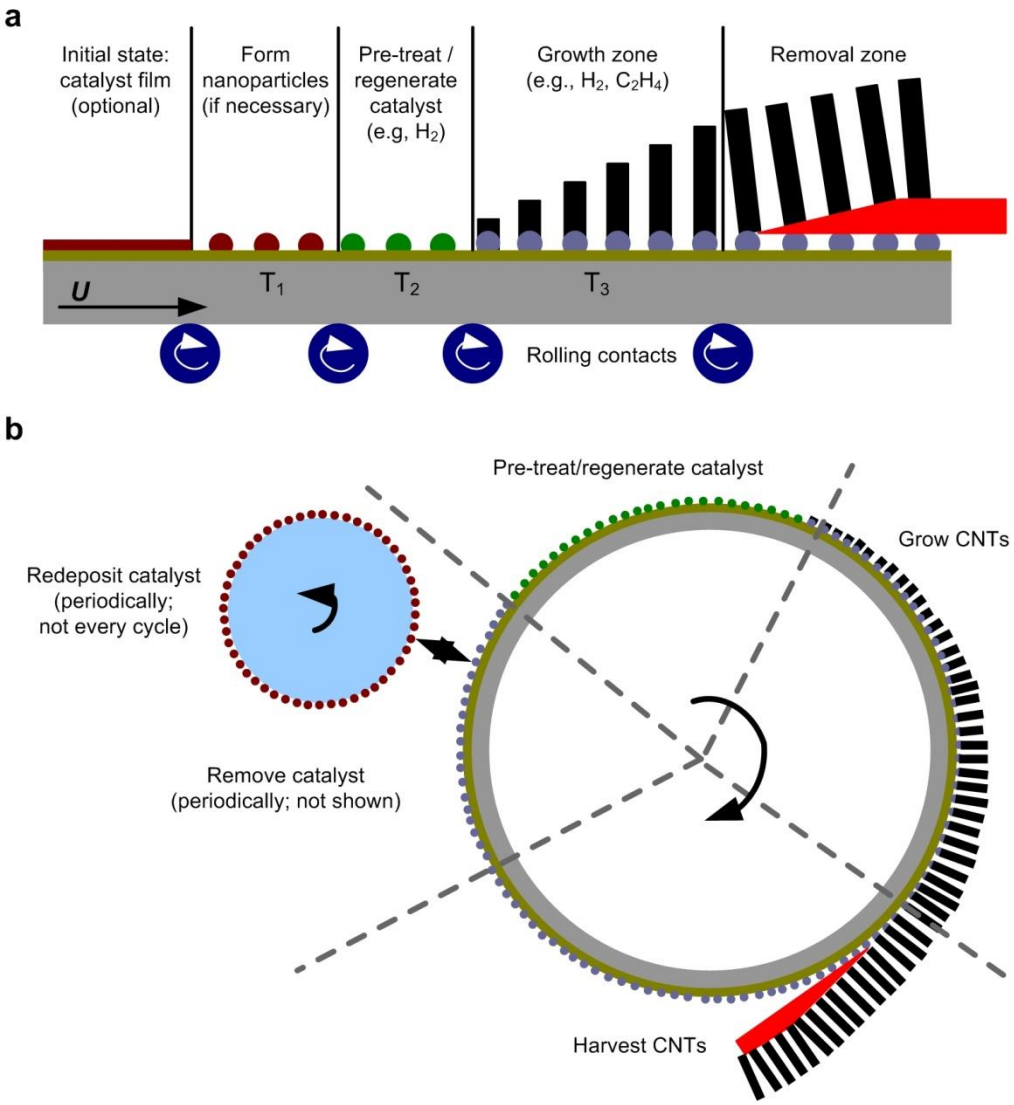

Figure 7-1. Continuous CNT forest manufacturing approaches. (a) Continuous feed of a catalyst-coated foil or fiber weave through a heated zone. (b) Catalyst re-use on a re-circulating substrate, with optional catalyst re-application.

7.2 System design

The continuous growth technique and system was designed with several critical performance characteristics in mind, and built upon our extensive study of batch-style CNT forest growth on centimeter-scale substrates. Based on our prior studies, the use of a decoupled CVD method enables the precise tuning of CNT diameter, structural quality, and growth kinetics of vertically aligned CNT forests [91]. Using this approach, the gas is thermally treated before reaching the

catalyst, which creates a polydisperse hydrocarbon atmosphere that is necessary for efficient growth of high-quality CNTs [311]. The catalyst-coated substrate is heated locally in a "cold wall" manner. Additionally, since the complete growth cycle undergoes distinct stages that are temporally separated in a batch process, each stage must be spatially maintained within a single apparatus to allow for continuous growth. Thus, each phase would need to occur in a separate spatial zone in order to sequentially achieve pre-treatment of the CNT growth catalyst, CNT growth, and optional printing to another substrate such as a graphite/epoxy prepreg. If the catalyst is to be re-used, careful removal of the CNT forest from the moving substrate must leave the catalyst behind, where it is subsequently re-used for a large number of cycles, avoiding costly re-application of catalyst each time. Figure 7-2 illustrates the overall flow diagram for the continuous growth process that incorporates catalyst activation and re-activation, CNT growth, and CNT removal.

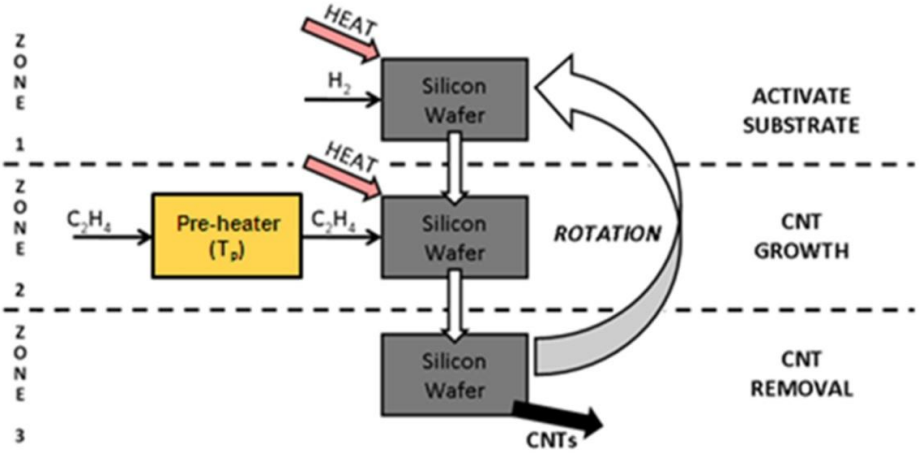

Figure 7-2. Process flow diagram for continuous CNT forest growth. Emphasis is placed on the decoupling of activation, growth, and removal operations.

Utilizing the key characteristics mentioned above, we conceptualized a desktop machine for studying continuous production of seamless CNT forests, wherein a circular substrate is rotated through a three-zone, atmospheric-pressure CVD reactor. Shown in Figure 7-3, the circular growth substrate is located below a quartz jar that allows for the chamber to be sealed, and for the substrate to be heated via radiation. The use of halogen lamps coupled with two reflectors (One above the lamps and one below the substrate) achieves uniformity and control of the substrate temperature (T_s). Catalyst annealing, CNT growth and delamination from the substrate

occur individually in their respective zones as the substrate rotates continuously. Also, additional ports along the walls of the growth chamber allow installation of thermocouples, or for connection of a mass spectrometer for online chemical analysis of the reaction atmosphere.

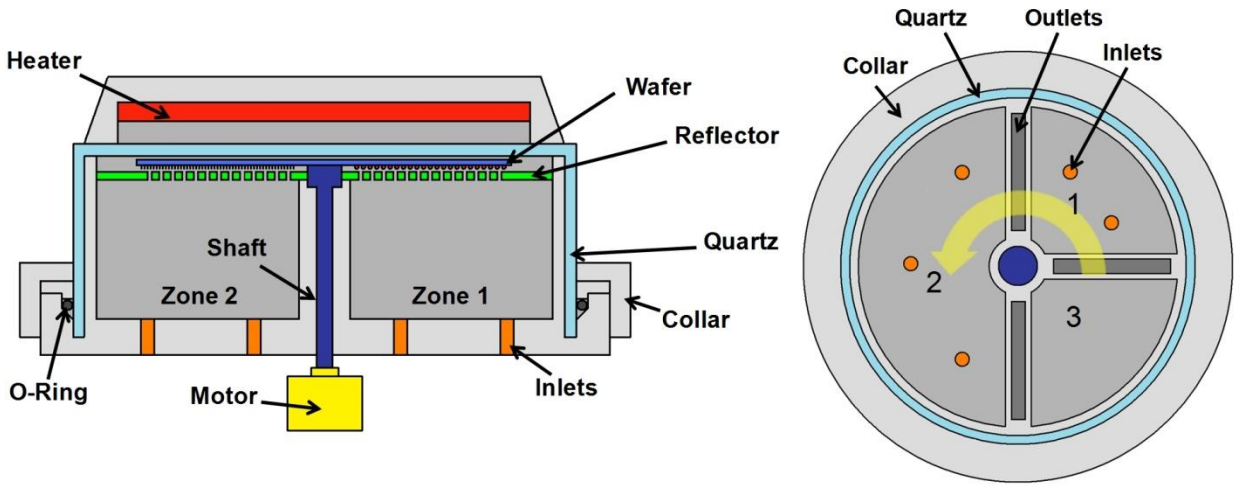

Figure 7-3. Schematic of the revolving substrate CVD machine for continuous CNT forest growth.

Flows, heat fluxes, and temperatures within the CNT manufacturing process were analyzed through thermal and CFD models developed using RadTherm and Star-CCM+ software packages. These models capture the boundary conditions within the chambers of the apparatus during CNT growth, and allow tradeoff studies to be conducted with regards to different structural and insulation materials, as well as different flow rates and compositions. Additionally, as a proof of concept for the fluid wall separation between the three zones in the chamber, 2D models were generated to confirm that this type of design is a viable solution for maintaining individual atmospheres. Figure 7-4 shows a steady-state snapshot of the annealing and growth zones with a map of the ethylene concentration. As illustrated, the ethylene is only present in the growth zone (right side) and flows through the hollow wall towards the exit before any mixing with the annealing zone occurs. The lack of mixing between the two zones verifies that the principle behind the zone separation is valid.

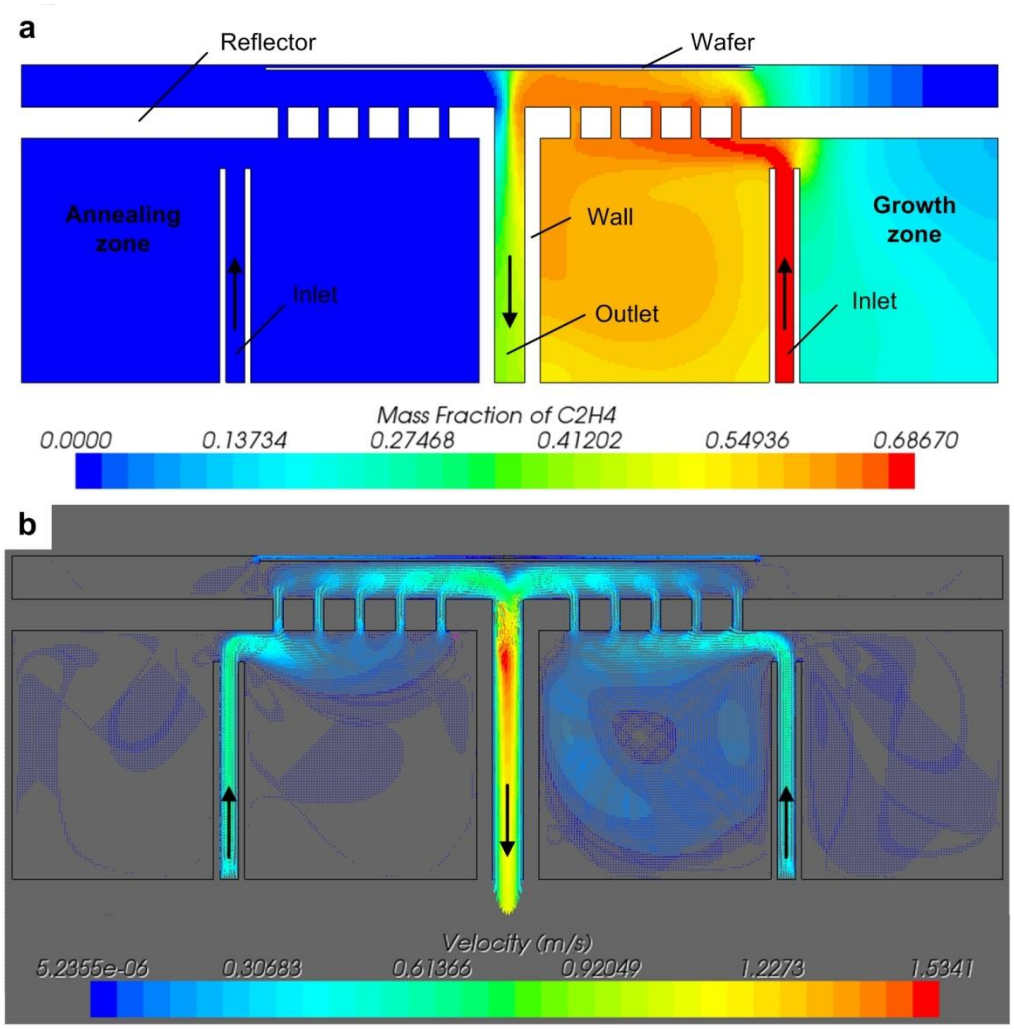

Figure 7-4. 2D CFD simulation of continuous CVD concept design. CFD results depict the steady-state mass fraction of C_2H_4 (a) and velocities (b) in both the growth and annealing zones of the continuous CVD concept design. Arrows indicate the gas flow direction.

7.3 Revolving substrate CVD prototype machine

Using the design concept as a guide, a desktop prototype was fabricated (Figure 7-5). The processing chamber is constructed from 6013 aluminum, with an outer diameter of 10.5", 1.25" thick side walls, and an overall height of 3.6" with a bottom floor thickness of 1". In order to separate the chamber into three zones, there are internal separating walls that rise to a height of 2" above the bottom floor of the chambers. Each of the separating walls features a hollow center, with ports at the bottom of the chamber for exhausting the reactant gases. Once the reactant

gases enter the chamber through the floor, they pass through the quartz/gold/quartz reflector via holes located beneath the substrate, impinge on the substrate, and then exit through slots in the reflector that line up with the hollow walls. This design allows for minimal mixing of the gases from each zone so as to retain three separate environments.

In order to enable substrate rotation, a 0.5" diameter piece of quartz tube is bonded to the center of the silicon wafer and then pinned to a central shaft that runs through the bottom of the chamber. Sealed by a polyurethane lip seal, and supported by PTFE sleeve bearings, the shaft is connected to a high-torque NEMA 17 step motor (Omega, OMHT17-075) at the bottom of the chamber to provide continuous rotation at low speeds.

The chamber is sealed with a Viton o-ring via a custom Ultra-Torr type fitting. With the quartz jar inverted over the chamber, the open end slips into a machined lip in the main chamber body. The o-ring slips over the jar and rests on an angled face in the chamber body. An aluminum insert then applies pressure to the o-ring via a threaded collar that mates to thread on the outside of the chamber. The quartz jar seals off the chamber from the surrounding environment, while allowing the wafer to be heated from above via radiation. Four 1000W halogen lamps supply the thermal energy to the wafer, and the rest of the exposed quartz jar is covered with a custom firebrick insulating cap. The heater is controlled via a PID controller and a phase angle SCR, with an IR temperature sensor feedback loop. A custom rotary device was designed to hold the IR temperature sensor and the halogen lamp assembly while rotating both at a rate of 12 rpm just above the quartz jar. The rotation minimizes the thermal gradients on the wafer.

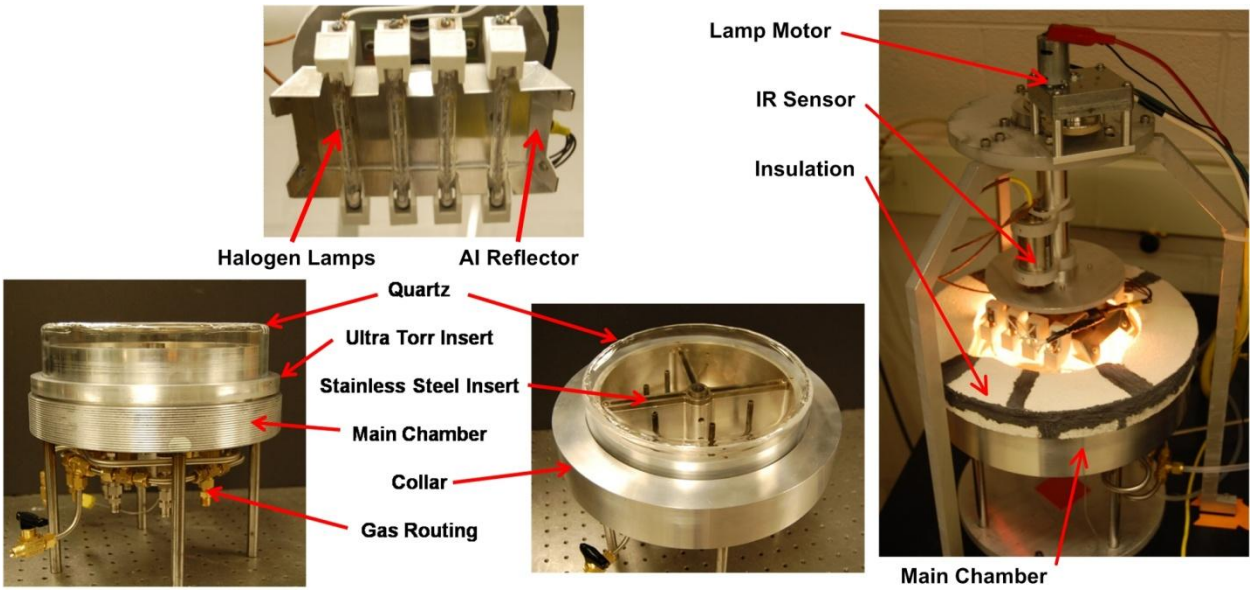

Figure 7-5. Revolving substrate CVD prototype. Optical images of the halogen lamp assembly (top), CVD chamber (bottom), and the rotary device for the lamp and IR sensor (right).

7.4 CNT Forest growth results

Prior to CNT forest growth a silicon wafer, coated with a supported catalyst film of 1/10 nm Fe/Al_2O_3 deposited by electron beam evaporation, is loaded into the chamber (or 1 cm x 1 cm samples from the wafer supported on a quartz wafer are loaded into the chamber). The chamber is then purged with He to establish an inert atmosphere before the wafer is heated. To ensure proper growth of CNT forests on the portion of the wafer that starts in the growth zone, each chamber is exposed to a 1:4 mixture of He and H_2 during the furnace temperature ramp to promote annealing. Once at temperature, the annealing zone receives a 1:4 mixture of He and H_2, and the growth zone receives a 4:1:1 mixture of He, H_2 and C_2H_4 (various total gas flows from 110 to 1000 sccm were attempted at these ratios). The substrate either remained stationary, for the purposes of investigating zone decoupling of the gas atmospheres, or was rotated at a rate of one revolution every 30 min. Once in the delamination zone, the CNT forests are optionally removed through mechanical means via a sharp edge to separate the forests from the substrate, and the process repeats.

While obtaining carbon deposits on a rotating wafer, we have only demonstrated static growth of CNT forests on individual substrates (1 cm x 1 cm) supported by a quartz wafer (Figure 7-6). The individual substrates were located at 90° intervals around the quartz wafer, corresponding to one location in the annealing zone, two in the growth zone, and one in the delamination zone. CNT forest growth on the substrates was found to be non-uniform, but we found that physical shielding, or "capping," of the catalyst improved film uniformity on individual samples. Unfortunately, this solution would impede the delamination of the CNT forests and subsequent re-growth, so it was not considered a viable option. Additionally, during these static experiments, carbon deposits or CNT forests were observed at each of the sample locations, indicating mixing of the gas treatment atmospheres. Reduced gas flow rates were used in an attempt to alleviate the issue of zone mixing and to increase the residence time potentially offered by the capping of the substrate. However, this did not combat either problem.

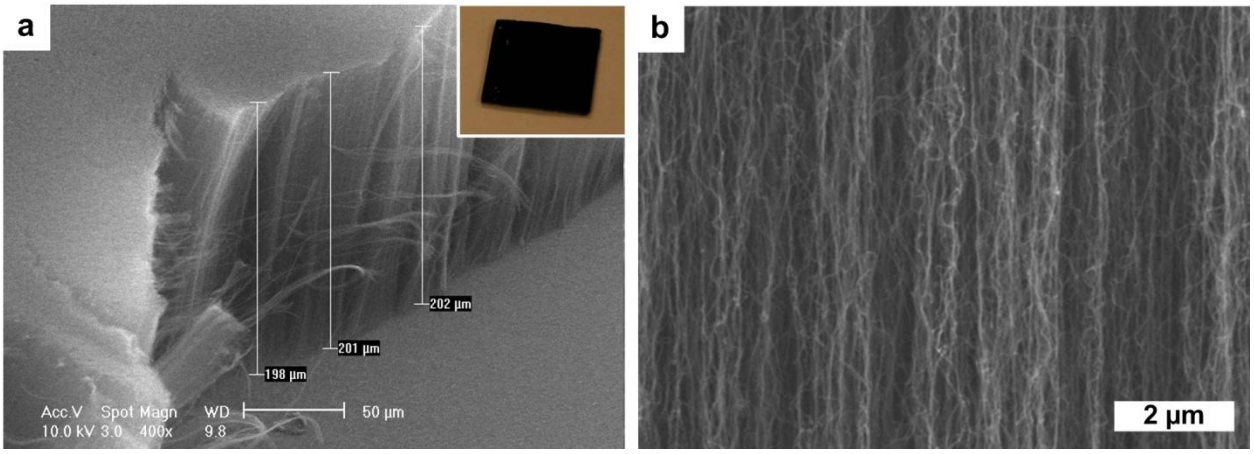

Figure 7-6. CNT forest growth from the CVD prototype machine. (a) SEM image of a CNT forest grown to a height of ~200 µm on a stationary sample in the CVD reactor, and an optical image of the 1 cm x 1 cm substrate (inset). (b) Magnified SEM image of the CNT forest sidewall from the sample in (a).

In an effort to reduce the mixing of the gas atmospheres and increase CNT forest uniformity, the gas outlets and inlets were switched. A custom cover for the hollow partition walls in the system was fabricated out of 304 stainless steel (Figure 7-7a). This cover directed the flow parallel to the wafer surface in an attempt to emulate the flow over a sample in a tube furnace reactor. However, we did not observe any noticeable differences in the CNT forest uniformity or mixing of gas atmospheres. A new 3D CFD model was created to study the mixing of the gases

(Figure 7-7b) and unlike the 2D model in Figure 7-4, a significant mass fraction of C_2H_4 (~ 0.2) was found in the annealing and delamination zones. Instead of exiting through the outlets in the zone floor, the gases flow over the zone partition walls and mix with the adjacent gases prior to exiting the system. Thus, a high temperature sealing or baffle solution is needed to achieve separate treatment zones.

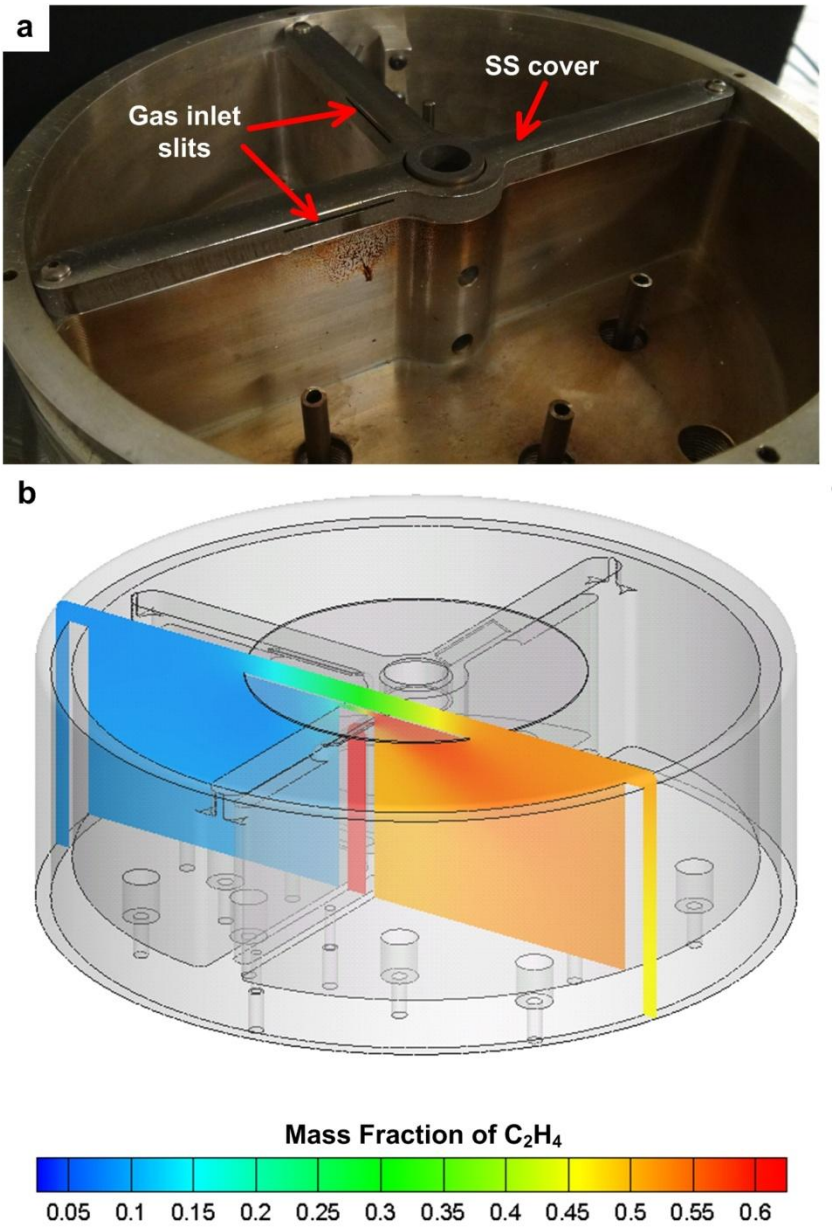

Figure 7-7. Modified gas flow in revolving substrate reactor. (a) Optical image of the SS wall cover and machined gas inlet slits. (b) 3D CFD model of C_2H_4 mass fraction. The contour slice shown bisects the annealing and growth zones where the mass fraction of C_2H_4 should be 0 and ~0.68 respectively.

7.5 CNT forest-substrate adhesion

The adhesion of the CNT forest to the substrate is a critical parameter for the delamination/transfer processing step. If the adhesion strength between the forest and the substrate is too low the forest could delaminate prior to the desired point in the process simply through substrate handling. This situation could cause loss of product or poorly controlled transfer to a secondary substrate due to wrinkling of the CNT forest. On the other hand, if the adhesion strength is too high the forest could become damaged or remove catalyst particles from the substrate during the delamination process. Pint et al. showed that post-growth cooling of the CNT forests in the growth atmosphere resulted in high adhesion strength to the substrate, and that a subsequent H_2O etch of the sample reduced the adhesion strength [272]. It has been hypothesized that the formation of an amorphous carbon layer on the CNT-catalyst particle interface during cooling in a carbon rich environment is the cause of this increase adhesion strength. Likewise, the subsequent etching of this layer reduces the interfacial adhesion strength. Understanding this phenomenon and developing post-growth treatment steps to engineer the adhesion strength would enable very controlled continuous delamination methods to be designed.

To gain an increased understanding of the CNT forest-substrate adhesion control afforded by post-growth treatments, we conducted delamination force measurments on multiple batch growths of CNT forests with varying post-growth treatments. Each sample was grown in a standard 1" tube furnace (Lindberg Blue M) at 775 °C using a gas composition of 400/100/100 $He/H_2/C_2H_4$ (all values are sccm), following an annealing step at the same temperature (10 min ramp and 10 min hold) and a gas flow of 100/400 He/H_2. The samples were grown for 30 min or 5 min, and the post-growth cooling step was completed in the growth gas environment or a flow of 1000 He. Delamination force was measured using a pressure transducer mounted to a vertical blade (Figure 7-8a). The sample was mounted on an adjustable z-axis stage such that the blade was ~20 µm above the CNT forest-substrate interface and normal to the substrate surface. A motorized liner stage translated the blade in the x-axis, making contact with the side of the forest, compressing it, and ultimately delaminating the forest from the substrate. The force versus displacement (collected by a laser displacement sensor) curves were collected and displayed through a Labview interface. Measurements were also conducted with a blade oriented parallel to the substrate, but forest buckling and slipping across the blade surface led to inconsistent data.

The results from the delamination force measurements verified that the adhesion strength was controllable, but not through the post growth treatments we used. CNT forests grown for both 5 and 30 min exhibited no change in forest-substrate adhesion whether they were cooled in He or the growth gases. However, the forests grown for 30 min exhibited much higher adhesion strength to the substrate than the forests grown for 5 min (Figure 7-8b). This was also indicated through the visible carbon layer remaining on the 30 min samples post delamination, whereas the 5 min samples were clean (Figure 7-8c). These growth times were selected based on knowledge that CNT forest growth terminates around 30 min with our catalyst and growth recipe. Therefore, we wanted to see the impact that terminated versus non-terminated growth had on the interface adhesion strength. While the terminated forest could have an amorphous layer of carbon binding the CNTs to the catalyst particles, decreased CNT density at the bottom of the forest could have also led to the buckling of CNTs and their subsequent alignment parallel to the substrate prior to growth termination [312]. These CNTs that are parallel to the substrate would have a much higher van der Waals interaction with the substrate and therefore act like a dry adhesive [71,287,313]. Regardless of the reason, this brief study added another tunable variable to enable the engineering of the CNT forest-substrate adhesion energy. Additional studies including multiple etchants, cooling rates and catalyst configurations are currently underway.

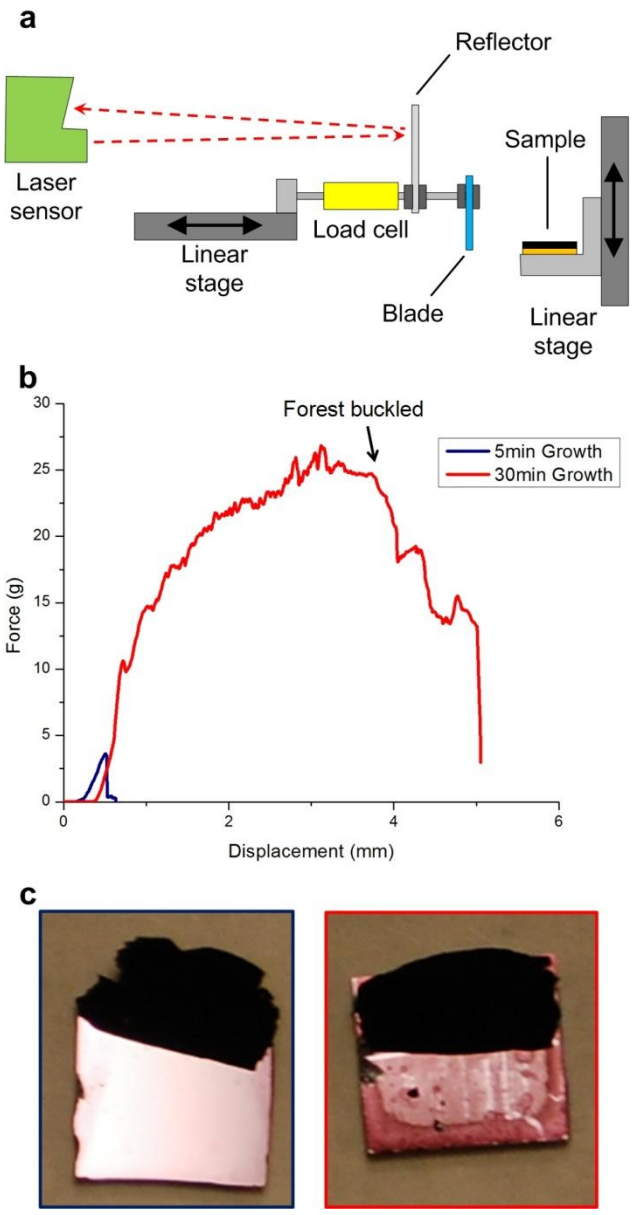

Figure 7-8. Delamination force measurements of CNT forests. (a) Schematic of the force measurement setup. (b) Comparison of delamination force vs. displacement for a 5 min and 30 min CNT forest growth. The forest for the 5 min sample completely delaminated prior to the blade translating across the entire surface. (c) Optical images of the 5 min (left) and 30 min (right) CNT forest growth samples after the delamination testing conducted in (b) (samples are 5 mm x 5 mm).

CHAPTER 8: CONTRIBUTIONS AND FUTURE WORK

8.1 Key contributions of this work

This thesis has investigated the CVD processing steps for the synthesis of CNT forests and graphene towards the goal of continuous, large-scale R2R implementation. Work towards this goal included: the understanding of control methods for each CVD processing step, a detailed study of CNT forest growth variation and the variables that impact the height and density of CNT forest growth, development of new techniques for large scale catalyst deposition and patterning using pre-formed catalyst particles, design and fabrication of a concentric tube CVD (CTCVD) reactor for R2R CNT forest and graphene growth on flexible substrates, and post-growth treatments to control the forest-substrate adhesion strength in conjunction with a revolving substrate CVD prototype reactor for CNT forest growth on Si wafers. The key contributions of this thesis include:

- A statistical analysis of 280 samples from 70 experiments over a 6 month period that identified key variables contributing to run-to-run variation in CNT forest growth [62]:
    - A standardized CNT forest growth procedure to enable the study of height and density variation;
    - Identified ambient humidity, barometric pressure, and sample position in the CVD furnace as the key variables that contributed significantly to experiment-to-experiment variation;
    - CVD system and process improvements including a continuous purge, accurate sample placement, and the use of stainless steel lines which reduced the run-to-run variation in CNT forest height and density by over 50%.

- Observation of a direct correlation between the catalyst particle size and spacing, and CNT diameter and spacing, with in-reactor humidity levels through quantitative AFM and SAXS analysis.

- Quantification of ambient water flux into an atmospheric CVD system through PTFE tubing.

- Development of a continuous-feed evaporative self-assembly process (blade-casting) to manufacture controllable arrays of nanoparticles from ferrofluids [63]:

    - Demonstration of carbon growth morphology and unprecedented decoupled diameter and density control for CNT forest growth through convective assembly process parameters (*i.e.*, concentration, particle diameter, and speed);

    - Achievement of CNT forest densities 3-fold higher that a typical thin-film catalyst at high particle concentration;

    - Demonstration of the R2R compatibility of the convective assembly process through initial CNT forest growth results achieved on flexible Cu foils;

    - Application of high vapor pressure solvent based ferrofluids for high speed convective assembly of catalyst particles towards commercial manufacturing rates.

- Concept, design and fabrication of a continuous R2R catalyst deposition machine that uses convective assembly.

- Process for scalable, cost effective method for depositing catalyst micropatterns for CNT growth, via laser printing of MICR toner [64]:

    - Control of CNT forest density through adjustable toner deposition via laser intensity;

    - Production of CNT forest micropillars with adjustable packing density using grayscale levels;
    - Demonstration of large-scale printing and transfer of laser printed MICR toner.

- Application of CNT forest micropillars grown from laser printed MICR toner as dry adhesives.
- Novel concept, design and fabrication of a concentric tube CVD (CTCVD) reactor:
    - Concentric tube design that enables the control of the reactor cross sectional area and a potential reduction of process gas volume by >90% compared to standard tube furnace CVD methods;
    - Decoupled gas treatment zones in a continuous thermal environment through the application of radial holes in the inner tube that enable the injection of the carbon precursor downstream in the system while annealing gases are injected at the upstream end of the concentric tube gap;
    - Increased substrate processing area through the application of substrate translation through a helical path around the inner tube.
- Demonstration of the first continuous CNT forest growth on metallic and ceramic fiber substrates where the CVD processes are in-line through the use of decoupled treatment zones at a rate of 33 mm/min using the CTCVD reactor.
- Graphene growth on Ni and Cu foils at rates of 25 - 495 mm/min using the CTCVD and Raman spectroscopy analysis of the post-growth substrates showing the quality dependence of the graphene on which processing steps the foil translates through.
- Design and fabrication of a revolving substrate CVD system for CNT forest growth on Si wafers by rotating through various processing zones and re-using the catalyst after forest delamination.

- *In situ* measurements of the CNT forest-substrate adhesion strength during delamination, and the control of this adhesion force through the variation of growth processing time resulting in an increased adhesion strength of >6x.

In addition to the work presented in this thesis, a collaborative effort with G. Nessim at Bar Ilan University resulted in the development and characterization of an easily controlled process for H_2O injection into a thermal CVD system by injecting small amounts of O_2 to react with H_2 and form H_2O [138]. This process provided additional control over the standard bubbler injection method.

8.2 Key questions and future directions

While the areas of CNT and graphene synthesis are rapidly expanding, with additional questions being answered every day, the work from this thesis raises some interesting research topics and questions about the materials and the processes used to create them. Several key R2R processing issues were raised in Chapter 2 and additional questions were discussed in the subsequent chapters regarding the synthesis of these materials. However, with the specific focus on CNT forests, the key question relating to commercial application is; what quantitative values need to be reached in order to match current bulk material performance?

Given their ability to withstand large mechanical loads and high current densities, CNTs offer a potential solution to the problems associated with using Cu for electrical contacts and vias with small dimensions in large scale integration (LSI) circuits [314]. However, to obtain the electrical currents needed to support current LSI devices, CNT forests are used instead of individual CNTs. Also, in order for the use of CNT forests to be beneficial, the electrical conductivity of the forest must meet or exceed that of Cu which is currently used in LSI circuits. Using a similar via example as Nihei et al., where the diameter and height are 100 nm and 500 nm respectively, the resistance of a Cu variant is approximately 6 Ω. Assuming ballistic transport through the CNTs, a quantum resistance of R = h/4e2 = 6.45 kΩ for each wall of the individual CNTs, and that all of the CNTs act as resistors in parallel, I calculated the necessary CNT forest properties needed to equal that of the Cu via (Figure 8-1). Each of the curves represents a number of CNT walls where the outer diameter (OD) and packing fraction (PF) of the CNTs in the forest needed to equal the resistance of Cu are shown. In order to exceed the

conductivity of Cu, the characteristic CNT values would need to be on the left side of the appropriate "number of walls" curve. While PF cannot exceed a hexagonally close packed (HCP) system, the values above this line are included only to assist in illustrating the required OD at the HCP limit to match Cu. The "X" represents the smallest OD (11.59 nm) CNT forest data from Ch. 4 which was generated from the 10 nm diameter ferrofluid catalyst particles.

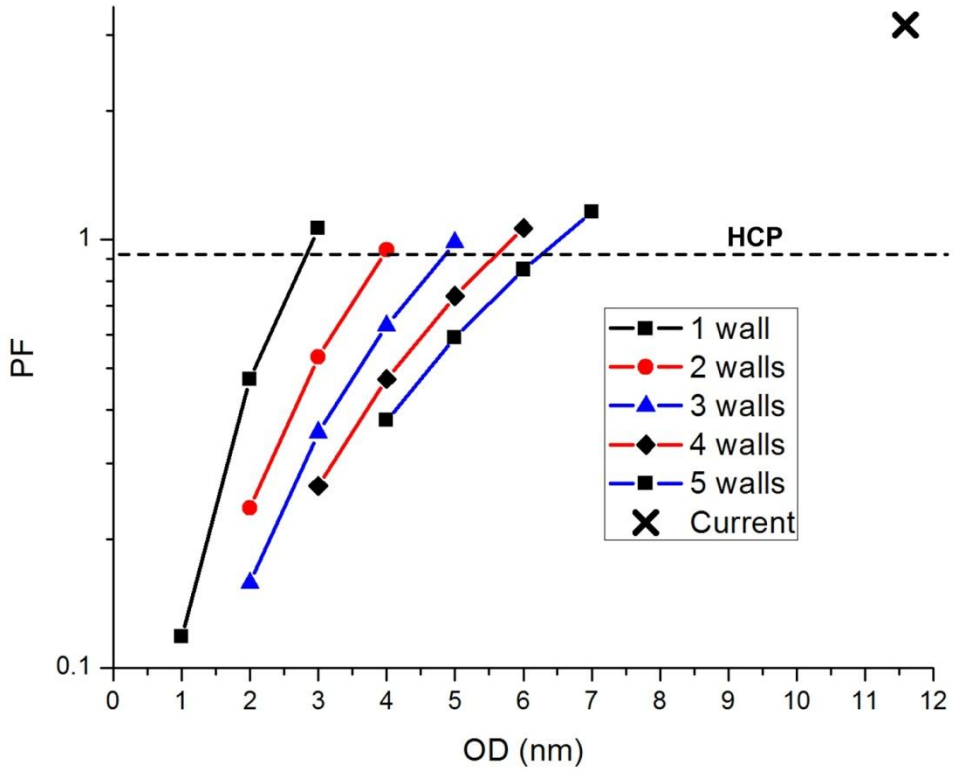

Figure 8-1. CNT forest characteristics needed to compete with Cu vias. The outer diameter (OD), packing fraction (PF) and number of walls shown are equal to the resistance of a similar Cu via.

Although it was shown in Ch. 4 that catalyst particles up to the HCP limit could be achieved, given the required PF of 3.2 for these particles, it is apparent that the OD of the CNTs, and thus the catalyst particles, must be reduced to create competitive electrical connections. Additionally, only ~6% of the catalyst particles were shown to produce CNTs, so the catalyst activation needs to be significantly increased to meet the PF requirements of the CNT forests. In Ch. 3 H_2O concentration was also shown to have a significant impact on the growth of CNTs. Thus, it is important to investigate the lower limit of preformed catalyst particle diameters along with answering questions aimed at providing a solution to these problems such as: How can the

catalyst particle activation be increased to realize bulk properties of CNT forests that rival some standard materials?; What is the effect of H_2O injection into the CVD system during the growth phase?; Does the H_2O increase particle activation only through the etching of amorphous deposits on the catalyst particles, or is it also playing a role in the hydrocarbon decomposition and formation of new species? Along with testing blade casting of smaller catalyst particles, experiments that explore thin film dewetting and CNT growth under various flows of H_2O injection into the CVD reactor will help answer these questions. Also, both H_2O injection via bubbler and injection of O_2 in separate experiments will reveal hydrocarbon species concentrations as a function of either the H_2O or residual un-reacted O_2, which will illustrate the individual effects of both compounds not specifically characterized in this thesis.

CNT forests can also be used as a thermal interface material (TIM) in place of conventional metal or ceramic particles in a silcone or similar polymer matrix. By utilizing a dry TIM, the limitations of temperature and lifetime due to a semi-fluid matrix are relaxed [315]. The goal of the TIM is to replace the air between the heat source (*i.e.* CPU) and the heat sink, which unless perfectly smooth create a gap between them known as the bond layer thickness (BLT). Given their high thermal conductivity (order of 1000 W/mK), CNTs much better thermal conductors than air (0.024 W/mK). However, given the purpose of a TIM, a compliant material is desired with good thermal contact between the heat source and the heat sink. While an increased number of CNTs in the forest are desired for thermal interfacial contact, a low CNT density enables a compliant structure and minimizes the interaction between individual CNTs. It is this interaction between the CNTs that increases phonon scattering and significantly reduces the overall thermal conductivity of the forest. Thus, by creating a set of high density micropillars of CNT forests that are slanted between the interface surfaces, an array of high thermal conductivity pillars could be created that can collapse upon loading to also provide a compliant structure. Of course to realize this, the mechanical coupling between CNTs and control of catalyst spacing will need to be investigated. Also, can catalyst particle monolayers be achieved through the tailoring of MICR toners and applying them to micropillar catalyst deposition via laser printing? If so, can the charge on the photoreceptor drum or laser intensity control the packing fraction and catalyst spacing? These questions require the development of dry powder toner mixtures with uniform pre-formed catalyst particles wrapped in polymer shells to act as the binder while not

creating an excessive binder to catalyst ratio, and design of a custom laser printing system with adjustable beam spot size, intensity and electrostatic forces.

Additionally, both of these applications, along with others, will require continuous processing of the materials and devices. What throughput would be expected from these techniques? Feeding into the throughput of a R2R system includes the investigation of each individual processing step and questions such as: How fast can catalyst particles be controllably assembled using convective assembly?; Can this technique be used to accomplished uniform assembly on large substrates using a very wide blade?; If a transfer technique is required to apply the materials on other substrates, what post-processing techniques enable the control of CNT-substrate adhesion, and how do they affect the quality of the CNTs?; Can these or similar techniques be applied to graphene without introducing defects in the crystal grains? Initial investigation of these questions can be accomplished through the further development of the continuous catalyst deposition machine, presented in Ch. 6, and characterization of the particle assembly at various speeds and temperatures towards the realization of commercial manufacturing speeds. If successful this would be followed by the creation of a larger scale system and subsequent characterization. Additionally, the design and fabrication of a continuous electrostatic delamination machine for use on CNT forests and graphene would enable a non-contact, continuous transfer technique. Significant studies of the nanomaterial interaction with the substrate and how to control this interface will also be needed to feed the design of the delamination process and machine.

These questions for the specific applications present many challenges in experimental planning and machine design of test devices, however they present the possibility of refined large scale processes for the synthesis of these materials. Answers to these questions will enable further tuning of CNT forest and graphene characteristics by adjusting process parameters. In addition to answering some of the questions above, my future research will also incorporate application of nanoscale materials and development of large scale nanometrology techniques and devices to control large scale uniformity. Thus, below are several exciting research topics that I will continue in 2013 at the University of Michigan, and further into my research career.

- Tailoring of metal alloy flexible substrates through metallurgical techniques to produce "super substrates" that increases catalyst density, lifetime and activation by controlling the catalyst particle size and distribution on the substrate for CNT forest growth. These substrates would ideally not require additional catalyst deposition.

- Design and fabrication of an *in situ* metrology device for large scale fabrication of nanomaterials. This system would most likely incorporate SAXS methods for detecting defects at the nanoscale. Development of real-time SAXS pattern analysis would also be studied towards the goal of this device being a feedback sensor for the CVD system.

- Design and test nanomaterial assemblies of flexible structures filled with ceramic nanoparticle solutions towards creating a damping material that then becomes very stiff as a load is applied (the ceramic nanoparticles jam together and create a stiff structure). Applications include underbody armor for vehicles that need to defeat both the shock wave of an explosion (damping) and hard projectiles that are later thrown at the vehicle by the blast (stiff).

The overall goal of each of these areas of research is the implementation of commercial manufacturing scales and speeds for the creation of CNT forests and graphene films for commercial applications. However, uniformity, repeatability and scalability still remain issues that prevent this transition. With the combination of the techniques and processes towards a complete R2R manufacturing process presented in this thesis, it is anticipated that continued interest in the area of R2R CVD synthesis of CNT forests and graphene will provide additional improvements in quality and throughput to catapult these techniques to full scale implementation. Given how far the community has come in the past decade, it is likely that we will successfully integrate these materials into multiple products that we use every day in the near future.

BIBLIOGRAPHY

[1] Y. Xia, P. Yang, Y. Sun, Y. Wu, B. Mayers, B. Gates, Y. Yin, F. Kim, H. Yan, *Advanced Materials* **2003**, *15*(5), 353–389.

[2] P. M. Ajayan, *Chemical Reviews* **1999**, *99*(7), 1787–1799.

[3] M. L. Terranova, V. Sessa, M. Rossi, *Chemical Vapor Deposition* **2006**, *12*(6), 315–325.

[4] E. T. Thostenson, Z. Ren, T.-W. Chou, *Composites Science and Technology* **2001**, *61*(13), 1899–1912.

[5] M. Treacy, T. Ebbesen, J. Gibson, *Nature* **1996**, *381*, 678–680.

[6] R. H. Baughman, A. A. Zakhidov, W. A. de Heer, *Science* **2002**, *297*(5582), 787–792.

[7] S. Berber, Y. Kwon, D. Tomanek, *Physical Review Letters* **2000**, *84*(20), 4613–6.

[8] P. Kim, L. Shi, a. Majumdar, P. McEuen, *Physical Review Letters* **2001**, *87*(21), 19–22.

[9] T. W. Ebbesen, H. J. Lezec, H. Hiura, J. W. Bennett, H. F. Ghaemi, T. Thio, *Nature* **1996**, *382*, 54–56.

[10] S. Frank, *Science* **1998**, *280*(5370), 1744–1746.

[11] J. M. Bonard, H. Kind, T. Stöckli, L. O. Nilsson, *Solid-State Electronics* **2001**, *45*, 893–914.

[12] E. Frackowiak, F. Béguin, *Carbon* **2002**, *40*(10), 1775–1787.

[13] K. Balasubramanian, M. Burghard, *Small* **2005**, *1*(2), 180–192.

[14] A. C. Dillon, K. M. Jones, T. A. Bekkedahl, C. H. Kiang, D. S. Bethune, M. J. Heben, *Nature* **1997**, *386*, 377–379.

[15] P. Avouris, Z. Chen, V. Perebeinos, *Nature Nanotechnology* **2007**, *2*(10), 605–615.

[16] O. Breuer, U. Sundararaj, *Polymer Composites* **2004**, *25*(6), 630–645.

[17] S. Iijima, *Nature* **1991**, *354*, 56–58.

[18] S. Iijima, T. Ichihashi, *Nature* **1993**, *363*, 603–605.

[19] M. Reibold, P. Paufler, a a Levin, W. Kochmann, N. Pätzke, D. C. Meyer, *Nature* **2006**, *444*(7117), 286.

[20] R. Bacon, *Journal of Applied Physics* **1960**, *31*(2), 283–290.

[21] A. Oberlin, M. Endo, T. Koyama, *Journal of Crystal Growth* **1976**, *32*, 335–349.

[22] M. Endo, *Chemtech* **1988**, *18*(9), 568–576.

[23] R. Baker, *Carbon* **1989**, *27*(3), 315–323.

[24] D. S. Bethune, C. H. Klang, M. S. de Vries, G. Gorman, R. Savoy, J. Vazquez, R. Beyers, *Nature* **1993**, *363*, 605–607.

[25] M. Endo, T. Hayashi, Y. A. Kim, M. Terrones, M. Dresselhaus, *Philosophical Transactions: Mathematical, Physical and Engineering Sciences* **2004**, *362*(1823), 2223–2238.

[26] T. W. Ebbesen, P. M. Ajayan, *Nature* **1992**, *358*, 220–222.

[27] H. Zhang, Y. Ding, C. Wu, Y. Chen, Y. Zhu, Y. He, S. Zhong, *Physica B: Condensed Matter* **2003**, *325*, 224–229.

[28] E. Munoz, W. K. Maser, A. M. Benito, G. F. de la Fuente, M. T. Martinez, *Synthetic Metals* **1999**, *103*, 2490–2491.

[29] A. a Puretzky, D. B. Geohegan, H. Schittenhelm, X. Fan, M. a Guillorn, *Applied Surface Science* **2002**, *197-198*, 552–562.

[30] M. Yudasaka, R. Kikuchi, T. Matsui, Y. Ohki, S. Yoshimura, E. Ota, *Applied Physics Letters* **1995**, *67*(17), 2477–2479.

[31] A. Magrez, J. W. Seo, R. Smajda, M. Mionić, L. Forró, *Materials* **2010**, *3*(11), 4871–4891.

[32] F. Danafar, a. Fakhru'l-Razi, M. A. M. Salleh, D. R. A. Biak, *Chemical Engineering Journal* **2009**, *155*(1-2), 37–48.

[33] M. Bedewy, E. R. Meshot, H. Guo, E. A. Verploegen, W. Lu, A. J. Hart, *The Journal of Physical Chemistry C* **2009**, *113*(48), 20576–20582.

[34] C. N. R. Rao, A. K. Sood, K. S. Subrahmanyam, A. Govindaraj, *Angewandte Chemie* **2009**, *48*(42), 7752–7777.

[35] S. Y. Zhou, G.-H. Gweon, A. V Fedorov, P. N. First, W. A. de Heer, D.-H. Lee, F. Guinea, A. H. Castro Neto, A. Lanzara, *Nature Materials* **2007**, *6*(10), 770–775.

[36] P. R. Wallace, *Physical Review* **1947**, *71*(9), 622–634.

[37] H. P. Boehm, A. Clauss, G. O. Fischer, U. Hofmann, *Journal for Nature Research Part B-Chemistry, Biochemistry, Biophysics, Biology and Related Areas* **1962**, *17*(3), 150.

[38] A. Morgan, G. Somorjai, *Surface Science* **1968**, *12*, 405–425.

[39] J. May, *Surface Science* **1969**, *17*, 267–270.

[40] T. A. Land, T. Michely, R. J. Behm, J. C. Hemminger, G. Comsa, *Surface science* **1992**, *264*, 261–270.

[41] A. J. Van Bommel, J. E. Crombeen, A. Van Tooren, *Surface Science* **1975**, *48*, 463–472.

[42] X. Lu, M. Yu, H. Huang, R. S. Ruoff, *Nanotechnology* **1999**, *10*(3), 269–272.

[43] K. S. Novoselov, A. K. Geim, S. V Morozov, D. Jiang, Y. Zhang, S. V Dubonos, I. V Grigorieva, A. A. Firsov, *Science* **2004**, *306*(5696), 666–669.

[44] A. Malesevic, R. Vitchev, K. Schouteden, A. Volodin, L. Zhang, G. Van Tendeloo, A. Vanhulsel, C. Van Haesendonck, *Nanotechnology* **2008**, *19*(30), 305604.

[45] S. Park, R. S. Ruoff, *Nature Nanotechnology* **2010**, *4*, 217–224.

[46] Y. Hernandez, V. Nicolosi, M. Lotya, F. M. Blighe, Z. Sun, S. De, I. T. McGovern, B. Holland, M. Byrne, Y. K. Gun'Ko, J. J. Boland, P. Niraj, G. Duesberg, S. Krishnamurthy, R. Goodhue, J. Hutchison, V. Scardaci, A. C. Ferrari, J. N. Coleman, *Nature Nanotechnology* **2008**, *3*(9), 563–568.

[47] S. Pei, H.-M. Cheng, *Carbon* **2012**, *50*(9), 3210–3228.

[48] D. Li, M. B. Müller, S. Gilje, R. B. Kaner, G. G. Wallace, *Nature nanotechnology* **2008**, *3*(2), 101–105.

[49] W. a. de Heer, C. Berger, X. Wu, P. N. First, E. H. Conrad, X. Li, T. Li, M. Sprinkle, J. Hass, M. L. Sadowski, M. Potemski, G. Martinez, *Solid State Communications* **2007**, *143*(1-2), 92–100.

[50] X. Li, W. Cai, J. An, S. Kim, J. Nah, D. Yang, R. Piner, A. Velamakanni, I. Jung, E. Tutuc, S. K. Banerjee, L. Colombo, R. S. Ruoff, *Science* **2009**, *324*(5932), 1312–4.

[51] C. Lee, X. Wei, J. W. Kysar, J. Hone, *Science* **2008**, *321*(5887), 385–388.

[52] A. A. Balandin, *Nature materials* **2011**, *10*(8), 569–81.

[53] J. Yu, G. Liu, A. V Sumant, V. Goyal, A. A. Balandin, *Nano Letters* **2012**, *12*(3), 1603–1608.

[54] K. S. Novoselov, V. I. Fal'ko, L. Colombo, P. R. Gellert, M. G. Schwab, K. Kim, *Nature* **2012**, *490*(7419), 192–200.

[55] F. Bonaccorso, Z. Sun, T. Hasan, A. C. Ferrari, *Nature Photonics* **2010**, *4*(9), 611–622.

[56] K. S. Kim, Y. Zhao, H. Jang, S. Y. Lee, J. M. Kim, K. S. Kim, J.-H. Ahn, P. Kim, J.-Y. Choi, B. H. Hong, *Nature* **2009**, *457*(7230), 706–710.

[57] Y. Zhang, Y.-W. Tan, H. L. Stormer, P. Kim, *Nature* **2005**, *438*(7065), 201–204.

[58] S. Yasuda, D. N. Futaba, T. Yamada, J. Satou, A. Shibuya, H. Takai, K. Arakawa, M. Yumura, K. Hata, *ACS Nano* **2009**, *3*(12), 4164–4170.

[59] S. Bae, H. Kim, Y. Lee, X. Xu, J. Park, Y. Zheng, J. Balakrishnan, T. Lei, H. R. Kim, Y. Il Song, Y. Kim, K. S. Kim, *Nature Nanotechnology* **2010**, *5*(8), 574–578.

[60] R. Guzmán de Villoria, S. L. Figueredo, a J. Hart, S. a Steiner, a H. Slocum, B. L. Wardle, *Nanotechnology* **2009**, *20*(40), 405611.

[61] T. Yamada, M. Ishihara, J. Kim, M. Hasegawa, S. Iijima, *Carbon* **2012**, *50*(7), 2615–2619.

[62] C. R. Oliver, E. S. Polsen, E. R. Meshot, S. H. Tawfick, S. J. Park, A. J. Hart, *ACS Nano* **2013**, DOI 10.1021/nn400507y.

[63] E. S. Polsen, M. Bedewy, A. J. Hart, *Small* **2013**, DOI 10.1002/smll.201202878.

[64] E. S. Polsen, A. G. Stevens, A. J. Hart, *ACS Applied Materials & Interfaces* **2013**, DOI 10.1021/am400148t.

[65] E. S. Polsen, S. M. Perkins, E. R. Meshot, D. Copic, M. Bedewy, A. J. Hart, A. Arbor, S. Figueredo, B. L. Wardle, in *Proceedings of the 17th Annual International Conference on Composite Materials (ICCM)*, **2009**.

[66] E. S. Polsen, S. H. Tawfick, E. R. Meshot, A. J. Hart, in *38th Annual North American Manufacturing Research Conference*, **2010**.

[67] Y. Liu, S. Kumar, *Polymer Reviews* **2012**, *52*(3-4), 234–258.

[68] E. Fitzer, W. Frohs, M. Heine, *Carbon* **1986**, *24*(4), 387–395.

[69] X. Huang, *Materials* **2009**, *2*(4), 2369–2403.

[70] Z. Ren, Z. Huang, J. Xu, J. Wang, P. Bush, M. Siegal, P. Provencio, *Science* **1998**, *282*(5391), 1105–1107.

[71] B. Chen, P. G. Oppenheimer, T. A. V. Shean, C. T. Wirth, S. Hofmann, J. Robertson, *The Journal of Physical Chemistry C* **2012**, *116*, 20047–20053.

[72] S. Dörfler, a. Meier, S. Thieme, P. Németh, H. Althues, S. Kaskel, *Chemical Physics Letters* **2011**, *511*(4-6), 288–293.

[73] N. T. Alvarez, A. Orbaek, A. R. Barron, J. M. Tour, R. H. Hauge, *ACS applied materials & interfaces* **2010**, *2*(1), 15–18.

[74] R. Haubner, W. Schwinger, J. Haring, R. Schöftner, *Diamond and Related Materials* **2008**, *17*(7-10), 1452–1457.

[75] B. Dittert, I. Bergmair, R. Haubner, R. Schöftner, *Surface and Coatings Technology* **2010**, *204*(21-22), 3647–3651.

[76] W. Z. Li, S. S. Xie, L. X. Qian, B. H. Chang, B. S. Zou, W. Y. Zhou, A. Zhao, G. Wang, *Science* **1996**, *274*(5293), 1701–1703.

[77] F. C. Krebs, *Solar Energy Materials and Solar Cells* **2009**, *93*(9), 1636–1641.

[78] T. Yamada, T. Namai, K. Hata, *Nature Nanotechnology* **2006**, *1*, 131–136.

[79] Y. Y. Wei, G. Eres, V. I. Merkulov, D. H. Lowndes, *Applied Physics Letters* **2001**, *78*(10), 1394–1396.

[80] K. Liu, Y. Sun, L. Chen, C. Feng, X. Feng, K. Jiang, Y. Zhao, S. Fan, *Nano letters* **2008**, *8*(2), 700–705.

[81] Y. Zhang, Y. Li, W. Kim, D. Wang, H. Dai, *Applied Physics A: Materials Science & Processing* **2002**, *74*(3), 325–328.

[82] E. F. Kukovitsky, S. G. L'vov, N. A. Sainov, V. A. Shustov, L. A. Chernozatonskii, *Chemical Physics Letters* **2002**, *355*, 497–503.

[83] N. T. Alvarez, F. Li, C. L. Pint, J. T. Mayo, E. Z. Fisher, J. M. Tour, V. L. Colvin, R. H. Hauge, *Chemistry of Materials* **2011**, *23*(15), 3466–3475.

[84] C.-H. Chang, H. J. In, S. Takahashi, M. Deterre, H. J. Choi, K. W. Gotrik, G. Barbastathis, *Nanotechnology* **2011**, *22*(3), 035301(1)–035301(5).

[85] G. S. Choi, Y. S. Cho, K. H. Son, D. J. Kim, *Microelectronic Engineering* **2003**, *66*(1-4), 77–82.

[86] S. S. Lee, C. Zhang, Z. a. Lewicka, M. Cho, J. T. Mayo, W. W. Yu, R. H. Hauge, V. L. Colvin, *The Journal of Physical Chemistry C* **2012**, *116*(18), 10287–10295.

[87] E. R. Meshot, E. Verploegen, M. Bedewy, S. Tawfick, A. R. Woll, K. S. Green, M. Hromalik, L. J. Koerner, H. T. Philipp, M. W. Tate, S. M. Gruner, A. J. Hart, *ACS Nano* **2012**, *6*(6), 5091–5101.

[88] C. V. Thompson, *Annual Review of Materials Research* **2012**, *42*(1), 399–434.

[89] R. D. Bennett, A. J. Hart, R. E. Cohen, *Advanced Materials* **2006**, *18*(17), 2274–2279.

[90] G. D. Nessim, A. J. Hart, J. S. Kim, D. Acquaviva, J. Oh, C. D. Morgan, M. Seita, J. S. Leib, C. V Thompson, *Nano Letters* **2008**, *8*(11), 3587–3593.

[91] E. R. Meshot, D. L. Plata, S. Tawfick, Y. Zhang, E. A. Verploegen, A. J. Hart, *ACS Nano* **2009**, *3*(9), 2477–2486.

[92] J. Robertson, G. Zhong, C. S. Esconjauregui, B. C. Bayer, C. Zhang, M. Fouquet, S. Hofmann, *Japanese Journal of Applied Physics* **2012**, *51*(1), 01AH01(1)–01AH01(8).

[93] S. Esconjauregui, M. Fouquet, B. C. Bayer, C. Ducati, R. Smajda, S. Hofmann, J. Robertson, *ACS Nano* **2010**, *4*(12), 7431–7436.

[94] S. Sakurai, H. Nishino, D. N. Futaba, S. Yasuda, T. Yamada, A. Maigne, Y. Matsuo, E. Nakamura, M. Yumura, K. Hata, *Journal of the American Chemical Society* **2012**, *134*(4), 2148–2153.

[95] A. Reina, X. Jia, J. Ho, D. Nezich, H. Son, V. Bulovic, M. S. Dresselhaus, J. Kong, *Nano letters* **2009**, *9*(1), 30–35.

[96] G. Odahara, S. Otani, C. Oshima, M. Suzuki, T. Yasue, T. Koshikawa, *Surface Science* **2011**, *605*(11-12), 1095–1098.

[97] L. Gao, J. R. Guest, N. P. Guisinger, *Nano letters* **2010**, *10*(9), 3512–3516.

[98] X. Li, W. Cai, L. Colombo, R. S. Ruoff, *Nano letters* **2009**, *9*(12), 4268–4272.

[99] R. S. Edwards, K. S. Coleman, *Accounts of chemical research* **2013**, *46*(1), 23–30.

[100] H. Ueta, M. Saida, C. Nakai, Y. Yamada, M. Sasaki, S. Yamamoto, *Surface Science* **2004**, *560*(1-3), 183–190.

[101] L. Nilsson, M. Andersen, J. Bjerre, R. Balog, B. Hammer, L. Hornekær, I. Stensgaard, *Surface Science* **2012**, *606*(3-4), 464–469.

[102] P. Zeller, S. Dänhardt, S. Gsell, M. Schreck, J. Wintterlin, *Surface Science* **2012**, *606*(19-20), 1475–1480.

[103] J. Coraux, A. T. N'Diaye, C. Busse, T. Michely, *Nano Letters* **2008**, *8*(2), 565–70.

[104] P. W. Sutter, J.-I. Flege, E. a Sutter, *Nature materials* **2008**, *7*(5), 406–411.

[105] D. Jiang, M.-H. Du, S. Dai, *The Journal of Chemical Physics* **2009**, *130*(7), 074705(1)–074705(5).

[106] A. T. Murdock, A. Koos, T. Ben Britton, L. Houben, T. Batten, T. Zhang, A. J. Wilkinson, R. E. Dunin-Borkowski, C. E. Lekka, N. Grobert, *ACS nano* **2013**, *7*(2), 1351–9.

[107] A. W. Robertson, J. H. Warner, *Nano letters* **2011**, *11*(3), 1182–9.

[108] S. Thiele, A. Reina, P. Healey, J. Kedzierski, P. Wyatt, P.-L. Hsu, C. Keast, J. Schaefer, J. Kong, *Nanotechnology* **2010**, *21*(1), 015601(1)–015601(9).

[109] M. E. Ramon, A. Gupta, C. Corbet, D. A. Ferrer, H. C. P. Movva, M. E. Ram, G. Carpenter, L. Colombo, G. Bourianoff, M. Doczy, D. Akinwande, E. Tutuc, S. K. Banerjee, *ACS Nano* **2011**, *5*(9), 7198–7204.

[110] Q. Yu, L. a Jauregui, W. Wu, R. Colby, J. Tian, Z. Su, H. Cao, Z. Liu, D. Pandey, D. Wei, T. F. Chung, P. Peng, N. P. Guisinger, E. a Stach, J. Bao, S.-S. Pei, Y. P. Chen, *Nature materials* **2011**, *10*(6), 443–449.

[111] K. Nishimura, N. Okazaki, L. Pan, Y. Nakayama, *Japanese Journal of Applied Physics* **2004**, *43*(No. 4A), L471–L474.

[112] S. Hofmann, R. Sharma, C. Ducati, G. Du, C. Mattevi, C. Cepek, M. Cantoro, S. Pisana, A. Parvez, F. Cervantes-Sodi, A. C. Ferrari, R. Dunin-Borkowski, S. Lizzit, L. Petaccia, A. Goldoni, J. Robertson, *Nano Letters* **2007**, *7*(3), 602–608.

[113] D. Plata, E. Meshot, C. Reddy, *ACS Nano* **2010**, *4*(12), 7185–7192.

[114] G. Zhong, S. Hofmann, F. Yan, H. Telg, J. H. Warner, D. Eder, C. Thomsen, W. I. Milne, J. Robertson, *The Journal of Physical Chemistry C* **2009**, *113*(40), 17321–17325.

[115] G. D. Nessim, M. Seita, D. L. Plata, K. P. O'Brien, A. J. Hart, E. R. Meshot, C. M. Reddy, P. M. Gschwend, C. V. Thompson, *Carbon* **2011**, *49*(3), 804–810.

[116] F. Ding, K. Bolton, A. Rose, *Journal of Physical Chemistry B* **2004**, *108*, 17369–17377.

[117] J. C. Burgos, H. Reyna, B. I. Yakobson, P. B. Balbuena, *The Journal of Physical Chemistry C* **2010**, *114*, 6952–6958.

[118] D. Schebarchov, S. C. Hendy, E. Ertekin, J. C. Grossman, *Physical Review Letters* **2011**, *107*(18), 185503(1)–185503(5).

[119] D. Futaba, K. Hata, T. Yamada, K. Mizuno, M. Yumura, S. Iijima, *Physical Review Letters* **2005**, *95*(5), 056104(1)–056101(4).

[120] D. N. Futaba, K. Hata, T. Namai, T. Yamada, K. Mizuno, Y. Hayamizu, M. Yumura, S. Iijima, *The journal of physical chemistry. B* **2006**, *110*(15), 8035–8.

[121] R. Xiang, E. Einarsson, J. Okawa, Y. Miyauchi, S. Maruyama, *The Journal of Physical Chemistry C* **2009**, *113*(18), 7511–7515.

[122] A. Magrez, J. W. Seo, V. L. Kuznetsov, L. Forró, *Angewandte Chemie* **2007**, *46*(3), 441–444.

[123] T. Yamada, A. Maigne, M. Yudasaka, K. Mizuno, D. N. Futaba, M. Yumura, S. Iijima, K. Hata, *Nano Letters* **2008**, *8*(12), 4288–4292.

[124] J. H. Yen, I. C. Leu, C. C. Lin, M. H. Hon, *Diamond and Related Materials* **2004**, *13*(4-8), 1237–1241.

[125] P. B. Amama, C. L. Pint, F. Mirri, M. Pasquali, R. H. Hauge, B. Maruyama, *Carbon* **2012**, *50*(7), 2396–2406.

[126] C. Zhang, R. Xie, B. Chen, J. Yang, G. Zhong, J. Robertson, *Carbon* **2013**, *53*, 339–345.

[127] G. H. Han, F. Güneş, J. J. Bae, E. S. Kim, S. J. Chae, H.-J. Shin, J.-Y. Choi, D. Pribat, Y. H. Lee, *Nano Letters* **2011**, *11*(10), 4144–4148.

[128] J. Gao, J. Yip, J. Zhao, B. I. Yakobson, F. Ding, *Journal of the American Chemical Society* **2011**, *133*(13), 5009–5015.

[129] Q. Li, H. Chou, J.-H. Zhong, J.-Y. Liu, A. Dolocan, J. Zhang, Y. Zhou, R. S. Ruoff, S. Chen, W. Cai, *Nano Letters* **2013**, *13*(2), 486–490.

[130] A. A. Puretzky, D. B. Geohegan, S. Jesse, I. N. Ivanov, G. Eres, *Applied Physics A* **2005**, *81*(2), 223–240.

[131] F. Ding, A. R. Harutyunyan, B. I. Yakobson, *Proceedings of the National Academy of Sciences of the United States of America* **2009**, *106*(8), 2506–9.

[132] A. R. Harutyunyan, G. Chen, T. M. Paronyan, E. M. Pigos, O. a Kuznetsov, K. Hewaparakrama, S. M. Kim, D. Zakharov, E. a Stach, G. U. Sumanasekera, *Science (New York, N.Y.)* **2009**, *326*(5949), 116–20.

[133] C. J. Strobl, C. Schäflein, U. Beierlein, J. Ebbecke, A. Wixforth, *Applied Physics Letters* **2004**, *85*(8), 1427–1429.

[134] A. Ural, Y. Li, H. Dai, *Applied Physics Letters* **2002**, *81*(18), 3464.

[135] T. Matsuda, M. Mesko, T. Ishikawa, J. Sato, A. Ogino, R. Tamura, M. Nagatsu, *Japanese Journal of Applied Physics* **2008**, *47*(9), 7436–7439.

[136] M. Stadermann, S. P. Sherlock, J.-B. In, F. Fornasiero, H. G. Park, A. B. Artyukhin, Y. Wang, J. J. De Yoreo, C. P. Grigoropoulos, O. Bakajin, A. a Chernov, A. Noy, *Nano Letters* **2009**, *9*(2), 738–744.

[137] K. Hata, D. N. Futaba, K. Mizuno, T. Namai, M. Yumura, S. Iijima, *Science* **2004**, *306*(5700), 1362–1364.

[138] G. D. Nessim, A. Al-Obeidi, H. Grisaru, E. S. Polsen, C. R. Oliver, T. Zimrin, A. J. Hart, D. Aurbach, C. V. Thompson, *Carbon* **2012**, *50*(11), 4002–4009.

[139] A. Magrez, J. W. Seo, R. Smajda, B. Korbely, J. C. Andresen, M. Mionić, S. Casimirius, L. Forró, *ACS nano* **2010**, *4*(7), 3702–8.

[140] K. Liu, P. Liu, K. Jiang, S. Fan, *Carbon* **2007**, *45*(12), 2379–2387.

[141] V. I. Artyukhov, Y. Liu, B. I. Yakobson, *Proceedings of the National Academy of Sciences of the United States of America* **2012**, *109*(38), 15136–15140.

[142] F. Banhart, J. Kotakoski, A. V Krasheninnikov, *ACS nano* **2011**, *5*(1), 26–41.

[143] Z. Sun, A. Raji, Y. Zhu, C. Xiang, Z. Yan, C. Kittrell, E. L. G. Samuel, J. M. Tour, *ACS Nano* **2012**, *6*(11), 9790–9796.

[144] M. Sarno, C. Cirillo, R. Piscitelli, P. Ciambelli, *Journal of Molecular Catalysis A: Chemical* **2013**, *366*, 303–314.

[145] D. Wei, B. Wu, Y. Guo, G. Yu, Y. Liu, *Accounts of chemical research* **2013**, *46*(1), 106–115.

[146] Z. Yan, J. Lin, Z. Peng, Z. Sun, Y. Zhu, L. Li, C. Xiang, E. L. Samuel, C. Kittrell, J. M. Tour, *ACS Nano* **2012**, *6*(10), 9110–9117.

[147] T. Wu, G. Ding, H. Shen, H. Wang, L. Sun, D. Jiang, X. Xie, M. Jiang, *Advanced Functional Materials* **2013**, *23*(2), 198–203.

[148] S. Chen, H. Ji, H. Chou, Q. Li, H. Li, J. W. Suk, R. Piner, L. Liao, W. Cai, R. S. Ruoff, *Advanced Materialss* **2013**, DOI 10.1002/adma.201204000.

[149] J. Bin In, D. Lee, F. Fornasiero, A. Noy, C. P. Grigoropoulos, *ACS nano* **2012**, *6*(9), 7858–7866.

[150] N. Patil, A. Lin, E. R. Myers, K. Ryu, A. Badmaev, C. Zhou, H. P. Wong, S. Mitra, *IEEE Transactions on Nanotechnology* **2009**, *8*(4), 498–504.

[151] E. J. Garcia, B. L. Wardle, a. John Hart, *Composites Part A: Applied Science and Manufacturing* **2008**, *39*(6), 1065–1070.

[152] T. Y. Tsai, C. Y. Lee, N. H. Tai, W. H. Tuan, *Applied Physics Letters* **2009**, *95*(1), 013107(1)–013107(3).

[153] A. Kumar, V. L. Pushparaj, S. Kar, O. Nalamasu, P. M. Ajayan, R. Baskaran, *Applied Physics Letters* **2006**, *89*(16), 163120(1)–163120(3).

[154] X. Li, Y. Zhu, W. Cai, M. Borysiak, B. Han, D. Chen, R. D. Piner, L. Colombo, R. S. Ruoff, *Nano letters* **2009**, *9*(12), 4359–63.

[155] X. Liang, B. a Sperling, I. Calizo, G. Cheng, C. A. Hacker, Q. Zhang, Y. Obeng, K. Yan, H. Peng, Q. Li, X. Zhu, H. Yuan, A. R. H. Walker, Z. Liu, L.-M. Peng, C. a Richter, *ACS Nano* **2011**, *5*(11), 9144–9153.

[156] C. J. Lockhart de la Rosa, J. Sun, N. Lindvall, M. T. Cole, Y. Nam, M. Löffler, E. Olsson, K. B. K. Teo, A. Yurgens, *Applied Physics Letters* **2013**, *102*(2), 022101(1)–022101(4).

[157] C. Kim, J. Y. Woo, J. Choi, J. Park, C.-S. Han, *Scripta Materialia* **2012**, *66*(8), 535–537.

[158] Z. Juang, C. Wu, A. Lu, C. Su, K. Leou, F. Chen, C. Tsai, *Carbon* **2010**, *48*(11), 3169–3174.

[159] K. Jiang, Q. Li, S. Fan, *Nature* **2002**, *419*, 801.

[160] K. Jiang, J. Wang, Q. Li, L. Liu, C. Liu, S. Fan, *Advanced Materials* **2011**, *23*(9), 1154–1161.

[161] R. Guzman de Villoria, A. J. Hart, B. L. Wardle, *ACS Nano* **2011**, *5*(6), 4850–4857.

[162] H. C. Malecki, M. Zupan, *Composites Part A: Applied Science and Manufacturing* **2012**, *43*(11), 1914–1920.

[163] T. Hiraoka, T. Yamada, K. Hata, D. N. Futaba, K. Hiroyuki, S. Uemura, M. Yumura, S. Iijima, *Journal of the American Chemical Society* **2006**, *128*(41), 13338–13339.

[164] S. Dörfler, I. Felhösi, I. Kék, T. Marek, H. Althues, S. Kaskel, L. Nyikos, *Journal of Power Sources* **2012**, *208*, 426–433.

[165] J. Chen, a. I. Minett, Y. Liu, C. Lynam, P. Sherrell, C. Wang, G. G. Wallace, *Advanced Materials* **2008**, *20*(3), 566–570.

[166] R. Andrews, D. Jacques, A. M. Rao, F. Derbyshire, D. Qian, X. Fan, E. C. Dickey, J. Chen, *Chemical Physics Letters* **1999**, *303*, 467–474.

[167] R. Xiang, G. H. Luo, W. Z. Qian, Y. Wang, F. Wei, Q. Li, *Chemical Vapor Deposition* **2007**, *13*(10), 533–536.

[168] D. Y. Kim, H. Sugime, K. Hasegawa, T. Osawa, S. Noda, *Carbon* **2011**, *49*(6), 1972–1979.

[169] F. Liu, Y. Zhang, *Carbon* **2010**, *48*(9), 2394–2400.

[170] C. Y. Su, A. Y. Lu, C. Y. Wu, Y. T. Li, K. K. Liu, W. Zhang, S. Y. Lin, Z. Y. Juang, Y. L. Zhong, F. R. Chen, L. J. Li, *Nano Letters* **2011**, *11*, 3612–3616.

[171] Y. Lee, S. Bae, H. Jang, S. Jang, S.-E. Zhu, S. H. Sim, Y. Il Song, B. H. Hong, J.-H. Ahn, *Nano Letters* **2010**, *10*(2), 490–493.

[172] T. Hesjedal, *Applied Physics Letters* **2011**, *98*(13), 133106(1)–133106(3).

[173] T. Kobayashi, M. Bando, N. Kimura, K. Shimizu, K. Kadono, N. Umezu, K. Miyahara, S. Hayazaki, S. Nagai, Y. Mizuguchi, Y. Murakami, D. Hobara, *Applied Physics Letters* **2013**, *102*(2), 023112(1)–023112(4).

[174] I. Vlassiouk, P. Fulvio, H. Meyer, N. Lavrik, S. Dai, P. Datskos, S. Smirnov, *Carbon* **2013**, *54*, 58–67.

[175] B. Chen, P. Wu, *Carbon* **2005**, *43*(15), 3172–3177.

[176] M. D. Abad, J. C. Sánchez-López, a. Berenguer-Murcia, V. B. Golovko, M. Cantoro, a. E. H. Wheatley, a. Fernández, B. F. G. Johnson, J. Robertson, *Diamond and Related Materials* **2008**, *17*(11), 1853–1857.

[177] S. K. Pal, S. Talapatra, S. Kar, L. Ci, R. Vajtai, T. Borca-Tasciuc, L. S. Schadler, P. M. Ajayan, *Nanotechnology* **2008**, *19*(4), 045610(1)–045610(5).

[178] C. Masarapu, B. Wei, *Langmuir : the ACS journal of surfaces and colloids* **2007**, *23*(17), 9046–9049.

[179] R. L. Vander Wal, T. M. Ticich, V. E. Curtis, *Carbon* **2001**, *39*(15), 2277–2289.

[180] S. P. Patole, H.-I. Kim, J.-H. Jung, A. S. Patole, H.-J. Kim, I.-T. Han, V. N. Bhoraskar, J.-B. Yoo, *Carbon* **2011**, DOI 10.1016/j.carbon.2011.04.051.

[181] P. M. Parthangal, R. E. Cavicchi, M. R. Zachariah, *Nanotechnology* **2007**, *18*(18), 185605(1)–185605(5).

[182] W. Lin, R. Zhang, K.-S. Moon, C. Wong, *IEEE Transactions on Advanced Packaging* **2010**, *33*(2), 370–376.

[183] B.-W. Kim, H.-G. Chung, B.-K. Min, H.-G. Kim, W. Kim, *Bulletin of the Korean Chemical Society* **2010**, *31*(12), 3697–3702.

[184] E. Garcia, B. Wardle, A. J. Hart, N. Yamamoto, *Composites Science and Technology* **2008**, *68*(9), 2034–2041.

[185] N. Yamamoto, a. John Hart, E. J. Garcia, S. S. Wicks, H. M. Duong, A. H. Slocum, B. L. Wardle, *Carbon* **2009**, *47*(3), 551–560.

[186] T. Shah, *Applied NanoStructured Solutions LLC Carbon Nanostructure (CN) Infusion*, **2011**.

[187] G. D. Nessim, D. Acquaviva, M. Seita, K. P. O'Brien, C. V. Thompson, *Advanced Functional Materials* **2010**, *20*(8), 1306–1312.

[188] W. M. M. (Erwin) Kessels, M. Putkonen, *MRS Bulletin* **2011**, *36*(11), 907–913.

[189] P. S. Maydannik, T. O. Kääriäinen, D. C. Cameron, *Chemical Engineering Journal* **2011**, *171*(1), 345–349.

[190] K. Lahtinen, P. Maydannik, P. Johansson, T. Kääriäinen, D. C. Cameron, J. Kuusipalo, *Surface and Coatings Technology* **2011**, *205*(15), 3916–3922.

[191] F. C. Krebs, S. a. Gevorgyan, J. Alstrup, *Journal of Materials Chemistry* **2009**, *19*(30), 5442–5451.

[192] F. C. Krebs, T. Tromholt, M. Jørgensen, *Nanoscale* **2010**, *2*(6), 873–886.

[193] N. G. Shang, Y. Y. Tan, V. Stolojan, P. Papakonstantinou, S. R. P. Silva, *Nanotechnology* **2010**, *21*(50), 505604(1)–505604(6).

[194] B. C. Bayer, S. Hofmann, R. Blume, C. Baehtz, S. Esconjauregui, C. T. Wirth, R. A. Oliver, C. Ducati, R. Schl, A. Goldoni, C. Cepek, J. Robertson, *The Journal of Physical Chemistry C* **2011**, *115*, 4359–4369.

[195] S. Hofmann, C. Ducati, J. Robertson, B. Kleinsorge, *Applied Physics Letters* **2003**, *83*(1), 135–137.

[196] M. Daw, M. Baskes, *Physical Review Letters* **1983**, *50*(17), 285–288.

[197] W.-T. Geng, A. J. Freeman, G. B. Olson, Y. Tateyama, T. Ohno, *Materials Transactions* **2005**, *46*(4), 756–760.

[198] B. Michel, a. Bernard, a. Bietsch, E. Delamarche, M. Geissler, D. Juncker, H. Kind, J.-P. Renault, H. Rothuizen, H. Schmid, P. Schmidt-Winkel, R. Stutz, H. Wolf, *IBM Journal of Research and Development* **2001**, *45*(5), 697–719.

[199] S. H. Ahn, L. J. Guo, *Advanced Materials* **2008**, *20*(11), 2044–2049.

[200] M. Jung, J. Kim, J. Noh, N. Lim, C. Lim, G. Lee, J. Kim, H. Kang, K. Jung, A. D. Leonard, J. M. Tour, G. Cho, *IEEE Transactions on Electron Devices* **2010**, *57*(3), 571–580.

[201] T.-M. Lee, J.-H. Noh, C. H. Kim, J. Jo, D.-S. Kim, *Thin Solid Films* **2010**, *518*(12), 3355–3359.

[202] K. Jain, M. Klosner, M. Zemel, S. Raghunandan, *Proceedings of the IEEE* **2005**, *93*(8), 1500–1510.

[203] M. C. Roco, C. A. Mirkin, M. C. Hersam, *Nanotechnology Research Directions for Societal Needs in 2020*, Springer, **2010**.

[204] H. Huang, C. H. Liu, Y. Wu, S. Fan, *Advanced Materials* **2005**, *17*(13), 1652–1656.

[205] A. M. Marconnet, N. Yamamoto, M. a Panzer, B. L. Wardle, K. E. Goodson, *ACS Nano* **2011**, *5*(6), 4818–4825.

[206] T. Tong, Y. Zhao, L. Delzeit, A. Kashani, M. Meyyappan, A. Majumdar, *IEEE Transactions on Components and Packaging Technologies* **2007**, *30*(1), 92–100.

[207] W. Fu, L. Liu, K. Jiang, Q. Li, S. Fan, *Carbon* **2010**, *48*(7), 1876–1879.

[208] S. Tawfick, K. O'Brien, A. J. Hart, *Small* **2009**, *5*(21), 2467–2473.

[209] G. D. Nessim, *Nanoscale* **2010**, *2*(8), 1306–1323.

[210] F. L. Deepak, a. Govindaraj, C. N. R. Rao, *Journal of Chemical Sciences* **2006**, *118*(1), 9–14.

[211] A. Cao, X. Zhang, C. Xu, J. Liang, D. Wu, B. Wei, *Journal of Materials Research* **2011**, *16*(11), 3107–3110.

[212] G. Zhang, D. Mann, L. Zhang, A. Javey, Y. Li, E. Yenilmez, Q. Wang, J. P. McVittie, Y. Nishi, J. Gibbons, H. Dai, *Proceedings of the National Academy of Sciences of the United States of America* **2005**, *102*(45), 16141–16145.

[213] D. N. Futaba, J. Goto, S. Yasuda, T. Yamada, M. Yumura, K. Hata, *Advanced Materials* **2009**, *21*(47), 4811–4815.

[214] D. L. Plata, A. J. Hart, C. M. Reddy, P. M. Gschwend, *Environmental Science & Technology* **2009**, *43*(21), 8367–8373.

[215] M. Bedewy, E. R. Meshot, M. J. Reinker, A. J. Hart, *ACS Nano* **2011**, *5*(11), 8974–8989.

[216] A. J. Hart, A. H. Slocum, *The Journal of Physical Chemistry B* **2006**, *110*(16), 8250–8257.

[217] S. Chakrabarti, T. Nagasaka, Y. Yoshikawa, L. Pan, Y. Nakayama, *Japanese Journal of Applied Physics* **2006**, *45*(28), L720–L722.

[218] S. W. Raudenbush, W. Liu, A. Martinez, J. Spybrook, **2011**.

[219] B. Jeon, Q. Van Overmeere, A. C. T. van Duin, S. Ramanathan, *Physical chemistry chemical physics : PCCP* **2013**, *15*(6), 1821–1830.

[220] W. Stumm, G. F. Lee, *Industrial and Engineering Chemistry* **1961**, *53*, 143–146.

[221] G. W. R. Leibbrandt, G. Hoogers, F. H. P. M. Habraken, *Physical Review Letters* **1992**, *68*(12), 1947–1950.

[222] M. Morita, T. Ohmi, E. Hasegawa, M. Kawakami, M. Ohwada, *Journal of Applied Physics* **1990**, *68*(3), 1272–1281.

[223] J. Bin In, C. P. Grigoropoulos, A. A. Chernov, A. Noy, *Applied Physics Letters* **2011**, *98*(15), 153102(1)–153102(3).

[224] J. Bin In, C. P. Grigoropoulos, A. A. Chernov, A. Noy, *ACS Nano* **2011**, *5*(12), 9602–9610.

[225] B. N. Wang, R. D. Bennett, E. Verploegen, A. J. Hart, R. E. Cohen, *Journal of Physical Chemistry C* **2007**, *111*(16), 5859–5865.

[226] E. R. Meshot, A. J. Hart, *Applied Physics Letters* **2008**, *92*(11), 113107(1)–113107(3).

[227] P. B. Amama, C. L. Pint, L. McJilton, S. M. Kim, E. A. Stach, P. T. Murray, R. H. Hauge, B. Maruyama, *Nano Letters* **2009**, *9*(1), 44–49.

[228] M. Bedewy, E. R. Meshot, a. J. Hart, *Carbon* **2012**, *50*(14), 5106–5116.

[229] A. Magrez, R. Smajda, J. W. Seo, E. Horváth, P. R. Ribic, J. C. Andresen, D. Acquaviva, A. Olariu, G. Laurenczy, L. Forró, *ACS Nano* **2011**, *5*(5), 3428–3437.

[230] R. Wischert, P. Laurent, C. Copéret, F. Delbecq, P. Sautet, *Journal of the American Chemical Society* **2012**, *134*(35), 14430–14449.

[231] G. Li, S. Chakrabarti, M. Schulz, V. Shanov, *Carbon* **2010**, *48*(7), 2111–2115.

[232] G. Eres, A. a Kinkhabwala, H. Cui, D. B. Geohegan, A. a Puretzky, D. H. Lowndes, *The Journal of Physical Chemistry B* **2005**, *109*(35), 16684–16694.

[233] H. Richter, J. . Howard, *Progress in Energy and Combustion Science* **2000**, *26*(4-6), 565–608.

[234] C. R. Oliver, W. Westrick, J. Koehler, T. Cruz-Gonzalez, A. Brieland-Shoultz, A. J. Hart, *(In Preparation)* **n.d.**

[235] D. Copic, S. J. Park, S. Tawfick, M. De Volder, A. J. Hart, *Journal of Visualized Experiments* **2012**, (65), e3980.

[236] B. J. Hinds, N. Chopra, T. Rantell, R. Andrews, V. Gavalas, L. G. Bachas, *Science* **2004**, *303*(5654), 62–65.

[237] A. Kalra, S. Garde, G. Hummer, *Proceedings of the National Academy of Sciences of the United States of America* **2003**, *100*(18), 10175–10180.

[238] L. Sun, R. M. Crooks, *Journal of the American Chemical Society* **2000**, *122*(49), 12340–12345.

[239] F. Javier del Campo, J. García-Céspedes, F. Xavier Muñoz, E. Bertrán, *Electrochemistry Communications* **2008**, *10*(9), 1242–1245.

[240] S. Fan, W. Liang, H. Dang, N. Franklin, T. Tombler, M. Chapline, H. Dai, *Physica E: Low-dimensional Systems and Nanostructures* **2000**, *8*(2), 179–183.

[241] S. Fan, M. G. Chapline, N. R. Franklin, T. W. Tombler, A. M. Cassell, H. Dai, *Science* **1999**, *283*(5401), 512–514.

[242] K. Yoshihara, S. Honda, J.-G. Lee, H. Mori, K. Oura, M. Katayama, *Japanese Journal of Applied Physics* **2008**, *47*(No. 4), 1941–1943.

[243] Y. T. Chou, Y. T. Ko, M. F. Yan, *Journal of the American Ceramic Society* **1987**, *70*(10), 280–282.

[244] H. J. Kim, M. J. M. Krane, K. P. Trumble, K. J. Bowman, *Journal of the American Ceramic Society* **2006**, *89*(9), 2769–2775.

[245] B. G. Prevo, O. D. Velev, *Langmuir* **2004**, *20*(6), 2099–2107.

[246] L. Malaquin, T. Kraus, H. Schmid, E. Delamarche, H. Wolf, *Langmuir* **2007**, *23*(23), 11513–11521.

[247] P. Kumnorkaew, Y. Ee, N. Tansu, J. F. Gilchrist, *Langmuir* **2008**, *24*(21), 12150–12157.

[248] M. I. Bodnarchuk, M. V Kovalenko, S. Pichler, G. Fritz-Popovski, G. Hesser, W. Heiss, *ACS nano* **2010**, *4*(1), 423–431.

[249] H. Yang, P. Jiang, *Langmuir* **2010**, *26*(16), 13173–13182.

[250] Y. Tian, B. Yu, X. Li, K. Li, *Journal of Materials Chemistry* **2011**, *21*(8), 2476–2481.

[251] Y. Zhu, F. Y. Jiang, K. Chen, F. Kang, Z. K. Tang, *Journal of Alloys and Compounds* **2011**, *509*(34), 8549–8553.

[252] C. Y. Wang, J. M. Hong, G. Chen, Y. Zhang, N. Gu, *Chinese Chemical Letters* **2010**, *21*(2), 179–182.

[253] S. Guo, D. Li, L. Zhang, J. Li, E. Wang, *Biomaterials* **2009**, *30*(10), 1881–1889.

[254] J. Salado, M. Insausti, I. Gil de Muro, L. Lezama, T. Rojo, *Journal of Non-Crystalline Solids* **2008**, *354*(47-51), 5207–5209.

[255] W. W. Yu, J. C. Falkner, C. T. Yavuz, V. L. Colvin, *Chemical Communications* **2004**, *40*(20), 2306–2307.

[256] S. G. Kwon, Y. Piao, J. Park, S. Angappane, Y. Jo, N.-M. Hwang, J.-G. Park, T. Hyeon, *Journal of the American Chemical Society* **2007**, *129*(41), 12571–12584.

[257] B. G. Prevo, D. M. Kuncicky, O. D. Velev, *Colloids and Surfaces A: Physicochemical and Engineering Aspects* **2007**, *311*(1-3), 2–10.

[258] B. G. Prevo, J. C. Fuller, O. D. Velev, *Chemistry of Materials* **2005**, *17*(1), 28–35.

[259] T. P. Bigioni, X.-M. Lin, T. T. Nguyen, E. I. Corwin, T. A. Witten, H. M. Jaeger, *Nature Materials* **2006**, *5*(4), 265–270.

[260] A. S. Dimitrov, K. Nagayama, *Langmuir* **1996**, *12*(5), 1303–1311.

[261] T. Cabioc'h, E. Thune, J. P. Rivière, S. Camelio, J. C. Girard, P. Guérin, M. Jaouen, L. Henrard, P. Lambin, *Journal of Applied Physics* **2002**, *91*(3), 1560–1567.

[262] C. He, N. Zhao, C. Shi, X. Du, J. Li, L. Cui, *Journal of Alloys and Compounds* **2006**, *425*(1-2), 329–333.

[263] Z. Abdullaeva, E. Omurzak, C. Iwamoto, H. S. Ganapathy, S. Sulaimankulova, C. Liliang, T. Mashimo, *Carbon* **2012**, *50*(5), 1776–1785.

[264] N. Latorre, E. Romeo, F. Cazana, T. Ubieto, C. Royo, I. Villacampa, A. Monzon, *The Journal of Physical Chemistry C* **2010**, *114*(11), 4773–4782.

[265] T. D. L. Arcos, F. Vonau, M. G. Garnier, V. Thommen, H.-G. Boyen, P. Oelhafen, *Applied Physics Letters* **2002**, *80*(13), 2383–2385.

[266] M. Retsch, Z. Zhou, S. Rivera, M. Kappl, X. S. Zhao, U. Jonas, Q. Li, *Macromolecular Chemistry and Physics* **2009**, *210*(3-4), 230–241.

[267] A. Dong, X. Ye, J. Chen, C. B. Murray, *Nano Letters* **2011**, *11*(4), 1804–1809.

[268] T. Wen, S. Majetich, *ACS Nano* **2011**, *5*(11), 8868–8876.

[269] L. Gao, A. Peng, Z. Y. Wang, H. Zhang, Z. Shi, Z. Gu, G. Cao, B. Ding, *Solid State Communications* **2008**, *146*(9-10), 380–383.

[270] D. N. Futaba, K. Hata, T. Yamada, T. Hiraoka, Y. Hayamizu, Y. Kakudate, O. Tanaike, H. Hatori, M. Yumura, S. Iijima, *Nature Materials* **2006**, *5*(12), 987–994.

[271] H. Wang, J. Feng, X. Hu, K. M. Ng, *Journal of Physical Chemistry C* **2007**, *111*(34), 12617–12624.

[272] C. L. Pint, Y.-Q. Xu, M. Pasquali, R. H. Hauge, *ACS Nano* **2008**, *2*(9), 1871–1878.

[273] B. Derby, *Annual Review of Materials Research* **2010**, *40*(1), 395–414.

[274] H. Schift, *Journal of Vacuum Science & Technology B: Microelectronics and Nanometer Structures* **2008**, *26*(2), 458.

[275] W. K. T. Coltro, D. P. de Jesus, J. A. F. da Silva, C. L. do Lago, E. Carrilho, *Electrophoresis* **2010**, *31*(15), 2487–2498.

[276] W. K. T. Coltro, E. Piccin, J. A. Fracassi da Silva, C. Lucio do Lago, E. Carrilho, *Lab on a chip* **2007**, *7*(7), 931–4.

[277] A. W. Martinez, S. T. Phillips, M. J. Butte, G. M. Whitesides, *Angewandte Chemie (International ed. in English)* **2007**, *46*(8), 1318–20.

[278] C. R. Barry, M. G. Steward, N. Z. Lwin, H. O. Jacobs, *Nanotechnology* **2003**, *14*(10), 1057–1063.

[279] L. Qu, L. Dai, M. Stone, Z. Xia, Z. Wang, *Science* **2008**, *322*(October), 238–242.

[280] J. Lee, A. Chandrashekar, in *Solid-State Sensors, Actuators and Microsystems*, **2005**, pp. 1943–1946.

[281] M. Mansoor, I. Kinloch, B. Derby, *Key Engineering Materials* **2010**, *442*, 7–14.

[282] J.-M. Bonard, N. Weiss, H. Kind, T. Stöckli, L. Forró, K. Kern, A. Chatelain, *Advanced Materials* **2001**, *13*(3), 184–188.

[283] A. M. Cassell, G. C. McCool, H. T. Ng, J. E. Koehne, B. Chen, J. Li, J. Han, M. Meyyappan, *Applied Physics Letters* **2003**, *82*(5), 817–819.

[284] Z.-M. Wang, J. Wagner, S. Wall, *Aerosol Science and Technology* **2011**, *45*(9), 1060–1068.

[285] A. Dupuis, *Progress in Materials Science* **2005**, *50*(8), 929–961.

[286] C. T. Wirth, B. C. Bayer, A. D. Gamalski, S. Esconjauregui, R. S. Weatherup, C. Ducati, C. Baehtz, J. Robertson, S. Hofmann, *Chemistry of Materials* **2012**, *24*(24), 4633–4640.

[287] L. Ge, S. Sethi, L. Ci, P. M. Ajayan, A. Dhinojwala, *Proceedings of the National Academy of Sciences of the United States of America* **2007**, *104*(26), 10792–5.

[288] L. Huang, W.-Y. Xu, Y.-D. Que, Y. Pan, M. Gao, L.-D. Pan, H.-M. Guo, Y.-L. Wang, S.-X. Du, H.-J. Gao, *Chinese Physics B* **2012**, *21*(8), 088102(1)–088102(5).

[289] J. H. Chu, J. Kwak, T.-Y. Kwon, S.-D. Park, H. Go, S. Y. Kim, K. Park, S. Kang, S.-Y. Kwon, *ACS Applied Materials & Interfaces* **2012**, *4*(3), 1777–1782.

[290] Y. Chen, D. Ciuparu, S. Lim, Y. Yang, G. L. Haller, L. Pfefferle, *Journal of Catalysis* **2004**, *225*(2), 453–465.

[291] J. Cheng, X. P. Zou, *Advanced Materials Research* **2011**, *264-265*, 837–842.

[292] W. Li, J. Wen, Z. Ren, *Applied Physics A: Materials Science & Processing* **2002**, *74*, 397–402.

[293] H. Kim, K. S. Kim, J. Kang, Y. C. Park, K.-Y. Chun, J.-H. Boo, Y.-J. Kim, B. H. Hong, J.-B. Choi, *Nanotechnology* **2011**, *22*(9), 095303(1)–095303(5).

[294] D. Park, Y. H. Kim, J. K. Lee, *Carbon* **2003**, *41*, 1025–1029.

[295] M. Meyyappan, *Journal of Physics D: Applied Physics* **2009**, *42*(21), 213001(1)–213001(15).

[296] J. L. Qi, W. T. Zheng, X. H. Zheng, X. Wang, H. W. Tian, *Applied Surface Science* **2011**, *257*(15), 6531–6534.

[297] S. Chiashi, Y. Murakami, Y. Miyauchi, S. Maruyama, *Chemical Physics Letters* **2004**, *386*(1-3), 89–94.

[298] P. Finnie, a. Li-Pook-Than, J. Lefebvre, D. G. Austing, *Carbon* **2006**, *44*(15), 3199–3206.

[299] L. Huang, Q. H. Chang, G. L. Guo, Y. Liu, Y. Q. Xie, T. Wang, B. Ling, H. F. Yang, *Carbon* **2012**, *50*(2), 551–556.

[300] W. Cai, R. D. Piner, Y. Zhu, X. Li, Z. Tan, H. C. Floresca, C. Yang, L. Lu, M. J. Kim, R. S. Ruoff, *Nano Research* **2009**, *2*(11), 851–856.

[301] M. L. Healy, L. J. Dahlben, J. a. Isaacs, *Journal of Industrial Ecology* **2008**, *12*(3), 376–393.

[302] H. C. Malecki, M. Zupan, *Composites Part A: Applied Science and Manufacturing* **2012**, *43*(11), 1914–1920.

[303] R. M. Taziev, V. Y. Prinz, *Nanotechnology* **2011**, *22*(30), 305705(1)–305705(10).

[304] A. Pirkle, J. Chan, A. Venugopal, D. Hinojos, C. W. Magnuson, S. McDonnell, L. Colombo, E. M. Vogel, R. S. Ruoff, R. M. Wallace, *Applied Physics Letters* **2011**, *99*(12), 122108(1)–122108(3).

[305] S. J. Chae, F. Güneş, K. K. Kim, E. S. Kim, G. H. Han, S. M. Kim, H.-J. Shin, S.-M. Yoon, J.-Y. Choi, M. H. Park, C. W. Yang, D. Pribat, Y. H. Lee, *Advanced Materials* **2009**, *21*(22), 2328–2333.

[306] N. T. Alvarez, C. E. Hamilton, C. L. Pint, A. Orbaek, J. Yao, A. L. Frosinini, A. R. Barron, J. M. Tour, R. H. Hauge, *ACS applied materials & interfaces* **2010**, *2*(7), 1851–1856.

[307] C. L. Pint, N. Nicholas, J. G. Duque, a. N. G. Parra-Vasquez, M. Pasquali, R. Hauge, *Chemistry of Materials* **2009**, *21*(8), 1550–1556.

[308] C.-C. Chiu, M. Yoshimura, K. Ueda, *Japanese Journal of Applied Physics* **2008**, *47*(4), 1952–1955.

[309] A. J. Hart, A. H. Slocum, B. L. Wardle, E. J. Garcia, *Continuous Process for the Production of Nanostructures Including Nanotubes*, **2006**.

[310] H. Ago, N. Ishigami, N. Yoshihara, K. Imamoto, S. Akita, *Journal of Physical Chemistry C* **2008**, 1735–1738.

[311] A. J. Hart, L. van Laake, A. H. Slocum, *Small* **2007**, *3*(5), 772–777.

[312] M. Bedewy, E. R. Meshot, E. S. Polsen, S. H. Tawfick, A. J. Hart, in *Society for the Advancement of Material and Process Engineering2*, **2010**.

[313] L. Qu, L. Dai, *Advanced Materials* **2007**, *19*(22), 3844–3849.

[314] M. Nihei, M. Horibe, A. Kawabata, Y. Awano, *Japanese Journal of Applied Physics* **2004**, *43*(4B), 1856–1859.

[315] R. Prasher, *Proceedings of the IEEE* **2006**, *94*(8), 1571–1586.